Matrix approach for ultrasound imaging and quantification

William Lambert

PSL UNIVERSITÉ PARIS

THÈSE DE DOCTORAT
DE L'UNIVERSITÉ PSL

Préparée à ESPCI PARIS

Matrix approach for ultrasound imaging and quantification

Approche matricielle de l'imagerie et de la quantification ultrasonore

Soutenue par
William LAMBERT
Le 14 décembre 2020

École doctorale n°564
Physique en Ile-de-France

Spécialité
Physique

Confidentielle jusqu'au 25/03/2022

Composition du jury :

Stefan CATHELINE Directeur de recherche, INSERM	*Président du jury*
Emmanuel BOSSY Professeur, Université de Grenoble	*Rapporteur*
Michael JAEGER Privat dozent, Universität Bern	*Rapporteur*
Habib AMMARI Professor, ETH Zurich	*Examinateur*
Marie MULLER Assistant professor, NCSU	*Examinateur*
Christophe FRASCHINI SuperSonic Imagine	*Co-Directeur de thèse*
Alexandre AUBRY Chargé de recherche, CNRS	*Directeur de thèse*
Mathias FINK Professeur, ESPCI Paris	*Directeur de thèse*

ESPCI PARIS | PSL

HOLOGIC SUPERSONIC imagine

Remerciements

Je souhaite avant tout remercier mes deux directeurs de thèse Alexandre Aubry et Mathias Fink pour leurs soutiens, leurs conseils toujours avisés et leur encadrement d'exception pendant ces presque quatre années de stage de master puis de thèse. Ils ont formé une équipe incroyable grâce à leurs grandes qualités humaines et scientifiques.

Plus précisément, je remercie Alexandre Aubry pour sa patience et sa disponibilité. Il a été un remarquable guide auprès duquel j'ai appris énormément et qui a toujours réussi à trouver une solution aux problèmes rencontrés. Ses connaissances scientifiques, son abnégation, sa rigueur et son intégrité en font un chercheur d'exception qui continue à m'impressionner quotidiennement. Je le remercie profondément pour tout ce qu'il m'a donné au cours de cette thèse. Enfin, merci d'avoir été présent jusque tard dans la nuit ou le week-end pour relire (et corriger) mon manuscrit de thèse et pour la préparation de la soutenance.

Merci à Mathias Fink que j'ai rencontré pour la première fois à Supersonic Imagine il y a 6 ans et qui a accepté de me recommander auprès de William Kupermann pour un stage de recherche en acoustique sous-marine à San Diego. Merci de m'avoir une nouvelle fois fait confiance pour mon stage de master qui a débouché sur cette thèse. Ses immenses connaissances dans le domaine de la physique des ondes (et en particulier dans le domaine des ultrasons) ont très souvent permis de faire avancer le projet dans la bonne direction. Malgré son emploi du temps de ministre, Mathias a toujours réussi à s'investir dans ce projet et son bureau m'a toujours été ouvert. Grâce à ses grandes qualités de pédagogue, son aide a été précieuse pour la préparation des différentes conférences et de la soutenance. Enfin, je souhaite souligner son optimisme, son dynamisme, son enthousiasme et son charisme exceptionnel qui m'ont permis de rester motivé tout au long de cette thèse et d'apprécier mon travail.

Je souhaite remercier l'entreprise Supersonic Imagine pour avoir financé et contribué au bon déroulement de cette thèse. Merci à Jacques Souquet, Jérémy Bercoff et Christophe Fraschini pour la mise en place de ce projet. Je remercie chaleureusement tous les membres du groupe ultrason tant passés (Mathieu, David, Jérémy, Fred, Ling) que présents (Christophe, Thomas, Laurent, Bo, Simon, Morgane, Natalia, Nicolas) qui m'ont toujours parfaitement accueilli à Aix, rendant ces visites dans le Sud des plus agréables. Je les remercie également pour leur intérêt dans ce projet et leur expertise clinique qui a permis d'envisager et d'orienter cette thèse vers de nombreuses applications potentielles. En particulier, je souhaite remercier Mathieu qui m'a encadré durant mon stage ingénieur et la première partie de cette thèse et qui a su faire naître en moi une véritable passion pour l'acoustique. Merci à Thomas et Christophe pour leur encadrement durant la seconde partie de cette thèse et pour leur soutien. Je remercie également Murielle Greusard pour

son investissement et sa rigueur (Ô combien nécessaire) dans l'élaboration des brevets. Je la remercie également pour avoir corrigé et relu mon premier chapitre de thèse. Merci à Patrice Loubat pour m'avoir initié à l'art du dépôt de brevet.

Je remercie les membres de l'équipe réminiscence avec qui j'ai pris plaisir à travailler. Merci à Victor Barolle et Laura Cobus pour avoir été présent au début de ma thèse et d'avoir répondu à mes premières questions sur l'approche matricielle. Merci à Flavien Bureau, Elsa Giraudat et Arthur LeBer pour avoir choisi de continuer les travaux de recherche sur l'approche matricielle en acoustique. Merci à Paul Balondrade, Ulysse Najar, Rita Touma et Thibault Blondel dont leurs propres travaux en optique et sismologie ont inspiré cette thèse. Je remercie également Cécile Brütt, Claire Prada, Jean-Luc Gennisson, Marion Bied, Pierre Millien et Jacques Marchal pour toutes les interactions scientifiques ou autres que j'ai eu au cours de cette thèse. En particulier, merci à Marion pour la relecture de mon manuscrit.

J'adresse également mes remerciements aux membres de mon jury, Pr. Emmanuel Bossy et Dr. Michael Jaeger, qui ont accepté de rapporter mon travail, ainsi que Pr. Habib Amari, Dr. Stefan Catheline et Dr. Marie Muller.

J'en viens aux remerciements plus personnels, merci aux membres du bureau R33 avec qui j'ai partagé de nombreuses journées (et petites lichettes), merci à François, Guillaume, Jeanne, Elise, Chloé, Gauthier, Benjamin, Arthur, Guillaume. Merci également aux autres doctorants du Langevin qui ont contribué à cette bonne ambiance et à ma bonne santé mentale (et à celle de mon foie). Merci aux amis de longue date Pierre, Théophile, Loïc, Edouard, Pierre; aux amis d'école Majid, Etienne, Johanne, Jet, Sarfate, Cécilia, Maxime, Régis, Elia, Florian; sans oublier les amis de prépa Julien et Ronan. Enfin j'aimerai remercier ma famille.

Je dédie cette thèse à Constance. Merci de tout mon cœur pour ton soutien sans faille et ses encouragements depuis de nombreuses années ... et merci de m'avoir accompagné pendant cette fin de thèse mouvementée.

Contents

Résumé

Au cours des dernières décennies, l'échographie médicale a connu une croissance exponentielle et est devenu aujourd'hui, l'une des modalités d'imagerie médicale les plus utilisées. Celle-ci permet le diagnostic d'un large spectre de maladies de façon non-invasif et à faible coût.

L'échographie médical a bénéficié de l'amélioration continue des systèmes électroniques. Les sondes sont maintenant constituées d'un grand nombre de transducteurs. Ceux-ci sont contrôlés de façon indépendante, permettant d'émettre et de mesurer des champs de pression complexes. De plus, l'accroissement des capacités de calculs des échographes a ouvert la voie au développement et à l'utilisation de techniques d'imagerie complexes. Celles-ci permettent d'accéder à une qualité d'image sans précédents et à de nouveaux outils de caractérisation des tissus mous. Cette thèse s'inscrit dans ce contexte et pose les bases d'une nouvelle approche matricielle pour l'échographie.

Les techniques d'imagerie confocales sont celles qui permettent aujourd'hui d'obtenir la meilleure qualité d'image. Elles sont basées sur une double focalisation à l'émission et en réception en chaque point du milieu, correspondant à chaque pixel de l'image. Deux hypothèses fondamentales sont nécessaires au processus de focalisation. Tout d'abord, le milieu est considéré comme homogène avec une vitesse du son constante. Ensuite, les échos mesurés par la sonde sont traités comme résultant uniquement de phénomènes de diffusion simple. Néanmoins, ces hypothèses ne sont pas toujours valides. Les tissus mous peuvent présenter de fortes disparités de vitesse du son. Ces fluctuations distordent les fronts d'onde incidents et réfléchis, ce qui réduit la qualité de focalisation des faisceaux acoustiques qui ne sont alors plus limités par les phénomènes de diffraction. De plus, des variations brutales de la vitesse du son du milieu peuvent générer des artéfacts de réverbérations. En outre des phénomènes de diffusion multiple apparaissent nécessairement entre des diffuseurs du milieu. Ceux-ci génèrent des échos parasites qui induisent un bruit de fond incohérent dans les signaux RF. Ces deux phénomènes indésirables, c'est-à-dire les aberrations et la diffusion multiple, dégradent la résolution et le contraste de l'image échographique et impactent le diagnostic d'un examen médical. Il y a donc un besoin évident à développer de nouveaux outils afin de quantifier ces phénomènes et d'améliorer la qualité des images.

L'image échographie mesure la réflectivité locale du milieu. Néanmoins, d'autre propriétés mécaniques peuvent être modifiées par la présence d'une maladie. Dans ce cas, un indicateur indirect basé sur une telle propriété du milieu est susceptible de devenir un biomarqueur pour la détection, le diagnostic et le suivit de cette maladie. C'est le principe de l'imagerie quantitative, dont le but est de fournir des informations quantitatives sur le milieu sondé. Par exemple, les échos multiplement diffusés, qui traditionnellement

ont été uniquement considérés comme une source de bruit, contiennent une information sur la microarchitecture des tissus. Ces échos peuvent donc être utilisés afin de mesurer les propriétés de diffusion du milieu. De même, il a été montré que l'atténuation, mais aussi la vitesse du son, sont deux biomarqueurs de la stéatose (maladie non-alcoolique du foie). Ces paramètres gouvernent la propagation des ondes à l'intérieur des tissus. De façon similaire, avoir accès à des informations sur les diffuseurs eux-mêmes est tout aussi utile. Par exemple, les tissus musculaires sont constitués d'un ensemble de fibres. Cette anisotropie de diffuseurs est une caractéristique fondamentale pour l'imagerie de ces tissus. De même, la détection et la caractérisation de structures résonnantes peuvent profondément améliorer l'utilisation de bulles comme agents de contrastes. L'objectif principal de cette thèse est de développer un nouveau formalisme matriciel permettant de traiter l'ensemble de ces problématiques à travers un unique processus d'imagerie. La première étape de cette imagerie matricielle consiste à mesurer la matrice de réflexion à l'aide d'un ensemble d'insonifications, formant une base d'émission. Cette matrice contient l'ensemble des réponses impulsionnelles du milieu. Celles-ci sont mesurées par les différents transducteurs de la sonde qui constituent alors une base de réception. L'ensemble des informations acoustiques accessible sur le milieu est alors contenu dans cette matrice. A l'aide de simples produits matriciels, cette matrice peut être projetée dans n'importe quelle base d'observation. Cela permet alors d'isoler et d'extraire une information utile pour une application particulière. Cette approche matricielle de la propagation des ondes est particulièrement flexible et constitue alors un puissant outil permettant le développement de nouvelles techniques d'imagerie.

La seconde étape du processus d'imagerie matricielle consiste à discriminer les signaux mesurés par la sonde en fonction de leur origine : (i) signaux issus de phénomènes de diffusion simple qui peuvent être utilisés pour l'imagerie mais qui ont potentiellement subit des aberrations lors de leur trajets aller-retour ; (ii) signaux issus de phénomènes de diffusion multiple qui sont soit filtrés à des fins d'imagerie, soit quantifiés afin de mieux caractériser le milieu ; (iii) Réflexions multiple et (iv) bruit électronique que l'on cherche à supprimer. Enfin, chacune de ces contributions est analysée séparément afin de dissocier les phénomènes induits par la propagation des ondes de ceux générés par la réflectivité du milieu.

Le premier chapitre a pour but de rappeler les caractéristiques des échos rétrodiffusés par des tissus mous et de présenter les différentes techniques d'imagerie développées afin de caractériser ces milieux. Dans un premier temps, nous décrirons en détail le processus de formation d'image. Alors que les méthodes conventionnelles reposent sur un ensemble d'excitations focalisées, les techniques d'imagerie avancée combines plusieurs excitations afin d'effectuer une double focalisation à l'émission et à la réception en chaque point du milieu. Cette analyse permet de mettre en évidence les limites fondamentales de l'imagerie : (i) fluctuations de la vitesse du son, (ii) diffusion multiple, (iii) phénomènes d'atténuation, (iv) manque d'information sur la réflectivité du milieu. Nous présenterons ensuite une brève revue des techniques développées afin de dépasser chacune de ces limites, soit dans un but d'améliorer la qualité d'image avec des techniques d'imagerie adaptative, soit afin de quantifier les propriétés mécaniques des tissus. Plus précisément, nous insisterons sur la mesure de la vitesse du son, de la diffusion multiple et de l'anisotropie de diffuseur.

Le second chapitre présente les principes fondamentaux de l'approche matricielle ainsi que les outils de bases qui seront utilisés dans les deux chapitres suivants. Il constitue

donc le cœur de cette thèse. Nous examinerons tout d'abord les travaux fondateurs qui ont permit l'émergence d'une approche matricielle de la propagation des ondes. Nous décrirons ensuite le concept d'imagerie matricielle qui repose principalement sur la séparation des positions de focalisation à l'émission et en réception. Combiné à une étude fréquentielle de la matrice de réflexion, ce processus permet d'extraire les réponses impulsionnelles entre transducteurs virtuels localisé à l'intérieur du milieu. L'ensemble de ces réponses forment la matrice de réflexion focalisée qui constitue la brique de base de l'approche matricielle. Un des avantages de cette approche réside dans la capacité à projeter la matrice de réflexion focalisée d'une base d'observation à une autre à l'aide de simple produits matriciels. Par exemple, cela permet d'observer les réponses impulsionnelles depuis la base des transducteurs, la base d'onde plane, ou la base focalisée qui contient l'ensemble des transducteurs virtuels du milieu. A travers cette analyse, nous démontrons que ce formalisme matriciel permet dans un premier temps de décrire toutes les techniques d'imageries actuelles. Puis nous utiliserons ces réponses afin (i) de quantifier la qualité de focalisation à l'aide d'un nouveau critère de focalisation et (ii) de construire une expérience de retournement temporel numérique permettant d'observer la propagation des ondes à l'intérieur du milieu à l'aide de films de propagation. Les deux derniers chapitres exploitent ce formalisme matriciel afin de corriger les aberrations induites par des fluctuations de vitesse du son [chap. 3] ; et de développer de nouvelles techniques d'imagerie quantitatives à partir de la matrice de réflexion focalisée [chap. 4].

Dans le chapitre 3, nous développons le concept de la matrice de distorsion. Cet opérateur connecte chaque point de focalisation à l'intérieur du milieu à la distorsion subie par le front d'onde généré depuis ce point. Nous montrerons que la décomposition de cette matrice en valeurs singulières permet dans un premier temps de déterminer le nombre d'aires d'isoplanétisme contenue dans le champ de vision via l'étude de son entropie de Shannon. Cette information permet de quantifier le nombre de lois de focalisation orthogonales requises afin de corriger parfaitement les aberrations sur l'ensemble de l'image. Puis nous décrirons comment un processus de retournement temporel basé sur la matrice de distorsion permet d'estimer la matrice de transmission du milieu. Celle-ci relie chaque transducteur de la sonde à chaque cellule de résolution du milieu. Les aberrations peuvent finalement être estimées et compensées afin d'obtenir une image échographique corrigée dont la résolution est prévue par les limites de la diffraction. Afin d'illustrer ce processus, nous appliquerons cette technique dans un premier temps à une expérience in-vitro sur phantom, puis sur une expérience in-vivo sur le mollet d'un volontaire sain.

Le quatrième et dernier chapitre est dédié à la caractérisation des tissus via une approche matricielle dont le but est de fournir des indicateurs quantitatifs liés aux propriétés mécaniques des tissus. A partir de la matrice de réflexion focalisée, nous montrerons : (i) comment les aberrations latérales puis axiales peuvent être utilisées pour construire des cartes de vitesse du son ; (ii) comment des phénomènes physiques tel que la diffusion cohérente ou la réciprocité spatiale peuvent être utilisés afin de quantifier le ratio d'intensité de diffusion multiple dans l'image échographique, formant ainsi un nouveau contraste d'imagerie ; et (iii) comment il est possible de mesurer localement la nature des diffuseurs et leur anisotropie grâce à des expérience de retournement temporel numériques qui donnent accès à leur réponse fréquentiel et à leur diagramme de rayonnement.

Introduction

For the past decades, the field of medical ultrasound has experienced an exponential growth to become, nowadays, one of the most widely used modality for clinical imaging and diagnosis. Compared to other medical imaging modalities, ultrasounds are non-invasive and low cost. Ultrasounds system are able to collect a huge quantity of information on various soft tissues that can then be used to diagnose and monitor all kind of diseases.

Medical ultrasound has benefited from the continuous improvement of hardware systems. Ultrasonic probes now consist in a large number of individually controlled transducers that can emit and receive ultrasound waves at will. At the same time, ultrasound systems provide ever greater computing capacity, unlocking the use and development of complex post-processing techniques to better image and characterize the medium. This thesis fits into this context and lays the foundation of a new matrix imaging approach for ultrasound.

State-of-the-art ultrasound images are based on a confocal method that consists in a double focusing, both in transmit and in receive, on each point of the medium corresponding to one pixel of the image. These focusing processes rely on two major assumptions. First, the medium is considered as homogeneous with a constant speed of sound. Second, the back-scattered wave-field only contains singly-scattered echoes. Nonetheless, the speed of sound varies greatly in different tissues. These fluctuations give rise to a distortion of the incident and back-scattered wave-fronts that reduces the ability to focus acoustic beams in a diffracted limited focal spot. Sharp variations of the medium speed of sound may also generates reverberation artifacts. Moreover, multiple scattering events can also occur between the scatterers of the medium. This multiple scattering contribution manifests itself as an incoherent background noise in the RF signal. Those two undesirable effects, namely aberrations and multiple scattering, thus lead to a loss of resolution and contrast in the ultrasound image that may impact the diagnosis of a medical exam. Therefore there is a strong need to develop new imaging techniques to assess these phenomenon and to enhance the image quality.

While the ultrasound image probes the medium reflectivity, other mechanical properties may be impacted by a disease. Any indirect indicator that is based on such properties then becomes a relevant bio-marker for assessing, monitoring and detecting the stage of this disease. This is the principle of ultrasound quantitative imaging whose aim is to provide quantitative information on the tissues under investigation. For instance, multiply-scattered echoes that have traditionally been seen as a nightmare for classical wave imaging, could be used to characterize the scattering properties of the medium. Similarly, it has been shown that attenuation, which imposes a maximal imaging depth

is also a bio-marker for the diagnosis of non-alcoholic fatty liver diseases. Similarly, the medium speed of sound could also be used to diagnose various kind of diseases. While these parameters govern the wave propagation within the tissues, additional knowledge on the scatterer themselves are equally useful. For instance, the anisotropy of scattering in tissues is a fundamental feature for mapping the orientation of fibers in muscles. The detection and characterization of resonant structures can also strongly improve the use of bubbles as ultrasound contrast agents.

The main objective of this thesis is to address all the aforementioned issues in a single imaging process. To that aim, the matrix formalism is particularly appropriate since the wavefield is controlled by an array of independent transducers. A first step in matrix imaging is the acquisition of the reflection matrix that contains the medium responses generated by successive insonifications, forming an input basis, and measured by all the probe transducers, *i.e.* an output basis. This matrix contains all the available information on the medium. By means of basic matrix operations that allows one to project these ultrasound data from one basis to another, relevant information are extracted for a given problem. Matrix imaging is thus a particularly flexible and powerful tool. It can be applied to the inspection of any organ or tissues.

A second step is to be able to discriminate the different nature of echoes reflected by the medium of interest: (*i*) single scattering contribution that can be directly used for imaging but that can suffer from aberrations; (*ii*) multiple scattering that can be taken advantage for characterization purposes; (*iii*) multiple reflections that we want to avoid but that could be in principle used for focusing if they are properly recombined with the single scattering contribution; (*iv*) electronic noise that we want to get rid of. Finally, each one of these above-mentioned contribution are analyzed separately to disassociate phenomena induced by the wave propagation to those generated by the medium reflectivity.

The first chapter aims to describe the nature of the back-scattered echoes generated by soft tissues and the various techniques developed to characterize such media. The whole image formation process is first presented. While conventional methods rely on an ensemble of focused insonifications, more advanced ones are based on a confocal method. This precise description points out the fundamental limits of ultrasound: (*i*) fluctuations of the medium speed of sound, (*ii*) multiple scattering process, (*iii*) attenuation phenomena, (*iv*) unknown nature of scatterers. We then provide a brief review of all the state-of-the-art methods used to overcome these limitations, either for improving the image quality via adaptive imaging techniques or characterize the mechanical properties of the medium. More precisely, we insist on the characterization of the medium speed of sound, the multiple scattering process and the medium anisotropy.

The second chapter constitutes the core of this thesis as it contains all the first building blocks of the matrix imaging concept. We briefly review all the major milestones that enable the emergence of a matrix approach of the wave propagation. We then describe the matrix imaging concept that basically consists in splitting the locations of the transmitted and received focal spots. Combined with a frequency and temporal analysis of the back-scattered echoes, this process gives access to the impulse responses between virtual transducers located within the medium at each pixel location. This set of responses form a so-called focused reflection matrix that contains all the available information on the medium under investigation. One of the major asset of the matrix approach lies in its ability to easily express the reflection matrix from one observing basis, *e.g.* the trans-

ducer, plane wave or focal basis to the other by simple matrix products. Throughout this analysis, we first show that this matrix formalism is able to describe all the current ultrasound imaging methods. Then we demonstrate how these responses can be taken advantage of for : (*i*) quantifying the focusing quality via a new focusing criterion and (*ii*) building a numerical time-reversal experiment that enables a propagation movie of the wave inside the medium. The last two chapters take advantages of this formalism for : (*i*) a local aberration correction method based on the distortion matrix concept; (*ii*) novel quantitative imaging modes deduced from the focused reflection matrix.

In chapter 3, the distortion matrix concept is developed. This operator essentially connects any focal point inside the medium with the distortion that a wave-front, emitted from that point, experiences due to heterogeneities. By means of a singular value decomposition of this matrix, the number of isoplanatic patches can be deduced from the Shannon entropy of this matrix. It highlights the number of orthogonal focusing laws that are required to fully correct for aberrations over the entire field of view. A time-reversal analysis of the distortion matrix enables the estimation of the transmission matrix that links each sensor and image voxel. Phase aberrations can then be unscrambled for any point, providing a full-field image of the medium at a diffraction-limited resolution. Here, we first present an experimental proof of concept on a tissue-mimicking phantom and then, apply the method to in vivo imaging of human soft tissues.

Finally, the chapter 4 is dedicated to a matrix approach of quantitative imaging. It aims to provide quantitative information of various mechanical parameters of the medium, which are relevant biomarkers for the diagnosis of some diseases. Based on the matrix formalism, we demonstrate : (*i*) how transverse and axial aberrations can be used to build maps of speed of sound,(*ii*) how physical phenomena such as the coherent backscattering effect or the spatial reciprocity of the wave propagation can be used to produce highly resolved spatial maps of the prevalence of multiple scattering in the ultrasound image, which constitutes a new and unique contrast for ultrasonic imaging, and (*iii*) how a local characterization of the scatterers nature and anisotropy could be extracted from their radiation pattern and frequency response, which are accessible via numerical time reversal experiments.

Chapter I

Ultrasound imaging, principles and limits

Contents

This chapter is divided in three parts and contains all the required information and notions that will be used in the next chapters for developing the concept of matrix imaging. First, we introduce some basic concepts of medical ultrasound imaging, which is an estimation of the medium reflectivity. We briefly review some characteristic features of the pressure field generated by the ultrasound probe. We then analysis in details the conventional image formation process that is based on an ensemble of focused insonifications. We provide additional information on back-scattered signals generated by soft tissues. We describe state-of-the-art synthetic beamforming techniques that are used to improve the image quality and/or frame-rate. Finally, the fundamental limits of ultrasound imaging are highlighted when faced to an unknown medium. The second part and third part of this chapter details the techniques developed to overcome those limits. The second part more precisely deals with the improvement of the image quality via adaptive focusing techniques. Finally, the third part covers the concept of quantitative imaging, whose aim is to map physical parameters such as the local speed-of-sound, a multiple scattering rate and to image specular reflector.

I.1 Basics of ultrasound imaging

I.1.1 Transmission and reception of ultrasound waves

I.1.1.1 Transducers

Soft tissues can be observed with various mechanical waves. However at ultrasonic frequencies, only longitudinal waves can be used. Shear waves are strongly absorbed by the high shear viscosity. In ultrasound, these longitudinal waves are characterized by a frequency spectrum that is higher than 20 kHz. For medical purposes, a wide range of frequencies are used. Due to attenuation phenomenon, the choice of frequency is mainly linked to the depth of the tissues under investigation. It goes from 1 MHz for deep organ imaging, *e.g.* liver imaging, to $40-60$ MHz for shallow depth imaging, *e.g.* skin or eye ultrasound imaging. Note that these values are extreme one, most of the ultrasound exam, are performed in the range from 3 MHz to 15 MHz. Ultrasound waves are generated and measured using ultrasound probes that are composed by an ensemble of transducer elements arranged in various geometries. The transducers are piezoelectric elements that converts an electric signal into a mechanical wave. Thanks to the reversibility of this

process, they are usually used to both generate and probe the pressure field at the surface of a medium under investigation. In transmission, a mechanical strain is generated by applying an electrical field while in reception, a mechanical stress induces electrical charges. In medical imaging, piezoelectric are currently made of a synthetic ceramic, most often a lead-zirconate-titanate (PZT). They are generally designed in a rectangular shape defined by a width w, height L and thickness d [Fig. I.1(a)], which defines the fundamental resonance frequency (f_0) [1] :

$$f_0 = \frac{c_p}{2d}, \tag{I.1}$$

where c_p denotes the compressional speed of sound inside the crystal. Thus, the choice of the fundamental resonance frequency imposes the thickness of the transducers. For instance, to design a PZT transducer element operating at 5 MHz, the thickness has to be set to 0.43 mm, given that the speed of sound in PZT is around $c_p = 4300$ m/s. In order to characterize a transducer element, we rely on the concept of acousto-electrical impulse response $h_{ae}(t)$, which corresponds to the pressure wave generated by the element as a response of an electrical pulse. Mathematically, such brief signal is modeled by the Dirac delta function noted $\delta(t)$. Reversely, it also corresponds to the electrical signal induced by a mechanical stress pulse.

Other parameters may be used to characterize the spectral bandwidth, such as the center frequency f_c or the fractional bandwidth B:

$$f_c = \frac{f^+ + f^-}{2} \qquad \text{and} \qquad B = \frac{f^+ - f^-}{f_c}, \tag{I.2}$$

where f^+ and f^- are the upper and lower frequencies of the transducer bandwidth. The latter ones are generally the frequencies for which the signal is -6 dB lower than its maximum value. Usually, the bandwidth is expressed as a percentage of the center frequency. In medical imaging, the order of magnitude of the -6 dB bandwidth is generally around 80% for state-of-the-art ultrasound transducers. Figure I.2 shows an example of the transducer impulse response $h_{ae}(t)$ and its associated spectrum of the transducer elements of the Verasonics L11-5V probe®. Such experiment is performed in a water tank, where the transducer is placed in front of a hydrophone. This transducer is excited by an electrical pulse that lasts for instance, one half period of the central frequency. The signal measured on the hydrophone then defines the impulse response of the transducer. The spectrum displayed in Fig. I.2(b) is characterized by a large frequency bandwidth (60%) around a center frequency of 7.8 MHz. Figure I.2(a) shows that the emitted signal is coherent and that transducer elements can transmit short acoustical pulses, of a fraction of a μs. We will see in paragraph I.1.2.1 that the duration of such pulses defines the axial resolution. However, to improve the intensity of the incident wave, and thus the one of the back-scattered echoes, longer pulses are required. This observation leads to a tradeoff between axial resolution and signal-to-noise ratio (SNR).

The electrical signal produced by the transducer results from the average pressure field at the transducer surface. This behavior rules the transducer radiation pattern. For rectangular transducers, the pressure field generated in the plane $\vec{e}_x, \vec{e}_z$ is then mainly governed by its width w along the axis $\vec{e}_x$ [Fig. I.1(c)]. In the Fraunhofer approximation, meaning in the far-field [Par. I.1.2.2], the pressure field $P(\theta)$ generated by the transducer

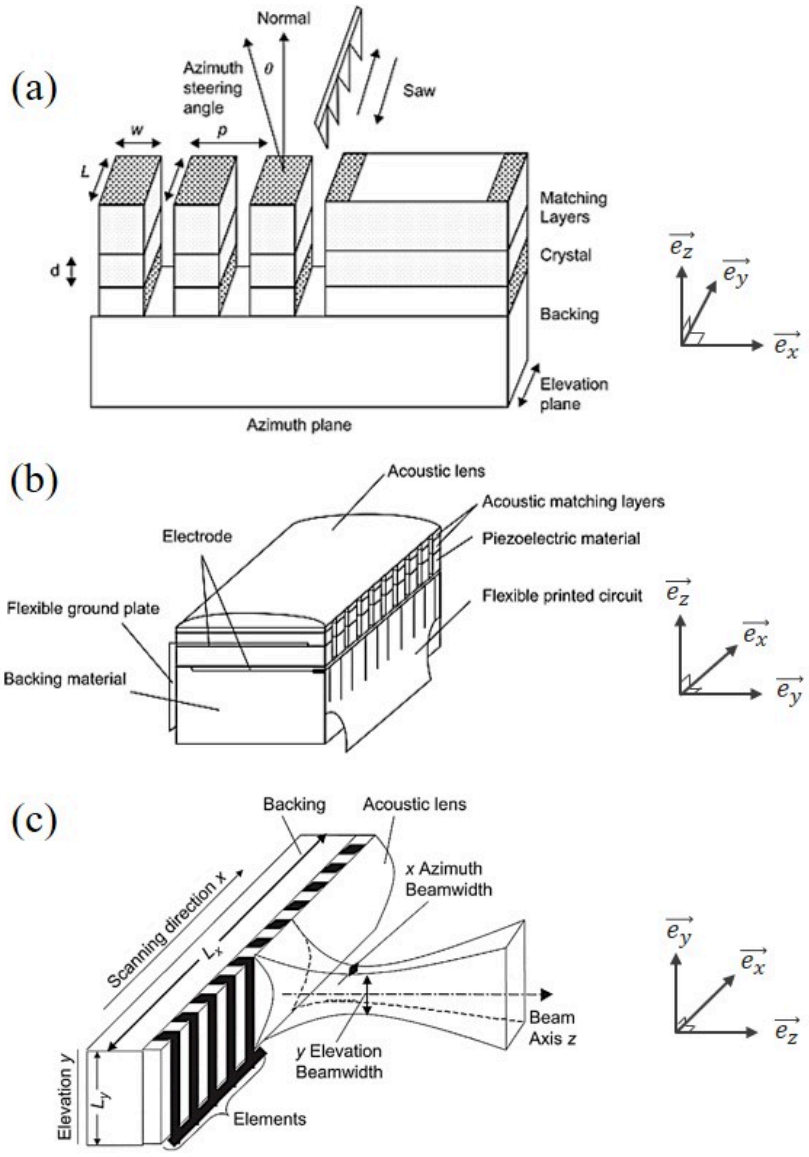

Fig. I.1 *(a) Construction of transducers from a single piezoelectric crystal. (b) Complete sketch of a linear probe. (c) 3D field of illumination of a focused beam. Adapted from [1].*

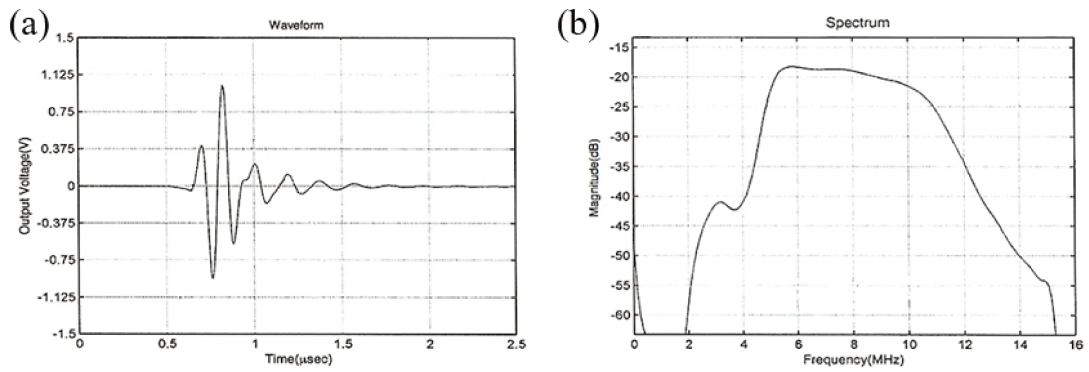

Fig. I.2 *(a) Impulse response $h_{ae}(t)$ and (b) corresponding frequency spectrum $h_{ae}(f)$ of the Verasonics L11-5V probe. Inspired by [2]. Note that these impulse responses are given advisory only. The probe used during this thesis are produced by Supersonic imaging I.1.1.3. Details of their impulse responses are classified as confidential information.*

is proportional to the spatial Fourier transform of the aperture function [3]. In our case, this aperture function is a rectangular one, which implies that:

$$P(\theta) \propto \text{sinc}\left(\pi \frac{w}{\lambda_c} \sin(\theta)\right), \tag{I.3}$$

with θ the angle from the normal of the transducer in the plane $\{\vec{e}_x, \vec{e}_z\}$, $\text{sinc}(X) = \sin(X)/X$ the sinus cardinal function, $\lambda_c = c/f_c$ the central wavelength defined at the central frequency and c the speed of sound in the propagation medium. Figure I.3(a) illustrates this phenomenon. It shows a 2D monochromatic simulation of the pressure field generated by a single transducer [Par. I.1.2.2]. The transducer width is $w = 0.2$ mm. The simulation is performed in the frequency domain at $f_c = 7.5$ MHz, the medium speed of sound is defined at $c_0 = 1540$ m/s, which implies that the wavelength is $\lambda_c \simeq 0.2$ mm. Figure I.3(b) shows the radiation pattern of this transducer for three frequencies $f = 5$, $f = 7.5$ and $f = 15$ MHz, corresponding to a ratio w/λ equal to 0.7, 1.0 and 1.9, respectively. We observed that if the ratio $w/\lambda > 1$, the transducer becomes directive and side lobes appears. It then reduces the field of view of the insonified region and introduced some noise as it excites unwanted areas of the medium. Note that this behavior appears both in transmission and in reception.

The following paragraphs demonstrate that the radiation pattern limits the lateral resolution of ultrasound image. This phenomenon should be carefully considered during the image construction process as it occurs both in transmission and in reception. The same behavior can be observed along the axis $\vec{e}_y$, however, an acoustic lens is generally placed on top of the transducer in order to collimate the acoustic beam along the plane $\{\vec{e}_x, \vec{e}_z\}$ [Par. I.1.1.2].

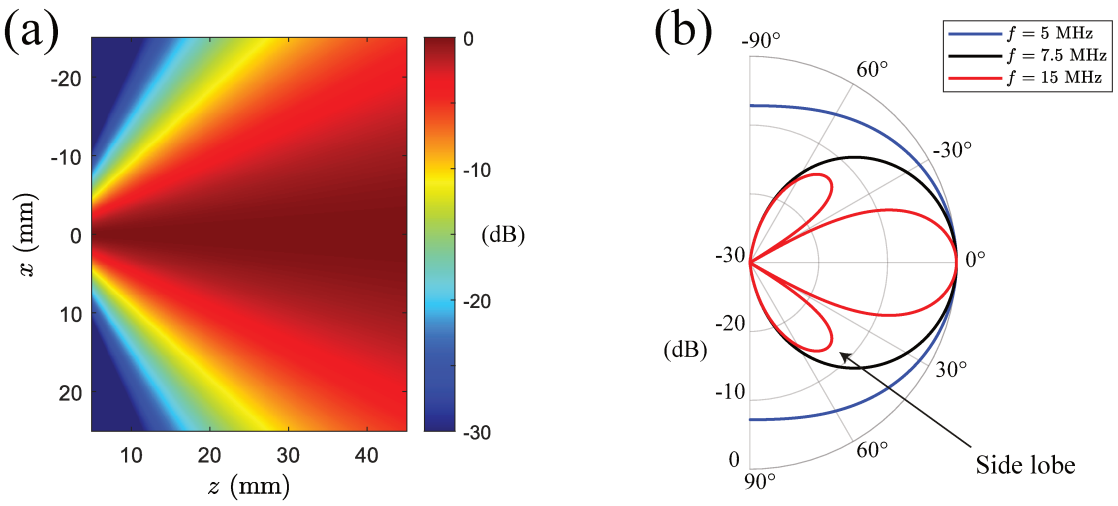

Fig. I.3 *(a) Simulated pressure field generated by a single transducer characterized by $w = 0.2$ mm at 7.5 MHz (b) Simulated radiation pattern for various frequencies.*

I.1.1.2 Ultrasound probes

Conventional ultrasound probes are composed by an ensemble of $N_p$individually controlled transducers. It means that each transducer can be excited by a dedicated electrical signal also called waveform. In practice, the same waveform is used during an insonification by each transmitting transducer. Each waveform can be delayed to produce a particular incident wave-front [Par. I.1.2]. Each transducer is individually powered by its own cable, which limits the number of transducers per probe. State-of-the-art clinical probes usually contain $N_p = 256$ transducers, but some probes, mostly dedicated to research can contain up to 1024 elements [4]. Compared to wave-front shaping experiments in optics, where spatial light modulators and CCD cameras are composed by billions of pixels, the number of transducers is relatively small in ultrasound imaging. Consequently, transducers are generally aligned within a same plane that is defined by the axes $\{\vec{e}_x, \vec{e}_z\}$ [Fig. I.4]. Such probe is then able to shape incident wave within this plane. As explained below, axial information is given by the time-of-flight of the echoes, while lateral information is given by the ensemble of transducers. A key parameter of an ultrasound probe is the pitch p, which is the distance between the center of neighboring transducers. This length is the sum of the transducers width w and the kerf that is the inter-element cut width [Fig. I.1(a)].

We differentiate three main types of multi-element probes, namely linear probes, curved probes and phased-array probes, whose usage depends on the target application [Fig. I.4(a)]. Linear probes acquire data to construct rectangular images of the region of interest. They are thus designed as wide as possible in order to maximize the imaging area. They are characterized by a center frequency ranging between 2.5 MHz and 12 MHz and a pitch equal to one wavelength. Such probes are typically used for shallow depth imaging until 70 mm. To increase the field of view both laterally and axially, we use convex

Fig. I.4 *Example of ultrasound probes developed by Supersonic Imagine. (a) linear probe SL15-4, (b) curved probe XC6-1, (c) phased-array probe XP5-1. The probes are named according to their type and frequency bandwidth, and figures are extracted from the company website*

probe whose transducers are arranged into a convex shape [Fig. I.4(b)]. Curved proves are typically characterized by a center frequency ranging between 1 MHz and 7.5 MHz and a pitch equal to one wavelength. They are generally used for abdominal examination and diagnosis of deep and large organs that require a wide field of view. Finally, phased-array probes are linear probe characterized by a pitch equal to one half-wavelength wide. Their length L_x is thus much shorter than a linear probe. They are used to produce wide field-of-view images in difficult-to-access regions where linear and convex probes cannot be used because they are too large, *e.g.* inter-costal cardiac examinations or transcranial imaging. Such probes usually operate at a lower center frequency than linear probes. Their typical frequency bandwidth spans from 2 MHz and 7.5 MHz.

The large field-of-view of phased-array probes is accessed by reducing the pitch at half-wavelength. Indeed, dividing the probe in multiple elements can be seen as a spatial sampling along the axis $\vec{e}_x$. The transducers then faithfully generate or measure spatial frequencies k_x only if the following spatial Shannon criterion is fulfilled:

$$\frac{k_x p}{2\pi} < \frac{1}{2}. \tag{I.4}$$

For example, if the probe is set to transmit a plane wave with angle θ at frequency f_c, grating lobes that are spatial aliasing may appear at angles θ_g defined by:

$$\theta_g < \pm \text{asin}\left(\frac{n\lambda_c}{p} + \sin(\theta)\right), \tag{I.5}$$

with n being an integer. For a linear probe, $\lambda/p \approx 1$, then for $\theta = 30$ deg, some energy is sent in direction $\theta = -30$ deg. For phased array probe, the ratio $\lambda/p \approx 0.5$, which ensures that the condition defined by equation I.4 is always fulfilled. Note that due to the reciprocity of wave propagation, the same phenomenon appears in reception when one tries to select echoes coming with a reflected angle θ.

To optimize an ultrasound probe from an acoustical point of view, three other components are added. First, the acoustic impedance of piezoelectric material such as PZT and soft tissues are extremely different. Table I.1 shows the impedance of a few soft

Tissue/material	c (m/s)	ρ (kg/m^3)	Z (MRayls)
Breast	1510	1020	1.540
Liver	1578	1050	1.657
Water (20 deg C)	1482.3	1000	1.482
PZT-5A	4350	7.75	33.71

Table I.1 – Properties of soft tissues and piezoelectric transducer materials, first three rows are from [5] and the last one is from [6].

tissues and piezoelectric transducer materials. To ensure an optimal transmission of the acoustic wave to the medium and *vice versa*, matching layers are added to the probe. This is a key component of an ultrasound probe. If no adaptive impedance is performed, 85% of the intensities of both the incident and back-scattered waves are reflected at the interface. Even if the matching layers improve the coupling between the transducers and soft tissues, a perfect adaptive impendence is never reached due to the large frequency bandwidth of the transducers. It means that a part of the incident wave is reflected within the probe. In addition, waves that are directly reflected during the transmission event can then be reflected a second time on the back of the probe, leading to more parasite signals. Such reflections would modify and enlarge the duration of the transmitted signal. This phenomenon is commonly circumvented by adding a backing material at the back of the probe.

Finally, as stated above, the ultrasound image probes only a slice of the medium that corresponds to the imaging plane defined by $\{\vec{e}_x, \vec{e}_z\}$. However, due to their rectangular shape, transducers also send energy in the elevation plane defined by $\vec{e}_y, \vec{e}_z$. This phenomenon generates unwanted back-scattered signals coming from scatterers located outside of the imaging plane. To counter this effect, an acoustic lens is added at the surface of the probe [darker part on the edge of ultrasound probes on figures I.1c]. Thanks to this passive material, the incident beams then remain as much colinear as possible to the imaging plane. More precisely, acoustic lens is made of a polymer whose speed-of-sound is lower than studied soft tissue speed of sound. By designing this material in a curved shape, the waves are focused on a focal length named elevation focus. This distance depends on the target application and on the type of probe. The order of magnitude of the elevation focus is around 20 mm for linear probes, 60 mm for curved probes and around 70 mm for phased array probes.

I.1.1.3 Probe frame and signal post-processing

Due to the spectral properties of the transducer elements, whose electro-acoustical impulse response has a frequency content concentrated around the center frequency, the element-raw data are bandpass signals. They can be directly stored unaltered and called Radio Frequency (RF) signals or demodulated using a Phase-Quadrature (IQ) demodulation at the central frequency of the transmitted pulse f_c. This demodulation is generally performed at a hardware stage to reduce the size of the stored data. In addition, if RF data are used, an enveloped detection is required [see par. I.1.2]. While, the RF signals

are real ones, the IQ data are complex ones. Their real and imaginary parts are associated with the in-phase and quadrature component of the original signal, respectively.

Note that, in the following of this thesis, the experiment has been carried out using a Supersonic Imagine probe SL15-4, which is characterized by $w = 0.175$ mm, $f_c = 7.5$ MHz, a frequency bandwidth between 4 and 15 MHz and an angular aperture of around 26 deg at -6 dB. We will neglect back-scattered echoes generated by scatterers located outside the imaging plane and use a 2D Cartesian frame whose origin is located at the center of the ultrasound probe. Each transducer is located by the transverse coordinate of its surface central point, noted u, (and axial one is null). The subscripts *in* and *out* will denote the transmitted and received parts of the wave propagation between the probe and the medium, *e.g.* a transmitting and a receiving transducer are identified by their lateral coordinates u_{in} and u_{out}, respectively.

Now that medical ultrasound probes have been fully characterized from an acoustical point-of-view, we describe in the next paragraph the conventional image formation process.

I.1.2 Conventional beamforming for focused insonifications

An ultrasound image also known as B-mode image is an estimation of the medium reflectivity that is constructed from a sequence of incident ultrasonic waves. Short-scale fluctuations of the medium impedance generate back-scattered echoes that are measured by the transducers. The B-mode image is then constructed using the process of Delay-And-Sum (DAS) beamforming. It consists in summing coherently all the measured back-scattered echoes that have been generated by each point of the medium. Each echo is selected by computing the round-trip time-of-flight ($\tau = \tau_{\text{in}} + \tau_{\text{out}}$) of the incident wave to propagate from the probe to the image voxel, time-of-flight τ_{in} and to go back, time-of-flight τ_{out} [Fig. I.5]. If a bright scatterer is indeed found at this location, the corresponding signals will constructively interfere, resulting in a high intensity signal associated with a bright pixel of the image. However, if the image voxel does not contain any scatterer, the selected signals are out-of-phase one compared to the other. Destructive interferences thus occur during the coherent summation, which results in a low intensity signal associated with a dark pixel.

The delicate step of computing the times-of-flight for each insonification and each focal point is achieved in most of clinical devices by assuming the medium as homogeneous with a constant speed of sound c_0. The times-of-flight are then simply computed by measuring the geometrical distance between the transducer and the image voxel. Although this assumption is required for real-time imaging, it may not be valid for some configurations where long-scale fluctuations of the medium speed-of-sound impact the wave propagation [7]. Paragraph I.2.1 provide an exhaustive description of the consequences of these aberrations on the image reconstruction process. By analyzing the beamforming step, we assume a direct link between the time-of-flight of a back-scattered echoes and the locations of the scatterers that generate this echo. This assumption is valid only for singly-scattered echoes that have interact only once with the medium. However, back-scattered signals may also contain multiply scattered echoes that have been scattered more than once by the scatterers in the medium. Even if those echoes are generally considered as a source of noise that degrade the image contrast, they contain additional information on the medium

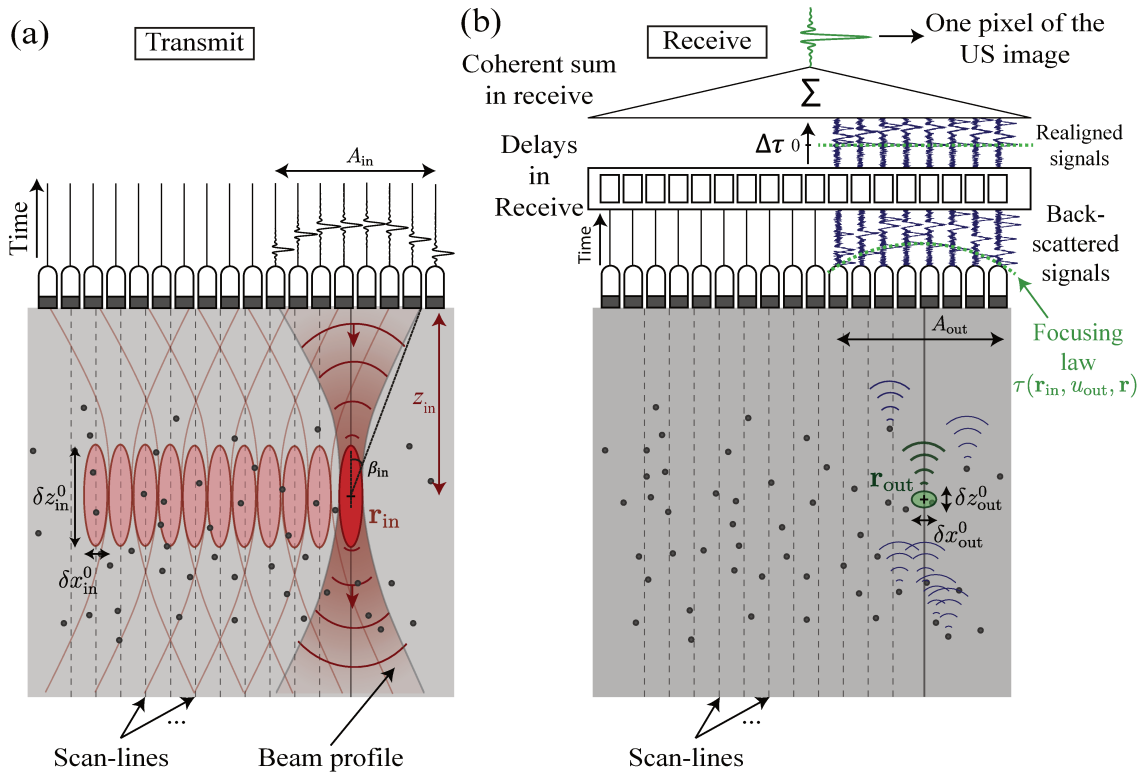

Fig. I.5 *Sketch of conventional beamforming based on focused excitation. (a) transmitted and (b) received steps.*

that can be extracted and taken into account for a better characterization of the medium [Par. I.3.2]. The combination of these two assumptions (i) homogeneous medium and (ii) single scattering process ensures that the time-of-flight of the back-scattered echoes are linearly proportional to the scatterer depth via c_0 : $z = c_0 t/2$, which drastically simplify the modeling of the wave propagation.

Conventional beamforming is based on N_{in} successive focused excitations, which are laterally shifted one compared to the other and individually used to construct the B-mode image column per column [Fig. I.5(a)]. The method consists in applying time-delays in transmission (τ_{ex}) in order to generate a focused beam that concentrates the incident wave at the transmitted focal point $\mathbf{r}_{\text{in}} = \{x_{\text{in}}, z_{\text{in}}\}$, and which propagated along a scan-line defined by the coordinate x_{in}:

$$\tau_{\text{ex}}(u_{\text{in}}, \mathbf{r}_{\text{in}}) = \frac{\sqrt{(x_{\text{in}} - u_{\text{in}})^2 + z_{\text{in}}^2}}{c_0} - \frac{z_{\text{in}}}{c_0}. \tag{I.6}$$

Back-scattered echoes are then measured by the transducers and the corresponding signals are stored in a so-called reflection matrix $\mathbf{R}_{ur} = [R(u_{\text{out}}, \mathbf{r}_{\text{in}}, t)]$ that contains the signal measured at time t by the transducer located at u_{out} when a focused wave is set to converge at location $\mathbf{r}_{\text{in}}$. For sake of simplicity, these signals will only be noted as $R(u_{\text{out}}, t)$ when only one transmitted event is considered. Any scatterer located along the scan-line at

location $\mathbf{r} = \{x_{\text{in}}, z\}$ is excited by the incident wave and generates a back-scattered wave that is measured by the transducers at time:

$$\tau(\mathbf{r}_{\text{in}}, u_{\text{out}}, \mathbf{r}) = \underbrace{\frac{z}{c_0}}_{\tau_{\text{in}}} + \underbrace{\frac{\sqrt{(x_{\text{in}} - u_{\text{out}})^2 + z^2}}{c_0}}_{\tau_{\text{out}}}, \tag{I.7}$$

where τ_{in} and τ_{out} are the transmitted and return times-of-flight, respectively. τ will be refered as the focusing law in the following. We insist on the fact that $\mathbf{r}$ is not necessarly located at the same depth than $\mathbf{r}_{\text{in}}$.

The image formation process actually consists in a numerical output beamforming that estimates the total intensity of the echoes captured by the probe and generated by each image voxel of coordinate $\mathbf{r} = \{x_{\text{in}}, z\}$ of the scan-line. Back-scattered signals are first delayed in reception to create the realigned signals:

$$\breve{R}\left(u_{\text{out}}, \mathbf{r}_{\text{in}}, \mathbf{r}, \Delta t\right) = R\left(u_{\text{out}}, \mathbf{r}_{\text{in}}, \tau(\mathbf{r}_{\text{in}}, u_{\text{out}}, \mathbf{r}) + \Delta t\right) \tag{I.8}$$

For conventional ultrasound imaging and for most of common ultrasound techniques, only the signals corresponding to $\Delta t = 0$ are computed. Thus, this variable will mostly be reminded only when $\Delta t \neq 0$. Then the realigned signals are coherently summed, hence the denomination Delay-And-Sum (DAS) beamforming [Fig. I.5(b)]:

$$R_b(x_{\text{in}}, z) = \frac{1}{N_{\text{out}}(\mathbf{r})} \sum_{u_{\text{out}}^-(\mathbf{r})}^{u_{\text{out}}^+(\mathbf{r})} \breve{R}\left(u_{\text{out}}, \mathbf{r}_{\text{in}}, \mathbf{r}, \Delta t = 0\right) \tag{I.9}$$

with $u_{\text{out}}^-(\mathbf{r})$ and $u_{\text{out}}^+(\mathbf{r})$ the first and last used transducers to perform the beamforming step and $N_{\text{out}}(\mathbf{r})$ the number of used transducers. The selected transducers form the received aperture $A_{\text{out}}(\mathbf{r})$ [Fig. I.5(b)] and is discussed in the following paragraphs. $R_b(x_{\text{in}}, z)$ corresponds to the beamformed signals associated with the column x_{in} of the final ultrasound image.

In conventional ultrasound imaging, each column is constructed based on one transmitted event. Consequently, to create images with high contrast, only the scatterers located close to this scanning-line should be excited. To do so, only the surrounding transducers are used in transmission to create a focused beam that is associated with a large field-of-depth δz_0^{in}. This distance corresponds to the length over which the beam remains collimated [Fig. I.5(a)]. In absence of aberration, this distance is predicted by the diffraction theory [8], such as:

$$\delta z_{\text{in}}^0(\mathbf{r}_{\text{in}}) = \frac{2\lambda_c}{\sin^2(\beta_{\text{in}}(\mathbf{r}_{\text{in}}))} \qquad \text{with} \qquad \beta_{\text{in}}(\mathbf{r}_{\text{in}}) = \operatorname{atan}\left(\frac{A_{\text{in}}(\mathbf{r}_{\text{in}})}{2z_{\text{in}}}\right). \tag{I.10}$$

where $\lambda_c = 2\pi f_c/c$ is the central wavelength defined at the medium speed of sound and $\beta_{\text{in}}(\mathbf{r}_{\text{in}})$ the maximum angle of illumination. It is generally defined from the transmitted aperture A_{in} that selects the transducer to be excited such as: $|x_{\text{in}} - u| < A_{\text{in}}/2$. In ultrasound imaging, the transmitted f-number $= z_{\text{in}}/A_{\text{in}}$ is defined to maintain the same illumination angle β_{in} for particular cases where the transmitted focal points $\mathbf{r}_{\text{in}}$ are

located at varying depth. At the focal depth, the lateral extension $\delta x^0_{\text{in}}(\mathbf{r}_{\text{in}})$ of the incident beam is [8] [Fig. I.5(b)]:

$$\delta x^0_{\text{in}}(\mathbf{r}_{\text{in}}) = \frac{\lambda_c}{2\sin(\beta_{\text{in}}(\mathbf{r}_{\text{in}}))}.\text{F}^{\#}_{\text{in}} \tag{I.11}$$

Note that $\sin(\beta_{\text{in}})$ is often known as the transmitted numerical aperture. For linear probe, the order of magnitude of the focal depth is $z_{\text{in}} \approx 20$ mm and the transmitted f-number is $\text{F}^{\#}_{\text{in}} \approx 3$, which corresponds to $\beta_{\text{in}} \approx 10$ deg. In this case, the spatial extensions of the transmitted beam at $f_c = 7.5$ MHz and $c_0 = 1540$ m/s are $\delta z^0_{\text{in}} = 13.6$ mm and $\delta x^0_{\text{in}} = 0.6$ mm (to be compared to the wavelength $\lambda_c \approx 0.2$ mm).

The same equations can be derived for the numerical output operation. Note that the transmit aperture is not too large in order to create focused beams characterized by a large depth-of-field. The objective is to insonify only scatterers that are located along the scan line. However, the receive aperture $A_{\text{out}}(\mathbf{r})$ is chosen as large as possible to get the highest lateral resolution as possible [Par. I.1.2.1]. However, A_{out} is limited by the radiation pattern of the transducer. Indeed, a transducer is not able to fully capture a back-scattered wave characterized by a large output angle. Therefore, the received f-number $F^{\#}_{\text{out}}$ is thus maintained constant for all focal point in order to defined a constant maximum angle of collection β_{out} (except at large depth or on the edge of the image where this aperture cannot be maintained due to the limited size of the transducer array). For linear probe, the order of magnitude of the received f-number is around $F^{\#}_{\text{out}} = 1.4$ and is lower (meaning larger aperture) than the transmitted one. The maximum angle of collection is then around $\beta_{\text{out}} = 20$ deg.

Each column $R_b(z, \mathbf{r}_{\text{in}})$ can be seen as a temporal signal where $z = c_0 t/2$. It is then a bandpass signal that can be expressed as:

$$R_b(\mathbf{r}) = \text{Re}\left[\mathcal{I}(\mathbf{r}) e^{i2\pi f_c \frac{2z}{c_0} + \phi}\right], \tag{I.12}$$

with Re[..] the real part operator, $\mathcal{I}(\mathbf{r})$ and ϕ the envelope and phase shift of the beamformed scan-line. For display purpose, the ultrasound images only the envelope as it is a smoother signal that is more pleasing for the human eye. Hence, the envelope is extracted by means of either a Hilbert transform or a in Phase-Quadrature (IQ) demodulation. Note that this step is not necessary for raw IQ data that have already been demodulated. In this case, $\mathcal{I}(r)$ is directly obtained by computing the absolute value of the beamforming output:

$$\mathcal{I}(\mathbf{r}) = |R_b(\mathbf{r})| \tag{I.13}$$

After the optional envelope extraction step, $\mathcal{I}(r)$ is log-compressed within a given dynamic range and eventually displayed with a gray-scale colormap in real-time. To better visualize the entire field-of-view and compensate for attenuation, $\mathcal{I}(r)$ is often multiplied by an increasing function of depth called Time-Gating-Compensation (TGC), which is manually adjusted [Par. I.1.3.4].

Figure I.6(a) displays an ultrasound image of a tissue-mimicking phantom, whose mechanical properties are similar to the one of soft tissue. This gel is a relevant tool for ultrasound imaging as it constitutes an ideal medium with known propagating properties, such as speed of sound or attenuation. Such phantom is generally composed by three types of scatterers:

- bright point-like targets that are in fact nylon monofilament placed orthogonally to the imaging plane. They are used to assess the local resolution of the ultrasound image.

- the fluctuating background characterized with a granular texture called speckle that results from the contribution of randomly distributed unresolved scatterers [see par. I.1.3.2].

- two disks located at depth $z = 40$ mm and characterized by a brighter granular texture, which is produced by a higher density of unresolved scatterers. They are actually cylinders in 3D, whose brightness difference with the background is calibrated. They are used to assess the contrast of the ultrasound image.

Figure (b) is an *in-vivo* ultrasound image of the liver of a healthy anonymousvolunteer. To perform the acquisition, the probe is placed between the ribs. Shallow depths of the resulting image are associated with a succession of fat and muscle intercostal tissues. The bottom part of the image (for depth $25 < z < 70$ mm) corresponds to the liver organ. It shows a characteristic speckle like aspect. We also detect dark circular areas that are veins. Blood scatterers are known to be weak scatterers.

I.1.2.1 Image resolution

The spatial resolution quantifies the ability of an imaging system to differentiate between two close points, which is intrinsically linked to the point spread function (PSF), *i.e.* the impulse response of the imaging system. In US imaging, the PSF is highly asymmetrical and we usually differentiate axial from lateral resolution.

The axial resolution is determined by the ability to separate two echoes that arrive at two different times-of-flight. It is thus linked to the temporal duration of the incident transmitted pulse. More precisely, the axial axis (along $\vec{e}_z$) can be seen as a temporal axis. Thus, the axial resolution δz_0 is often considered as half the length duration of the transmitted US pulse. In other words, it can be expressed as the inverse of the incident pulse bandwidth B :

$$\delta z_0 = \frac{c_0}{2 f_c} \tag{I.14}$$

The lateral resolution is linked to the capacity of the beamforming process to discriminate between echoes associated with scatterers located at the same depth. In any imaging system, the lateral resolution is governed by the maximum angle of illumination or collection β_{in} or β_{out} [Eq. I.11]. In the case of conventional beamforming that requires a dedicated transmitted event for each column, β_{in} is arbitrarily small to create beams that stay collimated to the scan-line. The resolution of the ultrasound image is thus given by the lateral extension of the received focal spot $\delta x_0 = \delta x^0_{\text{out}}$ [Eq. I.11].

Note that, in practice, a common way to quantify the spatial resolution of an ultrasound image consists in measuring the full width at half maximum (FWHM) of a bright point like scatterer (whose dimensions are smaller than the resolution cell). Such scatterer can be found in tissue-mimicking phantom [bright points on figure I.6(a_1)]. Actually, they are generally nylon monofilament wires (whose diameter is equal to 100 μm in this example).

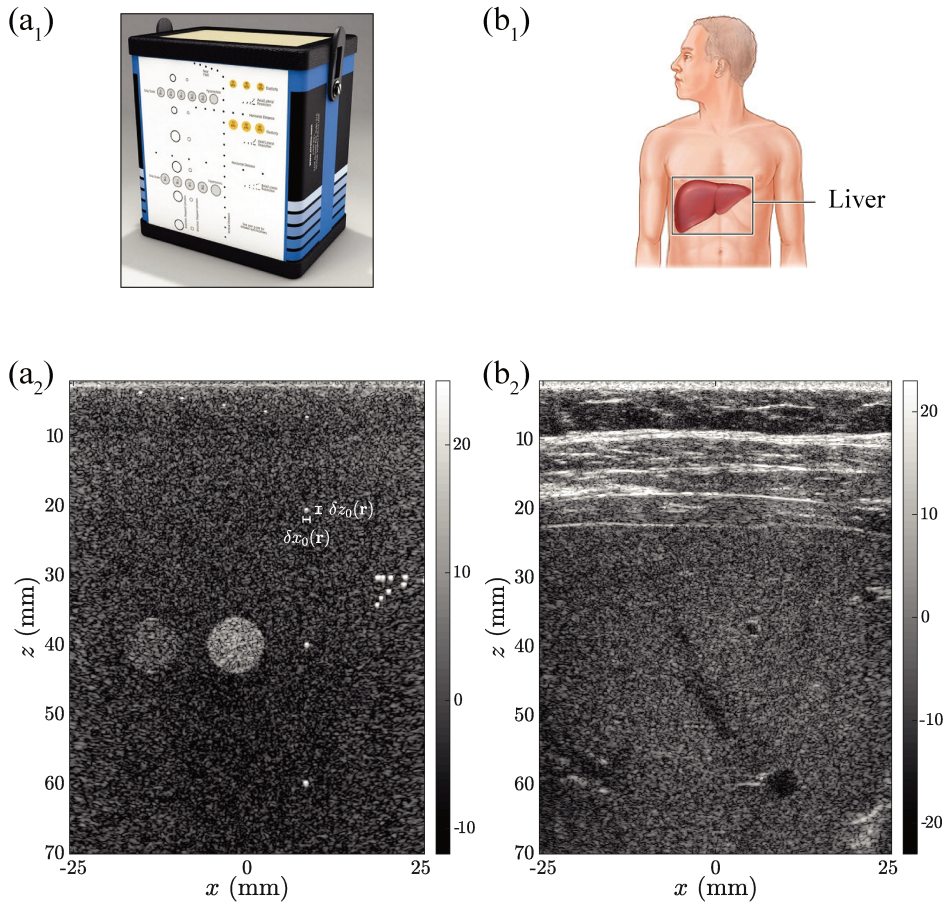

Fig. I.6 *Sketches and ultrasound images of (a) a tissue-mimicking phantom (CIRS general purpose phantom, Model 040GSE); and (b) the liver of a healthy volunteer. The probe used is the Supersonic Imagine SL15-4. The ultrasound images are displayed in dB and normalized by their average intensity level.*

Finally, we also define a temporal resolution that corresponds to the required time to construct an entire US image. The limiting step lies in the number of insonifications used to create an image and more precisely the need to wait for the required round-trip time-of-flight of the incident waves to reach a maximum depth $z_{\max}$. Also known as framerate and measured in frame per second (fps) or Hz, it is expressed as:

$$FR_{\max} = \frac{c_0}{2z_{\max}N_{\text{in}}}. \tag{I.15}$$

For instance, the frame rate associated with an ultrasound image of maximum imaging depth $z_{\max} = 60$ mm depth and built from 128 scan-lines is around $FR_{\max} = 100$ Hz. This frame-rate may not be high enough to capture and monitor fast moving tissues, such as cardiac motion, shear wave propagation or blood flow. Advance synthetic beamforming process have been developed to overcome this issue [Par. I.1.4].

I.1.2.2 Model for wave propagation

Modeling the exact pressure field generated by the ultrasound probe is a difficult task mainly as it should take into account many phenomena: (*i*) broadband signals, (*ii*) finite size of the transducers and probe, (*iii*) near field configurations, (*v*) medium attenuation, (*vi*) fluctuation of the medium speed of sound, (*vii*) multiple scattering process,(*viii*) coupling between the probe and the medium...

The wave propagation is fully described by the wave equation developed by d'Alembert. For the pressure field $P(\mathbf{r},t)$ this equation is expressed as:

$$\Delta P - \frac{1}{c_0^2}\frac{\partial^2 P}{\partial^2 t} = P_s(\mathbf{r},t) \tag{I.16}$$

with Δ being the Laplacian operator and $P_s(\mathbf{r},t)$ a source term. In the case of a transducer located at $mathbfu$, $P_s(\mathbf{r},t) = P_s(t)\delta(\mathbf{u}-\mathbf{r})$. To model the wave propagation, we rely on the temporal green's function $G(\mathbf{r},\mathbf{u},t)$, which is solution of the wave equation. In other word, this useful function describes the pressure field $P(\mathbf{r},\mathbf{t})$ at any point of the medium when a spatial Dirac source (*i.e.* a point-like source) located at $\mathbf{u}$ emits a brief pulse. However, modeling the wave propagation in the frequency domain is much easier as temporal convolutions are transformed into simple products. In the monochromatic regime at frequency f, the wave equation leads to the Rayleigh-Sommerfeld equation:

$$P(\mathbf{r},f) = \frac{1}{j\lambda}\int_{L_x} E_{\text{in}}(\mathbf{u},f)G(\mathbf{r},\mathbf{u},f)\cos(\theta)d\mathbf{u}, \tag{I.17}$$

where $\cos(\theta) = z/|\mathbf{r}-\mathbf{u}|$. This equation links the pressure field $P(\mathbf{r})$ at any point $\mathbf{r}$ of the medium to the distribution of pressure $E_{\text{in}}(\mathbf{u})$ along a surface of sources via the medium monochromatic green's function $G(\mathbf{r},\mathbf{u},f)$. Note that this equation assumes that no multiple scattering event occurs during the wave propagation.

This equation can be derived for 3D and 2D configuration, the difference lies in the choice of the monochromatic green function. Here, due to the probe lens that collimates the incident beams and the measured echoes within the imaging plane ($\{\vec{e}_x,\vec{e}_z\}$) we consider 2D Green's Function. In a homogeneous medium, $G(\mathbf{r},\mathbf{u},f)$ is equal to $G_0(\mathbf{r},\mathbf{u},f)$ the free-space 2D monochromatic Green's function [9]:

$$G_0(\mathbf{r},\mathbf{u}) = -\frac{i}{4}\mathcal{H}_0^1(k|\mathbf{r}-\mathbf{u}|) \underset{k|\mathbf{r}-\mathbf{u}|\gg 1}{\approx} \frac{-1+i}{2\sqrt{2\pi}}\frac{e^{jk|\mathbf{r}-\mathbf{u}|}}{\sqrt{k|\mathbf{r}-\mathbf{u}|}}, \tag{I.18}$$

with $\mathcal{H}_0^1$ the Hankel function of the first kind.

As an example, to model a monochromatic focused beam with a focal point located at $\mathbf{r}_{\text{in}}$, the pressure field at the surface of the probe is given by:

$$E(u) = E_0 e^{-jk|\mathbf{r}_{\text{in}}-\mathbf{u}|}W_{L_x}(\mathbf{u}), \tag{I.19}$$

where E_0 is an amplitude term and $W_{L_x}(u)$ a spatial window that account for the limited size of the ultrasound probe. Figure I.7 displays the corresponding pressure field of a typical focused beam generated by a linear probe for conventional ultrasound imaging.

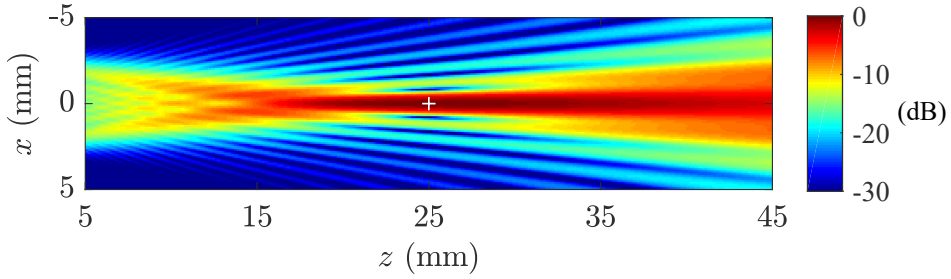

Fig. I.7 *Simulated pressure field obtained for a monochromatic focused beam characterized by focal point located at* $\{x_{in}, z_{in}\} = \{0, 25\}$ *mm (white cross) using a transmitted f-number* $F_{in}^{\#} = 4$ *and a central frequency* $f_c = 7.5$ *MHz. The pressure field is normalized by the intensity at the focus and shown in decibel (dB).*

I.1.3 Back-scattered echoes by soft tissues

In the previous section, we describe the conventional image formation process. We now review some basics about ultrasound scattering in tissues that directly influence the imaging process.

Short scale inhomogeneities of the refractive index, referred to as scatterers, cause incoming waves to be reflected. In acoustic the refractive index is the medium impedance $Z = \rho c$, where ρ is the local density and c the local speed of sound, that depends on the medium compressibility. Back-scattered echoes are then generated by fluctuations of the density and/or speed of sound in the medium. The pressure field reflected by a single scatterer depend both on the nature of the scatterer (contrast of compressibility or density) and on the relation of the scatterer shape or roughness to the incident wavelength. To distinguish between each type of scatterer, we usually compare its characteristic size a to the incident wavenumber k_c. Scatterers fall roughly into three groups: (i) the specular scatterers, whose one of its dimensions is larger than the central wavelength, *i.e.* $ak_c \gg 1$ (ii) unresolved scatterers that are much smaller than the central wavelength, *i.e.* *i.e.* $ak_c \ll 1$ and (*iii*)the rest that fall in between those extremes. The three types of scatterers can be found in soft tissues. For instance, the ultrasound image of the liver I.6(b) shows a speckle like aspect that is generated by unresolved scatterers. The tissue boundaries are specular scatterer. Indeed, at least one of their dimensions is larger than the central wavelength.

I.1.3.1 Pressure field reflected by a single scatterer

If the central wavelength is much smaller than at least one of the object dimensions $ka \gg 1$, the reflection process can be approximated by incident rays that are back-scattered at the surface of the object based on the Snell's laws. The back-scattered wavefront then contains information on the shape of the object. Figure I.8 illustrates this regime called specular regime. More precisely, for each incident angles, the surface of the scatterer generates back-scattered echoes only in a particular direction. As a

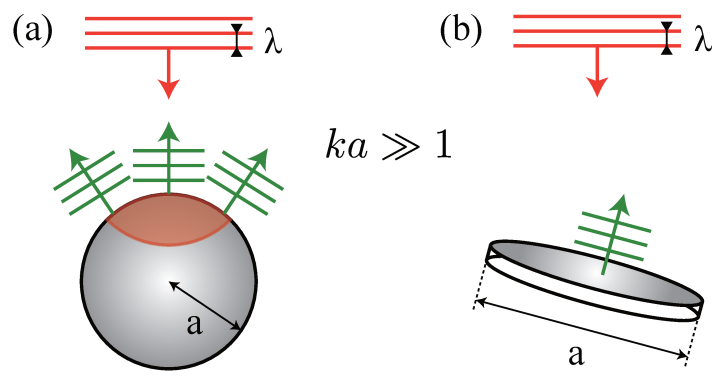

Fig. I.8 *Specular reflections of a plane wave of wavenumber $k = 2\pi/\lambda$ on large reflectors characterized by $ka \gg 1$. (a) Sphere of radius a, (b) disk of radius a.*

consequence, only these echoes should be used during the beamforming process of such scatterer [Par. I.1.5].

At the other extreme, when the wavelength is large compared to a scattering object, the roughness features of its surface fail to cause any noticeable interference effects. In other words, the phase differences between reflections from high and low points on the surface are insignificant. In this regime called Rayleigh scattering, the scattered intensity varies as the fourth power of frequency. For unresolved sphere, Chamber and Gautesen [10] have shown that a contrast of density is associated with a monopole, meaning that the reflected wave-field is isotropic [Fig. I.9(a)], while a contrast of compressibility is a dipole [Fig. I.9(b)]. However, in a pulse-echo configuration where the transducers are used both as source and receiver, it is difficult to distinguish between the two kinds of reflected wave fields. Indeed, the differences can only be probed at large angles of collection, which are not always available in this configuration. In addition, scatterers are neither pure monopoles nor pure dipoles but correspond to an in between configuration, depending on which contrast is the most predominant one. For this reason, no distinction is made in medical ultrasound between those two types of contrast.

I.1.3.2 Back-scattered echoes generated by unresolved scatterers

The complexity of soft tissues implies that the medium is mainly composed by unresolved scatterers. The medium is often modeled as a homogeneous matrix with embedded scatterers that are characterized by their own complex reflectivity. To better understand the back-scattered signals that are generated by such media, we first consider the configuration where only one transducer u_{in} illuminates the medium with a brief pulse and one transducer u_{out} is measuring the back-scattered echoes. In order to avoid complexity, in the following explanations, we only consider the imaging plane thanks to the probe lens; even if the wave propagation does happen in 3D [Fig. I.10a]. In this configuration, the incident wave is a diverging wave that excites all the scatterers of the medium. We observe that the ones that are located on an ellipse, whose foci coincide with the emitter and receiver locations, are characterized by the same round-trip time-of-flight t. At this given time, the signal measured by the receiver then results from the superposition of

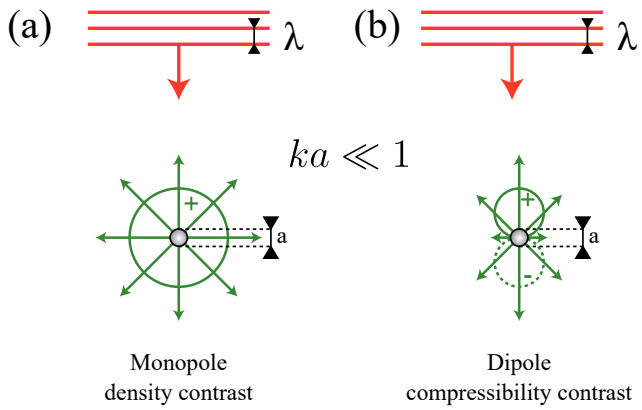

Fig. I.9 *Rayleigh scattering of a plane wave of wavenumber $k = 2\pi/\lambda$ on large reflectors characterized by $ka \gg 1$. (a) Sphere of radius a, (b) disk of radius a.*

the echoes generated by each one of these selected scatterers. The contribution of each scatterer is weighted by both the local amplitude of the incident wave that excited the scatterer and their scattering strength. In practice, the emitted pulse has a finite duration that enlarges the number of scatterers that contributed to the measured signal at time t. From this simple experiment, we define the isochronous volume as the ensemble of positions that share the same round-trip time-of-flight, for a given excitation (here a single transducer insonification), a given receiver and a given time-of-flight [11]. In other words, it contains all the potential locations of the medium that may participate to a given back-scattered signal.

For a more complex configuration where the incident wave is a focused one generated by an array of transducers, the isochronous volume defined at time t for a given receiver is deduced from the superposition of all the individual one computed for each couple emitter/receiver shifted by the transmitted time-delay. Due to the random reflectivity of the unresolved scatterer, this volume acts as a continuously moving incoherent acoustic source. Figure I.10(b) displays the isochronous volume associated with four successive time-of-flight induced by a focused incident beam. In this case, the intensity received by each scatterer depends on its location compared to the incident beam. The incoherent virtual sources are then limited to the illuminated field-of-view.

To sum up, each signal of the reflection matrix $R(\mathbf{r}_{\text{in}}, u_{\text{out}}, t)$ is associated with its own isochronous volume that delimits the spatial extension of the incoherent virtual source that generates this back-scattered echo. For a given image voxel located at $\mathbf{r}$ and a given excitation, the beamforming consists first in estimating the round-trip time-of-flight $\tau(\mathbf{r}_{\text{in}}, u_{\text{out}}, \mathbf{r})$ for each receiving transducer and then in summing coherently the corresponding signals. By constructive and destructive interferences, only the common part of all the selected isochronous volume will constructively interfere, which defines a new volume named received focal spot that is associated with the beamformed signals. Each pixel of the ultrasound image then results from an ensemble of unresolved scatterers randomly distributed within the corresponding focal spot. The back-scattered wavefront that arises from this area results from the superposition of echoes generated by each one

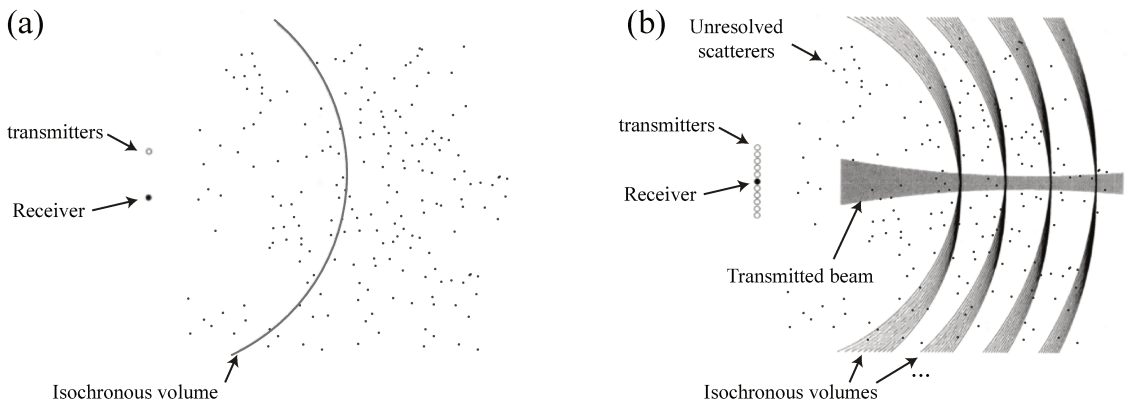

Fig. I.10 *Isochronous volumes cover all the scatterers that contribute to the received signal of a given transducer and a given time. (a) configuration where one transmitter emits a brief pulse that excites the entire medium. (b) configuration where multiple transmitters (white circles) emit a focused incident wave, whose back-scattered echoes are probed by one receiver (black circle). Four isochronous volumes are sketched at four different times. The shaded area corresponds to the width of the transmitted beam. Adapted from [11].*

of those scatterers. Due to the spatial random distribution of scatterers, the medium reflectivity appears as being random and is responsible for this granular texture observed on ultrasound images that is called speckle [Fig. I.6]. This texture is thus more dependent on the measuring system (involving the transmitted and received part) than on the tissues' nature itself.

I.1.3.3 Spatial coherence of back-scattered signals: the Van Cittert Zernike theorem

For a given transmitted focused beam and a given imaging point $\mathbf{r}$: the spatial coherence of the realigned signals $\breve{R}\left(u_{\text{out}}, \mathbf{r}_{\text{in}}, \mathbf{r}\right)$ can be studied as a function of the receiving transducer u_{out} to characterized the back-scattered signals of a random medium. Since at least a part of the transmitted focal spot is common to all their associated isochronous volumes, these realigned signals exhibit a spatial correlation even in a speckle regime. In this regime, the transmitted focal spot can be seen as an incoherent source for the back-scattered signals, whose spatial coherence is predicted by the Van Cittert Zernike (VCZ) theorem [12]. This theoretical result states that in a monochromatic regime and in a far-field configuration, the spatial correlation of a pressure field generated by an incoherent source is proportional to the Fourier transform of the intensity distribution of this source.

Mallart and Fink [11] adapted this theorem for a pulse-echo configuration, and more precisely, for the confocal configurations induced by a focused beam, *i.e.* when $\mathbf{r}_{\text{in}} = \mathbf{r}$. In absence of aberration, meaning that the medium is homogeneous, *i.e* with a constant speed of sound, the pressure field generated by the focused beam within the transmitted focal plane is predicted by the diffraction theory as [3]:

$$P(z_{\text{in}}, x) \propto \text{TF}\left[E_0(u)\right] \tag{I.20}$$

where TF[..] is the spatial Fourier Transform operator and $E(u)$ the pressure field generated at the surface of the transducers [Par. I.1.2.2]. From this equation, the correlation function of the realigned signals $\breve{R}\left(u^1_{\text{out}}, \mathbf{r}_{\text{in}}, \mathbf{r} = \mathbf{r}_{\text{in}}\right)$ and $\breve{R}\left(u^2_{\text{out}}, \mathbf{r}_{\text{in}}, \mathbf{r} = \mathbf{r}_{\text{in}}\right)$, noted $\breve{R}_{u_1}$ and $\breve{R}_{u_2}$ respectively, can be deduced from the VCZ theorem as:

$$S(\mathbf{r}_{\text{in}}, u_1, u_2) = \left\langle \breve{R}_{u_1} \breve{R}^*_{u_2} \right\rangle \propto \text{TF}(|P|^2) \left[\frac{u_1 - u_2}{\lambda z} \right] \tag{I.21}$$

where $\langle .. \rangle$ denotes a required average over multiple realizations of disorder. As the above equation depends only on the distance $\Delta u = |u_1 - u_2|$, this average is experimentally replaced by a spatial one over all couples of receiving transducers u_1 and u_2 distant of Δu, to measure the correlation function $S(r_{\text{in}}, \Delta u)$. It is also ingeniously improved by correlating realigned time-window signals $\breve{R}\left(u_{\text{out}}, \mathbf{r}_{\text{in}}, \mathbf{r}, \Delta t\right)$ where Δt denotes a centered time-window on $\Delta t = 0$ and whose temporal width is typically defined by a few periods of the central frequency.

Note that if the signals are not realigned, the spatial correlation of the back-scattered echoes shows an additional phase term $\exp\left[i 2\pi / \lambda Z (u_1^2 - u_2^2)\right]$ compared to equation I.21, which is linked to the difference of geometric curvature between the two selected elements.

In absence of aberration and in the case where the transmitted pressure field $E_0(u)$ is proportional to a rectangular function, the pressure field P produced in the focal plane is a cardinal sinus [Par. I.1.2.2]. Thanks to the Fourier transform properties, the Fourier transform of a product is the convolution of the Fourier transform of each term. If the above assumption is fulfilled, it then leads to the fact the spatial correlation function of the realigned signals $S(r_{\text{in}}, \Delta u)$ is a triangular function that depends on the distance Δu. In presence of aberrations, the author shows that the size of the input focal spot increases, which reduces the width of the spatial correlation [Par. I.2.2.3]. Based on this phenomenon, the author introduced the focusing factor that quantify the quality of focus in a speckle regime.

I.1.3.4 Attenuation in soft tissues

To complete the description of back-scattered echoes generated by soft-tissues, we briefly evoke the attenuation phenomenon and how it is handled in B-mode imaging. When ultrasound waves propagate in soft tissues, it put them in movement, which necessary generates some friction. This effect results in a loss of acoustic energy that is transformed in weak local heating. This loss called absorption, is generally described by an exponential decaying that is a function of the traveled distance (or time-of-flight). The characteristic length of this phenomenon is called the absorption length l_a

Absorption is not the only source of losses that impacts the incident wave throughout its propagation inside the medium. The scattering process also reduces the intensity of this incident wave. It is characterized by the mean-free-path l_e, which can be seen as the mean distance between two scattering events [Par. I.3.2]. Both l_a and l_e are two fundamental properties of the propagation medium. However, separate absorption from scattering losses is a difficult task that requires a subtle analysis of the back-scattered echoes to first accurately quantify the multiple scattering process [13]. In wave physics, the combination of these two phenomena is characterized by the extinction length l_{ex} such

as:

$$\frac{1}{l_{ex}} = \underbrace{\frac{1}{l_e}}_{\text{scattering}} + \underbrace{\frac{1}{l_a}}_{\text{absorption}} . \tag{I.22}$$

In the field of ultrasound, the pressure field generated by a monochromatic plane wave propagating along the axis $\vec{e}_z$ at frequency f_c is often modeled as:

$$P(z,t) = P_0 e^{i(2\pi f_c t - k_c z)} e^{-\alpha(f_c) z} \tag{I.23}$$

where P_0 is the pressure field at time $t = 0$ and $z = 0$ and $\alpha(f_c)$ is the attenuation factor expressed here in terms of nepers-per-centimeter in this form and defined as $l_{\text{ex}} = 1/\alpha$. As indicated, the attenuation factor strongly depends on the frequency and generally obeys a frequency power law, defined as [14]:

$$\alpha(f) = \alpha_0 + \alpha_1 f^y \tag{I.24}$$

where α_0 is often neglected and y is close to one in soft tissues. Consequently, attenuation in tissue-mimicking phantom is often given in (dB/MHz/cm). This behavior implies that higher frequencies are more attenuated than lower ones. The spectrum of back-scattered signals then evolves with the time-of-flight, and thus with the depth of the scatterers. Figure I.11 illustrates this behavior by showing the average spectrogram of echoes used during the beamforming process [Par. II.2.3 provides more details on its computational details]. In addition to a global intensity loss, we observe a shift of the central frequency towards the low frequencies at large depth, which reduces the resolution of the ultrasound image (in addition to the potential diffraction phenomena).

For the past thirty years, many studies have investigated the global attenuation encounter in soft tissues and it has been shown that the mean free path is much larger than the absorption length ($l_e \gg l_a$). Consequently, the attenuation coefficient mostly described the absorption phenomenon that can be used as a bio-marker for the diagnoses of some diseases. For instance, inflamed and cirrhotic livers were shown to suffer from less and higher losses than healthy liver respectively [15]. Three types of techniques have been proposed to quantify these losses [16]:

- the spectral shift technique that probes the downshift in the center frequency with respect to depth [17, 18, 19];
- the spectral difference method, which measures the decay of the power spectrum frequency components with respect to depth to estimate the attenuation coefficient as a function of frequency. These methods are based on the comparison with measurements performed on known tissue-mimicking phantom [20, 21]; and
- the hybrid method, which is a combination of the first two techniques, *i.e.* a downshift estimation of the center frequency associated with the comparison with tissue mimicking phantoms [22].

To limit the impact of these losses on the ultrasound image and to avoid a drop of the image brightness at large depth, $\mathcal{I}(\mathbf{r})$ is often multiplied by an increasing function of depth called Time-Gain-Constant (TGC) that is manually and/or empirically adjusted.

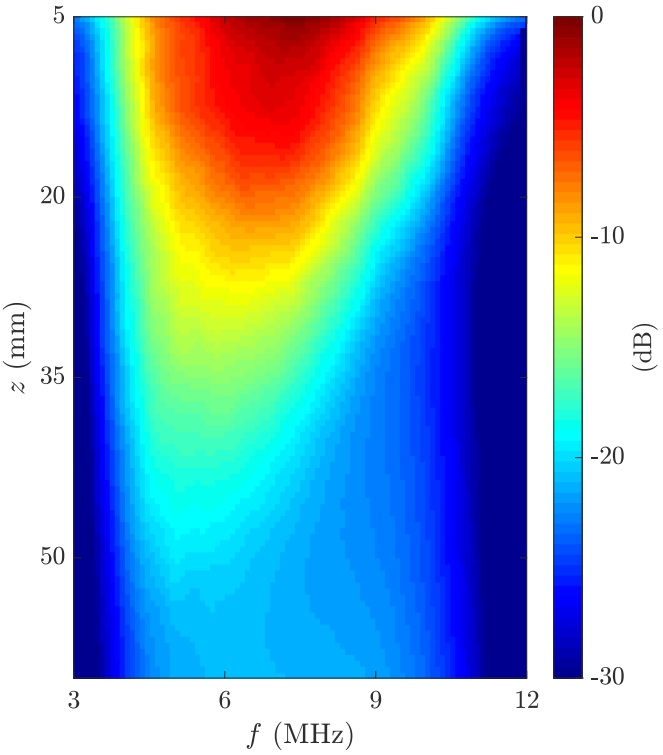

Fig. I.11 *Spectrum of echoes used during the beamforming process as a function of depth [see Par. II.2.3]. The transmitting sequence is composed by* 41 *plane waves spanning* -20 *to* 20 *deg and the transmitted pulses have a central frequency defined at* 7.5 *MHz. The probe used is the SL15-4 whose bandwidth is between* 4 *and* 15 *MHz.Experiment on a homogeneous tissue-mimicking phantom without targets characterized by an attenuation coefficient:* $\alpha = 0.5$ *dB/cm/MHz.*

I.1.4 Synthetic beamforming

In the paragraph I.1.2, we introduced the conventional image construction process that is based on focused insonification. This technique is characterized by the fact that each pixel of the ultrasound image is constructed based on the back-scattered signals of a single transmitted event. Inspired by experiments in underwater acoustic and RADAR, some forty years ago [23, 24], another technique has been proposed to combined the wavefield obtained from multiple insonifications to construct each pixel of the ultrasound image. Thanks to the hardware development of ultrasound systems, this technique called synthetic beamforming has been widely used over the past twenty years to produce high image quality. We first describe in this paragraph its pro and cons from an acoustical point-of-view. A more fundamental analysis is developed in paragraph II.1.3 as it contains many links with the matrix approach developed in chapter 2.

I.1.4.1 Coherent plane wave imaging

While conventional beamforming based on focused insonification is widely used by clinical ultrasound systems, one of its major drawbacks is the poor framerate, usually around 30 to 40 Hz (or fps). Even if it is high enough for real-time B-mode imaging, this imaging technique fails to capture fluctuations of the medium reflectivity that are characterized by higher frequencies such as heart beats or blood flows. The limiting step lies in the number of insonifications used to create an image and, more precisely, the need to wait for the round-trip time-of-flight. To tackle this issue, two different strategies has been developed: (*i*) send simultaneously multiple focused beams in order to reconstruct multiple scan-lines during a single insonification (in practice, the simultaneous insonified scan-line are not adjacent in order to avoid cross talks) [25]. (*ii*) Modify the shape of the incident been in order to insonify larger part of the medium for each insonification. To this aim, Montaldo *et al.* (2009) [26] introduced the coherent plane-wave compounding that allows to reach high frame rate (around 1 kHz) with a decent image quality. This imaging technique successfully mixes two ingredients *plane wave imaging* (PWI) and *coherent compounding*.

Plane wave imaging consists in insonifying the entire medium with a single plane wave θ_{in}. A beamforming is then performed in reception for each focal point [Fig. I.12]. For linear probe, a plane wave with an incident angle θ_{in} is created by exciting all the probe transducers with transmitted time-delays that linearly depend on the location of the ultrasound transducers:

$$\tau_{ex}(\theta_{\text{in}}, u) = \frac{u \sin(\theta_{\text{in}})}{c_0}. \tag{I.25}$$

The DAS beamforming is then performed by first realigning signals with the appropriate delay that corresponds to the required round-trip time-of-flight for a plane wave θ_{in} to travel from the probe to the image voxel $\tau_{\text{in}}(\theta_{\text{in}}, \mathbf{r})$ and to come back to each receiver $\tau_{\text{out}}(u_{\text{out}}, \mathbf{r})$:

$$\tau(u_{\text{out}}, \theta_{\text{in}}, \mathbf{r}) = \underbrace{\frac{x \sin(\theta_{in}) + z \cos(\theta_{\text{in}})}{c_0}}_{= \tau_{\text{in}}(\theta_{\text{in}}, \mathbf{r})} + \underbrace{\frac{\sqrt{(x - u_{\text{out}})^2 + z^2}}{c_0}}_{= \tau_{\text{out}}(u_{\text{out}}, \mathbf{r})}. \tag{I.26}$$

Then the coherent sum is performed for realigned signals at $\Delta t = 0$ [Par. I.1.2]. Eventually, this sum is weighted by apodisation terms that are linked to the 2D free-space green function [Par. I.1.2.2 and II.2.1]. Even if this imaging technique produces ultrasound images with a relatively poor quality [Fig. I.13(c_1)], its main advantage is that an entire ultrasound image is created from a single insonification [27]. This imaging technique allows to reach very high framerates, which allows the observation of fast movements such as the propagation of shear waves inside soft tissues [28].

Coherent compound is based on the idea of combining multiple images of the same scatterers that have been differently insonified. While incoherent compound has been widely used since the early 1980s [29] for speckle reduction and signal to noise improvement, coherent compounding, also known as synthetic beamforming, has first been studied some twenty years later in the 2000s. First mentioned in the context of limited diffraction beams [30, 31], this technique has been very successful via the pioneer work of Montaldo *et. al.* [26], where it constitutes a key part of the transient elastography

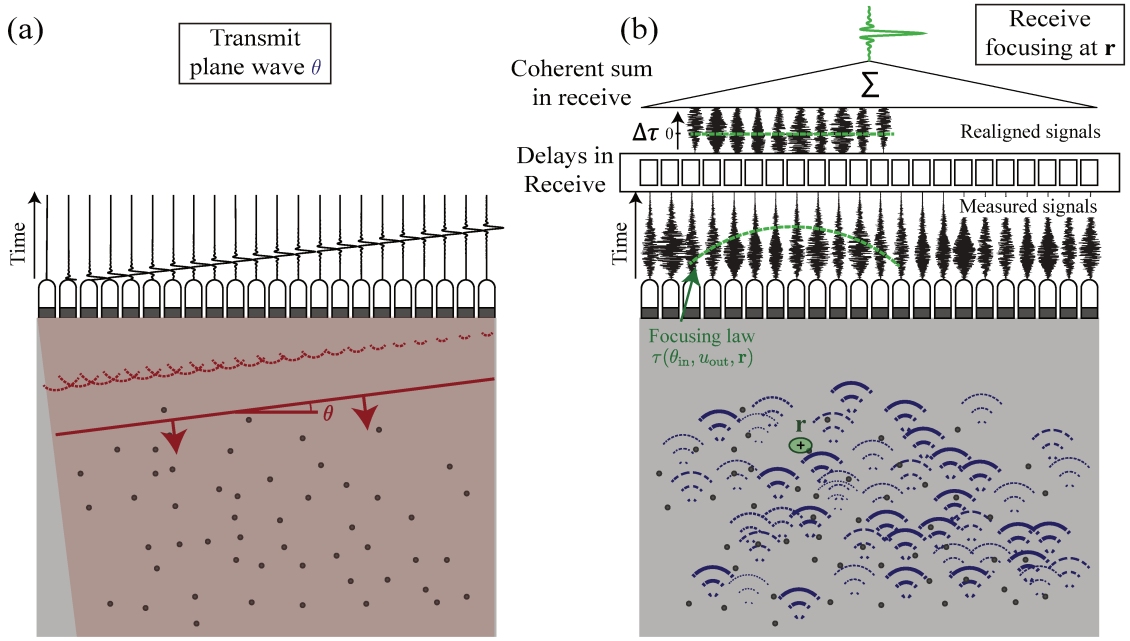

Fig. I.12 *Plane wave beamforming. (a) An incident plane wave characterized by an angle θ_{in} insonifies the entire medium. (b) back-scattered signals are first measured by the transducers, delayed and sum for each image voxel* $\mathbf{r}$.

technique. By coherently recombining back-scattered echoes from different illuminations, we numerically improve both the resolution and contrast of the ultrasound image. In the case of coherent plane wave illuminations, the medium is insonified by an ensemble of plane waves that are characterized by their incident angle θ_{in}. back-scattered signals measured by the transducer u_{out} at the time-of-flight t are stored in a so-called reflection matrix $\mathbf{R}_{u\theta} = [R(u_{\text{out}}, \theta_{\text{in}}, t)]$. For each plane wave a received beamforming is performed to produce low quality images that are then coherently summed. Similarly, to the focused beamforming [Eq. I.9], the synthetic plane wave beamforming consists in first realigning signals for each focal point $\mathbf{r}$ [Fig. I.12]:

$$\breve{R}(u_{\text{out}}, \theta_{\text{in}}, \mathbf{r}, \Delta t) = R(u_{\text{out}}, \theta_{\text{in}}, \tau(u_{\text{out}}, \theta_{\text{in}}, \mathbf{r}) + \Delta t), \tag{I.27}$$

before coherently sum the ones that are defined by $\Delta t = 0$:

$$R_b(\mathbf{r}) = \frac{1}{N_{\text{out}}(\mathbf{r}) N_{\text{in}}(\mathbf{r})} \sum_{\theta_{\text{in}}^-(\mathbf{r})}^{\theta_{\text{in}}^+(\mathbf{r})} \sum_{u_{\text{out}}^-(\mathbf{r})}^{u_{\text{out}}^+(\mathbf{r})} \breve{R}(u_{\text{out}}, \theta_{\text{in}}, \mathbf{r}, \Delta t = 0), \tag{I.28}$$

where $N_{\text{in}}(\mathbf{r})$ is the number of angles used to reconstruct the pixel at location $\mathbf{r}$. It is defined by $\theta_{\text{in}}^-(\mathbf{r})$ and $\theta_{\text{in}}^+(\mathbf{r})$, the first and last transmitted used angles. By combining multiple insonifications, this beamforming numerically mimics a focused insonification for each pixel of the ultrasound image [Fig.I.13(a,b)]. Mathematically, this phenomenon is observed via the summation over the angles θ_{in} that plays the same role as the summation over the receiving transducers u_{out}. The idea of synthetic beamforming is thus to

select all potential back-scattered echoes generated by each image voxel for each couple $\{\theta_{\text{in}}, u_{\text{out}}\}$, which leads to a double focusing in transmission and in reception. This imaging technique then falls under the scope of confocal imaging that are characterized by at least an improved SNR as the spatial extension of the isochronous volume is minimized both by the input and output focusing for each focal point. The resolution of the ultrasound image could also be improved if the maximum angle of illumination $\beta_{\text{in}}(\mathbf{r})$ is higher than the one of collection $\beta_{\text{out}}(\mathbf{r})$ [Par. I.1.2.1]. Figure I.13 displays the reconstructed ultrasound image of a breast phantom (CIRS, model 0073), based on various number of transmitted plane waves. We logically observed that the image quality increases with the number of illuminations and Figure I.13(c_4), which is constructed based on the highest number of plane waves, shows the best image quality, meaning the best resolution and contrast. The resolution can be assessed by looking at the size of the scatterers located within the white ellipse that are unresolved micro-calcifications. To compare the contrast of these US image, we remind the reader that the US images are normalized by their mean intensity and displayed with the same dynamic. Therefore, the image associated with the best contrast is the one that show both the darker (*e.g.* rectangle area) and brighter structures. More interestingly, figures I.13(c_2, c_3) are built from the same number of illuminations but with a different angle step (c_2 is based on a larger angle step and a larger maximum angle of illumination). This example illustrates that while large angles of illumination are required to improve the resolution of the image, a low angle step improves the contrast of the ultrasound image.

I.1.4.2 Comparison between focused and plane wave illumination

The transmitted focusing is the major difference between conventional beamforming that relies on focus insonification and the coherent plane wave compounding that uses plane wave illuminations (PWI) to perform numerical transmitted focusing. To successfully perform the numerical transmitted focusing, the PWI assumes that the wave propagation is a linear process and that the medium stay fixed during the entire transmitting sequence. If these hypotheses are valid, the two transmitted focusing are strictly equivalent (the comparison also requires that the energy of the incident waves is the same). Note that the numerical transmitted focusing requires a larger computational cost. Performing real time B-mode beamforming based on PWI that uses the same number of illuminations as the focus one is a real challenge that can be achieved only for state-of-the-art ultrasound system.

In practice, the PWI is used to reduce the number of illuminations. Figure I.14 compares the ultrasound image obtained via the two techniques in the case of *in-vivo* carotid imaging of a healthy volunteer. The probe is placed perpendicularly the artery axis (the dark disk located at the center of the images). To image approximately the same area, the medium is insonified successively by the two illumination sequences. The plane wave image is based on 41 plane waves spanning from -20 to 20 deg, while the conventional image uses 256 focused insonifications characterized by a focal depth $z_{\text{in}} = 22$ mm and a transmitted f-number $\text{F}_{\text{in}}^{\#} = 3.3$. The transmitted parameters have been arbitrary chosen and are close to the optimal ones used for each imaging mode related to this example. Even if those two sequences are not strictly equivalent, they constitute a relevant example to compare the pro and cons of each techniques.

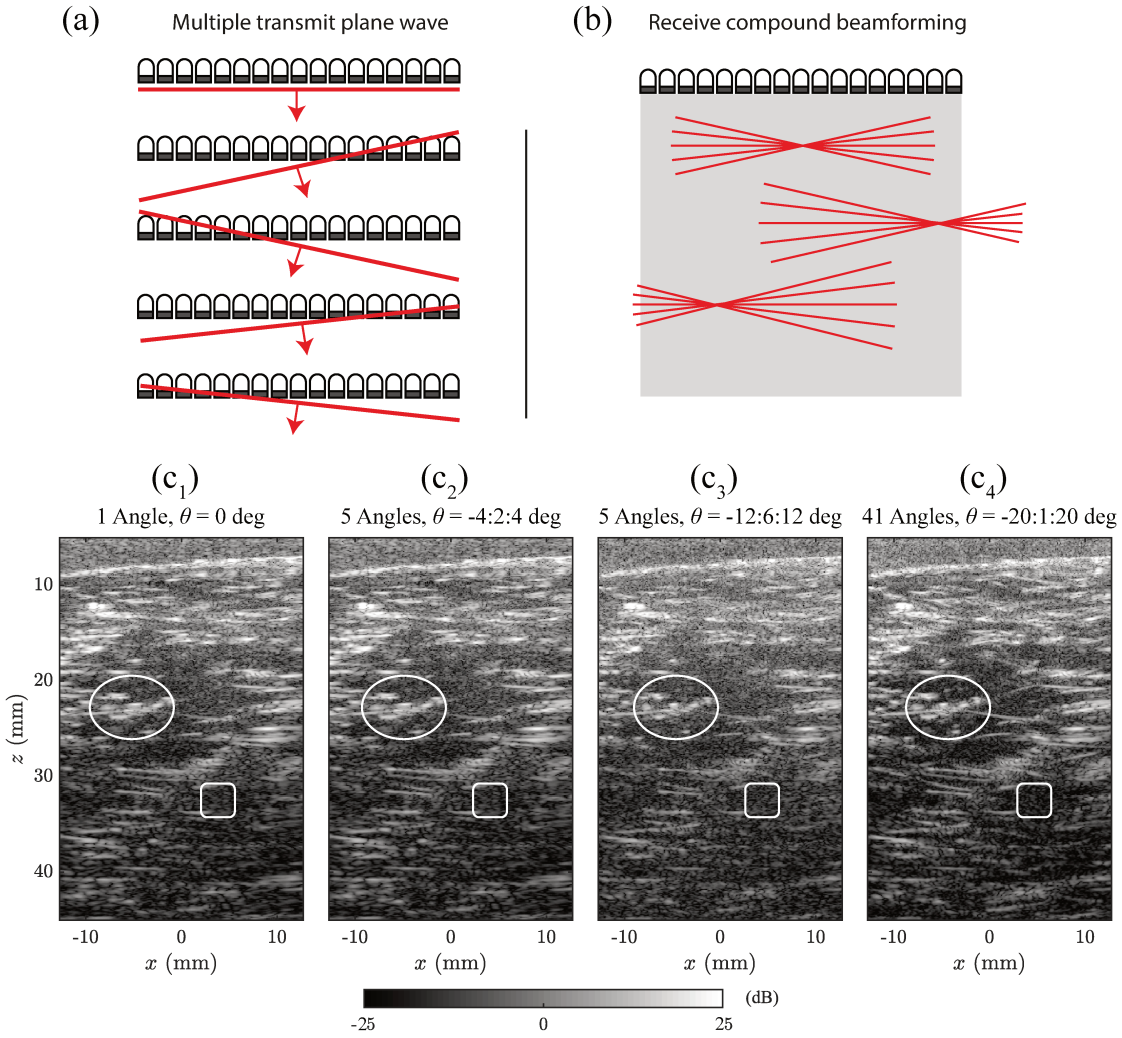

Fig. I.13 *Coherent plane wave compounding. (a) Multiple plane waves are used to insonified the entire medium. (b) A DAS beamforming is then performed to coherently combine all the measured echoes generated by each image voxel. (c) Ultrasound plane wave imaging of a breast phantom (CIRS model 073) with various plane wave sequences. The number of used angles, the range and the angle step are indicated above each image. Inspired from [26].*

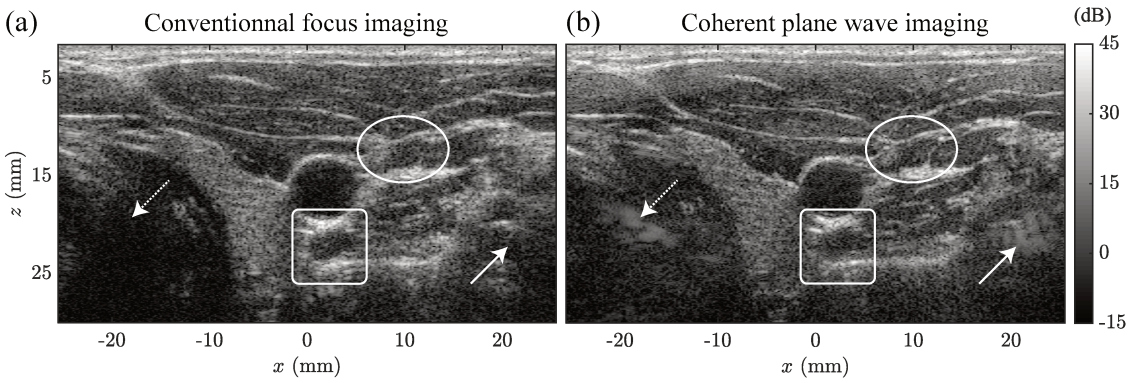

Fig. I.14 *Comparison of coherent plane waves compounding and focused insonifications. In-vivo carotid imaging of a healthy volunteer. (a) Conventional focus imaging technique based on* 256 *focused insonifications characterized by a focal depth* $z_{in} = 22$ *mm and a transmitted f-number* $F_{in}^{\#} = 3.3$. *(b) Coherent plane wave imaging based on* 41 *plane waves spanning from* -20 *to* 20 *deg [Par: I.1.4].*

Through this example, we observe that although the number of illuminations is more than 6 times lower for PWI, the two resulting images are quite similar. From a signal processing point-of-view, it implies that the reflection matrix obtained from focused insonification contains more redundancies on the medium reflectivity. Therefore, PWI may be seen as a spatial compressed sensing process that is able to better extract uncorrelated information on the medium.

Going deeper into the details, the overall resolution of the PWI ultrasound image seems to be higher than the focus one (see structures inside the white ellipse). Two complementary phenomena could justify this observation. First, the maximum angle of illumination, which is linked to the image resolution, is higher for the PWI image, $\beta_{\text{PWI}} = 20$ deg than for the focus case $\beta_{\text{focus}} = 8.5$ deg in this example. Then PWI is a confocal imaging, which by nature generates a better image quality as it involves smaller isochronous volumes. Note that for pixels located around the focal depth of the focused beams, the conventional beamforming is also a confocal technique. This characteristic explains why the difference of resolution between the two images is reduced for pixels located between 20 mm and 25 mm depth [see the structures inside the white squares].

To compare the contrast of the two images, two areas are investigated in this example: (i) first the carotid itself, which is the dark disk at the center of the image. Blood constitutes a weak scattering medium, which should appear as dark as possible; (ii) then bones, whose acoustic impedance is much larger than the ones of surrounding tissues. Therefore, most of the incoming wave energy is reflected at its boundaries and only a weak refracted part can probe the inner part of the bone. This drives to dark areas on the ultrasound image [*e.g.* bottom left part of the images]. Focus beamforming shows a better contrast than PWI. This observation illustrates the lack of information on the medium in the case of PWI. Indeed, to extract the maximum of information on a scatterer reflectivity, the complete radiation pattern must be acquired. It consists in measuring in the scatterer frame, all the possible back-scattered signals in the direction

θ_{out}, for any incident plane wave θ_{in}. In other word, this scatterer should be insonified by all transmitted spatial wave number defined at the central frequency $k_{\text{in}} = k_c \sin(\theta_{\text{in}})$. In the case of focus beams, and for scatterers located around the focal plane, the incident beam contains all the transmitted spatial wave number between $k_{\text{in}}^- = k_c \sin(\theta_{\text{in}}^-)$ and $k_{\text{in}}^+ = k_c \sin(\theta_{\text{in}}^+)$. To the contrary, in the case of PWI, the scatterers are only insonified by some incident transmitted numbers k_{in}, which correspond to the transmitted plane wave. This phenomenon can be seen as a sampling of the k_{in}-space. As with any kind of sampling, the k_{in} step must be small enough to fully capture all the back-scattered information on this scatterer. This criterion is thus linked to the spatial coherence of the back-scattered echoes that can be observed from one insonification to the other. This spatial coherence is maximum for unresolved bright stars and can be deduce from the Van Cittert Zernike theorem for unresolved scatterer.

In addition, some artifacts on the PWI image are observed and pointed out by the white arrows. These artifacts are due to bright specular reflectors that belong to the isochronous volume associated with the pixels of interest. Even if those scatterers generate signals that are out-of-phase for these realigned signals, the destructive interferences that should erases them during the coherent summation is not optimal due to a lack of information.

Finally, the hypothesis of a motionless medium is more critical for PWI than focused illumination. While, each pixel of the conventional ultrasound image is constructed based on a single illumination, the coherent compounding uses multiple illuminations for each one of them. If some movement occurs during the transmission sequence, the relative position of the scatterers will be distorted on both US images. However, in the case of coherent compounding, such movements will induce in addition some destructive interferences as back-scattered echoes are out-of-phase from one illumination to the other. Such situations appear *in-vivo* around arteries or close to the heart due to heart beats, but also if the probe is moved relatively to a fixed medium.

These observations explain why plane wave imaging is able to produce very high-quality images with few plane waves in tissue-mimicking phantom (motionless and without specular scatterers) [26] but may produce some artifact in more complex configurations.

I.1.4.3 Other insonification sequences for synthetic imaging techniques

The idea of combining multiple insonification to improve the image quality is not limited to the case of plane wave insonification but can be applied to any type of illumination including the focused one [32]. Indeed, for small transmitted f-number $\text{F}_{\text{in}}^{\#}$ (meaning large apertures) the insonified region is not a straight line but a cone [Fig. I.15b]. Therefore, scatterers located above or below are insonified by multiple focused beam [Fig. I.15(a)]. Coherent compounding can then be applied to focus insonifications to mimic a transmitted focusing on each image voxel, leading to a confocal imaging technique characterized by a better image quality. The versatility of this state-of-the-art imaging technique makes it useful in a number of applications, from increased image quality in systems using conventional transmitted focusing, to high framerate, and from high performance systems, to low-cost high image quality scanners.

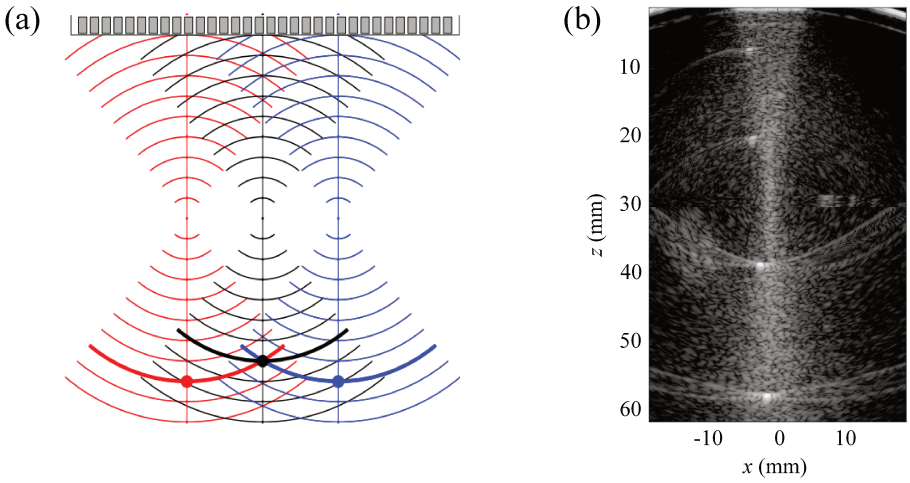

Fig. I.15 *Principle of synthetic focus beamforming. (a) Each image voxel (e.g. dark dot for instance) is illuminated by multiple beams whose back-scattered echoes can be coherently combined. Inspired from [32]. (b) Ultrasound image obtained from a single focused insonification. Each focus beam insonified a cone whose angle is defined by the transmitted f-number and location of the focal point. Extracted from [33]*

I.1.5 Fundamental limits of ultrasound imaging

Throughout the description of the image construction process, we briefly mentioned some hypotheses that are required to successfully produce a high image quality. However, due to the various configurations where the beamforming process is applied, some of these hypothesis may no longer be valid. In this section, we enumerate all the required assumption and discuss their potential impacts on the resulting images:

Homogeneous medium. The delicate step of computing the transmitted and received times-of-flight are achieved in any clinical device by assuming that the medium is homogeneous, with a constant speed-of-sound. Although this assumption is required for real-time imaging, it may not be valid for some configurations where long-scale fluctuations of the medium speed-of-sound impact the wave propagation [7]. In soft tissues, speed of sound ranges from 1400 m/s (*e.g.* fat tissues) to 1650 m/s (*e.g.* skin, muscle tissues) [14]. The order of magnitude of the fluctuations is then around 5%. Figures I.16(a,b) illustrate the impact of a wrong speed of sound model on the ultrasound image in a simple *in-vitro* experiment where a phantom is imaged through a water layer (b). The two media have different speed of sound ($c_{\text{water}} = 1480$ m/s and $c_{\text{phantom}} = 1540$ m/s), which invalidates the hypothesis of homogeneous medium with a constant speed of sound $c_0 = 1540$ m/s. We observed that compared to a standard phantom experiment without aberrations (a), the point-like targets (monofilaments) indicate that the image resolution is strongly impacted by the medium heterogeneities. Figures (c-d) are liver imaging of an "easy" and "difficult-to-image" patient, respectively. Liver being a highly vascularized organ, it appears that veins can easily be detected on figure (c), while they completely

blurred on figure (d), due to the heterogeneities induced by the shallow fat and muscle layers. Consequently, strong aberrations may impact the diagnosis of a medical exam. More details on the impact of aberrations on the beamforming process are described in paragraph I.2.1. In addition to the degradation of the image quality, a wrong model of speed of sound induces axial aberrations, whose first order impact implies that the location of the scatterers on the US image is biased. Indeed, the axial axis of the US image is in fact, a temporal one. It has been translated into a spatial axis based on the hypothesis of speed of sound. A hypothesis of homogeneous assumes that a back-scattered echo measured at time t has been generated by scatterer located at depth $z = c_0 t/2$. A modification of the speed of sound hypothesis then produce an axial translation of the resulting image. This effect then impacts any medical exams that are based on the measurement of distances on the ultrasound image. For example, the nuchal translucency (NT) scan is used to detect chromosomal abnormalities in a fetus. This scan simply consist in mesuring the thickness of the nuchal translucency of a fetus. While normal NT is characterized by a thickness that is lower than 3 mm, the risk of abnormalities and postnatal death, increases with NT thickness [34]. Even if statistics takes into account the uncertainties of the measure due to a wrong speed of sound model, correcting axial aberrations could strongly reduce the number of false positive and negative, and avoid additional invasive testing. Figure I.17 shows normal and abnormal NT scan, which illustrates the measurement conditions and demonstrates the need for any improvement of ultrasound image quality.

Single scattering regime: Independently of the speed of sound of the medium, the link between the location of the scatterer and the time-of-flight of the back-scattered echoes is valid only in the single scattering regime where we assume that the waves interacts only once with the medium. However, in a more realistic description, multiple scattering process occur, which implies that each back-scattered signal results from the combination of echoes generated by single and multiple scattering process. For ultrasound imaging, multiple scattering process acts as a source of incoherent noise which decreases the contrast of the resulting imaging. More precisely, it enlarges the spatial extent of the isochronous volumes as multiple scattered paths can have the same time-of-flight than single one [Fig. I.18a]. Intuitively, the probability to induce a multiple scattering process increases with the density of scatterers, their scattering strength and the time-of-flight, which directly influence the ratio of multiple scattering intensity over single intensity γ. Aubry *et. al.* [35] confirm that in *in-vivo* breast imaging, the ratio γ increases with the time-of-flight and reaches 50% at 40 μs. For singly-scattered echoes, it corresponds to scatterer located at 35 mm deep [Fig. I.18(b,c)]. Note that this ratio is estimated before any focusing step, it thus characterized the RF signal and not the US image. More details on multiple scattering are provided in paragraph [Par. I.3.2].

Speckle regime: the choice of the received aperture during the beamforming process derives from two phenomena. First it is limited by the radiation pattern of the transducer. Second, it stems from an assumption on the radiation pattern of the scatterers and thus on the direction of back-scattered echoes. By using a received aperture that is centered on the lateral position of the pixel of interest, we assume that this region generates back-scattered echoes in every direction and thus that this region is composed by unresolved scatterers. In the case of specular objects such as biopsy needle or muscle

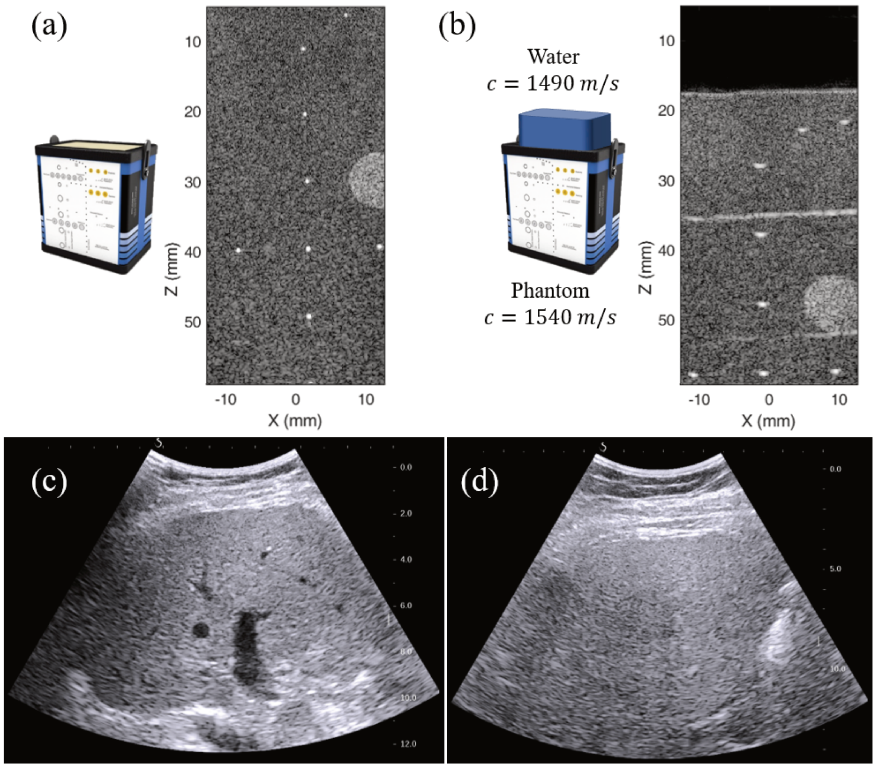

Fig. I.16 *Example of aberrations. (a,b) Phantom plane wave imaging without and with a water aberrating layer. The images are reconstructed according to a hypothesis of homogeneous medium $c_0 = 1540$ m/s. Linear probe: Supersonic SL15-4. (c,d) Liver imaging of a "easy" and "difficult-to-image" patient. On figure (d), the vascularized structured is completely blurred due to aberrations. Curved probe used: Supersonic XC6-1.*

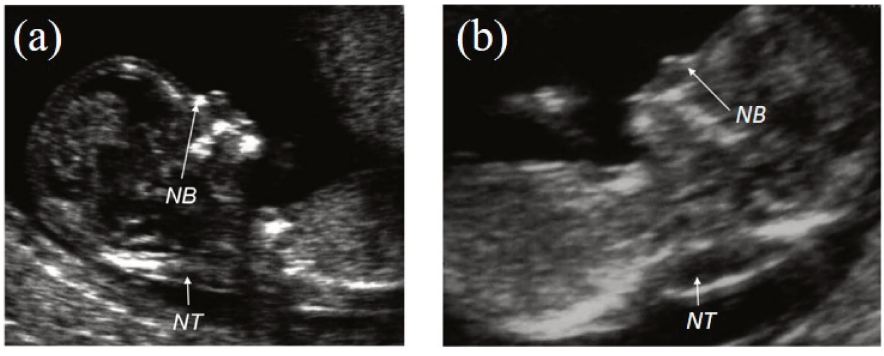

Fig. I.17 *Ultrasound images of 12-weak fetus: (a) with a normal nuchal translucency (NT) and a present nosal bone (NB); (b) with increased NT thickness and an absent nasal bone, which are biomarkers of trisomy 21. Figures are extracted from [34].*

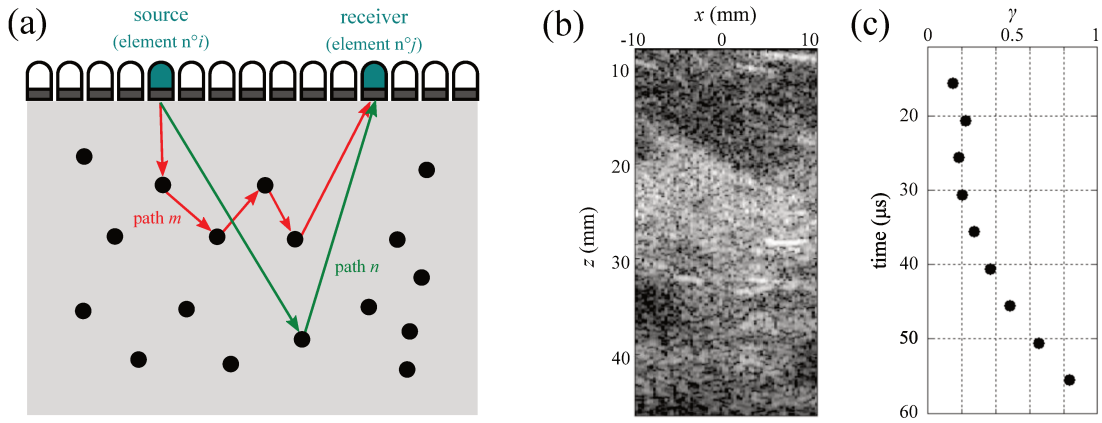

Fig. I.18 *Multiple scattering process. (a) Sketch of a single scattered path n (green curve) and a multiple scattered one m (red curve) that have the same time-of-flight. (b,c) In-vivo Breast imaging. Ratio of multiply-scattered intensity over single scattered intensity. Figures are inspired from [35].*

tissues that are anisotropic media composed by aligned fibers, echoes are back-scattered only in a privileged direction. By assuming a speckle regime, we coherently sum echoes that have not been generated by the image voxel, which induces destructive interferences.

Motionless medium: As stated above, an ultrasound image results from multiple insonifications that last at least 25 ms (corresponding to a framerate of 40 Hz). To avoid any distortion of the image, the medium is considered as motionless during the entire acquisition sequence. This assumption is even more crucial in the case of synthetic beam-forming as each pixel results from multiple insonifications via a coherent summation. In this last case, any movement automatically degrades the image quality. Nonetheless, the amplitude of displacement during the acquisition sequence must be compared to half the wavelength of the incident wave.

attenuation compensation: The last assumption performed by clinical ultrasound system consist in applying a TGC to compensate for for the global attenuation losses. The objective is to propose a more pleasant image for the human eye. Some systems propose to automatically set the TGC, but it is usually based on empirical measurements and can always be manually adjusted.

Even if ultrasound imaging is based on many fundamental assumptions, this technique became the most widely used imaging modality for medical purposes, proving in the same times its robustness and the wide range of applications where it can be successively used. Nonetheless, many efforts are still done to overcome these limitations that fall within two lines of research. On the one hand, improving the image quality to better estimate the medium reflectivity for difficult-to-image configurations such as brain ultrasound imaging. On the other hand, better characterize the mechanical properties of soft tissues that constitutes biomarkers for the diagnosis and the monitoring of some diseases. The two

following sections of this chapter provide a description of the state-of-the-art techniques developed for these two purposes.

I.2 Ultrasound adaptive imaging of heterogeneous media

In this section, we first describe the impact of aberrations on the US image construction process. We then detail the principle of adaptive imaging that is used to correct for aberrations, and finally we analyze the state-of-the-art techniques used to correct for these aberrations in the particular case of soft tissues imaging, characterized by a speckle regime.

I.2.1 Impact of aberrations on the beamforming process

I.2.1.1 Aberrations in transmission and reception

As stated above, ultrasound imaging results from a double focusing that are performed by applying time delays in transmission and in reception. These delays are computed based on times-of-flight estimations of the wave propagation, which stem from a speed of sound model. In the case of aberrations, this model is no longer valid. The times-of-flight are no longer accurate, which damage the focusing quality. More precisely, during the transmitted focusing, the wave is no longer confined in a diffraction limited area [Fig. I.19a]. It reduces the pressure field of the exciting wave at the focal spot and generates unwanted back-scattered signals coming from surrounding areas. In reception, the coherent summation is not optimal as it mixes echoes coming from different part of the medium [Fig. I.19b]. In other word, the isochronous volumes associated with each pixel are increased, which strongly degrade the image resolution and contrast. Astronomers were the first to deal with aberration issues in wave imaging. Their approach to improve image quality was to measure and compensate for the wave front distortions induced by the spatial variations of the optical index in the atmosphere. Based on deformable mirrors, this concept is known as adaptive optics and proposed as early as the 1950s [36]. Similarly, ultrasound adaptive imaging consists in inserting additional time delays [Fig. I.19e] in transmission and in reception in order to compensate for the medium heterogeneities [Fig. I.19c,d]. In transmission, this correction enables to create a diffraction limited focal spot, while in reception it selects echoes coming from this region. In this case, aberrations are typically modeled as a near-field phase screen $A(u)$ located at the face of the transducer, which induces both time-shifts called aberration laws and attenuation. Generally, the attenuation term is not compensated as it implies enhancing low SNR signals (corresponding to signals that have been largely attenuating), which is a delicate operation that may degrade the image quality instead of improving it. Therefore, only the time-shifts noted $\tau_{\text{ab}}(u)$ are generally investigated. The difficult task of any adaptive imaging technique lies in the determination of these additional time-delay (or phase mask in the frequency domain) that would adaptively compensate for the medium heterogeneities [37].

Even if the near-field phase screen model accurately describes aberrations that are concentrated in a thin layer near the transducers, it constitutes a helpful approximation for theoretical studies that can be extended to more complex configurations. As aberrations take place at the surface of the probe in this model, they are easily modeled by delaying

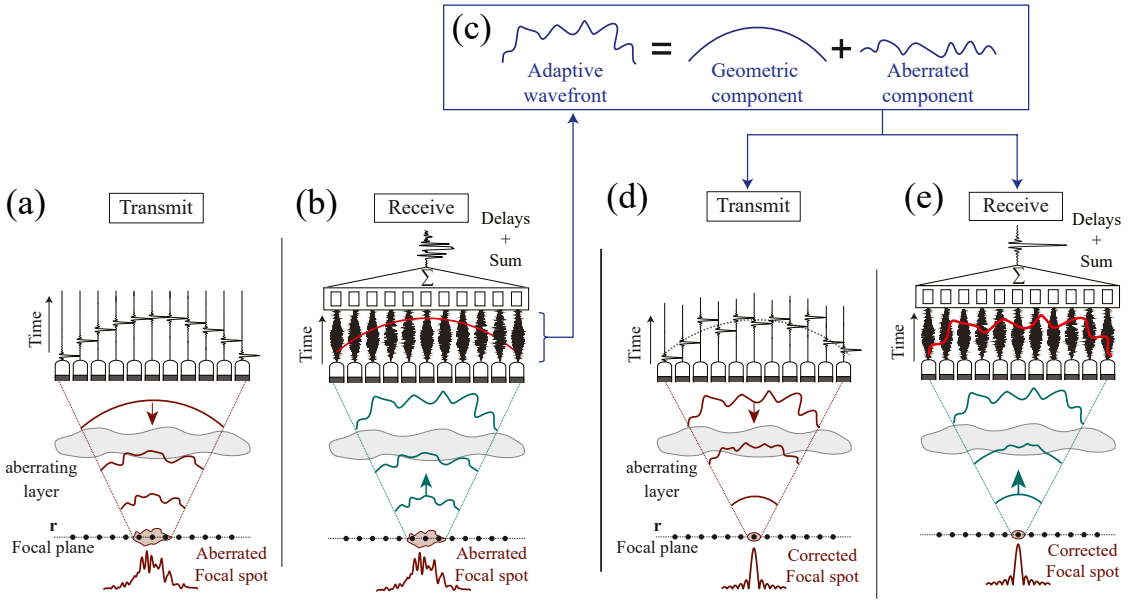

Fig. I.19 *(a, b) Impact of transmitted and received aberrations on the image construction process. (c) Adaptive focusing consists in modifying the initial focusing laws by means of suitable additional delays (the aberrated component). (d,e) This process enable to compensate for the impact of aberrations both in transmission and reception, leading to a high quality of focus.*

the transmitted pressure field induced by the surface of the transducers $E(u,t)$:

$$E^{\text{ab}}(u,t) = E(u, t - \tau_{\text{ab}}(u)). \tag{I.29}$$

Following the work done in optic [36], it is more convenient to study aberrations in the frequency domain as a time shift is translated into a frequency shift thanks to the properties of the Fourier transform, hence the name of adaptive phase aberration correction [38]. Aberrations then behave as a simple complex transmittance function:

$$E^{\text{ab}}(u,f_c) = E(u,f_c)e^{-i2\pi f_c \tau_{\text{ab}}(u)} \tag{I.30}$$

Impact of aberrations on the incident wave can then be investigated based on Fourier acoustic laws [3].

Nonetheless, this principle only corrects first order aberrations and do not take into account any other phenomena, such as interferences, diffraction or multiple scattering that may occur during the wave propagation. To correct more complex aberrations, the green function of the heterogeneous media under investigation has to be determined. Based on the principle of time-reversal mirror [39], some techniques have demonstrated the ability to focus on isolated bright target through a complex reverberating media in a reflection configuration [See Par. II.1.1].

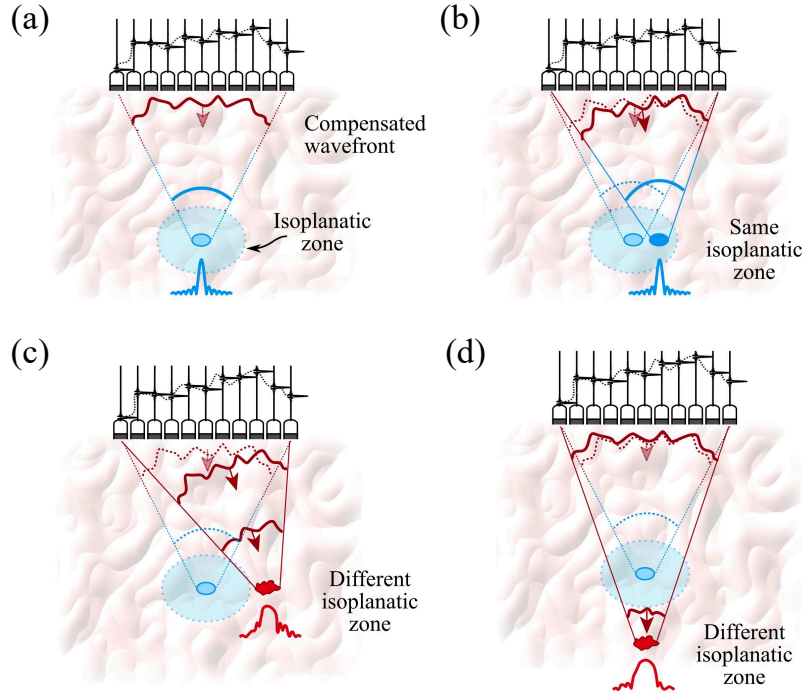

Fig. I.20 *Adaptive focusing in ultrasound imaging. (a) Adaptive focusing consists of adjusting the time delays added to each emitted and/or detected signal in order to focus on certain position inside the medium. (c) Tilting the same adaptive phase law allows the focal spot to be scanned over the vicinity of the initial focal point. The area over which adaptive focusing remains effective is called an isoplanatic patch. (C and D) Beyond this zone, the correction is no longer efficient. Figures are extracted from [40]*

I.2.1.2 Memory effect and isoplanatic patches

For heterogeneous tissues and organs such as the breast, or for body types that have large subcutaneous layers the accuracy of the near-field phase screen model dropped as a phase mask is only valid over a restricted area called an isoplanatic patch [Fig. I.20]. This is the region over which the aberration phase law is spatially invariant. To better understand this phenomenon, we consider two focal points closed enough one the other *i.e.* in the same isoplanatic patch. Their incident wavefront (and back-scattered echo) travel through the same area of the aberrator, resulting in the same distortion of the wavefront [[Fig. I.20](b)]. We can intuit from this visualization that the dimensions of the isoplanatic patches depend on the complexity of the heterogeneities that are characterized by their correlation length, on their location (near field or far field) and on the shape of the incident wavefront (focused, plane wave or diverging wave).

This physical phenomenon is often referred as the memory effect [41, 42, 43] or isoplanatism [36, 44] in wave physics. Usually, this phenomenon is considered in a plane wave basis. When an incident plane wave is rotated by an angle θ, the far-field speckle

image is shifted by the same angle θ [41, 42] (or $-\theta$ if the measurement is carried out in reflection [45, 46]). Interestingly, this class of field–field correlations also exists in real space: waves produced by nearby points inside a complex medium can generate highly correlated, but tilted, random speckle patterns in the far field [47, 11, 48, 38, 49]. Consequently, the point spread function (or focal spot) is invariant over an area called the isoplanatic patch.

The size of the isoplanatic patch is a key parameter for adaptive imaging techniques as it sets the required number of independent aberrations laws used for correcting a single image [Fig. I.20]. It also delimits the region of interest used to determine each aberration law. Unfortunately, it is often an unknown parameter. If the hypothesis of a near field phase screen aberration is correct, meaning that the aberrations is located at the surface of the transducers, then the spatial extension of the isoplanatic patch is infinite and aberration are perfectly corrected by this model. Indeed, aberrations are in fact located in the plane where wavefronts can be adjusted and controlled. However, if the aberration appears between the control plane and the imaging plane, its associated isoplanatic patch size is reduced. One can refer to the work of Mertz *et al.* in optics (2005) [44], who demonstrated that in the case where the wavefront is controlled in the pupil plane, *i.e.* in the far field, then the order of magnitude of the lateral extension l_x of the isoplanatic patch can be deduce from the statistics of the aberration laws:

$$l_x = \frac{2l_\phi}{\sqrt{1+2\sigma_\phi^2}}, \tag{I.31}$$

where the phase mask is deduced from a normal distribution of standard deviation σ_ϕ and a correlation length l_ϕ. This demonstration is based on the properties of the Fourier transform that links the pupil plane to the focal plane.

In acoustic, few studies have tried to characterize the dimension of the isoplanatic patches for *in-vivo* experiment. However, they studied different configurations with different techniques leading to various results:

- Ng (1997) [50] reported simulation measurements of the isoplanatic patch size using a 5 MHz linear array. Echoes from a point target were propagated through aberrating screens located at varying distances from the transducer surface. The array of transducers was translated in the lateral direction, and the radio frequency (RF) signals from the point target were correlated. Ng illustrated the near-infinite stability of near-field phase screens, and demonstrated that the size of the isoplanatic patch shrinks as the aberrating screen is moved further away from the transducer. As a result, at a distance of 20 mm between the transducers and the aberrating layer, the isoplanatic patch size was approximately $l_x = 13.9$ mm.

- Liu and Waag (1998) [51] measured the lateral and axial isoplanatic patch size of 20 mm thick post-mortem abdominal tissues using a time-shift compensation technique, and a linear array operating at 3.63 MHz. In this experiment, the abdominal tissue was placed directly beneath the transducers in water, and a point target was placed beneath the tissue layer, at a distance of 95 mm from the transducers. They applied identical compensation to the received waveforms from a point target as the target was translated in lateral and axial dimensions. The isoplanatic patch size

was determined to be twice the distance required to increase the width of the point target image by 10%. The average lateral and axial dimension of the isoplanatic patch was determined to be $[l_x, l_z] = [16.7, 39.0]$ mm.

- Tanter *et al.* (1998) [52] studied the time reversal process in absorbing media. More precisely, they recorded an enhancement of the focusing quality for targets located 15 mm away from the location where the aberration law has previously been estimated.

- Dahl *et al.* (2005) [53] studied the spatial stability of measured aberration profiles in breast, liver, and thyroid tissues at 5 MHz ($\lambda = 0.3$ mm). Relatively high stability was measured in breast and thyroid, with less stability in the liver. At 70% correlation, for example, lateral isoplanatic patch sizes l_x for breast, liver, and thyroid tissue were determined to be 1.1, 0.44, and 1.0 mm. For the same amount of correlation, axial isoplanatic patch sizes l_x were 2.0, 1.2, and 2.9 mm, respectively.

To illustrate the impact of aberrations on the focusing process, figures I.21(a,b) show simulated pressure field without and with an aberrated phase screen depicted on figure I.21(c). The simulation is performed at 5 MHz with a transmitted f-number $\mathrm{F}^{\#}_{\mathrm{in}} = 3$. The aberration stems from a random process based on a normal distribution and is characterized by a standard deviation $\sigma_{phi} = 40$ μs and a correlation length $l_{phi} = 5$ mm. These values where chosen to fit the one obtained by Dahl *et. al.* [53]. In this example, we observe that the centered of the focal spot is deviated both laterally and axially from the initial target.

I.2.2 Estimation of the aberration laws for ultrasound imaging of soft tissues

First adaptive imaging techniques developed for astronomers benefit from the presence of nearby bright stars or beacons to estimate the aberration laws that is valid for a region of interest. Based on the memory effect, this phase mask is then tilted in order to correct for aberration over the entire isoplanatic patch [Fig. I.20(b)]. Unfortunately, soft tissues are not embedded by such bright point-like scatterers that can be used as a reference. Ultrasound adaptive imaging technique have then been developed to deal with the particular case of speckle regime.

To simplify the determination of the transmitted and received aberration laws, only one is generally estimated. The other one is often determined based on the reciprocity of the wave propagation, which could induce some errors. We distinguish three types of techniques to estimate the aberrations law.

I.2.2.1 Optimization based on an image parameter

A first alternative to adaptive focusing is to correct for aberrations not by measuring the distortion of the wavefronts, but by simply optimizing the image quality. However, such process requires an indicator that characterizes the image quality. Nock *et al.* [54] proposed to optimize the image brightness.

Such methods generally imply a time-consuming iterative focusing process with potential converging issues. In addition, while the proof-of-concept is performed for a phantom

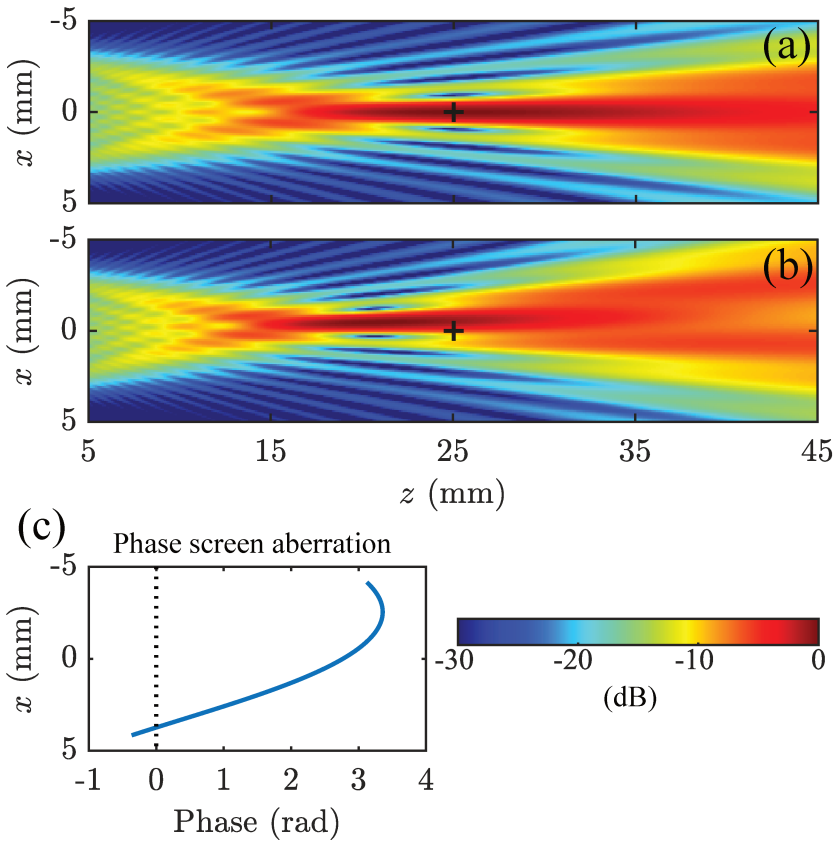

Fig. I.21 *Simulated pressure fields at 5 MHz characterized by a transmitted f-number* $F_{in}^{\#} = 3$. *The pressure fields are normalized by their maximum intensity. (a) Without aberration. (b) With a phase screen aberration depicted on (c). The aberration is characterized by a spatial correlation length* $l_\phi = 5$ *mm, a standard deviation:* $\sigma_\phi = 40$ *µs.*

experiment that contains only unresolved scatterer, soft tissues contains a mix of unresolved and specular scatterers that makes the assessment of the image quality difficult.

I.2.2.2 Modeling the wave propagation based on an estimation of the medium speed-of-sound

A second alternative is to deduce the focusing laws from an estimation of the speed-of-sound distribution of the medium [55, 56]. Such estimation can be obtained either by an ultrasound method [see par. I.3.1] or by a complementary imaging technique such as a CT scan in the case of aberration induce by the skull [56]. The travel times are then determined via numerical simulations that are computationally intensive. Many techniques have been developed in the field of seismology or underwater acoustics [57] to solve this problem. Ray tracing is one of the most widely used that consist in solving the

Eikonal equation:

$$|\nabla\tau|^2 = \frac{1}{c(\mathbf{r})} \tag{I.32}$$

where τ defines the time-of-flight from a certain source define by initial condition and $\nabla\tau$ is a vector perpendicular to the wavefront. The eikonal equation accurately models refraction and can be solved efficiently using the fast-marching method [58]

I.2.2.3 Spatial correlations of aberrated wavefronts

A third strategy consists in extracting the aberrating phase laws from the spatial or angular coherence of the reflected wavefield, without estimating the fluctuation of the medium speed of sound. To benefits from the best imaging conditions, most adaptive imaging techniques estimates aberrations by investigating confocal signals that are obtained either by a physical transmitted focusing or a synthetic method.

Early techniques studied the correlation between the RF signals measured by neighboring sensors for focused insonification [47, 11]. In the case of speckle regime, Mallart and Fink (1994) [11] adapted the Van Cittert Zernike theorem to the pulse-echo configuration [Par. I.1.3.2] and used it for the estimation of a phase screen aberration. Transmitted aberrations damage the focusing quality and enlarge the transmitted focal spot that acts as an incoherent virtual source in speckle. In a monochromatic regime, the intensity distribution of the incoherent source is given by the Fourier transform of the aberrated transmitted beam $E^{\text{ab}}(u)$. In reception, confocal realigned signals $\breve{R}_{u_1}$ and $\breve{R}_{u_2}$ measured by sensors u_1 and u_2 respectively, are out-of-phase due to aberrations on the way back, leading to an additional term in the spatial correlation matrix of the realigned signal [Eq. I.21]:

$$S^{\text{ab}}(\mathbf{r}_{\text{in}}, u_1, u_2) = \left\langle \breve{R}_{u_1} \breve{R}^*_{u_2} \right\rangle \propto e^{i2\pi f[\tau_{\text{ab}}(u_1)-\tau_{\text{ab}}(u_2)]} \text{TF}\left(|\text{TF}(E^{\text{ab}})|^2\right)\left[\frac{u_1-u_2}{\lambda z}\right]. \tag{I.33}$$

As the phase of this matrix is not exactly defined, the author first proposed to estimate the aberration law by correlating the realigned signals with an arbitrarily chosen one, set as a reference. Figure I.19 illustrates the impact of aberrations on the back-scattered signals $R(u_{\text{out}}, \mathbf{r}_{\text{in}}, t)$ generated by a converging wave that focuses at $\mathbf{r}_{\text{in}}$ in speckle. In absence of aberration [Fig. I.22(a)], the back-scattered signals are characterized by a large spatial coherence, visible between each line of the figure. This observation is expected by the conventional Van Cittert Zernike theorem. This spatial coherence drops in presence of aberrations [Fig. I.22(b)]. More precisely, the drop is due to the correlation term in equation I.33, which depends directly on the size of the incoherent virtual source, *i.e.* the aberrated transmitted focal spot. By correcting the aberration in transmission [Fig. I.22c], we create a diffraction limited input focal spot, which restores the spatial coherence. One can clearly see the shape of the aberrated wavefronts that can be decomposed into two contributions: (i) a geometric component, which contains the ideal wave-front induced by the transmitted focal spot that would be obtained in the homogeneous medium used to model the wave propagation; (ii) a distorted component induced by the aberrations [Fig. I.19(e)]

More efficiently, it has been shown that the entire correlation matrix can be used to extract the aberration laws (2003) [59]. Notably, Angelsen *et. al.* (2003-2004) [38, 60]

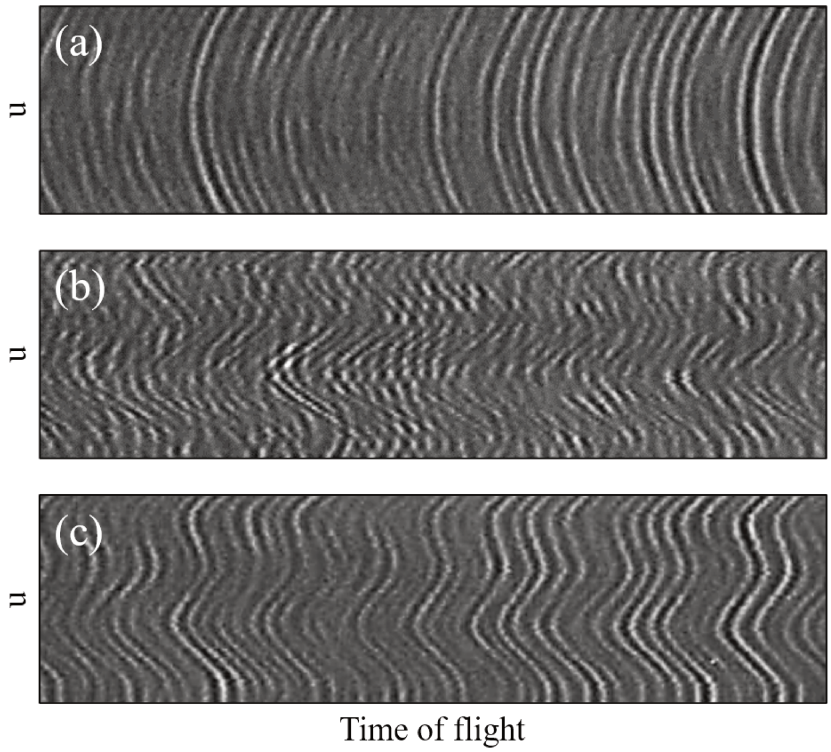

Fig. I.22 *Impact of aberrations on RF signals generated by focused insonification. Grey scale representation of the signals received by the array elements. Negative signals values are black, positive ones are white; each horizontal line corresponds to the signal received on an array element* $[R(u_{out}, \mathbf{r}_{in}, t)]$*. (a) RF signals received from a non-aberrating scattering medium. (b) RF signals received from an aberrating scattering medium without any correction. (c) RF signals received from an aberrating scattering medium for a corrected transmitted beam. Inspired from [11].*

demonstrated that in cases where the correlation matrix converges toward its covariance matrix, the aberration phase law can be extracted from the phase of the first eigenvector of this matrix. This condition requires to average over enough independent realizations of disorder (and is carefully examined in chapter 3). Robert *et. al.* [61, 49] experimentally validated this approach via the FDORT method [Par. II.1.3.1] that uses focused insonifications.

To improve the estimation of the aberrations law and thus force the convergence of the correlation matrix towards its covariance matrix, more recent works take full advantage of the memory effect. Indeed, each converging waves that focuses on each resolution cell $\mathbf{r}_{\text{in}}$ of a given isoplanatic patch creates realigned signals $\breve{R}(u_{\text{out}}, \mathbf{r}_{\text{in}}, t)$ that are impacted by the same aberrations. Their associated correlation matrix can then be analyzed as multiple independent realizations of disorder of a covariance matrix associated with the studied isoplanatic patches. More precisely, back-scattered signals generated from the

same isoplanatic patch contain invariant aberrated components while their geometrical components are location dependent [Fig. I.23(a,b)]. In addition, these wavefronts are generated by various incoherent sources (input focal spot in speckle). They are thus out-of-phase one compared to the others, due to the random reflectivity of the medium [Par. I.1.3.2]. As the geometrical components are fully described by the speed of sound model used to perform the beamforming, they can be manually adjusted to simulate signals that artificially originates from a reference virtual source located at $\mathbf{r}_{\text{in}}{}^{ref}$ but which are still associated with the reflectivity of their initial virtual source [Fig. I.23(c)]. By manually compensating the phase-shift due to the random reflectivity, Montaldo *et. al.* (2011) [62] coherently summed these tilted realizations of disorder and managed to artificially create the back-scattered signals generated by a bright star located at $\mathbf{r}_{\text{in}}{}^{ref}$. The aberration law associated with the studied isoplanatic patch can then be extracted from such beacon [Fig. I.23(e)] and time reversed to correct for transmitted aberrations [Par. III.2.3], [Fig. I.23(f)]. This process called *time reversal of speckle noise*, is then iterated to improve the estimation of the aberration laws. In the particular case of a moving speckle that can be observed for instance within veins, Osmanski *et. al.* (2012) [63] successfully increased the number of independent realizations associated with a chosen isoplanatic patch by investigating back-scattered signals that originates from successive transmitted sequences.

More directly, the geometrical component of the back-scattered signals is compensated when computed the realigned back-scattered signals, *i.e.* the signals that will be coherently summed during the conventional beamforming process. Consequently, the most recent studies investigate the correlation matrices of the realigned signals, which are spatially averaged over multiple realizations of disorder associated with each confocal focusing [65, 66, 40]. In order to developed real-time adaptive imaging, these techniques use synthetic beamforming *i.e.* single transducer insonifications [65] or plane wave insonifications [66, 40] and differ from several key points that will be deeply studied in chapter 3. (i) insonification sequence, (ii) pre-filtering, (ii) transmitted or received aberration estimation, (iv) amplitude and phase correction or just phase correction, (v) iteration process.

Finally, using moving windows that select the virtual sources that are supposed to belong to the same isoplanatic patch, allow these recent techniques to correct for multiple isoplanatic patches within a single image. However, such process requires to define the size of the moving window that should match the spatial dimension of the isoplanatic patches.

I.3 State-of-the-art of quantitative imaging

The first and second part of this chapter provide an extensive review on ultrasound image formation processes and on adaptive imaging techniques, respectively. These methods are used to perform optimal US images that faithfully estimate the medium reflectivity. However, the reflectivity is not the only mechanical property that characterizes the medium under investigation. In this part, we now review some of the techniques used to provide indicators based on quantitative measurements of mechanical parameters. We now turn our attention to the quantification of the medium speed of sound, the propagation prop-

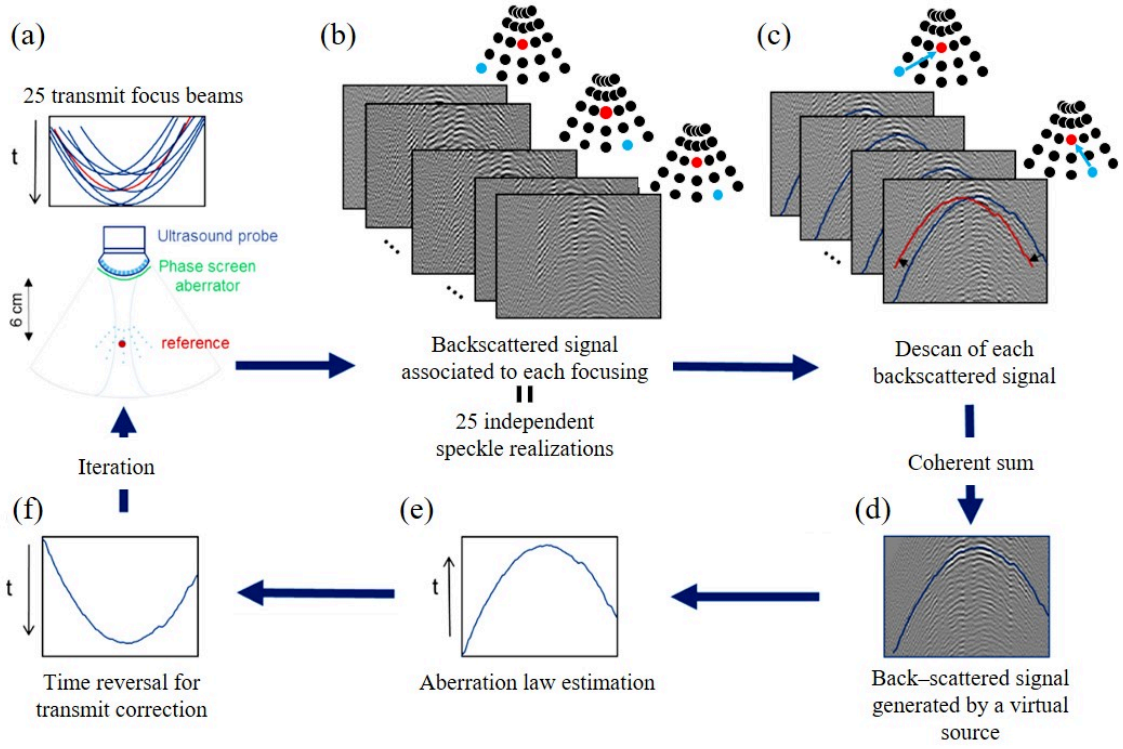

Fig. I.23 *Time reversal of speckle noise. (a,b) By focusing on multiple closed focal spot that belong to the same isoplanatic patch, back-scattered signals are impacted by the same aberrations. (c,d) They are then tilted and coherently summed to numerically simulate echoes generated by a bright star. (e,f) This beacon is then used to estimate the aberration laws. Figures are inspired from [64].*

erties that rule the generation of multiply-scattered echoes and the detection of specular reflector within the medium. These indicators have been studied during this thesis and illustrate the wide range of applications that can be tackled by the matrix approach.

A disease generally modifies some of the mechanical properties of the medium. Any indirect indicator that is based on such properties then becomes a relevant bio-indicator for assessing, monitoring and detecting the stage of this disease. In addition, these indicators may provide useful information on the medium under investigation that can be used to improve the image quality during the beamforming process.

I.3.1 Speed-of-sound estimation

Speed of sound (SoS) quantification constitutes a major candidate for the diagnosis of liver diseases. More precisely, it has been shown that it is a relevant biomarker for non-alcoholic fatty liver diseases (NAFLD), also known as steatosis [64], which are characterized by the accumulation of fat droplets within the liver cells. Speed of sound of fat tissues differs from the one of a healthy liver tissues ($c_{fat} \approx 1480$ m/s vs $c_{liver} \approx 1600$ m/s). From the

ultrasound point of view, those droplets are unresolved scatterers that will impact the effective SoS of the medium. To produce a useful indicator for clinical purposes, a near real-time map of SoS with an accuracy of around 10 m/s is required, which corresponds to an error of around 0.5%.

The major difficulty, once again, lies in the determination of the round-trip time-of-flight between scatterers (or resolution cells) and the array of transducers. This time-of-flight only contains a global information on the traveled path. Many techniques have been developed for the last thirty years. They fall into two categories: integrated sound-speed estimators, which estimate the average SoS between the surface of the transducers and the focal depth, and local sound speed estimators, which estimate the SoS in a localized region.

One of the simplest ideas consists in observing that the image quality is optimal when the assumed SoS model coincides with the medium one. Therefore, it is possible to estimate an integrated SoS by imaging the same region with different SoS hypothesis and picking the one that maximizes the image quality. Based on the Van-Citter-Zernike theorem, the image quality can be assessed by maximizing the spatial coherence of the realigned signals [67]. More directly, this spatial coherence is directly linked to the enhancement factor that occurs during the beamforming process due to constructive interference. Therefore, similar results can be derived by maximizing the brightness and/or sharpness of the ultrasound image [68], or more ingeniously the coherent energy (beamformed signals) normalized by the incoherent intensity (resulting from an incoherent sum over realigned signals). More recently, Lambert *et. al* (2020) [69] introduced the focusing criterion that is based on a local quantification of the resolution of the US image. It is thus able to highlight aberrated areas [Par. II.2.4]. Note that a special attention must be paid on the fact that the axial component of the ultrasound image is actually a time axis that is translated into a distance thanks to the SoS model. A change of the SoS model implies an axial translation of the resulting image. This difficulty is overcame by working at a constant time-of-flight. In this case, only the curvature of the focusing law is changed from one SoS hypothesis to another. Note that to probe only the impact of the SoS model, diffraction phenomena should be similar from one hypothesis to the other [70]. A simple way to ensure this, consists in studying confocal signals obtained with a constant transmitted and received apertures for each SoS hypothesis. For *in-vivo* imaging, such techniques are thus particularly suited to synthetic beamforming and more precisely to the case of plane wave beamforming. In this case, only the transmitted angles need to be updated according to the Snell-Descartes laws:

$$\frac{\sin(\theta)}{c} = \text{constant}. \tag{I.34}$$

Even if these techniques are able to measure integrated SoS with a high accuracy (a few m/s), they are computationally intensive as they require to produce multiple US images of a region of interest and only provide an averaged SoS.

SoS quantification and aberration correction are deeply linked as aberrations stems from a wrong SoS model. The second idea then simply consists in estimated the medium SoS based on an estimation of an aberrated wavefront. By assuming that the medium is homogeneous with an unknown speed-of-sound c, the round-trip time-of-flight I.7 of confocal signals located at $\mathbf{r} = \{x, z\}$ can be developed using a Taylor expansion based

on the hypothesis that $z = ct >> |x - u|$:

$$\tau(\mathbf{r}, u_{\text{out}}) = 2\frac{z}{c} + \frac{|x - u_{\text{out}}|^2}{2zc} \tag{I.35}$$

We observe from this equation that the integrated SoS can be extracted from the curvature of the aberrated wavefront as a function of $|x - u_{\text{out}}|$. Almost all techniques developed for aberration correction in the contest of adaptive imaging have been derived to the estimation of the medium SoS [71, 64, 72]. Nonetheless, an iteration process is required to obtain accurate measurements of the medium integrated SoS.

These techniques provide accurate measurement of the integrated speed of sound. However, they have low accuracy in the presence of inhomogeneities, which makes them unsuitable for in vivo measurements through layers of subcutaneous fat and connective tissue. For instance, the average SoS estimator proposed by Anderson and Trahey (1998) [71] yields highly accurate measurements in homogeneous media (bias less than $0.2\% \simeq 3$ m/s and standard deviation less than $0.52\% \simeq 8$ m/s). In a stratified medium, the integrated SoS should not be directly used as an estimation of the local medium SoS. For instance, Anderson and Trahey show a 30 m/s biases in a two-layer phantom composed of water and agar-graphite.

The second category of techniques aims to produce local speed of sound measurements and are based on the resolution of an inverse problem. Three different ideas have been investigated. The first one consists in deducing the local SoS of the medium based on a profile or a map of an integrated SoS estimation. Local SoS profiles are then deduced from a numerical inversion [72] or a physical one, where the SOS model is considered as a stratified one that is determined from shallow to deep depth [69]. The second one proposed by Byral *et al.* (2012) [73] is based on the estimation of times-of-flight required to travel between two virtual detectors or sensors embedded within the medium [Fig. I.24b]. To do so, this technique is decomposed in two steps. The first one aimed to measure the return time-of-flight associated with each virtual sensor. This is done by measuring half the delay of the leading edge of the aberrated wavefronts [Fig. I.24a]. The second step then consists in generating a diverging wave whose source is aligned with the two virtual detectors. By comparing the round-trip time-of-flight associated with these virtual detectors, the time-of-flight between those two virtual detectors can be estimated by deducting the return time-of-flight established during the first step, which directly gives access to the integrated SoS between the two transducers. The last idea, which is the most promising one, estimates the aberrations, *i.e.* additional time delays, as a function of the transmitted ϕ and/or received ψ angles. Therefore, spatial information on the traveled paths are kept along the process, which is a key feature in order to produce a 2D map of the medium SoS based. Based on this concept, Kondo *et al.* (1990)[74] developed and implemented on clinical device the crossed beam method which is strongly linked to the virtual detector method. More than twenty years later, Jaeger *et. al.* (2015) [75] introduced the Computed Ultrasound Tomography in Echo Mode method or CUTE. By illuminating each resolution cell with different transmitted angles, while keeping the received beamforming process constant, this first version investigates the aberrations in the transmitted mode along transmitted traveled path. As the received part [Fig. I.25(b,d)] remains unchanged from one transmitted angle to the other, phase delays are only due to input aberrations [Fig. I.25(a,c)]. The latter one are extracted

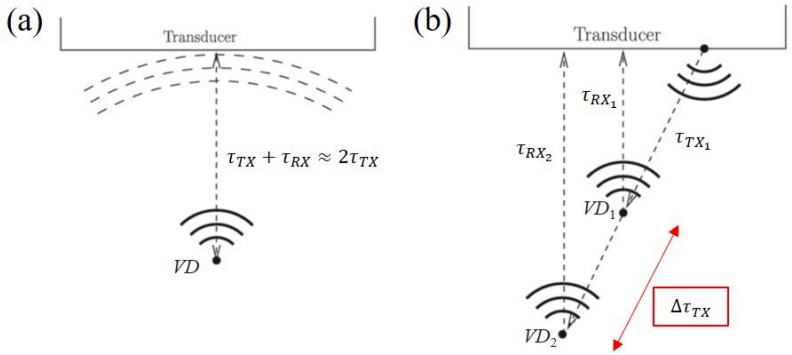

Fig. I.24 *Principle of the virtual detector method. (a) received time-of-flight τ_{RX} are first estimated for each virtual detector VD based on confocal focusing. (b) transmitted time-of-flight $\Delta\tau_{TX}$ between two virtual detectors embedded within the medium are estimated based on a diverging wave, whose source is aligned with the two chosen virtual detectors. This give access to the average speed of sound of the medium between the two virtual detectors. Figures are inspired from [73].*

by studying the spatial correlation of the wave-field in reflection (similarly to the recent work done by Bendjador *et al.* [66]). More recently, this technique has been improved by investigation correlations between realigned signals that share the same common-mid-angle $\gamma = 1/2(\phi+\psi)$ [76] [Fig. I.25(e)]. It also corrects for potential errors on the location of each scatterer leading to one of the first *in-vivo* SoS map obtained with a conventional US probe that combine both resolution and accuracy.

I.3.2 Multiple scattering quantification

In ultrasound imaging, the equivalence between the time-of-flight of a back-scattered echo and the location of the scatterer is ensured by the single-scattering assumption (first Born approximation). However, there is no such thing as a purely single scattering medium. Back-scattered signals always contain a multiple scattering contribution, albeit negligible (or assumed as negligible) compared to the single scattering one in soft tissues. For conventional imaging purposes, only the single scattering contribution is of interest. Multiply-scattered ones act as an incoherent source of noise that degrades the image contrast. From an other point of view, these undesired echoes enlarges the isochronous volume associated with each signal. Indeed, multiple scattered paths may arise with the same time-of-flight. To overcome this issue, some techniques have been developed to reduce the influence of multiply-scattered echoes. To this end, the coherent summations, which occurs during the beamforming process, drastically enhances the single scattering contribution thanks to constructive interference. The multiply-scattered echoes are incoherent from one realigned signal to the other. Therefore, beamformed signals shows an improvement of the ratio of single scattered intensity over the multiple one compared to the RF signals. Nonetheless, there is still a need for new techniques to overcome and filter multiply-scattered echoes that are often referred to as clutter in ultrasound imaging.

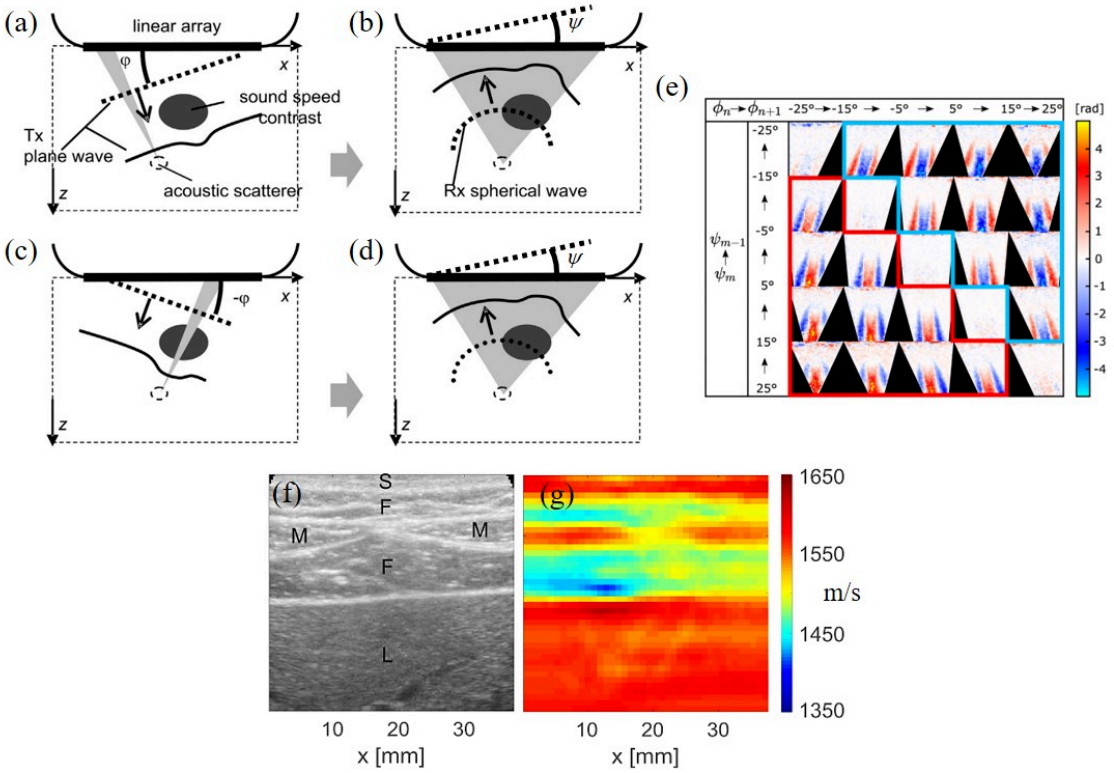

Fig. I.25 *Principle of the CUTE method. (a-d) By investigating the spatial correlation of the realigned signals associated with each resolution cell as a function of the transmitted ϕ and received angle ψ, aberrations are studied along travelled path to produce phase shift maps. (e) Phase shift map of a 15 m/s SoS contrast inclusion obtained by correlating the signals with the same common-mid-angles. A numerical inversion is then performed to compute the local speed of sound map. (f,g) US image of an in-vivo liver and its associated local SoS map. Figures are from [75, 76].*

From another point-of-view, even though multiply-scattered echoes are considered as the "enemy" of classical imaging techniques, they contain additional information on the micro-architecture of the medium. Indeed, the capacity of a medium to generate multiply-scattered echoes is strongly linked to the density of scatterers, their scattering strength and their potential resonances. More precisely, a wave propagating in a highly scattering medium can be thought of as a random walker that undergoes multiple scattering events, with two essential parameters: the elastic mean-free-path l_e, which defines the mean distance between two scattering events and the diffusion constant D (expressed in m^2/s), which characterizes the growth rate of the diffusive halo [77]. For strongly scattering media, meaning that the thickness L of the medium is much higher than the medium mean-free-path $L \gg l_e$, multiple scattered paths are too complex to be analyzed individually. This phenomenon is then studied via a statistical approach based on multiple realizations of disorder that are generally replaced by spatial and/or frequency averages.

It has been shown that for strongly scattering media, the temporal propagation of the incoherent energy, which results from the contribution of multiply-scattered echoes, obeys a diffusion equation. In the field of ultrasound, multiple scattering has been extensively studied, first in the 1990s and in a transmission configuration, where a slab of strongly disordered media is placed between a source and one or multiple receivers. By investigating the spatial-temporal evolution of the average coherent or incoherent intensity, the group led by John Page in Manitoba (Canada) studied the wave transport parameters D, l_e, v_e (the energy transport velocity) that characterize wave transport through multiple scattering media [78, 79, 80, 81, 82].

At the same time, experiments in reflection have been conducted first by Bayer and Niedderdränk in (1993) [83], then by Tourin *et al.* at the LOA (predecessor of Institute Langevin) [84, 13, 85], who investigated the multiply-scattered intensity in a dynamic regime to investigate the coherent-back scattering process [See following paragraph]. These fundamental studies lead to the PhD work of Aubry who developed (*i*) a new measurement of a local diffusion constant $D(\mathbf{r})$ thanks to transmitted and received Gaussian beam [86, 87] and (*ii*) a new filter to extract or remove multiple scattering contributions from RF signals [88, 89, 35] both in weakly and strongly scattering media. This filter enables to distinguish between absorption and scattering losses [Par: I.1.3.4].

In the two following paragraphs, some properties of each contribution of the back-scattered signals are first highlighted, *i.e.* (*i*) the single-scattering contribution, (*ii*) the multiple scattering contribution and (*iii*) and the electronic noise. Then we highlight how each contribution can be individually studied or filtered.

I.3.2.1 Separation of single and multiple scattering contributions

In order to characterize the wave propagation properties with one of the above-mentioned techniques, the multiply-scattered intensity needs to be isolated or, at least, its relative ratio compared to the total back-scattered intensity needs to be established. However, in weakly scattering media the analysis of multiple scattering parameters is challenged by the predominance of singly-scattered echoes. To overcome this issue, the techniques developed by Aubry *et. al.* are based on the properties of each contribution in a matrix approach of the reflection matrix. To describe the back-scattered signals, we base our description on the single transducer illumination. This insonification sequence corresponds to the case where the medium is probed successively by one transducer, while the back-scattered echoes are measured by all the other transducers. These impulse responses constitute a 3D reflection matrix that depends on the location of the transmitting u_{in} and receiving u_{out} transducers and on the time-of-flight of the echoes: $\mathbf{R}_{uu}(t) = [R(u_{\text{out}}, u_{\text{in}}, t)]$. Also named Full Matrix Capture (mainly in non-destructive testing), this matrix contains all the available information on the medium [Par. II.1].

On the hand one, Aubry *et al.* show that even if the scatterers d are randomly distributed and characterized by their own complex reflectivity A_d, the single scattering component exhibits long-scale correlations along its anti-diagonals [Fig. I.26(a)]. These correlations are a consequence of the memory effect induced by the single scattering process. Mathematically, the single scattering component of the reflection matrix measured at time-of-flight t and frequency f (obtained experimentally by a Fourier transform of a

time-gated reflection matrix) can be expressed as:

$$R(u_{\text{in}}, u_{\text{out}}, z, f) \propto \frac{1}{z_d}\sum_{d=1}^{N_d} \underbrace{A_d}_{\text{scattering}} \underbrace{\exp\left(jk\sqrt{(u_{\text{in}}-x_d)^2)+z_d^2}\right)}_{\text{transmission}} \underbrace{\exp\left(jk\sqrt{(u_{\text{out}}-x_d)^2)+z_d^2}\right)}_{\text{reception}} \quad \text{(I.36)}$$

where $\{x_d, z_d\}$ are the coordinates of the N_d scatterers located at depth $z_d = t_c/2$. In a paraxial approximation, which assumes that $z_d \gg |u_{\text{in}} - x_d|$ and $z_d \gg |u_{\text{out}} - x_d|$, this equation can be approached by:

$$R(u_{\text{in}}, u_{\text{out}}, z, f) \propto \underbrace{\frac{\exp(j2kz_d)}{z_d}\exp\left(jk\frac{(u_{\text{in}}-u_{\text{out}})^2}{4z_d}\right)}_{\text{deterministic term}} \underbrace{\sum_{d=1}^{N_d} A_d \exp\left(jk\frac{(u_{\text{in}}+u_{\text{out}}-2X_d)^2}{4z_d}\right)}_{\text{random term}} \quad \text{(I.37)}$$

This equation highlights a deterministic part that only depends on the distance $|u_{\text{out}} - u_{\text{in}}|$ and is responsible for the long-scale correlations of the reflection matrix. The second term is random as it depends explicitly on the locations of the scatterers. This term implies that a deterministic phase relation should appear along the anti-diagonal of the reflection matrix.

On the other hand, the multiply-scattered echoes results from the constructive and destructive interferences of the wavelets generated by each multiple scattered path p [Fig. I.27(e)]. It implies that the multiple scattering component exhibits a random pattern with no long-term correlations [Fig. I.26(b)]. It is nonetheless a symmetric component due to the reciprocity of the wave propagation.

Based on the memory effect of the single scattering component, Aubry and Derode [89] proposed a method to separate the single and multiple scattering contributions. It consists in projecting the reflection matrix on a subspace that is defined from the deterministic term of the single scattering component [Eq. I.37]. This single scattering subspace depends both on the frequency ($k = 2\pi f/c$) and the time-of-flight ($z_d = cT_d/2$). To performed this projection, the reflection matrix $\mathbf{R}_{uu}(t)$ is first time-gated by a moving time-window that selects back-scattered echoes generated by scatterers located around the plane z_d. A Fourier transformed is then applied to perform a frequency dependent analysis on the resulting matrix $\mathbf{R}_{uu}(T_d, f)$. The projection on the single scattering space enables the extraction of single scattering signals that fulfilled the par-axial approximation, but also a residual part of the multiple scattering component as the filter is not orthogonal to the multiple scattering contribution. In addition, this filter is extremely sensitive to aberrations that can alter the coherence along the anti-diagonals of $\mathbf{R}_{\text{uu}}(z, f)$, Aubry et Derode [35] proposed an improved version of this technique where the separation of the single and multiple components is no longer defined by a theoretical deterministic relation, but results from a singular value decomposition (SVD). The SVD decomposes a matrix into two subspaces: a signal subspace (a matrix characterized by an important correlation between its lines and/or columns) and a noise subspace (a random matrix without any correlations between its entries). Here, the SVD is applied to a rotated

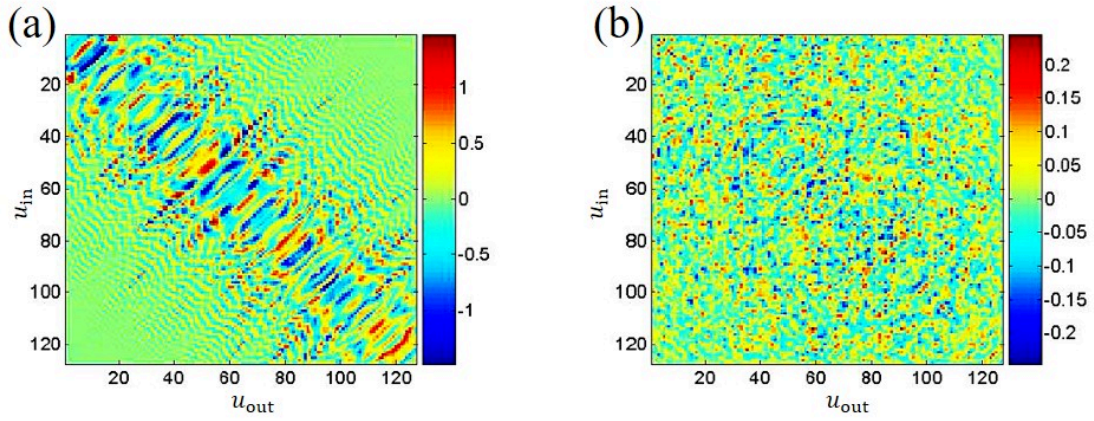

Fig. I.26 *Real part of the reflection matrices acquired with a single transducer illumination at two different time. (a) At short time, when the single scattering contribution is dominating (b) At long time, when the multiple scattering contribution is dominating. Figures are from [90]*

matrix that contains all the anti-diagonals alongs its columns. The single scattering contribution emerges along the signal subspace (largest singular values) while most of the random multiple scattering background should lie into the noise subspace (smalles singular values))

The major challenge then lies in the determination of the rank of the single scattering subspace. This issue is overcame thanks to random matrix theory. Based on the single/multiple scattering separation two applications have been proposed:

- an estimation of the ratio γ of single scattering intensity compared to the total back scattered intensity. A breast *in-vivo* experiment reports that $\gamma = 30\%$ at 30 mm depth [Fig. I.18].

- an estimation of the attenuation length l_a, mean free path l_e and extinction length l_{ext}. These parameters are deduced from the evolution of the global, single and multiple back-scattered intensity. These estimations has been performed in weakly scattered signals where double scattering dominates the multiple scattering process (and for which the derived model is exact).

I.3.2.2 Estimation of the local diffusion constant via a dynamic analysis

The advance filtering method described in the previous paragraph does not require any assumption on the disordered medium under investigation and can be applied to both strongly and weakly scattering media. While, this technique characterizes the multiple scattered intensity as a whole, complementary techniques are required to measure locally the transport parameters.

As depicted at the beginning of this paragraph, information on the wave properties can be extracted by investigating the statistics of the multiple scattering process. Therefore,

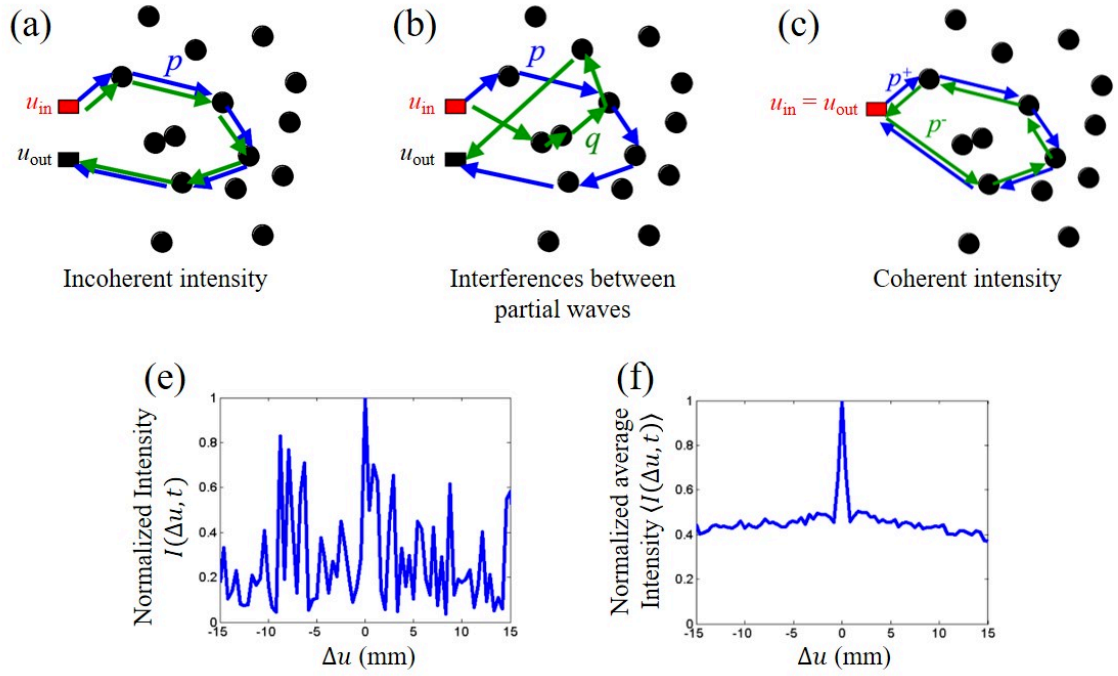

Fig. I.27 *Sketch of multiple back-scattered paths that occur in reflection. (a) Coherent multiple scattered paths, (b) incoherent scattered paths whose contribution vanish by average process across multiple realizations of disorder. (c) Coherent and reciprocal path that contribute to the factor 2 at exact backscattering. (e,f) One realization and average back-scattered intensity at a given time-of-flight respectively. Figures are inspired from [90].*

the back-scattered intensity $< I(\Delta u, t) >$ is averaged over multiple realizations of disorder as a function of the distance $\Delta u = u_{\text{out}} - u_{\text{in}}$, the distance between the emitter and the sensor and time-of-flight. Experimentally this average can be replaced by moving the source-detector couple along the surface of the sample while keeping their distance Δu constant. Since the scatterers are randomly distributed from one realization of disorder to the other with the same statistical properties, we expect that the averaging process erases any fluctuation of $< I(\Delta u, t) >$ to produce a plateau that is independent of Δu for each time-of-flight. Experiments show that indeed, a plateau $< I >_{\Delta \neq 0}$ is reached for $\Delta u > 0$. However, a narrow, steep peak is observed in the vicinity of the source location at $\Delta u = 0$ [Fig. I.27(f)], whose amplitude is two times the one of the plateau: $< I >_{\Delta \neq 0} = 2 < I >_{\Delta > 0}$. This well-known phenomenon named coherent back-scattering (CBS) is generated by the interference of waves with their reciprocal counterparts [Fig. I.27(c)]. It results in an enhancement (of around two) in intensity at exact back-scattering. Originally discovered in the plane-wave basis [91, 92, 93, 94], this phenomenon has also been observed in a point-to-point basis, whether the points be real sensors [83, 84, 95] or created via focused beamforming [86, 87, 69].

The origin of CBS, which is also known as weak localization can be explain using a

simple model. Each back scattered signal can be modeled as the sum of all the contributions of the multiple scattered path p, which individually create a complex pressure field on the surface of the transducer. The intensity of the back-scattered signal then results from the ensemble of the interference term between two partial waves. These interferences fall into three configurations:

- the incoherent sum of the intensity associated with each partial wave. These contributions form the incoherent intensity plateau $< I >_{\Delta u \neq 0}$ as no privileged back-scattered direction are observed.

- the interferences between partial waves that follow different paths, *e.g.* p and q [Fig. I.27(b)]. As these paths are not correlated, the resulting contribution disappear when averaging over disorder.

- At exact back-scattering, each wave that travels along the path p^+ can interacts with the one that follow the exact same path but in a reverse order p^- [Fig. I.27(c)]. These interferences between reciprocal paths form the coherent intensity observed at $\Delta u = 0$, whose intensity level matches the one of the incoherent intensity.

To sum up, the multiple scattering component of the reflection matrix displays a random feature. Its elements are random variables but they are not fully independently distributed because of spatial reciprocity that implies a symmetric reflection matrix. They are neither identically distributed because the CBS implies that the diagonal coefficients of the reflection matrix exhibit a double variance compared to its off-diagonal elements [96].

To measure the diffusion constant in reception, the idea consists in measuring the time evolution of the diffusive "halo" either in a far-field configuration via the analysis of the CBS peak or in a near-field one via the analysis of the incoherent intensity.

The temporal evolution of the CBS pic exhibits a behavior that depends on the observing basis. In the far-field, *i.e.* in the configuration where the average back-scattered intensity is measured between couple of incident and back-scattered plane wave, the incoherent background is constant and the peak width $\Delta\theta_{coh}$ reduces with the time-of-flight as [84]:

$$\Delta\theta_{coh}(t) \propto \frac{\lambda_c}{\sqrt{Dt}}, \tag{I.38}$$

where λ_c is the central wavelength. An estimation of D is thus possible from the analysis of this behavior.

In a near-field configuration, the CBS peak remains constant and equal to $\lambda_c/2$. The coherent intensity no longer contains information on the growth of the diffusive halo. In this case, this information is carried out by the incoherent intensity. In strongly scattering media, this growth is ruled by a diffusion equation that can be written as [13]

$$I_{\text{inc}}(u_{\text{in}}, \Delta u, T) \propto \frac{1}{\sqrt{4\pi DT}} \exp\left(-\frac{\Delta u^2}{4DT}\right), \tag{I.39}$$

Nonetheless, the analysis of incoherent intensity of the back-scattered echoes in the transducer plane only provides a global estimation of the diffusion constant. To measure locally

this parameter, Aubry *et. al.* (2007) [86] developed a matrix approach based on transmitted and received focus Gaussian beams to characterize the growth of the incoherent energy between virtual transducers located within the medium. This work goes beyond the concept of confocal imaging and show many similarities with the one developed during this thesis [Chap. 2]. Gaussian beamforming at emission creates a virtual source at $\mathbf{r}_{\text{in}} = \{x_{\text{in}}, z_{\text{r}}\}$, whose dimension and directivity are fully characterized by the diffraction theory of the incident beam. Gaussian beamforming in the received mode are then performed around this virtual source in the same imaging plane to create virtual sensors that are identified by their position at $\mathbf{r}_{\text{out}} = \{x_{\text{out}}, z_{\text{r}}\}$ [Fig. I.28(a)]. By inserting an additional delay T between the transmitted and received time-of-flight [Δt in Eq. I.8], these virtual sensors are able to probe the energy spreading $I(\mathbf{r}_{\text{in}}, \Delta x, T)$ along the imaging plane after the virtual source insonified the medium. [gray curve of Fig. I.28(b)]. By averaging this intensity profile over multiple adjacent virtual source and multiple frequency band, the diffusive constant D is locally measured based on equation I.39.

Nonetheless, in these experiments a particular attention must payed to the electronic noise. Indeed, noise consists in a fully random contribution that decreases the contrast of an ultrasound image in the same way as multiply-scattered echoes. It contributes to a roughly constant background level that may vary with the time-of-flight of the echoes due to potential non-linear post processing such as hardware TGC. Therefore, if the averaging process does not take into account enough realization of independent realization of disorder, this artifact may skew the estimation diffusive constant. It should not be neglected when one tries to quantify multiple scattering. The key to separate this contribution to the multiple scattering one is to investigate the spatial reciprocity or the coherent back-scattering effect that, unlike noise, are both exhibited by the multiple scattering contribution.

This technique has been used experimentally to probe the diffusion constant of the trabecular bone [87]. More recently, the group of Marie Muller have shown that the diffusion constant can be used as a biomarker for the diagnosis of some diseases. For instance, it can be applied to:

- the detection of pulmonary edema within the lung parenchyma [97]. Healthy lung constitutes a strongly scattering media characterized by a low diffusion constant due to the numerous interfaces between air and soft tissues. However, in the case of pulmonary edema, which characterizes the accumulation of fluid within the lung alveoli, the scattering strength is drastically reduced, which implies an improvement of the diffusion constant.

- the detection of tumor when combining with contrast agent. Micro-bubbles are resonant scatterers that are used as contrast agents in ultrasound imaging for vascular diagnosis. Most solid tumors are characterized by highly dense, isotropic vessel networks. Therefore, the scattering strength of such structures is deeply enhanced compared to healthy tissues when adding bubbles. This difference is then captured by the evaluation of the diffusion constant.

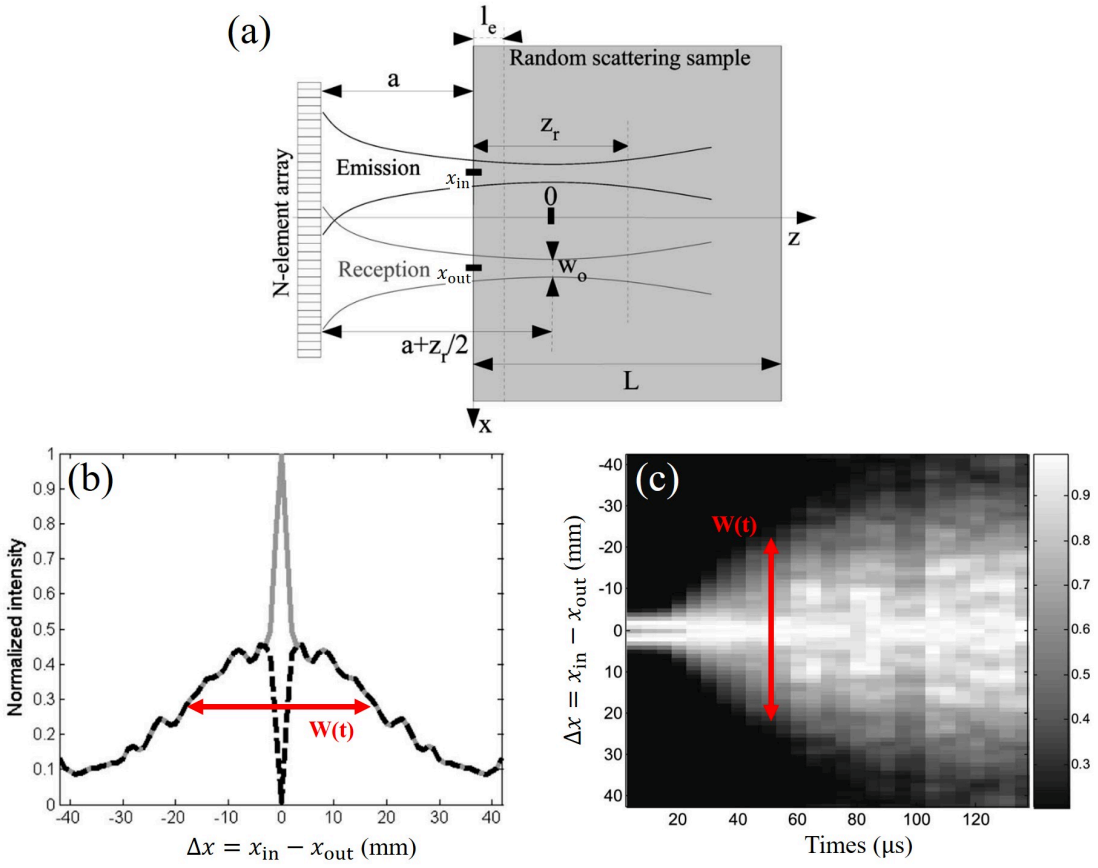

Fig. I.28 *Estimation of the diffusion constant in strongly disordered media. (a) The medium is emerged in water and insonified by Gaussian beams at* $\mathbf{r}_{in}$*, while Gaussian beamforming is performed in receive at* $\mathbf{r}_{out}$*, both focal spots are located at the surface of the medium. (b) Estimation of the spatial extent* $W(\mathbf{r}_{in}, T)$ *of the incoherent intensity* $I_{inc}(x_{in}, \Delta x, T)$ *from the average back-scattered intensity obtained from standard Gaussian beamforming* $I(\Delta x, T)$ *(gray curve). The black curved corresponds to an "anti-symmetric" beamforming used to reduce the impact of the noise level on the determination of* $W(\mathbf{r}_{in}, T)$*. (c) Evolution of the incoherent intensity. The intensity is normalized with its maximum at each time. Figures are adapted from [86]*

I.3.3 Characterization of the scatterer anisotropy

During the image formation process, we generally assumed that the medium is composed of unresolved scatterers that isotropically radiate energy towards the probe. In this case, the measured signals are angularly limited by the radiation pattern of the transducers and only the one located above the point of interest are used during the beamforming process [Fig.I.5]. However, this assumption is not always valid for imaging soft tissues that contain many specular structures. These reflectors are characterized by the fact that at least one of their dimensions is larger than the resolution cell. As stated in paragraph I.1.3.1], for a given incident beam, these structures radiate energy only in a privileged direction. Figure I.29(a) shows a sketch of an incident plane wave θ_{in} that is reflected by a plane interface of angle η compared to the probe surface. The main direction of the back-scattered wave θ_{out} can be easily deduced from the Snell-Descartes laws. Therefore, for this given plane wave, only the transducers located along and around this particular direction should be used for the beamforming process. If additional received angles are used (meaning other received transducers), the image quality associated with this scatterer may decreases as the beamforming process mixes echoes that have been generated by other scatterers. For instance, figure I.29 shows the conventional ultrasound image of a biopsy needle inserted within a pork tissue. Even if the biopsy needle constitutes a strong reflector, the beamforming process failed to image this structure.

As a result, knowledge of the local scatterer anistropy could strongly enhance the image quality. This is especially the case for the subfield of ultrasound musculoskeletal imaging that consists in imaging bones, joints and muscle tissues, which are mainly composed of specular structures. For instance, muscle tissues are composed of an ensemble of aligned fibers. They can be seen either as unresolved scatterer if the probe is orthogonally placed compared to the fibers or as specular reflectors if the probe is aligned with them. This phenomenon can be seen on figure I.30 that shows the *in-vivo* ultrasound images of a human calf of a healthy volunteer associated with these two configurations.

In addition, in the case of anisotropic media such as muscle tissues, all the mechanical properties vary with the orientation of the anisotropy. Therefore, any quantitative imaging technique such as elastography or the speed of sound measurement should take into account the local scatterer anisotropy to accurately characterize the propagation medium. Finally, the scatterer anisotropy itself can be used as a biomarker for the diagnoses of anisotropic injured tissues [98, 99]. Figure I.31 shows examples of injured muscle and tendon. In both cases, we observe that a loss of the characteristic anisotropic aspect of the ultrasound image of these structures.

To our knowledge, two approaches has been followed to probe locally the scatterer anisotropy. The first technique is based on the maximization of the spatial coherence of the back-scattered signals generated by fibrous media. Derode and Fink (1993) [100] initially studied this spatial coherence as a function of the angle formed between the linear ultrasound array and the medium fiber [Fig.I.32](a). If the probe is placed orthogonally to the medium fibers, they appear as unresolved scatterer. Therefore, the focal spot induced by a focused insonication acts as a random source that generates backscattered signals whose spatial coherence is predicted by the Van Cittert Zernike theorem (1994) [11]. By aligning the probe with the fiber orientation, the coherence of the source formed by the focal spot increases as the spatial coherence of the back-scattered echoes [Fig.I.32](b).

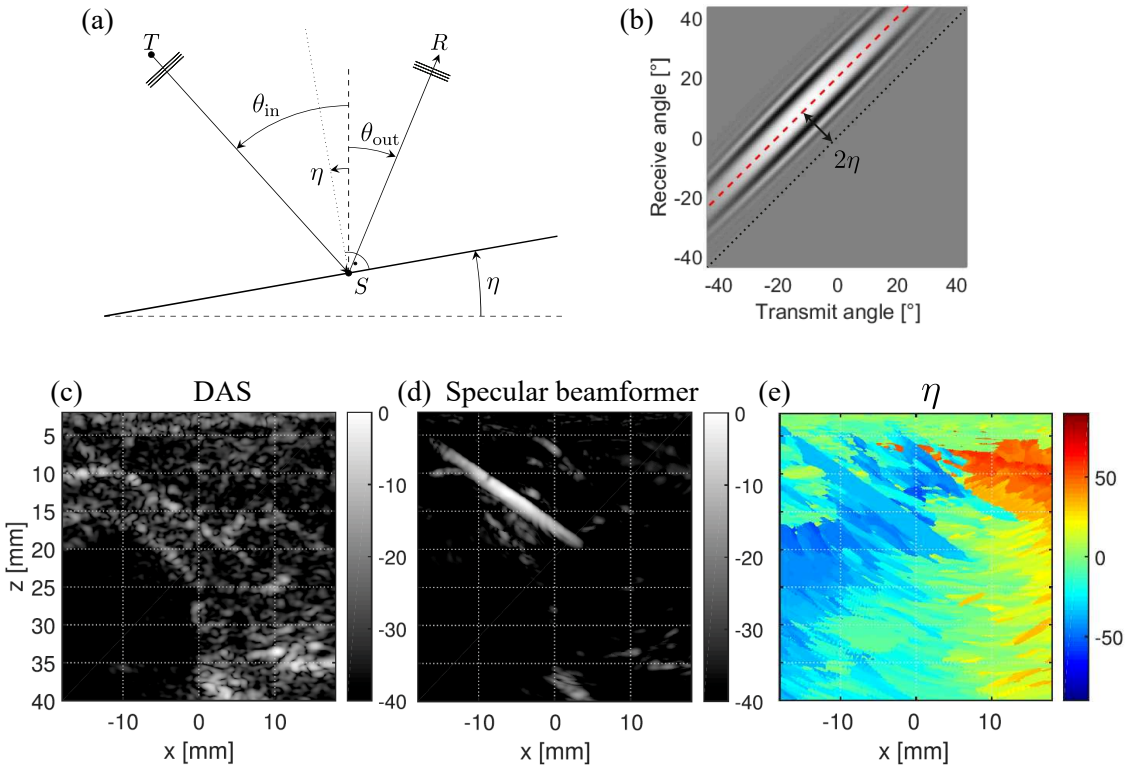

Fig. I.29 *Specular beamforming based on plane wave illumination. (a) Sketch of the experiment. If a planar reflector of angle η is found at point* $\mathbf{r}$*, (b) it induces strong echoes for realigned signals that fulfill the conditions given in equation I.40. In the plane wave basis, these particular signals are located along one of the anti-diagonal of $\breve{R}(\theta_{out}, \theta_{in}, \mathbf{r})$. the coherent sum of these echoes leads to the specular beamformed signal at optimal common-mid-angle, while the angle $\eta(\mathbf{r})$ can be deduced from the distance from the main anti-diagonal 2η. (c,d,e) Conventional US image, specular beamformed image and optimal fiber orientation of a biopsy needle inserted within a pork tissue, respectively.*

This early work was performed on anisotropic composite solid materials. More recently, Papadacci *et al.* applied this concept to the characterization of muscle tissues, first with a conventional linear array [101] then with a 2D array[102]. Based on this technique, they managed to build 3D orientation maps of the myocard at various time of a cardiac cycle [Fig. I.32]. Nonetheless, as this technique probes the transverse spatial correlation, it is only able to characterize the projection of the fibers on the focal plane. The characterization of the fiber orientation is not complete as no information on the projection along the axial direction is available. This drawback limits the efficiency of this technique as the fibers may not be contained within the focal plane, which reduces the accuracy of the transverse measurement.

The second approach is dedicated to the imaging of specular objects. It is based on the Snell-Descartes law, which states that an incident plane wave of angle θ_{in} is reflected

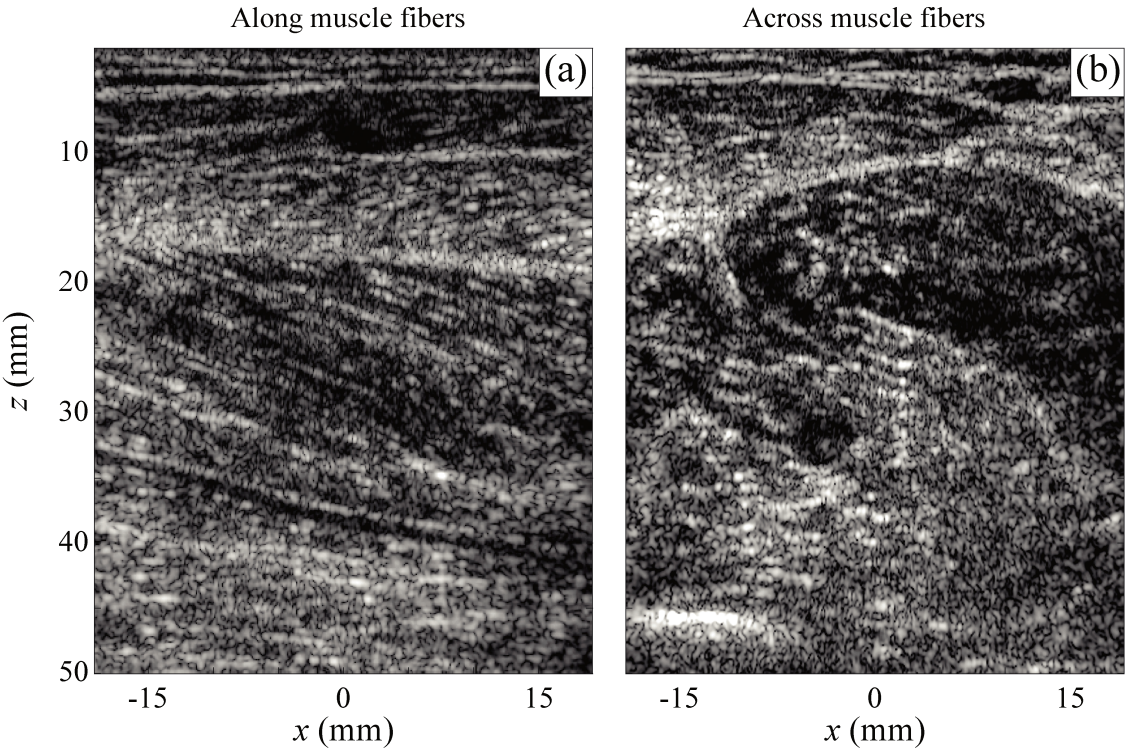

Fig. I.30 *Conventional ultrasound images of the human calf of a healthy volunteer. (a) The probe is aligned with the muscle fibers. (b) The probe is orthogonal to the muscle fibers.*

by a planar reflector of angle η in the direction θ_{out} such as:

$$\theta_{\text{in}} = \theta_{\text{out}} + 2\eta. \tag{I.40}$$

Therefore, for each focal point, the matrix of realigned signals is constructed and expressed as a function of a transmitted angle θ_{in} and received angle θ_{out}, $\breve{R}(\theta_{\text{out}}, \theta_{\text{in}}, \mathbf{r})$. Note that the received plane wave basis is obtained either via a matrix approach [Chap. 2] or simply deduced from the apparent angle under which the scatterer is seen from each transducer of the received aperture [Fig. I.29(a)]. If a planar reflector of angle η is found at focal point $\mathbf{r}$, the signals $\breve{\mathbf{R}}_{\theta\theta}(\mathbf{r})$ that validate the above equation are characterized by a strong intensity level. Similarly, to the work of Stähli *et al.* [76] on the speed of sound measurement, we observe that these signals share the same common-mid-angle and are located along the same associated anti-diagonal. Therefore, based on the matrix of realigned signals, signals that share the same common-mid-angle are coherently summed to create an ensemble of beamformed signals $P_s(\mathbf{r}, \eta)$ for a given hypothesis specular orientation η:

$$P_s(\mathbf{r}, \eta) = \sum_{\theta_{\text{in}}} \breve{R}(\theta_{\text{out}} = \theta_{\text{in}} - 2\eta, \theta_{\text{in}}, \mathbf{r}) \tag{I.41}$$

The maximum intensity of each profile is associated with the angle η of an assumed specular plane [Fig. I.29(e)], while the probability that this reflector is indeed specular

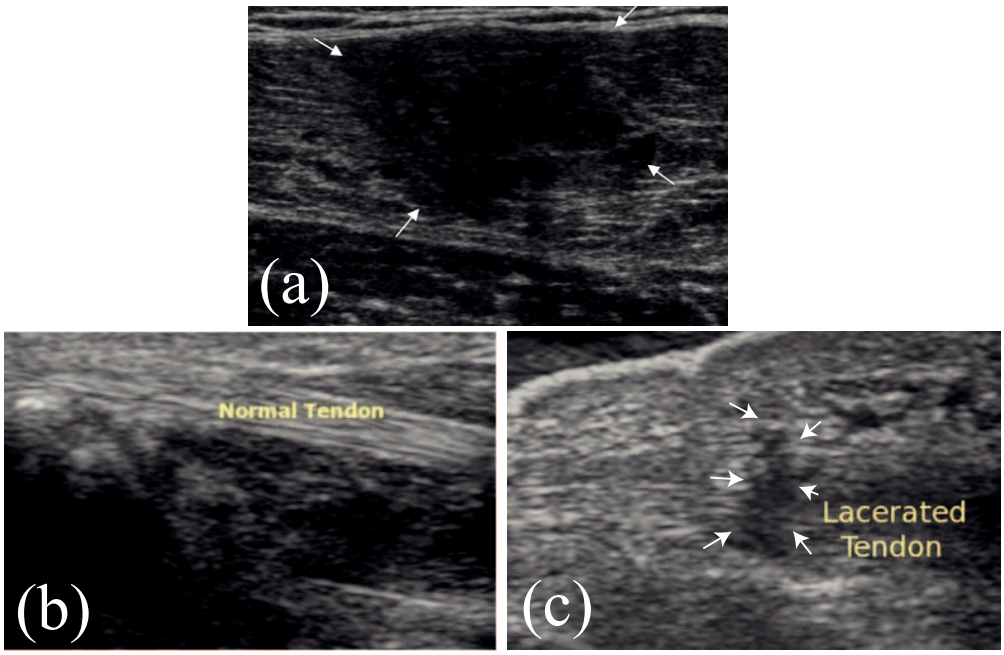

Fig. I.31 *(a) US image of a muscle contusion: Axial image of rectus femoris in a 24-year-old rugby player after a direct blow to the leg. The contusion is characterized by a loss of normal internal muscle striation because of microhemorrhage dissecting between muscle fibers with resultant inflammation and edema. (b,c) US images of both an intact and lacerated hand flexor tendon, respectively. Figures are extracted from [98, 99].*

is measured from the angular extension of the intensity peak [Fig. I.29(d)]. This process enables to accurately detect, image and characterized the location of the biopsy needle in the pork tissue. Even if this technique has been developed for planar reflector, it would be interesting to see its capacity to measure the fiber orientation in fibrous medium.

Finally, we observe that these techniques aim to quantify the anisotropy of scatterer via the spatial analysis of the back-scattered signals generated by each resolution cell. It can be seen as the characterization of the radiation pattern associated with each virtual source. The same physical phenomenon is used in chapter 3 [Par. III.1]. By removing unwanted specular angles that share the same common-mid-angle, it is possible to remove some reverberation artifacts induced by multiple reflection. Finally, based on a matrix formalism, we exploit the correlations between echoes generated by adjacent focal spots to measure the orientation of muscle fibers within the imaging plane [Par. IV.3].

I.4 Conclusion

For the past decades, the field of medical ultrasound has known an exponential growth, to become one nowadays of the most widely used modality for clinical imaging and diagnosis. It is indeed a very efficient and harmless tool, easy to use and without need of additional

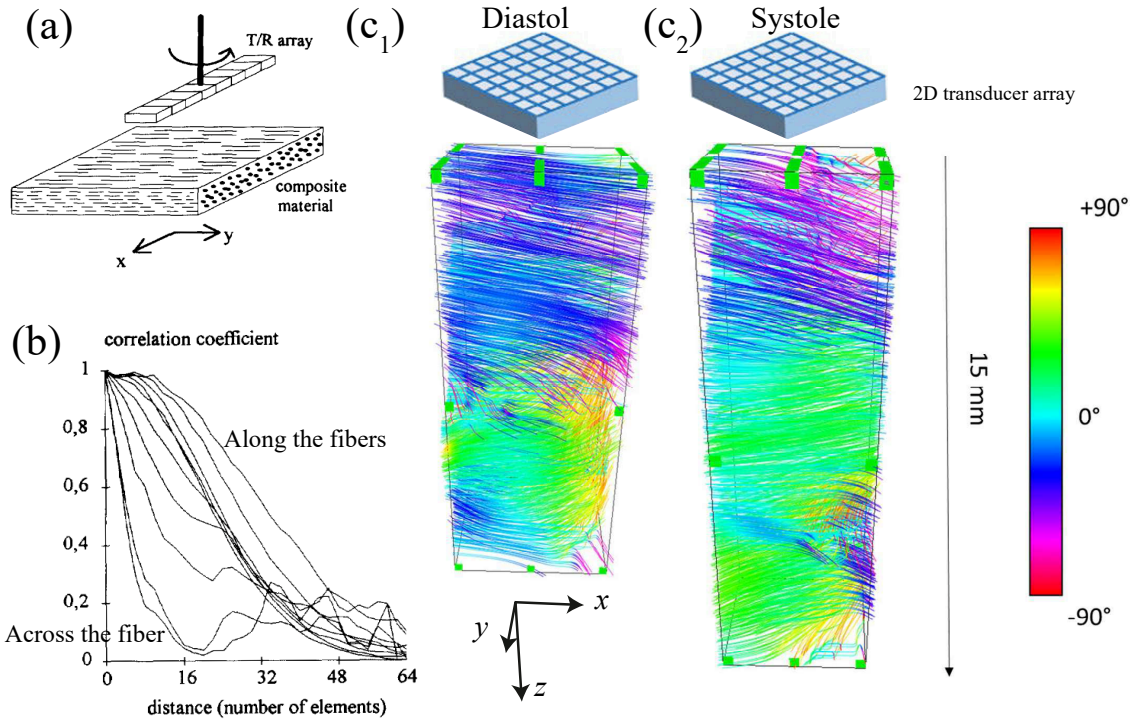

Fig. I.32 *Maximization of the spatial coherence of back-scattered signal to probe the orientation of fiber within the focal plane. (a,b) The spatial coherence of an anisotropic composite material is probe by rotation of a linear array. (c) 3D Maps of in-vivo myocardial fiber orientation in the human heart measured during the diastole and systole by means of a 2D array. Figures are extracted from [100, 102].*

equipment nor impact on the patient.

Numerous techniques have been developed to either improve the image quality or better characterize soft tissues, improving thus the diagnostics qualitys. The above-mentioned techniques constitute a state-of-the-art description of the main techniques and physical phenomenon used for either adaptive beamforming or the quantification of the speed-of-sound and multiply-scattered echoes. The main objective of this thesis is to propose a new formalism, based on a matrix approach, that can be applied to any applications and or configuration encountered in medical ultrasound imaging. More generally, this work fits into a larger picture elaborated by the team of Alexandre Aubry at Institute Langevin. It consists in developing new tools around a common matrix formalism that can be applied to any type of waves where multiple sources and multiple sensors are used to shape incident wavefronts and analyze reflected ones. This thesis then constitutes the ultrasound part of this picture and has been inspired by the work of Amaury Badon, Victor Barolle and Thibault Blondel in the field of optics and seismology.

The next chapter [Chap. 2] is dedicated to the matrix formalism in ultrasound. It is the core of this work as it contains all the first building blocks that are then used for aberration correction via an adaptive imaging technique [Chap. 3] and for quantitative

imaging of speed of sound, multiple scattering and scatterer anisotropy [Chap. 4].

Chapter II

Matrix approach of ultrasound imaging

Contents

In the first chapter, we reviewed some fundamental bases of ultrasound imaging from a purely acoustical point-of-view. This angle is generally the one that is chosen by medical ultrasound books [1]. Simultaneously to the development of ultrasound imaging, a matrix approach of the wave propagation has been developed for the past 30 years. This concept was initially developed in a reflection configuration in acoustic via the pioneering work of Fink on the time-reversal process [39, 103], followed by the one of Fink and Prada [104, 105, 106] on the DORT method. In wave physics, a matrix formalism is particularly appropriate when the wavefield can be controlled by transmission or reception arrays of N independent elements. This powerful approach has brought new insights for the coherent control of wave-front through complex media, *e.g.* (*i*) selective focusing in multi-target media [104, 105, 106], (*ii*) optimal focusing through scattering media [107, 108], (*iii*) optimize multiple input - multiple output communations through complex media [109, 110]. It also provides a new tool for for revisiting and going beyond conventional imaging techniques [111, 69].

The present chapter is divided as follow: we first explicit the notion of matrix approach of wave propagation and propose a brief review of the major milestones of this promising research field. We then adapt the recent development made in optics during the PhD of Amaury Badon [112], to the field of acoustics. Generally, an image of a medium in reflection is built by focusing waves, either physically or numerically, on a single point at emission and reception. An image is then obtained by scanning simultaneously the input and output focusing beams. This is the principle of ultrasound imaging, phase array and confocal microscopy or optical coherence tomography in optics. Here, the location of the transmitted and received focal spots are split. It enables the construction of the focused reflection matrix that contains the medium responses between arrays of virtual sensors located at the same focal plane within the medium. Finally, we extended this matrix approach to virtual sources and sensors located at different depths and beyond the ballistic time. This idea leads to the concept of numerical time-reversal experiments.

All the matrices and post-processing developed in the last two sections of this chapter constitute the building block of a new range of techniques that are encompassed under the concept of *matrix imaging*. Besides describing all the current ultrasound imaging methods under a common matrix formalism, the matrix imaging is able to take up several challenges that will be studied in this chapter and in the following ones: (*i*) quantify and enhance the ultrasound image quality via a local focusing criterion [Chap. 2] and a matrix aberration correction [Chap. 3]; (*ii*) develop novel quantitative imaging modes by building maps of the speed-of-sound and of a multiple-scattering-rate that may constitute relevant biomarkers for ultrasound diagnosis [Chap. 4]; (*iii*) characterize locally the nature and anisotropy of the scatterers via their frequency response and radiation pattern [Chap. 4].

II.1 A brief history of the matrix approach of the wave propagation

The matrix approach is based on the idea that the whole system can be analyzed as a linear and time-invariant process. This whole system encompasses all the required steps to obtain digital signals of the backscattered or transmitted echoes, *i.e.* (*i*) the wave propagation within the medium, (*ii*) its interaction with the medium via the scattering

process, (*iii*) the transducer behavior that is modeled by the transducer impulse response and (*iv*) the electronic of the ultrasound system, which contains at least an analogic-digital convertissor and an electronic amplifier. In other words, we assume that all phenomena obey the laws of linear acoustics. This process can thus be seen as a black-box with multiple inputs and multiple outputs, and whose output signals linearly depends on the input ones. Such system is fully characterized by the inter-element impulse response matrix. In wave physics, this matrix is also called either reflection matrix $\mathbf{R}$, if the sources and sensors are located on the same side of the medium, *e.g.* in ultrasound imaging; or transmission matrix $\mathbf{T}$ if the medium is located between the sources and the sensors. Note that if sources and sensors are located on both sides, the inter-element impulse matrix is called the scattering matrix $\mathbf{S}$ that contains both the transmission and reflection matrices. These matrices are used to link the received signals to the transmitted ones. In ultrasound, the reflection matrix is generally acquired experimentally by means of a single transducer insonification (one transducer emits successively a short pulse. Back-scattered signals are then generated and measured by all transducers). Thanks to the linearity of the system, once this matrix has been acquired, the output signals $\mathbf{E}_{\text{out}}$ can directly be determined from any combination of incident waves $\mathbf{E}_{\text{in}}(u_{\text{in}}, t)$ via the following equation:

$$\mathbf{E}_{\text{out}}(u_{\text{out}}, t) = \sum_{u_{\text{in}}} R(u_{\text{out}}, u_{\text{in}}, t) \overset{t}{\circledast} \mathbf{E}_{\text{in}}(u_{\text{in}}, t), \tag{II.1}$$

where $\overset{t}{\circledast}$ denotes a convolution product over the variable on top of the symbol (here the time). For instance, this process can be used to determined numerically in post-processing the backscattered echoes generated by a focused insonification. In that case, $\mathbf{E}_{\text{in}}(u_{\text{in}}, t)$ just contained appropriate time delayed signals: $\mathbf{E}_{\text{in}}(u_{\text{in}}, t) = E_0\ \delta(t - \tau_{\text{ex}})$, where τ_{ex} is defined by equation I.6. In the frequency domain (accessible experimentally via a temporal Fourier transform), this equation becomes:

$$\mathbf{E}_{\text{out}}, (u_{\text{out}}, f) = \sum_{u_{\text{in}}} R(u_{\text{out}}, u_{\text{in}}, f)\ \mathbf{E}_{\text{in}}(u_{\text{in}}, f). \tag{II.2}$$

Under a matrix formalism, this equation can be expressed as:

$$\mathbf{E}_{\text{out}}(f) = \mathbf{R}_{uu}(f) \times \mathbf{E}_{\text{in}}(f), \tag{II.3}$$

where $\times$ denotes a matrix product. Therefore, the back-scattered signals generated by any incident wave can be simulated in post-processing by means of simple matrix product involving the reflection matrix. This matrix then contains all the available information on the medium that can be acquired with this array. The recent developments of this approach consist in finding optimal techniques to extract specific information or properties of this medium.

II.1.1 Early developments: the time-reversal concept and DORT method

This approach has first been successfully applied to the concept of time-reversal process [39], which exploits the reciprocity of the wave propagation. Figure II.1 illustrates this concept in a pulse-echo configuration for aberration correction. (a) One transducer

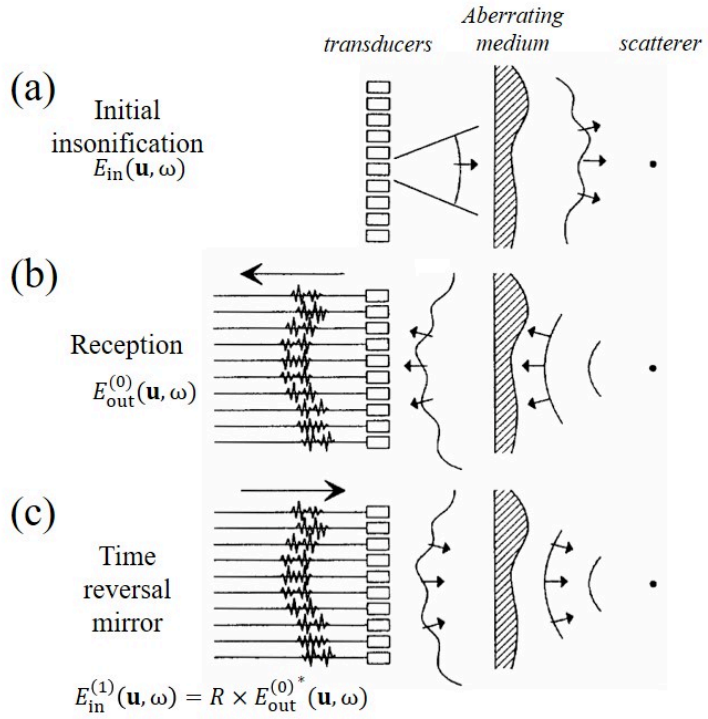

Fig. II.1 *Time-reversal process in pulse-echo configuration, application to aberration correction. (a) One transducer insonified a complex medium composed by a single scatterer. (b) The backscattered echoes are recorded by the transducers. (c) These echoes are time-reversed, and used as a new incident waveform that propagates inside the medium exactly in a reverse order than the back-scattered one. Figures are inspired from [39].*

insonified a heterogeneous medium composed by a single scatterer and (b) the back-scattered echoes are recorded by the transducers. (c) These echoes are time-reversed *i.e.* the end becomes the beginning and *vice-versa*, and used as a new excitation. The transducers then act as time-reversal mirror to create new incident waves, which propagates inside the medium in a reverse order compared to the back-scattered one. Thanks to both time reversal invariance and spatial reciprocity of the wave propagation, this new incident wave focuses on the scatterer that had originally been excited. As a consequence, the aberrations initially undergone by the reflected wave-front are perfectly corrected. For optimal focusing in the case of multiple scatterer, this process required to be iterated to correct for the transmitted aberrations as well. In this case, the process converges towards the optimal focusing law that is associated with the most echogenic scatterer.

In the monochromatic regime, the time-reversal operation is equivalent to a phase conjugation. The experiment depicted on figure II.1 is then easily modeled by means of a matrix formalism. By noting $\mathbf{E}_{\text{in}}$ and $\mathbf{E}_{\text{out}}^{(0)}$ the initial input and output signals

[Fig. II.1(a)], the output signals obtained after one and n iterations are:

$$\mathbf{E}_{\text{out}}^{1} = \mathbf{R}_{\text{uu}} \times \mathbf{E}_{\text{out}}^{(0)\,*} = [\mathbf{R}_{\text{uu}} \times \mathbf{R}_{\text{uu}}^{*}] \times \mathbf{E}_{\text{in}}^{*}, \tag{II.4a}$$

$$\mathbf{E}_{\text{out}}^{n} = \mathbf{R}_{\text{uu}} \times \mathbf{E}_{\text{out}}^{(n-1)^{*}} = [\mathbf{R}_{\text{uu}} \times \mathbf{R}_{\text{uu}}^{*})^{n}] \times \mathbf{E}_{\text{in}}^{*}; \tag{II.4b}$$

where $\mathbf{E}_{\text{in}}$ and $\mathbf{E}_{\text{out}}^{(0)}$ are the initial input and output signals. We recall that $\times$ and * are the matrix product and conjugate operator. For sake of simplicity, note that the frequency dependence is implicit. This operation reveals the time-reversal operator $[\mathbf{R}_{\text{uu}} \times \mathbf{R}_{\text{uu}}^{*}]$. Thanks to the reciprocity of the wave propagation, the reflection matrix is symmetric. This operator is equal to $\left[\mathbf{R}_{\text{uu}} \times \mathbf{R}_{\text{uu}}^{\dagger}\right]$, which can be diagonalized. † is the transpose conjugate operator. Its eigenvectors are orthogonal and its eigenvalues are positives. Prada and Fink [105] have shown that the phase of the first eigenvector of this matrix contains the ideal wave-front that focuses on the target. This wave-front then constitutes an invariant of this operator. To understand this property, we observe that if we send the perfect wave-front that adaptively focus on the target, the reciprocity of the wave propagation implies that the back-scattered signal will be the exact reverse wave-front, which is exactly the definition of an invariant vector. Moreover, the authors have shown that if the medium is composed by N point-like targets, the decomposition of the time-reversal operator (or DORT in French) highlights N significant eigenvalues, whose associated eigenvectors contain the ideal wave-front to focus on each one of them. Even more interesting, the eigenvalues are directly ranked by the reflectivity of their associated scatterer [106]. Note that these results are valid only for configurations where the targets are unresolved scatterers and well resolved by the imaging system, *i.e.* the minimum distance between each scatterer is higher than the optimal resolution cell of the imaging system [113]. This condition can be understood by the fact that the eigenvectors are by definition orthogonal. This property is then valid only if the imaging system is able to fully distinguish between each scatterer and thus, being able to excite one without exciting another. This condition is not fulfilled for specular reflectors that have at least one of their dimensions that is higher than the resolution cell. It implies that various inputs $\mathbf{E}_{\text{in}}$ are able to produce an optimal focusing on such scatterer. In this case, multiple eigenvectors are associated with a single scatterer [114] and the first one (characterized by the highest eigenvalue) maximizes the back-scattered energy by focusing on a part or several parts of this scatterer [115].

This fundamental work mostly performed by Prada and Fink can be applied to any type of waves and brought new perspectives and ideas for various applications based either on the reflection or on the transmission matrix: (*i*) Aberration correction [116, 117, 118, 108]; (*ii*) Target detection in complex media where multiple reverberation may hide the presence of such scatterer, *e.g.* Flaw detection in solid for non-destructive testing [119] or objects detection in shallow water for underwater acoustic; (*iii*) optimized wireless communications. [107, 120, 110].

However, the DORT method contains three fundamental drawbacks that limits its application to the particular case of medical ultrasound imaging:

- It has been developed for monochromatic signals, while ultrasound imaging is based on broadband ones. It is nonetheless possible to extract the impulse Green's function of the medium that links a target to the transducer array by (*i*) applying the

DORT method at each frequencies of the back-scattered signals; (*ii*) picking the eigenvector associated with this given target for each frequency, and (*iii*) performing an inverse Fourier transform to obtain a temporal signal [121]. However, the second step is difficult in practice as the scatterers reflectivity generally varies with frequency. Therefore, the first eigenvector is not necessarily associated with the exact same target across the entire frequency band. Figure II.2 illustrates one example of experiment demonstrating the DORT method in the time domain. An ultrasound probe is used to insonify a medium composed by submerged rods that are made of various materials and characterized by various diameters. The DORT method is then applied at each frequency and the resulting normalized eigenvalues are shown on figure II.2(b). Monochromatic singular vectors are combined based on their eigenvalue [red circles on figures II.2(b)] in order to create broadband signals. Finally, an inverse Fourier transforms are performed to obtain optimal pulses that focuses on each target. These signals constitute an estimation of the medium impulse Green's functions that link each scatterer to the transducer plane. We observe that an eigenvalue is not always associated with the same scatterer [dark dotted ellipses]. Therefore, some attention must be paid to the selection of the eigenvectors, which makes the implementation of this technique more complex.

- Its formalism and most outstanding results have been performed in the case where the scatterers or targets of interest are well resolved. More importantly, this technique requires that the number of scatters is lower than the number of transducers. Soft tissues are composed by a countless number of unresolved scatterers with no point-like bright star that could have been used as beacon.

- It is based on both the time-reversal invariance and the spatial reciprocity of the wave propagation. However time reversal invariance can be broken in dissipative media such as the skull bone. This principle can be broken by some phenomena such as the medium attenuation or the limited aperture of a time-reversal mirror. Tanter *et al.* [52] illustrated this drawback by demonstrating that skull bone induced aberrations are better corrected when the time-reversal process is coupling to an amplitude compensation in order to tackle the attenuation loss.

II.1.2 Analysis of the transmission matrix

These observations encouraged the pursuit of optimal focusing by analyzing the time-reversal process via the transmission matrix [Fig. II.3]. By means of a single transducer insonification, the transmission matrix $\mathbf{T}$ is acquired. This matrix contains all the available information on the wave propagation between an array of sources and an array of sensors. Similarly to the reflection case, the output signals induced by any input one can be deduced in post-processing from the transmission matrix thanks to the linear and time-invariant assumptions of the wave propagation:

$$\mathbf{E}_{\text{out}}(f) = \mathbf{T}(f) \times \mathbf{E}_{\text{in}}(f) \tag{II.5}$$

Again, the spatial reciprocity of the wave propagation, implies that the transpose of the transmission matrix ${}^{t}\mathbf{T}$ corresponds to the propagation matrix from the array of sensors and to the array elements. In particular, a focusing process can be performed by

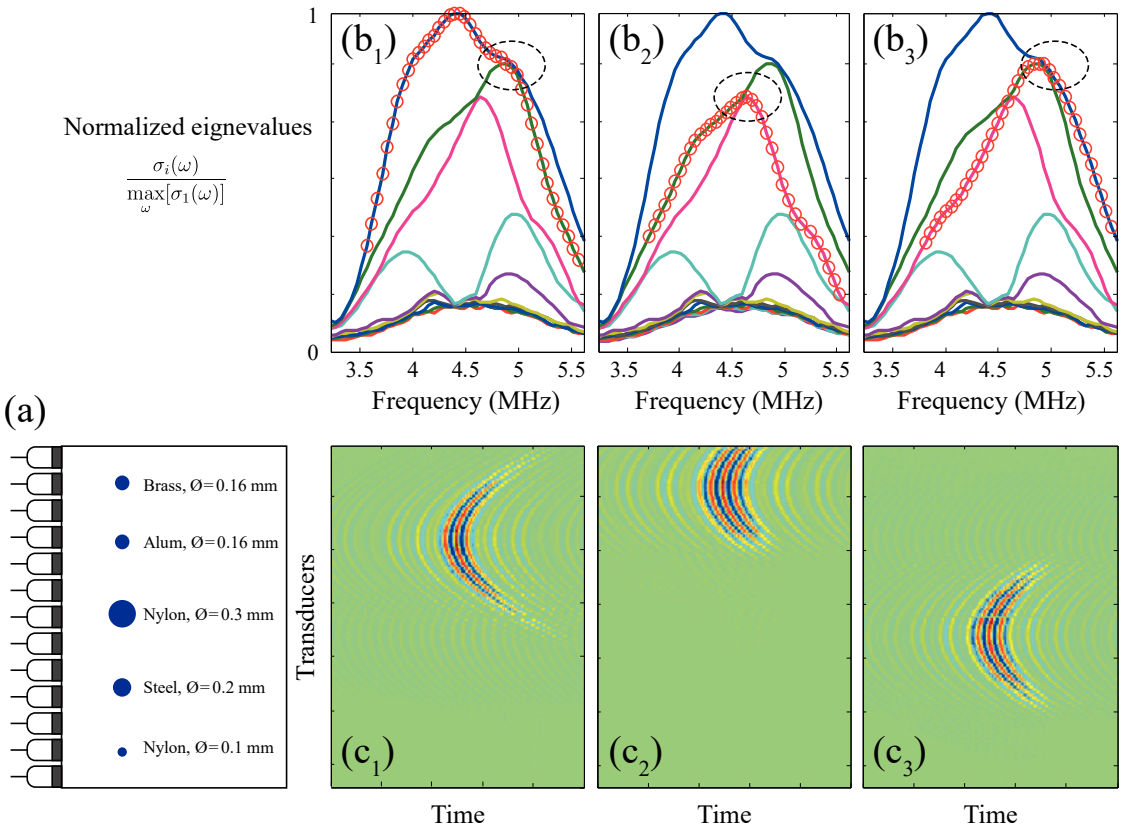

Fig. II.2 *Extraction of the impulse Green's functions between bright point like targets and an array of transducers based on the DORT method. (a)Sketch of the experiment. The reflection matrix is acquired and the DORT method is performed at each frequency. (b) The normalized eigenvalues are used to create broadband eigenvectors in the Fourier domain (red circles). (c) Temporal pulses are then calculated by means of inverse Fourier transform. Courtesy of Claire Prada.*

numerically time-reversing the signal that would have come from a particular point of the sensor array:

$$\mathbf{E}^{\mathrm{TR}}_{\mathrm{out}}(f) = \mathbf{T} \times \left(\mathbf{T}^{\top} \times \mathbf{E}^{0}_{\mathrm{out}}\right)^{*} = \left[\mathbf{T} \times \mathbf{T}^{\dagger}\right] \times \mathbf{E}^{0*}_{\mathrm{out}}, \tag{II.6}$$

where $^{\top}$ is the transpose operator and $\mathbf{E}^{0}_{\mathrm{out}}$ is the expected pressure field to generate in the sensor plane, *e.g.* $\mathbf{E}^{0}_{\mathrm{out}}$ can be a Dirac function or more reasonably the expected focal spot obtained in an homogeneous medium. These simple equations highlight once again the time-reversal operator $\left[\mathbf{T} \times \mathbf{T}^{\dagger}\right]$. The reciprocity of the wave propagation is the only assumption on the medium. Therefore, this concept also holds for complex configurations where multiple scattering appears, *e.g.* in disordered media [122] or in wave-guide [123]. In the time domain, it is easy to visualize that for such scattering medium, the impulse-responses are characterized by long time signals that account for all the potential multiple scattered paths. Therefore, the complexity of such medium is captured and stored as a

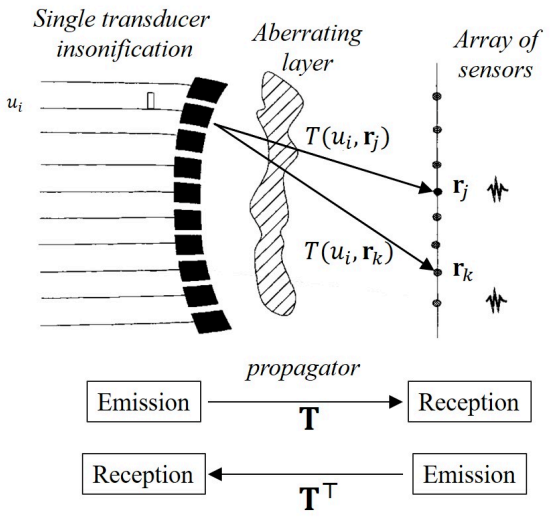

Fig. II.3 *Sketch of the transmission matrix acquisition. Inspired from [116]*

temporal information within the transmission matrix. Note that an optimal focusing is still possible in strongly scattering media if the entire impulse responses are measured and time-reversed [122]. More strikingly, it has been shown that the time-reversal process can benefit from multiple scattering process to improve the focusing quality. The medium behaves as a scattering lens characterized by a larger numerical aperture than in free space and that time-compressed the long time-reversed signals [109, 120].

The time-reversal process can be seen as a spatio-temporal matched filter. It provides the optimal linear solution for maximizing the amplitude at the focal point, even in the presence of noise. However, such filter does not guaranty a low side lobe level. To solve this problem, Tanter *et al.* [117, 118] introduced the inverse filter based on the following observation. For aberration correction, the ultimate goal is to find the signal to transmit $\mathbf{E}_{\text{in}}^{\text{inv}}$ that produces the optimal focusing $\mathbf{E}_{\text{out}}^{0}$ in the focal plane. Mathematically, this vector can be found by the inversion of the propagation matrix:

$$\mathbf{E}_{\text{in}}^{\text{inv}} = \mathbf{T}^{-1} \times \mathbf{E}_{\text{out}}^{0} \tag{II.7}$$

As is the case of all inverse problems, the inversion of the propagation matrix $\mathbf{T}$ is ill-conditioned. Numerically, the solution to the inversion does not depend continuously on the data, but rather, small errors in these data produce very large errors in the reconstructed results. Many regularization techniques have been proposed to overcome this issue. The idea consists in finding a filtered matrix $\hat{\mathbf{T}}$, whose inversion process is constrained. For instance, Tanter *et al.* [117, 118] proposed to perform a singular value decomposition (SVD) of $\mathbf{T}$ and to inverse only the signal subspace $\hat{\mathbf{T}}$ that is composed of the combination of singular vectors associated with the highest singular values. The lowest considered eigenvector is chosen based on the diffraction theory and noise level. This new matrix is then used to compute the optimal input signals $\mathbf{E}_{\text{in}}^{\text{inv}}$ that generates a close to desired output:

$$\mathbf{E}_{\text{out}}^{\text{inv}} = \mathbf{T} \times \mathbf{E}_{\text{in}}^{\text{inv}} = \left[\mathbf{T} \times \hat{\mathbf{T}}^{-1}\right] \times \mathbf{E}_{\text{out}}^{0} \tag{II.8}$$

this equation highlights the inverse-filter operator ($\mathbf{T} \times \hat{\mathbf{T}}^{-1}$). By performing this operation at each frequency, the authors construct a spatio-temporal inverse-filter. Even if $\mathbf{T}^{-1}$ and $\hat{\mathbf{T}}^{-1}$ are not strictly identical, leading to some difference between $\mathbf{E}_{\text{out}}^{\text{inv}}$ and $\mathbf{E}_{\text{out}}^{0}$, it has been shown that in dissipative media, such spatio-temporal inverse-filter strongly improves the focusing quality compared to time-reversal beamforming.

Similar works have known a great success in the field of optics with the pioneer experiment of Vellekoop and Mosk (2007) [124]. The authors demonstrated that, by means of a Spatial Light Modulator (SLM), an incident wave-front can be shaped to image through opaque scattering layers. Popoff *et al.* (2011) [108, 107] then experimentally demonstrated the proprieties of the time-reversal operator to focus through scattering media by simple means of a pseudo-inversion of the transmission matrix [Eq. II.6]. These works open new perspectives for MIMO (Multiple-Input-Multiple-Output) communications [125, 126]. More recently, Del Hougne *et. al.* (2019) [127] have shown that the effective rank of the transmission matrix can be used as a figure of merits for optimizing the Shannon capacity of the communication channel in a microwave experiment, *i.e.* they optimized the disorder of the medium by modifying the boundary condition of a reverberating cavity by means of tunable meta-surfaces. As the Shannon capacity is a direct indicator of the number of independent propagation channels of the medium, this optimization drastically improves the amount of information that can be simultaneously transmitted from the emitters to the receivers.

In the meantime, fundamental work on the optimal transport of the wave energy has been performed over the past decade. Experiments in the field of ultrasound and optics (2014) [128, 110], have shown that open and closed channels can be excited based on the analysis of the transmission matrix. Predicted by Dorkhov in solid state physics more than thirty years go [129], these particular channels are associated with particular incident wave-front whose energy is totally transmitted or reflected by the medium, respectively.

We finally evoke the work done by the group of Stephan Rotter on the scattering matrix, which encompasses both the transmission and reflection matrix and corresponds to the configurations where sources and sensors are located on both side of the medium. By means of the Wigner-Smith operator, this group has been able to isolate particle like wave packets that follow either a direct path or a multiple scattered one based on their time of arrival [130, 131], but also detect the modification of a single scatterer (position or scattering strength) within a disordered medium [132].

This short overview of the matrix approach in waves physics enables to better define this concept and resulting applications. Regarding the field of optics, more information are gathered in the review of Rotter and Gigan (2017) [133]. At the end of the day, we note that one of the major strengths of the above-mentioned techniques is that they require no *a priori* information on the propagating medium. For instance, the medium speed of sound is not required to apply the time-reversal beamforming of the DORT method. In the following, we explicit the recent development done in reflection configuration for imaging and quantification and we show how conventional state-of-the-art ultrasound imaging can be interpreted under the scope of the matrix approach.

II.1.3 State-of-the-art of matrix imaging

Inspired by experiments in underwater acoustics for SONAR and in electro-magnetism for RADAR, the reflection matrix has been used in ultrasound for more than 40 years, via the concept of synthetic beamforming [23, 24]. These techniques are based on the combination of back-scattered signals generated by multiple insonifications. This combination only requires time delays and coherent summation. It is thus also based on the assumption of a linear and time-invariant process.

Nonetheless, the ultrasound image contains less information on the medium than the reflection matrix. For instance, once the beamformed image has been computed, it is not possible to numerically simulate the back-scattered signals obtained for another incident wave [Par. II.1.1]. By injecting additional knowledge on the medium via the assumed sound-speed model and the single scattering hypothesis, the ultrasound image is able to extract some local features on the medium, *e.g.* its reflectivity. In paragraph II.2 we show how to combine both approaches, *i.e.* how to make use of all the available information contained in the reflection matrix to locally probe and characterize the medium.

II.1.3.1 The insonification sequence, a choice of input basis

In the field of ultrasound, all the above-mentioned ultrasound matrix techniques, *e.g.* the DORT method, are based on the single transducer insonification. Even if this transmission sequence enables to capture all the available information on the medium, it suffers from two drawbacks for *in-vivo* imaging. First the number of required transmitted event is equal to the number of transducers, which generally goes up to 256 for state-of-the-art medical probe. This condition drastically reduces the acquisition frame-rate, which increases the probability of movement during the insonification sequence. Such phenomenon damages the time-invariant assumption, which impacts the results provided by the matrix approach. Second, as the medium is insonified by a single transducer, the energy of the incident wave is quite low and the back-scattered signal level is further reduced. Due to attenuation, it limits the maximal depth that can be imaged. Any signal level that drops below the sensitivity threshold of the transducers breaks reciprocity and linearity of the acquisition process. To overcome the SNR issue, two solutions have been developed. Gammelmark *et al.* proposed to use long encoded sequences [134], *i.e.* instead of sending short pulses, each transducer successively sends encoded signals such as chirp. As the wave propagation is linear, the signal back-scattered by a single scatterer is also a chirp weighted by the scatterer reflectivity. The reflection matrix is then deduced from the back-scattered signals by using a pulse-compression technique. Such techniques are generally based on the convolution of the backscattered signals by the transmitted encoded signal. It time-compresses all the transmitted energy to numerically simulate a short pulse. However, this signal processing tool is computationally intensive and highly sensitive to any phenomena that distort the incident waves, for instance the attenuation modifies the frequency content of the incident wave as it propagates within the medium. The other technique consists in using multiple transducers for a given transmitted event. Such option requires to modify the definition of the reflection matrix and is studied in the following paragraphs.

Transducer vs plane wave insonifications

To tackle those issues, synthetic beamforming is usually based on a plane wave insonification I.1.4.1. Single and plane wave insonifications are closely linked as the latter one can be viewed as the spatial Fourier transform of the first one. To better illustrate this observation, we remind the reader, that based on the conventional reflection matrix $\mathbf{R}_{\text{uu}}$, the backscattered signals generated by any insonification can be simulated. More precisely, by combining equations II.3 and I.25, this concept applies to any incident plane wave characterized by its incident angle θ_{in} or transverse wave-number at frequency f, $k_{\text{in}}^{\text{x}} = 2\pi f/c_0 \cdot \sin(\theta_{\text{in}})$:

$$R(u_{\text{out}}, \theta_{\text{in}}, f) = \sum_{u_{\text{in}}} R(u_{\text{out}}, u_{\text{in}}, f) e^{-jk_{\text{in}}^{\text{x}} u_{\text{in}}}. \tag{II.9}$$

For sake of simplicity, in the following, the transverse wave-number k_{in}^{x} will simply be noted k_{in} or referred by its associated angle θ_{in}. This equation directly simply corresponds to a spatial Fourier transform. Therefore, single and plane wave insonifications can be seen as two relevant input bases of the reflection matrix. Matrix-wisely, this change of basis can be expressed as:

$$\mathbf{R}_{\text{u}\theta} = \mathbf{R}_{\text{uu}} \times \mathbf{T}_0^{\top}, \tag{II.10}$$

where $\mathbf{T_0}$ is the Fourier transform operator, whose elements link any transverse wave number k_{x} in the Fourier space to the transverse coordinate x of any point of the supposed homogeneous medium:

$$T_0(k^{\text{x}}, x) = \exp\left(ik^{\text{x}}x\right). \tag{II.11}$$

As in any Fourier transform, $\mathbf{R}_{\text{uk}}$ and $\mathbf{R}_{\text{uu}}$ contain the same amount of information and one matrix can be deduced from the other if and only if a Shannon criterion is fulfilled. Mathematically, this criterion links the angular step $\delta\theta$ (or wavenumber step δk) and the angles of maximal amplitude $\theta_{\text{in}}^{\max}$ (or wave number max $k_{\text{in}}^{\max}$) to the size of the transducer array $L_x = pN_p$ and to the probe pitch p:

$$\frac{\delta k_{\text{in}}}{2\pi} < \frac{1}{2L_x} \qquad \text{and} \qquad \frac{k_{\text{in}}^{\max}}{2\pi} < \frac{1}{2p}. \tag{II.12}$$

From a physical point-of-view, the second equation exactly highlights the limiting angles of the transducer radiation pattern predicted by the diffraction theory. The use of higher incident angles will generate grating lobes [Par: I.1.1.2]. For a conventional linear probe defined by $f_c = 7.5$ MHz, $p = 0.2$ mm and $N_p = 256$, equations II.12 leads to $\delta\theta_{\text{in}} < 0.1$ deg and $\theta_{\text{in}}^{\max} < 30.9$ deg, which unsurprisingly leads to nearly 256 transmitted plane waves. However, we discuss in paragraph I.1.4.2 that roughly the same image quality can be achieved with fewer transmitted plane waves. This observation can be explained by the spatial coherence of the backscattered wave-field that induces some redundant information in the measured signals. Therefore, reducing the number of transmitted plane waves (by increasing the angular step $\delta\theta$) can be viewed as a compressed sensing operation, which occurs in the spatial Fourier domain. However, we insist on the fact that the capacity of reducing the number of insonifications relies on the medium properties that govern the spatial coherence of the back-scattered wavefield and more precisely the spatial coherence of the realigned signals. It thus depends on the nature of the scatterers, specular or speckle regime, but also on the accuracy of the speed of sound model. In addition, we

observe that in the presence of aberration, it is precisely those redundancies that are able to first determine the aberration laws and then to correct for them [Par. I.2.2.3].

The focusing process: a change of basis towards virtual transducers

Focused insonifications are the most widely used transmitted sequences for B-mode imaging. The idea of combining multiple focused insonifications to enhance the image quality has been used for more than a decade via the so-called synthetic focused beamforming [135, 136, 32]. This technique enables to numerically simulate a transmit focusing at each point of the medium associated with each pixel of the image [Par. I.1.4.3]. This confocal imaging technique leads to the useful concept of virtual source. To illustrate this idea, we first take a closer look at the propagation of an incident beam that focuses at $\mathbf{r}_{\text{in}}$. This propagation can be split in three steps, which are separated by the transmit time of flight $t_{\text{in}} = z_{\text{in}}/c_0$. At a time of flight $t < t_{\text{in}}$, one observes a converging wave [Fig. II.4(a)]. As the wave gets closer to $\mathbf{r}_{\text{in}}$, the lateral extension of the wave front reduces. At time $t_{\text{in}} = z_{\text{in}}/c_0$, the wave front is at $\mathbf{r}_{\text{in}}$, most of the energy is concentrated in a diffraction limited area (in absence of aberrations). The wave-front does not stop at $\mathbf{r}_{\text{in}}$, and one then observes a diverging wave that propagates outward at $t > t_{\text{in}}$ [Fig. II.4(b)]. This focused wave then illuminates all the scatterers located within a cone, whose aperture is the maximum angle of illumination β_{in} that is governed by the transmitted f-number $\text{F}_{\text{in}}^{\#}$ [Par. I.1.2]. Passman and Ermert (1996) [137] demonstrated in simulation that for an observer located at point $\mathbf{r}_2$ (located below the focal point, $z_2 > z_{\text{in}}$), the incident wave looks like it originates from a virtual source located at point $\mathbf{r}_{\text{in}}$. This virtual source is characterized by a radiation pattern that matches the aperture of the insonifying cone [Fig. II.4(c)], and its size is delimited by the spatial extension of the transmit focal spot [Par. I.1.2.1]. Similarly, an observer located at $\mathbf{r}_1$ (above the focal point $z_1 < z_{\text{in}}$) witnesses an incident wave that is identical to the time-reversed one produced by the virtual source located at $\mathbf{r}_{\text{in}}$. In other words, the back-scattered signals induced by a focused insonification can be interpreted as the one produced by a virtual source located within the medium at the focal spot.

A sequence of transmitted focused beams can thus be seen as another input basis of the reflection matrix. In this case, the reflection matrix is noted $\mathbf{R}_{\text{ur}}(t)$ and contains the impulse response of the medium between an array of virtual sources at the input and the array of transducers at the output. While the first two bases, *i.e.* the transducer and plane wave bases do not require any *a priori* knowledge on the medium, this focused basis requires a hypothesis on the medium speed of sound. This additional assumption enables to extract a more local information on the medium. Based on this reflection matrix, Robert and Fink (2008-2009) [61, 49] developed the fDORT method. This technique is the enhanced version of the DORT method for focused insonifications. Based on the location of the virtual source, this technique is able to analyze back-scattered aberrated wave-fronts that originate from a precise region of the medium. This local information enables to correct for multiple isoplanatic patches within a single image.

Note, we derived the notion of virtual source for focused insonification. However, based on the matrix approach, the back-scattered signals generated by a focused wave can be numerically simulated from other input bases such as transducer or plane wave bases, or even from focused insonification in order to create a virtual source at each point of the medium. The focusing step can thus be seen as a change of basis that is either

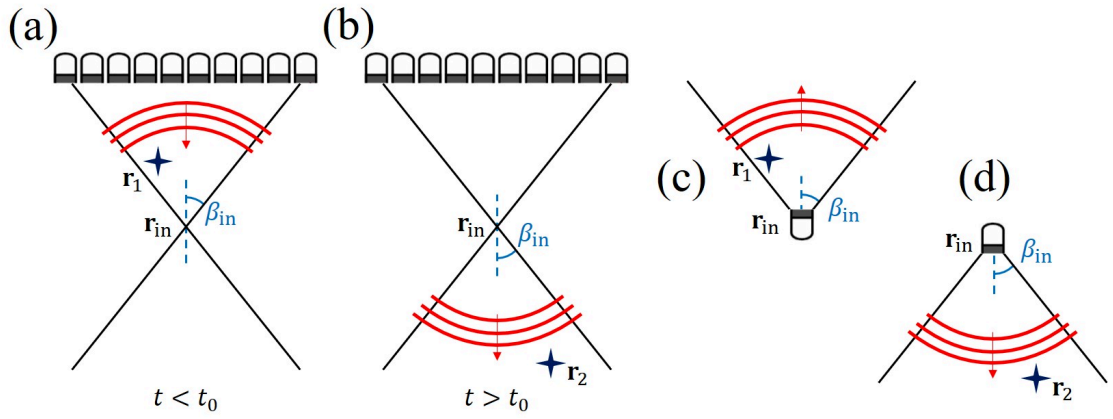

Fig. II.4 *Principle of the virtual source. The pressure field generated by a focused transmitted beam is analogue to the one generated by a virtual source located at the transmit focal spot r_{in}. Inspired from [61].*

performed physically by using focused beams or numerically via a synthetic beamforming.

Finally, we describe the concept of virtual sources located within the medium. However, this concept can apply to virtual sources located behind the medium. In that case, multiple transducers are used to generate diverging waves, whose wave-front curvature depends on the distance between the virtual source and the array of transducers. This illumination is widely used for phased array probes as it enables large field-of-views (still limited by the transducer radiation pattern). In addition, as multiple transducers are used in transmission, the energy of the incident wave is more intense than the diverging wave created by a single transducer illumination. By moving the virtual source away from the transducers, the curvature of the diverging wave is reduced, which limits the field-of-view. Following this concept, a plane wave illumination can be viewed as the extreme case where the virtual source is located at infinity (either behind or below the probe), hence the term far-field illumination commonly used in optics (thanks to optical lens).

II.1.3.2 Taking advantage of the reciprocity: the virtual sensor

In the previous paragraph we developed the concept of virtual source that is accessible via a focusing step. Based on the reciprocity of wave propagation, a similar concept *i.e.* a virtual sensor can be derived from a received beamforming process. To better understand the nature of the virtual sensor, we can rely on the principle of the isochronous volume developed in paragraph I.1.3.2. The coherent summation of echoes, whose associated isochronous volume contains a common region, enables to select echoes that have been generated by this received focal spot, called virtual sensor. Similarly to the virtual source, the virtual sensor is characterized by a radiation pattern that depends on the received aperture used during the beamforming process and more precisely on the maximum angle of collection $\beta_{out}(\mathbf{r}_{out})$. Its spatial dimension corresponds to the size of the output focal spot.

By means of a double focusing both in transmission and in reception, a change of basis is performed to probe the medium responses between an array of virtual sources and an array of virtual sensors embedded within the medium. These responses form the so-called focused reflection matrix $\mathbf{R}_{\mathrm{rr}}$, that will be intensively described in the following section. In other words, the echoes of this matrix are obtained by splitting the location of the transmitted and received focal spots. The first traces of this matrix can be found in the PhD work of Aubry (2008) [138], where Gaussian beamforming in transmission and reflection where used to create virtual sources and virtual sensors at the surface of a submerged medium [114, 86]. Additional time delays Δt were used during the beamforming process $\mathbf{R}_{\mathrm{rr}}(\Delta t)$ to measure the growth of the diffusive halo in order to map the diffusion constant of the scattering medium [Par. I.3.2.2]. This matrix has then been more intensively studied by the group of Aubry at Institut Langevin (Paris) at the ballistic time *i.e.* $\Delta t = 0$. First during the PhD of Badon [112] in the field of optics, where the focused reflection matrix is directly acquired by a so called smart-OCT technique [139]. It has then been briefly investigated in the field of ultrasound by Camille Trottier [140] during his PhD work for NDT applications. Finally, these works lead to the PhD work of Barolle [141], Blondel [142] and mine in the field of optics, seismology and ultrasound respectively.

II.2 The focused reflection matrix

We now show how all of the aforementioned imaging steps can be rewritten under a matrix formalism. The reflection matrix contains the medium responses between one or two mathematical bases. The bases implicated in this work are: (*i*) the recording basis which here corresponds to the transducer array, (*ii*) the illumination basis which is composed of the incident plane waves, and (*iii*) the focused basis in which the ultrasound image is built.

In the following, two experiments are used to illustrate our analysis of the reflection matrix: (*i*) a conventional phantom experiment without aberration and (*ii*) an *in-vivo* experiment on the calf of a healthy volunteer. Their respective experimental configurations are described in the annex II.A. For each experiment, we acquire the plane wave reflection matrix $\mathbf{R}_{\mathrm{u}\theta}(t) \equiv [R(u_{\mathrm{out}}, \theta_{\mathrm{in}}, t)]$.

II.2.1 Monochromatic focused reflection matrix

Following the work of Badon *et al.* [112], we performed the beamforming process in the frequency domain. In this case, simple matrix products allow ultrasonic data to be easily projected from the illuminating and recording bases to the focused basis where local information on the medium properties can be extracted.

Consequently, a temporal Fourier transform should be first applied to the experimentally acquired reflection matrix $\mathbf{R}_{u\theta}(t)$:

$$\mathbf{R}_{u\theta}(f) = \int dt\ \mathbf{R}_{u\theta}(t)\ e^{-j2\pi ft}. \tag{II.13}$$

with f the temporal frequency. To perform the transmitted and received beamforming, *i.e.* to project the reflection matrix in the focused basis, transmission matrices should be

defined beforehand to model wave propagation from the plane wave or transducer bases to any focusing point $\mathbf{r} = (x, z)$ in the medium. Assuming an homogeneous medium of constant speed-of-sound c_0, free-space transmission matrices, $\mathbf{P_0}(f)$ and $\mathbf{G_0}(f)$, are considered. Their elements correspond to plane waves or 2D Green's functions [9] propagating in a fictive homogeneous medium:

$$P_0(\theta, \mathbf{r}, f) = \exp -(i\mathbf{k}\cdot\mathbf{r}) \tag{II.14a}$$
$$= \exp -[ik_0(z\cos\theta + x\sin\theta)],$$
$$G_0(\mathbf{r}, \mathbf{u}, f) = -\frac{i}{4}\mathcal{H}_0^{(1)}(-k_0|\mathbf{r}-\mathbf{u}|). \tag{II.14b}$$

with $k_0 = 2\pi f/c_0$ the wave number. Those transmission matrices are then used to beamform the reflection matrix in transmission and reception:

$$\mathbf{R}_{\mathrm{rr}}(f) = \mathbf{G_0^*}(f) \times \mathbf{R}_{u\theta}(z) \times \mathbf{P}_0^{\dagger}(f), \tag{II.15}$$

where the symbols $*$, $\dagger$ and $\times$ stand for phase conjugate, transpose conjugate and matrix product, respectively. Each row of $\mathbf{P}_0^{\dagger} = [P_0^*(\theta_{\mathrm{in}}, \mathbf{r}_{\mathrm{in}})]^T$ defines the combination of plane waves that should be applied to focus on each input focusing point $\mathbf{r}_{\mathrm{in}} = \{x_{\mathrm{in}}, z_{\mathrm{in}}\}$ at a desired frequency. Similarly, each column of $\mathbf{G}_0^* = [G_0^*(u_{\mathrm{out}}, \mathbf{r}_{\mathrm{out}})]$ contains the amplitude and phase that should be applied to the signal received by each transducer u_{out} in order to sum coherently the echoes coming from the output focusing point $\mathbf{r}_{\mathrm{out}} = \{x_{\mathrm{out}}, z_{\mathrm{out}}\}$. Fig. II.5 illustrates the matrix focusing process. For sake of clarity, the input focusing operation is represented by means of a cylindrical wave-front instead of a coherent combination of plane waves. This is justified by the fact that plane wave synthetic beamforming numerically mimics focused excitations [26].

While, in standard synthetic ultrasound imaging, the input and output focusing points coincide, they are here decoupled. At emission, the incident energy is concentrated at the focusing point $\mathbf{r}_{\mathrm{in}}$. This point can then be seen as a virtual source. Similarly, in reception, a virtual sensor is synthesized by selecting echoes coming from the focusing point $\mathbf{r}_{\mathrm{out}}$. Therefore, each coefficient $R(\mathbf{r}_{\mathrm{out}}, \mathbf{r}_{\mathrm{in}}, f)$ of $\mathbf{R}_{\mathrm{rr}}$ contains the monochromatic responses of the medium between a set of virtual transducers corresponding to each pixel of the ultrasound image. In other words, one line of this matrix contains the pressure field probed by the various virtual sensors located at $\mathbf{r}_{\mathrm{out}}$ when a transmitted focusing is set to focus the incident wave at $\mathbf{r}_{\mathrm{in}}$ at the focusing time, *i.e.* at the time where the incident wave is set to be focused.

Figure II.6(a_2) shows the x-projection $\mathbf{R}_{\mathrm{xx}}(z, f)$ of $\mathbf{R}_{\mathrm{rr}}(f)$ at $z = 18$ mm and frequency $f = 5$ MHz in the phantom experiment. First, note that the coefficients $R(\mathbf{r}_{\mathrm{out}}, \mathbf{r}_{\mathrm{in}}, f)$ associated with a transverse distance $|x_{\mathrm{out}} - x_{\mathrm{in}}|$ larger than a superior bound $\Delta x_{\max}$ are not displayed. $\Delta x_{\max}$ is actually fixed to avoid the spatial aliasing induced by the incompleteness of the plane wave illumination basis: $\Delta x_{\max}$ is inversely proportional to the angular step $\delta\theta$ of the plane wave illumination basis: $\Delta x_{\max} \sim \lambda_{\max}/(2\delta\theta)$ (see Appendix II.B), with λ the wavelength.

As shown by Fig. II.6(a_2), most of the signal in $\mathbf{R}_{\mathrm{rr}}(f)$ is concentrated around its diagonal. This indicates that single scattering dominates at these depths [69], since a singly-scattered wave-field can only originate from a virtual detector in the vicinity of the virtual source. In fact, the elements of $\mathbf{R}_{\mathrm{rr}}$ which obey $\mathbf{r}_{\mathrm{in}} = \mathbf{r}_{\mathrm{out}}$ hold the information which would be obtained via multi-focus (or confocal) imaging in which transmit

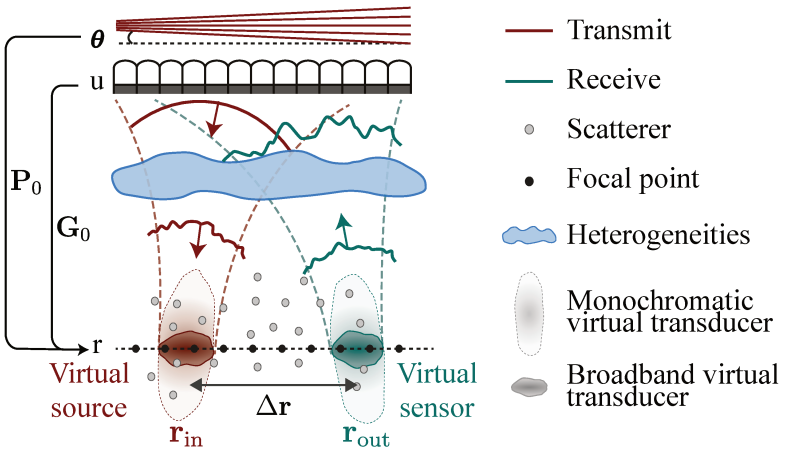

Fig. II.5 *Principle of the focused reflection matrix. Matrix imaging consists in splitting the location of the transmit ($\mathbf{r}_{in}$) and receive focusing ($\mathbf{r}_{out}$) points, thereby synthesizing virtual transducers that act as a source and a detector, respectively, at any point in the medium. In a monochromatic regime, the synthesized virtual transducers display an elongated shape in the $z-$direction because of diffraction. In the broadband domain, the axial resolution is inversely proportional to the signal bandwidth, leading to a much thinner virtual transducer in the $z-$direction.*

and receive focusing are performed at the same location for each point in the medium. The ultrasound image at a single frequency, $\mathcal{I}_m(\mathbf{r}, f)$, can be directly deduced from the diagonal elements of $\mathbf{R}_{\mathrm{rr}}(\mathrm{f})$

$$\mathcal{I}(\mathbf{r}, f) \equiv |R(\mathbf{r}, \mathbf{r}, f)|^2 . \tag{II.16}$$

The corresponding image is displayed in Fig. II.6(a_1). Compared to a standard ultrasound image built from broadband signals (a_2), this image displays a bad axial resolution that will be explained below. The same observations can be done on the *in-vivo* experiment on the human calf [Fig II.7]. In the following, we show that the off-diagonal elements of $\mathbf{R}_{\mathrm{rr}}$, on the contrary, provide a lot of information on the physical properties of the medium as well as on the wave focusing quality.

To prove this assertion, the recorded reflection matrix is modeled as the results of three successive events. Transmit propagation from the probe to the focal plane. Interaction of the wave with the medium and back-propagation to the probe. In the Fourier domain, the measured reflection matrix can then be expressed as:

$$\mathbf{R}_{\mathrm{u}\theta}(f) = \mathbf{G}^{\top}(f) \times \mathbf{\Gamma}(f) \times \mathbf{P}(f), \tag{II.17}$$

where the matrix $\mathbf{\Gamma}$, defined in the focused basis, describes the scattering process that occurs inside the medium. In the single scattering regime, $\mathbf{\Gamma}$ is a diagonal matrix and its elements correspond to the medium reflectivity $\gamma(\mathbf{r}, f)$. $\mathbf{P}$ and $\mathbf{G}$ are the true propagating matrices of the medium, which are estimated by $\mathbf{P_0}$ and $\mathbf{G_0}$ in the beamforming process. By using the equations II.15 and II.17, the focused reflection matrix can be expressed as:

$$\mathbf{R_{rr}}(f) = \mathbf{H}^{\top}_{\mathrm{out}}(f) \times \mathbf{\Gamma} \times \mathbf{H_{in}}(f), \tag{II.18}$$

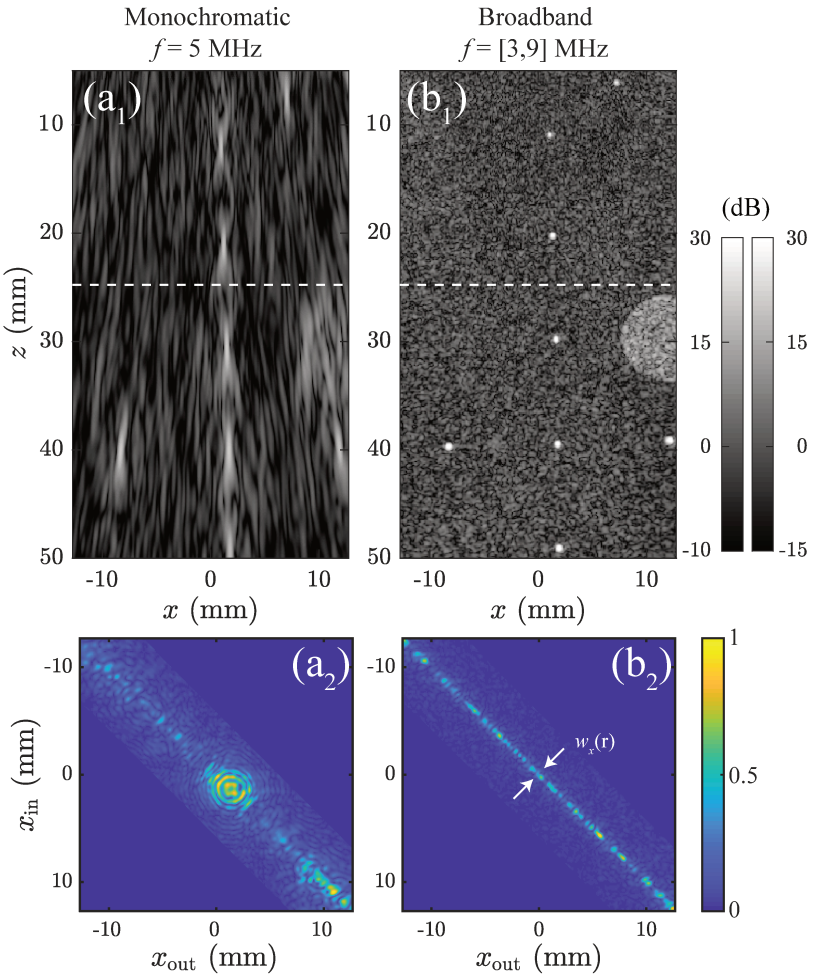

Fig. II.6 *Matrix imaging in a homogeneous phantom experiment. (a, b) Monochromatic ($f = 5$ MHz) and broadband regime. (1, 2) Ultrasound images ($\mathcal{I}(\mathbf{r})$ and $\overline{\mathcal{I}}(\mathbf{r})$ and focused reflection matrices ($\mathbf{R}_{xx}(z)$ and $\overline{\mathbf{R}}_{xx}(z)$) computed at $z = 25$ mm. Note that the US images are displayed with a different dynamic.*

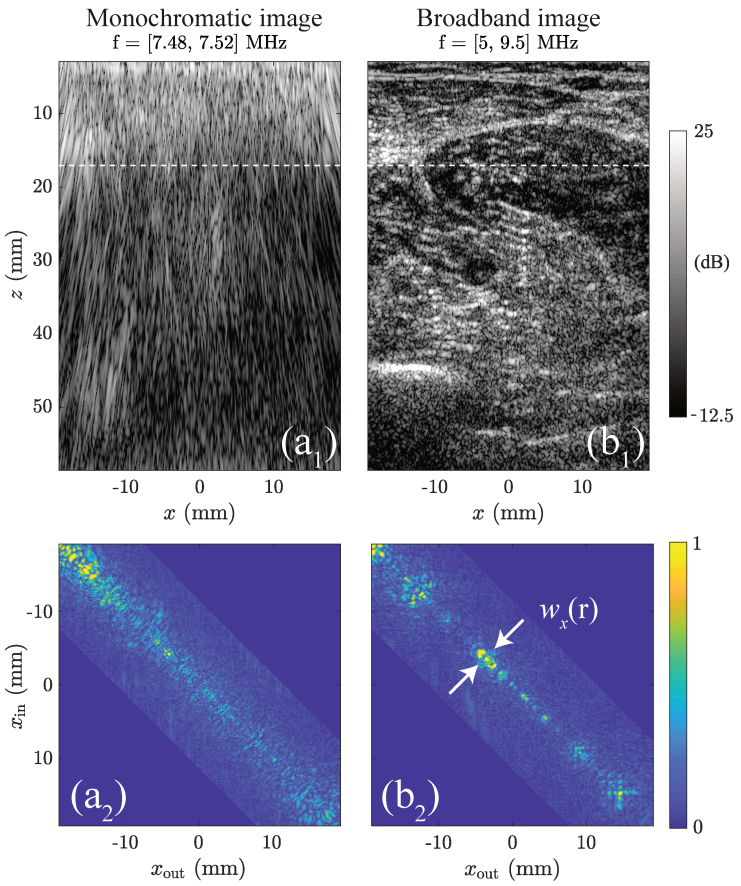

Fig. II.7 *Matrix imaging of an in-vivo calf experiment on a healthy volunteer. (a, b) Monochromatic ($f = 7.5$ MHz) and broadband regime. (1, 2) Ultrasound images ($\mathcal{I}(\mathbf{r})$ and $\overline{\mathcal{I}}(\mathbf{r})$) and focused reflection matrices ($\mathbf{R}_{xx}(z)$ and $\overline{\mathbf{R}}_{xx}(z)$) computed at $z = 18$ mm.*

where

$$\mathbf{H}_{\text{in}}(f) = \mathbf{P}(f) \times \mathbf{P}_{\mathbf{0}}^{\dagger}(f) \tag{II.19}$$

and

$$\mathbf{H}_{\text{out}}(f) = \mathbf{G}(f) \times \mathbf{G}_{\mathbf{0}}^{\dagger}(f) \tag{II.20}$$

$\mathbf{H}_{\text{in}}(f)$ and $\mathbf{H}_{\text{out}}(f)$ are the input and output focusing matrices, respectively. Each column of $\mathbf{H}_{\text{in}} = [H_{\text{in}}(\mathbf{r}, \mathbf{r}_{\text{in}})]$ and $\mathbf{H}_{\text{out}} = [H_{\text{out}}(\mathbf{r}, \mathbf{r}_{\text{out}})]$ corresponds to the transmitted and received point-spread functions (PSFs) at frequency f, *i.e.* the spatial amplitude distribution of the input and output focal spots that result from a transmitted and received focusing at $\mathbf{r}_{\text{in}}$ and $\mathbf{r}_{\text{out}}$, respectively. In the rest of the paragraph, for sake of lighter notations, the dependence on frequency f of each physical quantity is made implicit. Equation II.18 can be rewritten in terms of matrix coefficients as follows:

$$R(\mathbf{r}_{\text{out}}, \mathbf{r}_{\text{in}}) = \int d\mathbf{r} H_{\text{out}}(\mathbf{r}, \mathbf{r}_{\text{out}}) \gamma(\mathbf{r}) H_{\text{in}}(\mathbf{r}, \mathbf{r}_{\text{in}}). \tag{II.21}$$

This last equation confirms that the diagonal coefficients of $\mathbf{R}_{\rm rr}(f)$ form the confocal image at frequency f. For these particular signals ($\mathbf{r}_{\rm in} = \mathbf{r}_{\rm out}$), equation II.21 consists in a spatial convolution between the sample reflectivity $\gamma(\mathbf{r})$ and an imaging PSF, H, which corresponds to the product of the input and output PSFs: $H = H_{\rm in} \times H_{\rm out}$.

The resolution of such a confocal image is thus dictated by the support of $H_{\rm in}$ and $H_{\rm out}$ that define the characteristic size of each virtual source at $\mathbf{r}_{\rm in}$ and virtual sensor at $\mathbf{r}_{\rm out}$. In absence of aberration, the transverse and axial dimensions of these focal spots, $\delta x_0(\mathbf{r})$ and $\delta z_0(\mathbf{r})$, are only limited by diffraction [8]:

$$\delta x_0(\mathbf{r}) = \frac{\lambda}{2\sin[\beta(\mathbf{r})]}\,,\ \delta z_0(\mathbf{r}) = \frac{2\lambda}{\sin^2[\beta(\mathbf{r})]}, \tag{II.22}$$

with $\beta(\mathbf{r})$ the maximum angle under which each focal point is illuminated or seen by the array of transducers. The virtual transducers display a characteristic elongated shape in the $z-$direction ($\delta x_0 << \delta z_0$), which accounts for the bad axial resolution exhibited by the monochromatic image in Fig. II.6(a_1). Notably, while no bright targets are located at $z = 25$ mm in the phantom experiment, the focused reflection matrix Rxx highlights Fresnel rings that are induced by a target located above(at $z = 20$ mm) or below (at $z = 30$ mm) [See the broadband US image (b1) that is analyzed below]. This phenomenon is often observed in optics due to a defocus.

II.2.1.1 Quantification of the focusing quality, the common-mid-point frame.

The off-diagonal points in $\mathbf{R}_{\rm rr}(f)$ can be exploited for assessing the local focusing quality of the ultrasound image. To that aim, the relevant observable is the intensity profile along each anti-diagonal of $\mathbf{R}_{\rm rr}(f)$ [69]:

$$I(\mathbf{r}_m, \Delta\mathbf{r}) = \left|R(\mathbf{r}_m + \Delta\mathbf{r}/2, \mathbf{r}_m - \Delta\mathbf{r}/2)\right|^2. \tag{II.23}$$

All signals located on a given anti-diagonal have the same mid-point $\mathbf{r}_m = (\mathbf{r}_{\rm out} + \mathbf{r}_{\rm in})/2$, but different spacing $\Delta\mathbf{r} = (\mathbf{r}_{\rm out} - \mathbf{r}_{\rm in})$. In the following, $I(\mathbf{r}, \Delta\mathbf{r})$ is thus referred to as the common-mid-point (CMP) intensity matrix.

To express theoretically this quantity, the first approximation consists in making, in the vicinity of each common mid-point, the isoplanatic hypothesis. In other words, we assume that all virtual transducers are impacted by the exact same aberrations. The input and output PSF are then locally spatially invariant, such that

$$H_{\rm in/out}(\mathbf{r}, \mathbf{r}_{\rm in/out}) = H_{\rm in/out}(\mathbf{r} - \mathbf{r}_{\rm in/out}, \mathbf{r}_m). \tag{II.24}$$

In order to assess the local resolution of the medium regardless of the medium reflectivity, while keeping a satisfactory spatial resolution, a spatial average over a few resolution cells is required. To do so, a spatially averaged intensity profile $I_{\rm av}(\mathbf{r}, \Delta\mathbf{r})$ is computed at each point $\mathbf{r}$, such that

$$I_{\rm av}(\mathbf{r}_m, \Delta\mathbf{r}) = \langle W_L(\mathbf{r} - \mathbf{r}_m) I(\mathbf{r}, \Delta\mathbf{r})\rangle_{\mathbf{r}} \tag{II.25}$$

where the symbol $\langle..\rangle_{\mathbf{r}}$ denotes the spatial average and $W_L(\mathbf{r})$ is a spatial window function, such that

$$W_L(\mathbf{r}) = \begin{cases} 1 & \text{for } |r| < L/2 \\ 0 & \text{otherwise.} \end{cases} \tag{II.26}$$

Note that L is arbitrarily chosen and will govern the spatial resolution of the estimation of the local image resolution. $I_{\text{av}}(\mathbf{r}_m, \Delta\mathbf{r})$ is an estimation of the spatially-dependent intensity response to an impulse at $\mathbf{r}_m$. This means that whatever the scattering properties of the sample, $I_{\text{av}}(\mathbf{r}, \Delta x)$ allows an estimation of the input-output PSFs. However, its theoretical expression differs slightly depending on the characteristic length scale l_γ of the reflectivity $\gamma(\mathbf{r})$ compared to the typical width δx of the input and output focal spots. Two regimes can be distinguished, the specular regime ($l_\gamma \gg \delta x$) and the speckle one ($l_\gamma \ll \delta x$).

CMP intensity profile in the speckle scattering regime In this regime ($l_\gamma \ll \delta x$), the medium is composed of a random distribution of unresolved scatterers that can be modelled by a random reflectivity I.1.3.2:

$$\langle \gamma(\mathbf{r_1})\gamma^*(\mathbf{r_2})\rangle = \langle|\gamma|^2\rangle\delta(\mathbf{r_2}-\mathbf{r_1}), \tag{II.27}$$

where $\langle\cdots\rangle$ denotes an ensemble average and δ is the Dirac distribution. By injecting Eqs. II.21, II.24 and II.27 into Eq. II.23, the following expression can be found for each common mid-point intensity:

$$I(\mathbf{r}_m, \Delta\mathbf{r}) = \int d\mathbf{r} |H_{\text{out}}\left(\mathbf{r} - \Delta\mathbf{r}/2, \mathbf{r}_m\right)|^2 |H_{\text{in}}\left(\mathbf{r} + \Delta\mathbf{r}/2, \mathbf{r}_m\right)|^2 \times |\gamma(\mathbf{r}+\mathbf{r}_m)|^2. \tag{II.28}$$

Finally, the spatial average [Eq. II.25] enables to replace $|\gamma(\mathbf{r})|^2$ in the last equation by its ensemble average $\langle|\gamma|^2\rangle$. $I_{\text{av}}(\mathbf{r}, \Delta\mathbf{r})$ then directly provides the convolution between the incoherent input and output PSFs, $|H_{\text{in}}|^2$ and $|H_{\text{out}}|^2$:

$$I_{\text{av}}(\mathbf{r}_m, \Delta\mathbf{r}) = \langle|\gamma|^2\rangle \left(|H_{\text{in}}|^2 \overset{\mathbf{r}}{\circledast} |H_{\text{out}}|^2\right)(\Delta\mathbf{r}, \mathbf{r}_m). \tag{II.29}$$

where the symbol $\overset{\mathbf{r}}{\circledast}$ stands for a spatial convolution.

CMP intensity profile in the specular scattering regime In the specular scattering regime, the characteristic size l_γ of reflectors is much larger than the width of the focal spot δx ($l_\gamma \gg \delta x$). $\gamma(\mathbf{r})$ can thus be assumed as invariant over the input and output focal spots. Equation II.21 then becomes:

$$R(\mathbf{r}, \Delta\mathbf{r}) = \gamma(\mathbf{r}) \times \left(H_{\text{in}} \overset{\mathbf{r}}{\circledast} H_{\text{out}}\right)(\Delta\mathbf{r}). \tag{II.30}$$

The injection of Eq. II.30 into Eq. II.23 yields the following expression of the average CMP intensity profile:

$$I_{\text{av}}(\mathbf{r}, \Delta\mathbf{r}) = |\gamma(\mathbf{r})|^2 \times \left(\left|H_{\text{in}} \overset{\mathbf{r}}{\circledast} H_{\text{out}}\right|^2\right)(\Delta\mathbf{r}). \tag{II.31}$$

We observe that in the specular regime, I_{av} is directly proportional to the convolution between the coherent input and output PSFs, H_{in} and H_{out}.

In any case, the averaged CMP intensity profile $I_{\text{av}}(\mathbf{r}_m, \Delta\mathbf{r})$ is a direct indicator of the focusing quality at each point $\mathbf{r}_m$ of the medium as it measures the overlap between each virtual source and detector.

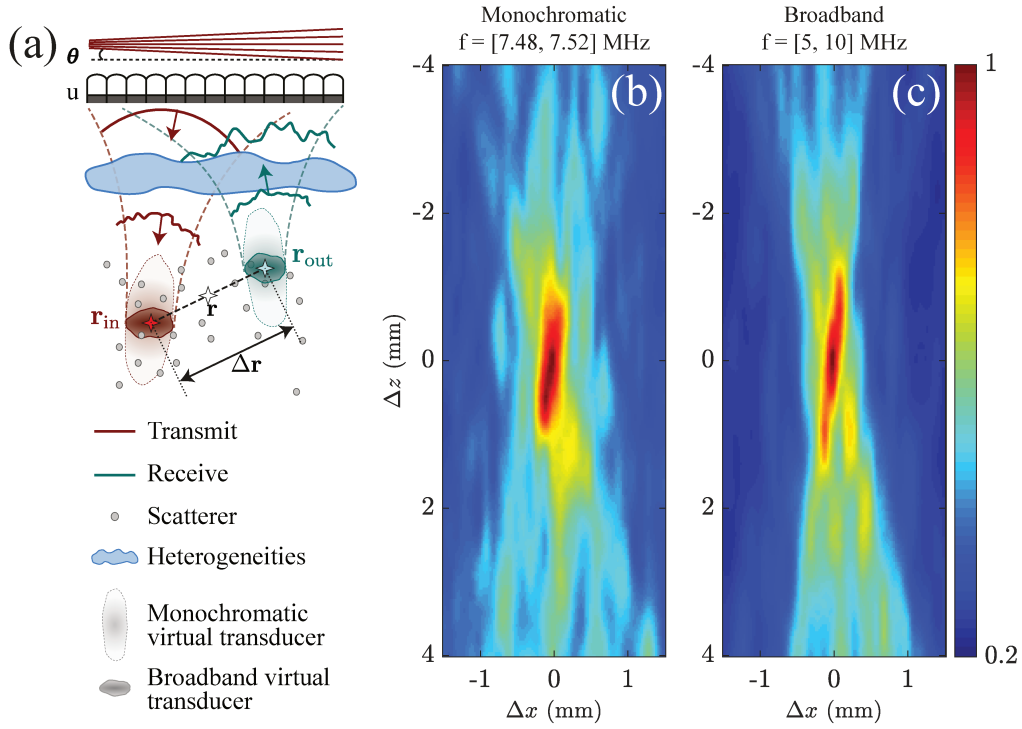

Fig. II.8 *Bi-dimensional common mid-point analysis* $I_{\text{av}}(\mathbf{r}, \Delta\mathbf{r})$ *measured in the calf experiment. (a) 2D matrix imaging consists in splitting the location of the transmit* ($\mathbf{r}_{in}$) *and receive focusing* ($\mathbf{r}_{out}$) *points both in the axial and transverse directions. (b,c) Monochromatic* ($f = 6$ *MHz) and broadband common mid-point intensity profile [Eq. II.23] averaged over a set of common mid-points* $\mathbf{r}$ *located at* $z = 18$ *mm. Both profiles have been normalized by their maximum.*

In absence of aberrations, we recall that the input and output PSFs can be expressed as:

$$H_{\text{in/out}}(\Delta x) = \text{sinc}(2\pi\Delta x \sin\beta/\lambda). \tag{II.32}$$

We finally denote w_x the transverse input-output resolution as the full width at half maximum along the x-direction:

$$w_x(\mathbf{r}) = \text{FWMH}\left[I_{\text{av}}(\mathbf{r}, \Delta x)\right] \tag{II.33}$$

In absence of aberration, w_x is roughly equal to δx_0. More description is provided below on the comparison between this experimental resolution and theoretical one to quantify locally the focusing quality.

Figure II.8(b) displays an example of CMP intensity profile. The corresponding cross-section of this profile at $\Delta z = 0$ is displayed in Fig. II.9(a). The latter one has been averaged over a set of common mid-points $\mathbf{r}$ located at depth $z = 18$ mm [white dashed line in Fig.II.7]. Similarly to the monochromatic input/output PSFs H_{in} and H_{out} (Eq. II.22), the incoherent input-output PSF $|H_{\text{in}}|^2 \overset{\mathbf{r}}{\circledast} |H_{\text{out}}|^2$ displays a cigar-like shape. However, while its axial FWHM w_z is close to the diffraction limit ($w_z \sim \delta z_0 \sim 2.2$ mm, with $\beta = 25$

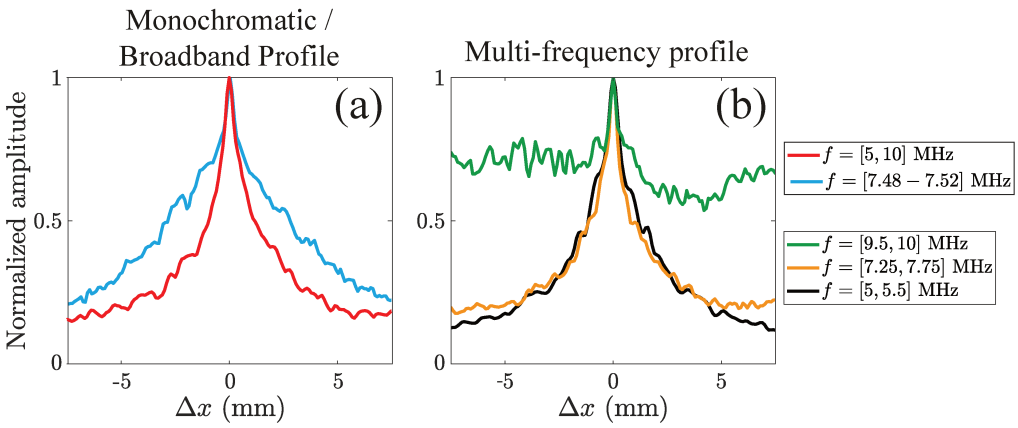

Fig. II.9 *1D-dimensional frequency dependent common mid-point analysis* $I_{av}(\mathbf{r}, \Delta x, f)$ *[Eq. II.23]. The profiles are measured in the calf and averaged over focal point located at* $z = 18$ *mm [White dashed lines Fig. II.7 and II.10] in the calf experiment. (a) Monochromatic and broadband regime. (c) Multi-frequency regime.*

deg), its transverse FWHM w_x is far from being ideal ($w_x \sim 1$ mm $>> \delta x_0 \sim 0.25$ mm). Two reasons can be invoked to explain this bad resolution. First, long-scale variations of the speed-of-sound give rise to aberrations that distort the input and output PSFs [40]. Second, out-of-focus reflectors can also enlarge the PSFs since the expansion of the input and output beams is larger out-of-focus that right at focus [Fig. II.8(a)]. Third, short-scale heterogeneity can induce multiple scattering events that give rise to an incoherent background in the common mid-point intensity profile [69]. Fourth, the electronic noise can also contribute to this incoherent background. Here, it can be discriminated from multiple scattering by investigating the spatial reciprocity of ultrasound signals, *i.e* the symmetry of $\mathbf{R_{rr}}$. This technique will be extensively studied in chapter 4. For the focused reflection matrix displayed in Fig. II.7(a_2), this symmetry degree is close to 50% for off-diagonal coefficients. Therefore, the incoherent background of -14 dB in Fig. II.9(a_3) contains multiple scattering and electronic noise in equal proportion. Nevertheless, note that, in a monochromatic regime, aberrations and multiple scattering effects can be hardly discriminated from the singly-scattered echoes taking place out-of-focus. To reduce the latter contribution and improve the axial resolution of the ultrasound image, a time-gating operation is required.

II.2.2 Broadband focused reflection matrix

Under the matrix formalism, the time gating operation can be performed by building a broadband focused reflection matrix. Besides improving the axial resolution and contrast of the ultrasound image, this broadband matrix is shown to exhibit a reduced and flat multiple scattering background, thereby allowing a clear distinction between the single and multiple scattering contributions.

In the frequency domain, each focused reflection (FR) matrix is built by dephasing each RF signal in order to make scattering paths going through both input and output

focal spots constructively interfere [Eq. II.15]. A coherent sum over the overall bandwidth Δf can then be performed to build a broadband focused reflection matrix:

$$\overline{\mathbf{R}}_{\mathbf{rr}}(\Delta f) = \int_{f_-}^{f_+} df\ \mathbf{R}_{\mathrm{rr}}(f). \tag{II.34}$$

with $f_\pm = f_c \pm \Delta f/2$ and f_c the central frequency of the RF signal bandwidth. In our experiment, $f_c = 7.5$ MHz and $\Delta f = 5$ MHz. One row of the broadband FR matrix corresponds to the situation where the transmit focusing is set to deposit energy at $\mathbf{r}_{\mathrm{in}}$ while the virtual detector probes the spatial spreading of this incident waves across the focal plane at the same time ($t = 0$ in the focused basis) [Fig. II.5].

On the contrary, the second matrix is built from the combination of all frequencies. While, we describe a temporal frequency-domain beamforming, this broadband FR matrix can be built based on a time-domain beamforming. To this aim, we simply adapt the focusing law used in conventional plane wave imaging [Eq. I.26]:

$$\tau(u_{\mathrm{out}}, \theta_{\mathrm{in}}, \mathbf{r}_{\mathrm{out}}, \mathbf{r}_{\mathrm{in}}) = \underbrace{\frac{x_{\mathrm{in}}\sin(\theta_{in}) + z_{\mathrm{in}}\cos(\theta_{\mathrm{in}})}{c_0}}_{=\ \tau_{\mathrm{in}}(\theta_{\mathrm{in}},\mathbf{r}_{\mathrm{in}})} + \underbrace{\frac{\sqrt{(x_{\mathrm{out}}-u_{\mathrm{out}})^2 + z_{\mathrm{out}}^2}}{c_0}}_{=\ \tau_{\mathrm{out}}(u_{\mathrm{out}},\mathbf{r}_{\mathrm{out}})}. \tag{II.35}$$

The broadband focused reflection matrix finally results from the transmitted and received beamforming.

By summing the monochromatic FR matrix over the whole frequency bandwidth, the axial resolution of the virtual transducers should be drastically improved [Fig. II.5]. To prove this assertion, one can express theoretically the broadband FR matrix. For sake of simplicity and analytical tractability, the par-axial and isoplanatic approximations are made. It consists in decomposing the monochromatic PSFs as follows:

$$H_{\mathrm{in/out}}(\mathbf{r}, \mathbf{r}', f) = \overline{H}_{\mathrm{in/out}}(\mathbf{r} - \mathbf{r}', f) e^{j2\pi f(z-z')/c} \tag{II.36}$$

where $\overline{H}_{\mathrm{in/out}}$ represents the envelope of the PSF. Injecting Eqs. II.21 and II.36 into Eq. II.34 leads to the following expression for the coefficients of $\mathbf{R}_{\mathrm{rr}}(\Delta f)$ (see Appendix II.C):

$$\begin{aligned}\overline{R}(\mathbf{r}_{\mathrm{out}}, \mathbf{r}_{\mathrm{in}}, \Delta f) = {} & e^{j2\pi f_c(2z - z_{\mathrm{in}} - z_{\mathrm{out}})/c} \\ & \int d\mathbf{r}\ \mathrm{sinc}\left(\frac{\pi\Delta f}{c}(2z - z_{\mathrm{in}} - z_{\mathrm{out}})\right)\ \overline{H}_{\mathrm{out}}(\mathbf{r} - \mathbf{r}_{\mathrm{out}})\ \gamma(\mathbf{r})\ \overline{H}_{\mathrm{in}}(\mathbf{r} - \mathbf{r}_{\mathrm{in}}).\end{aligned} \tag{II.37}$$

where we have assumed, in first approximation, that $\overline{H}_{\mathrm{in/out}}$ is constant over the frequency bandwidth. The occurrence of the sinc factor in the integrand of the last equation shows that, in the broadband regime, the axial resolution $\overline{\delta z}_0$ is dictated by the frequency bandwidth, such that

$$\overline{\delta z}_0 \sim \frac{c}{2\Delta f}. \tag{II.38}$$

This gain in axial resolution is clearly visible on the ultrasound image $\overline{\mathcal{I}}(\mathbf{r}, \Delta f)$ built from the diagonal of $\overline{\mathbf{R}}_{\mathbf{rr}}(\Delta f)$ (Eq. II.16). While the original monochromatic images II.6(a_1) and II.7(a_1) display an elongated speckle grain, the coherent sum of Eq. II.34 drastically improves the axial resolution and the contrast of the image [Fig. II.6(a_2) and II.7(a_2)]. In the calf experiment, the whole micro-architecture of the muscle is revealed.

Figures II.6(b_2) and II.7(b_2) show the section $\overline{\mathbf{R}}_{xx}(\Delta f, z)$ of the broadband FR matrix $\overline{\mathbf{R}}_{\mathbf{rr}}(\Delta f)$ at depth $z = 25$ mm and $z = 18$ mm, in the phantom and calf experiment, respectively [dotted white line on corresponding US image]. Compared to its monochromatic counterpart [Fig. (a2)], the single scattering contribution along the diagonal of $\overline{\mathbf{R}}_{\mathbf{rr}}$ is enhanced compared to the off-diagonal coefficients. The coherent sum of FR matrices over the whole frequency bandwidth provides an optimized time-gating to select back-scattered echoes generated by scatterers located at the chosen depth. The contribution of reflectors that sit ahead and back of the focal plane is eliminated. The singly-scattered echoes are now concentrated in the vicinity of the diagonal of $\overline{\mathbf{R}}_{\mathbf{rr}}$. Note that, similarly, the multiply-scattered echoes whose time-of-flight differs from the ballistic time are also removed in the same proportion. The single-to-multiple scattering ratio is thus preserved through the time-gating operation. We observe that the ratio between the intensity of confocal signals compared to the intensity of off-diagonal signals seems to be lower in the calf experiment. It suggests that the single-to-multiple scattering ratio is lower in this case. This observation is not surprising, as the calf is composed of many echogenic scattering structures that can generate multiple scattering events. A quantitative method is proposed in chapter 4 to measure this ratio [Par. IV.2].

The transverse resolution improvement is also highlighted by the bi-dimensional broadband CMP intensity profile displayed in figure. II.8(c). The blue curve of figure II.9 shows its transverse cross-section. Compared to the monochromatic regime [Fig. II.8(b) and II.9 red curve], it now shows a clear feature: a confocal, steep peak on top of a flat multiple scattering background. Surprisingly, although we are in a broadband regime, the 2D focal spot in Fig. II.8(c) still exhibits a cigar-like shape. To understand the reason for this observation, the broadband CMP intensity profile can be expressed using the paraxial approximation [Eq. II.36], see Appendix II.C.

$$\overline{I}_{\rm av}(\mathbf{r}, \Delta\mathbf{r}) = C \int df \left[|\overline{H}_{\rm in}|^2 \overset{\Delta\mathbf{r}}{\circledast} |\overline{H}_{\rm out}|^2 \right] (\Delta\mathbf{r}, f). \tag{II.39}$$

with C a constant. In the broadband regime, the CMP intensity profile corresponds to the sum over the frequency bandwidth of the incoherent input-output PSF $|\overline{H}_{\rm in}|^2 \overset{\Delta\mathbf{r}}{\circledast} |\overline{H}_{\rm out}|^2$. This explains why it does not exhibit the time-gating process undergone by the broadband FR matrix (Eq. II.37). Nevertheless, the broadband CMP intensity profile remains a relevant observable to estimate the transverse resolution of an imaging PSF averaged over the frequency bandwidth. Similarly to the monochromatic study, the full width at maximum height (FWMH) of $\overline{I}_{\rm av}(\mathbf{r}, \Delta\mathbf{r})$ is denoted as the broadband transverse input-output resolution $\overline{w}_x(\mathbf{r})$. On the focused reflection matrix $\mathbf{R}_{\rm xx}(z)$, we can see that $w_x(\mathbf{r})$ probes the average spatial extension of the halo of single-scattered signals along the anti-diagonals of this matrix [Fig. II.6(b_2) and II.7(b_2)]. The red curve of figure II.9(a) shows $\overline{I}_{\rm av}(\mathbf{r}, \Delta\mathbf{r})$ measured in the calf experiment and laterally averaged over common-midpoints located at $z = 18$ mm. It shows that the input-output resolution, and thus the image resolution is far from being optimal: $\overline{w}_x(\Delta f) \sim 0.5$ mm $\gg \delta x_0(f_c) \sim 0.25$ mm. It suggests that the assumed speed of sound model does not exactly match the medium speed of sound, which decreases the focusing quality.

In paragraph II.2.4, we will define a quantitative parameter to assess the focusing quality at any pixel of the ultrasound image. This observable will consider the broadband

diffraction-limited resolution $\overline{\delta x}_0(\Delta f)$ as a reference. To make our measurement quantitative, the theoretical prediction of $\overline{\delta x}_0(\Delta f)$ should be as accurate as possible. To that aim, a time-frequency analysis of the focused reflection matrix should be performed. This is the aim of the next section.

Lastly, we described the monochromatic and broadband focused reflection matrix. While the first one contains a frequency dependent information on the back-scattered signals, it is characterized by a very poor axial resolution that limits its use. On the contrary, the second matrix is built from the combination of all frequencies to improve the axial resolution. An in-between configuration is studied in the following paragraph.

II.2.3 Time-frequency analysis of the focused reflection matrix

A time-frequency analysis of the focused reflection matrix is required to investigate the evolution of absorption and scattering as a function of frequency. To do so, the coherent sum of the monochromatic FR matrices [Eq. II.34] is performed over a sub-frequency band, centered on a given frequency f and characterized by a smaller bandwidth δf:

$$\overline{\mathbf{R}}_{\mathbf{rr}}(f,\delta f) = \int_{f-\delta f/2}^{f+\delta f/2} df\ \mathbf{R}_{\mathrm{rr}}(f) \tag{II.40}$$

As derived in Eq.II.38, the axial dimension $\overline{\delta z}_0$ of the virtual transducers is inversely proportional to the frequency bandwidth δf. A compromise has thus to be made between the spectral and axial resolutions. Here, the following choice has been made: $\delta f = 0.5$ MHz and $\overline{\delta z}_0 = 3$ mm.

Figures II.10(a1,b1,b1) show the ultrasound images associated with the calf experiment, over three different frequency bandwidths: $5-5.5$ MHz, $7.25-7.75$ MHz, $9.5-10$ MHz. The axial resolution in each ultrasound image is of course deteriorated compared to the broadband image [Figure II.7(b1)]. Yet, the time-frequency analysis of the FR matrices yields the evolution of the SNR versus depth and frequency. At $z = 18$ mm, for instance, the FR matrix at $f = 9.75MHz$ exhibits a tiny confocal enhancement on top of a predominant noise background (SNR$\sim$3dB). On the contrary, the FR matrices at $f = 5.25$ and 7.5 MHz exhibit a CMP intensity profile close to its broadband counterpart. This weak SNR at 9.75 MHz can be partially explained by the finite bandwidth of the transducers ($5-10$ MHz). However, absorption losses undergone by ultrasonic waves in soft tissues have also a strong impact on the ultrasound image. Figure II.10(d) illustrates the effect of absorption by displaying the normalized spectrum of the confocal signal, $\left\langle \overline{\mathcal{I}}(\mathbf{r},f)\right\rangle_x$, as a function of depth. This spectrum is shown to shift towards low frequencies as a function of depth. This frequency shift is characteristic of absorption losses, the attenuation coefficient exhibiting a linear dependence with frequency in soft tissues [14].

Beyond absorption, the time-frequency analysis of the FR matrix also shows that the ultrasound image $\overline{\mathcal{I}}(\mathbf{r},f,\delta f)$ can fluctuate as a function of frequency. For instance, while a bright scatterer [white arrow in Figure II.10(b1)] is clearly visible in the broadband or low frequency FR matrix around $x = 12.5$ mm and $z = 18$ mm, its presence is not revealed by the FR matrices at higher frequencies. A time-frequency analysis can thus be of interest for characterization purposes: The frequency response of bright scatterers can indeed reveal their size and nature.

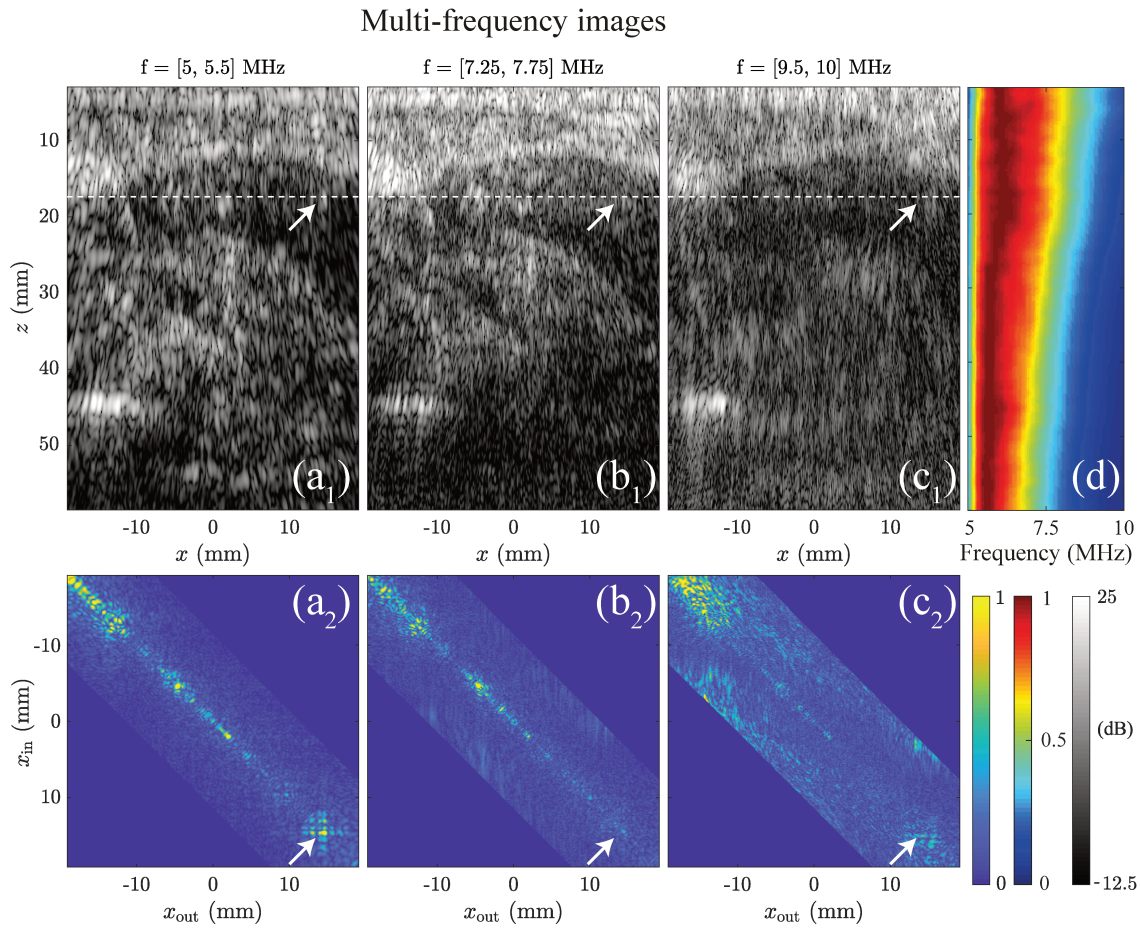

Fig. II.10 *(a,b,c) Ultrasound images and focused reflection matrices computed in the multi-frequency regime ($5-5.5$ MHz, $7.25-7.75$ MHz, $9.5-10$ MHz), respectively. (d) Spectrogram of the confocal signals versus depth z extracted from the diagonal elements of $\mathbf{R}_{xx}(z)$ (linear scale). The confocal spectrum is normalized by its maximum at each depth.*

In this short paragraph we introduce an in-between situation, which consists in a time-frequency analysis of the reflection matrix. Whether it is due to absorption or scattering, the frequency spectrum variation of backscattered echoes has a strong impact on the local resolution at any pixel of the ultrasound images.

In the next section, we show how to predict it precisely in order to establish a quantitative focusing parameter from the CMP intensity profile.

II.2.4 The local focusing criterion

Aberrations caused by the medium heterogeneities degrade the resolution of the ultrasound image and induce a spreading of singly-scattered echoes over the off-diagonal coefficients of $\overline{\mathbf{R}}_{\mathbf{rr}}$. In the speckle regime, it is difficult to detect at first sight if the image is aberrated, and if it is, which areas are the most impacted. Interestingly, the transverse

width $\overline{w}_x$ of the CMP intensity profile can yield an unambiguous answer. In the speckle regime, the CMP intensity profile actually yields the convolution between the incoherent input-output PSF averaged over the frequency bandwidth (Eq. II.39). Admittedly, this PSF is not equal to the confocal imaging PSF, $\left(\overline{H}_{\text{in}}\overline{H}_{\text{out}}\right)(\Delta\mathbf{r})$ (Eq. II.37). Nevertheless, the incoherent input-output PSF fully captures the impact of transverse aberrations. It thus constitutes a relevant observable for assessing the focusing quality.

The width δx of the imaging PSFs is dictated by two distinct phenomena, namely diffraction and aberration. In the ideal case (*i.e* no aberrations), the image resolution δx is only impacted by diffraction and, more precisely, dictated by the angular aperture $\beta(\mathbf{r})$ (Eq. II.22). The latter one tends to decrease with depth and on the edge of the image. In presence of aberrations, diffraction and wave-front distortions both alter the imaging PSF. In order to provide an indicator that is only sensitive to aberrations, the estimator $\overline{w}_x$ of the image resolution should be compared to its ideal value $\overline{w}_0(\mathbf{r})$ computed at each focal point. We then defined a local focusing criterion $F(\mathbf{r})$ as:

$$F(\mathbf{r}) = \overline{w}_0(\mathbf{r})/\overline{w}_x(\mathbf{r}). \tag{II.41}$$

To estimate this parameter, the major challenge lies in the determination of the ideal resolution $\overline{w}_0(\mathbf{r})$ for broadband signals. Two techniques have been developed that both take into account the frequency spectrum of the ultrasound image. For each point $\mathbf{r}$, $\mathcal{I}(\mathbf{r}, f)$ is an estimation of the frequency spectrum of echoes generated by each focal point and measured by the probe [Fig. II.10(d)].

II.2.4.1 Construction of the focusing criterion

The first technique consists in an extension of equation II.22, which rules the transverse resolution of monochromatic focused beam to the case of broadband signals. To that aim, $\mathcal{I}(\mathbf{r}, f)$ is used as a weighting factor. The expected lateral resolution is then given by:

$$\overline{\delta x}_0(\mathbf{r})^{(1)} = \left\langle W_L(\mathbf{r}' - \mathbf{r}) \frac{\int_{f_-}^{f_+} df\ \mathcal{I}(\mathbf{r}', f)\ \delta x_0(f, \mathbf{r}')}{\int_{f_-}^{f_+} df\ \mathcal{I}(\mathbf{r}', f)} \right\rangle_{\mathbf{r}'}. \tag{II.42}$$

By using $\overline{\delta x}_0$ as an estimation of $\overline{w}_0(\mathbf{r})$, the focusing criterion, $F^{(1)}(\mathbf{r})$, can be computed from equation II.41. Figure II.11(b) displays this first focusing criterion superimposed to the US image in a phantom experiment without aberration. We observe that $F^{(1)}$ is close to 1 and relatively constant over the entire field of view. Its average and standard deviation are $\langle F^{(1)} \rangle = 0.84 \pm 0.09$, which confirms that the assumed speed of sound model accurately describes the medium speed of sound. Nonetheless, this criterion is slightly lower than one, and we can see some edge effects due to the diffraction phenomena that are not perfectly well modeled. If no aberration appears in this experiment, meaning that $\overline{w}_x$ is the optimal input-output experimental resolution, therefore, the ideal resolution $\overline{\delta x}_0(\mathbf{r})^{(1)}$ is overestimated (meaning smaller length). Two phenomena can account for these observations. First the broadband aspect of the backscattered echoes is simply taken into account via $\mathcal{I}(\mathbf{r}, f)$. This method does not separate singly-scattered echoes from noise and multiply-scattered echoes. The signal-to-noise ratio decreases with frequency due to attenuation (See the spectrogram of the calf experiment [Fig .II.10(d)]). Therefore,

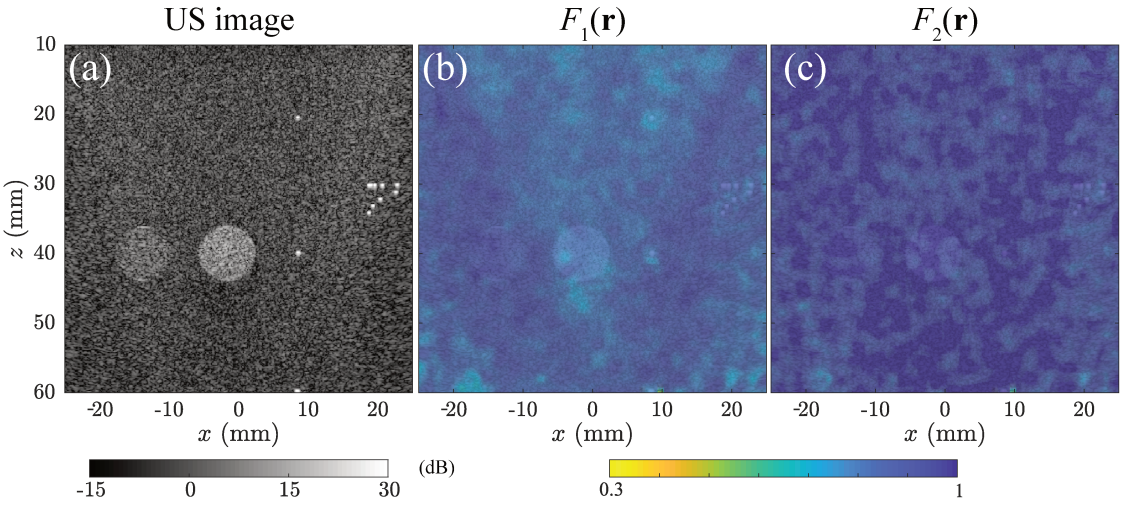

Fig. II.11 *Impact of the expected lateral resolution on the focusing criterion in a phantom experiment without aberrations. (a) US image. (b) Focusing criterion based on* $\overline{\delta x}_0^{(1)}(\mathbf{r})$ *[Eq. II.42], the barycenter of monochromatic lateral resolution. (b) Focusing criterion obtained from a simulation of the FR matrix.*

this measurement can consider some high frequency noise as relevant signals, leading to an improvement of the ideal resolution. Second, $\overline{\delta x}_0(\mathbf{r})^{(1)}$ characterizes the image resolution (product of the broadband input and output PSFs), while $\overline{w}_x(\mathbf{r})$ characterizes the spatial extension of the CMP intensity profile (linked to the spatial convolution of the two incoherent PSF). Their nature is thus slightly different which can lead to some residual discrepancy.

To overcome these limitations, we propose a second technique that consists in measuring the input-output resolution of a simulated broadband focused reflection matrix $\overline{\mathbf{R}}^0_{\mathrm{xx}}(z)$. Two assumptions are made for this simulation. First, the wave propagation is perfectly described by the free space propagation matrices, meaning that there is no aberration during the beamforming process, leading to $\mathbf{P} = \mathbf{P}_0$ and $\mathbf{G} = \mathbf{G}_0$. Second, only single scattering process occurs in the simulation. It enables to define a scattering matrix $\mathbf{\Gamma}^0(z, f)$ that is diagonal and whose elements corresponds to a simulated medium reflectivity $\gamma_0(\mathbf{r}, f)$ (more details are provided below). Based on equation II.17, a simulated reflection matrix can be computed as:

$$\mathbf{R}^0_{\mathrm{u}\theta} = \mathbf{G}_0^{\top}(f) \times \mathbf{\Gamma}^0(f) \times \mathbf{P}_0(f). \tag{II.43}$$

This matrix simulates the Fourier transform of the experimentally acquired reflection matrix $\mathbf{R}_{u\theta}(f)$. By means of this matrix, a transmitted and received beamforming is performed exactly as described above [Eq. II.18 and II.34], leading to the simulated broadband focused reflection matrix $\overline{\mathbf{R}}^0_{\mathrm{xx}}(z)$. Finally, the ideal input-output resolution $\overline{w}_0(\mathbf{r})^{(2)}$ is computed from the FWMH of its averaged CMP intensity profile [Par. II.2.2]. It is used to compute the focusing criterion $F^{(2)}(\mathbf{r})$.

At last, the simulated medium reflectivity $\gamma_0(\mathbf{r}, f)$ needs to be defined. As stated above, the frequency content of the back-scattered signals needs to be taken into account.

Once again, we build this reflectivity upon $\mathcal{I}(\mathbf{r}, f)$. In addition, we demonstrated in paragraph II.2.1.1 that the theoretical expression of the CMP intensity profiles relies on the nature of the medium reflectivity, speckle or specular regime. To that aim, we distinguish the two regimes:

The specular regime In this regime, the medium reflectivity varies slowly compared to the characteristic sizes of the input and output PSF ($l_\gamma \gg \delta x$). Therefore, the frequency-dependent confocal signals constitute an accurate estimation of the medium reflectivity and

$$\gamma_0(\mathbf{r}, f) = \frac{\mathcal{I}(\mathbf{r}, f)}{\int_{f_-}^{f_+} df\ \mathcal{I}(\mathbf{r}, f)}. \tag{II.44}$$

The speckle regime In this regime, the random reflectivity of the medium is not captured by the frequency dependent ultrasound images (due to the spatial extension of the product of the two PSFs). To simulate this behavior, the amplitude of the ultrasound image is modulated by a random term $\xi(\mathbf{r}, f)$. Its modulus is defined by the normal probability distribution and its phase by the uniform distribution on the interval $[0, 2\pi]$. The medium reflectivity is thus given by:

$$\gamma_0(\mathbf{r}, f) = \frac{\mathcal{I}(\mathbf{r}, f)}{\int_{f_-}^{f_+} df\ \mathcal{I}(\mathbf{r}, f)}\ \xi(\mathbf{r}, f). \tag{II.45}$$

Figure II.11(c) displays the second focusing criterion $F^{(2)}$ superimposed to the US image in a phantom experiment without aberration. We observe that compared to $F^{(1)}$, its mean value is closer to one, $\langle F^{(2)} \rangle = 0.96 \pm 0.10$, meaning that $F^{(2)}$ perfectly characterizes the absence of aberration in this experiment. In addition, no longer long-scale fluctuations are observed, meaning that the diffraction phenomena are perfectly modeled. However, to achieve this result, the computational cost is heavy. Indeed it requires to fully simulate back-scattered echoes based on an ideal propagation model. The relevance of this method is thus discussed after the analysis of an *in-vivo* example.

Figure II.12 displays the first focusing criterion $F^{(1)}(\mathbf{r})$ superimposed to the conventional B-mode image of the human calf. The extension of the spatial window L has been set to $7\lambda_c$, with $\lambda_c \approx 0.21$ mm, the central wavelength defined at $f_c = 7.5$ MHz. While high values of F ($F \sim 1$, blue areas testify of a good image quality, low values of F ($F < 0.3$, yellow areas) indicate a poor quality of focus and gray areas point out areas associated with a low SNR. Those areas seem to be blurred on the ultrasound image [Fig. II.12a]. Indeed, these areas correspond to the situation where the estimation of the image resolution has failed, meaning that there is no intensity enhancement of the close-diagonal coefficients in $\mathbf{R}_{xx}(z, \Delta f)$. Two complementary reasons can explain this behavior. Either the single scattering contribution is drowned into a much predominant background noise (caused by multiple scattering process and electronic noise), or the aberrations are so intense that the confocal spot spreads over an extended imaging PSF, thereby pushing the single scattering intensity at focus below the noise level. Not surprisingly this situation appears at large depth and in areas where the medium reflectivity is weak. In any case, parts of the ultrasound image associated with these areas should be carefully interpreted in case of a medical diagnosis.

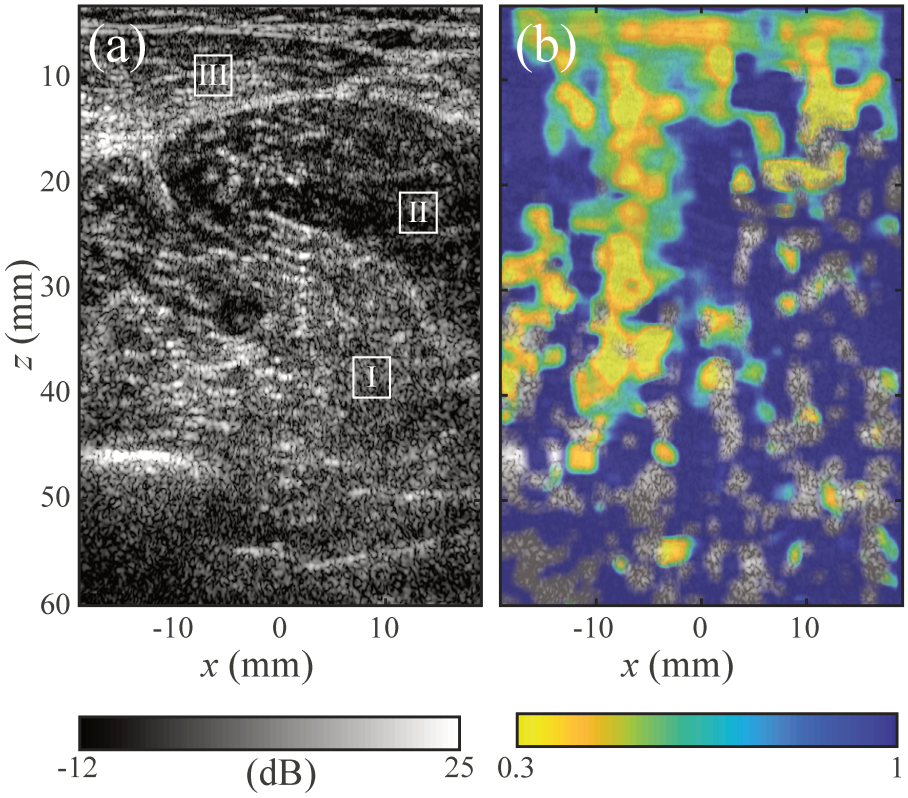

Fig. II.12 *(a) US image of the calf. (b) Focusing criterion F. Blue and yellow areas correspond to a high and low quality of focus respectively. Gray areas highlight location where the estimation of the focusing criterion have failed, implying a very low quality of focus and/or a low SNR.*

Figure II.12(b) reveals a poor focusing quality at shallow depth that can be due to a mismatch between the skin speed of sound $c_{skin} \approx 1500 - 1700$ m/s and the assumed one. The ultrasound image shows different structures that are associated with their own speed of sound: (i) muscles tissues with three different fiber orientations (areas I, II, III on figure II.12a); (ii) two Veins located at $x, z = 12,5$ mm and $-5,33$ mm; (iii) the fibula, located on the bottom left of the figure $-12,45$ mm. However, finding the link between quality of focus provided by the focusing criterion and the spatial distribution of the medium speed of sound is a difficult task that is beyond the scope of the present analysis.

Finally, we observe that the slight errors induced by the diffraction effect initially observed in the phantom experiment are completely masked in the focusing criterion map of the calf experiment, due to the prevalence of aberrations. Therefore, the choice of using $F^{(1)}$ or $F^{(2)}$ should be determined by the pros and cons of each method according to the available computation time and the current objective. In the following, we will indicate when one technique is more suitable to the other.

II.2.4.2 The focusing criterion, a robust and local indicator of the image quality

The results presented above provide new insights in the construction of the focused reflection matrix and the focusing criterion based on the *in-vivo* example of human calf imaging. This medium is representative of *in-vivo* ultrasound imaging where the medium under investigation is heterogeneous and composed by different kinds of tissues. It includes both highly and weakly scattering areas, associated with unresolved scatterers and specular reflectors. In chapter 4 we use the parameter F as a virtual guide star for adaptive focusing techniques, as it is done in literature with the coherence factor C [62, 143, 144]. In chapter 3 we will use the local resolution of the image at each step of the matrix aberration correction process to monitor the improvement of the image quality.

Admittedly, $F(\mathbf{r})$ shows similarities with the coherence factor C [11, 145] but there is a main difference. On the one hand, the coherence factor C investigates the spatial coherence of the reflected wave-field based on the Van Cittert Zernike theorem. It enables to probe the incoherent input PSF $|\overline{H}_{\text{in/out}}|^2$. On the other hand, the focusing parameter F directly provides the incoherent input-output PSF $|\overline{H}_{\text{in}}|^2 \circledast |\overline{H}_{\text{out}}|^2$. The latter parameter is thus more sensitive to aberrations since it accumulates in one shot the wave-distortions undergone by the incident and reflected waves. A second advantage of the $F-$parameter lies in its spatial resolution. The resolution of the F and C-maps are actually dictated by the PSF of the corresponding ultrasound images. While the F-parameter relies on a confocal image, whose PSF scales as $\overline{H}_{\text{in}} \times \overline{H}_{\text{out}}$, the $C-$map is based on a single-sided focused image of PSF $\overline{H}_{\text{in}}$. The $F-$parameter thus benefits from a confocal gain in terms of resolution. Depending on the nature of the PSF, this gain can vary between 1 (window PSF) and 2.

Last but not least, the parameter F enables a local measurement of the focusing quality almost independent of the local reflectivity. This property results from the choice of analyzing the backscattered intensity between couples of virtual transducers sharing the same common mid-point [Fig. II.13(b1,b2)]. Indeed, for various distance $\Delta x = x_{\text{out}} - x_{\text{in}}$, signals along a given CMP profile results from the combination of echoes generated by roughly the same scatterers (yellow scatterer on the sketches). Differently the $C-$factor investigates the pressure field generated by a single virtual source that results from a focused insonification. This pressure field corresponds to the realigned signal associated with $\breve{R}(u_{\text{out}}, \mathbf{r}_{\text{in}}, \mathbf{r}_{\text{in}}, \Delta\tau = 0)$ [Eq. I.9]. While the initial method probes the spatial correlation in the transducer basis, this signal can be analyzed in the focused basis. In this case it corresponds to one row of the focused reflection matrix (associated with $\mathbf{r}_{\text{in}}$), *i.e.* a virtual detector probing the energy around a fixed input focusing point $\mathbf{r}_{\text{in}}$ [Fig. II.13(c1,c2)]. For various distance Δx the signals associated with the same row does not result from the exact same scatterers. To compare the two approaches, we then measure $v_x(\mathbf{r})$ the FWMH of each row. Figure II.13(b3,c3) show the map of $w_x(\mathbf{r})$ (CMP) and $v_x(\mathbf{r})$ associated with a phantom experiment. The US image is displayed on figure II.13(a). For each parameter, the corresponding intensity profiles have been averaged over a spatial window W_L of size $L = \lambda_c = 0.21$ mm (Eq. II.26). This tiny window is chosen to reveal the fluctuations of $v_x(\mathbf{r})$ and $w_x(\mathbf{r})$ with respect to the local reflectivity. Both quantities exhibit a similar averaged value of 0.31 mm close to the diffraction-limited resolution $\overline{\delta x}_0$. However, their standard deviation σ is pretty different: $\sigma_v = 0.16$ mm vs $\sigma_w = 0.14$ mm.

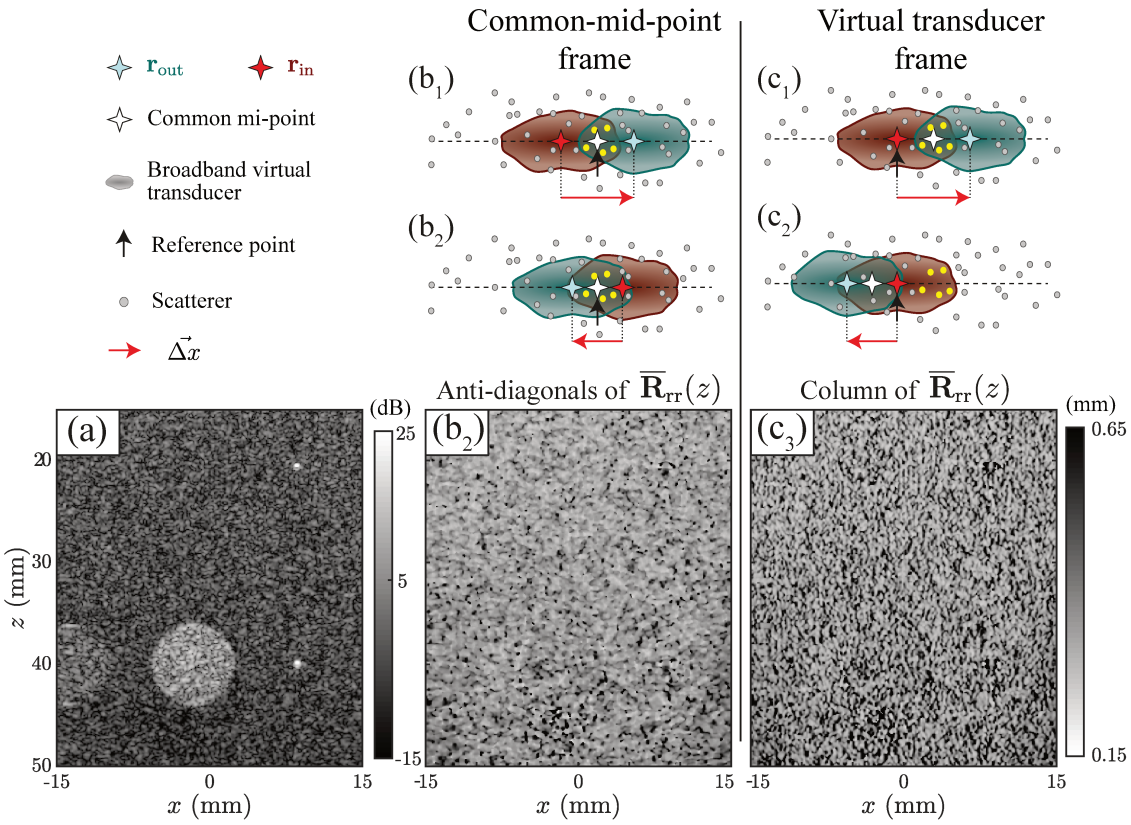

Fig. II.13 *Comparison between the input-output PSF extracted from (b) the anti-diagonals and (c) the rows of the FR matrix using an experiment on a tissue-mimicking phantom. (a) US image of the phantom. (1,2) Sketches of the experiment for two distances* $\Delta x = x_{out} - x_{in}$. *(b,c) Maps of* $w_x(\mathbf{r})$ *and* $v_x(\mathbf{r})$, *the widths of the PSF extracted from the anti-diagonals and rows of* $\mathbf{R}_{xx}(z)$, *respectively.*

Although this difference seems subtle, it is nonetheless visible on the two maps displayed in Figures II.13(b-c). The map of $v_x(\mathbf{r})$ is clearly modulated by the speckle pattern of the ultrasound image. On the contrary, $w_x(\mathbf{r})$ exhibits a relatively constant value almost independent from the sample reflectivity.

II.2.5 Conclusion

In this section, we developed the concept of focused reflection matrix which contains the medium responses between virtual transducers located within the medium. We have shown that this matrix provides a wealth of information on the medium that goes well beyond a single confocal image. By splitting the location of the transmit and receive focal spots, the local resolution of the ultrasound image can be assessed at any pixel. By performing a time-frequency analysis of the reflection matrix, the contributions of single and multiple scattering and their impact on the resolution and contrast are carefully

investigated. This time-frequency study of the focused reflection matrix paves the way towards a quantitative characterization. Some promising routes are studied in chapter 4 for the quantification of the medium attenuation or the characterization of the nature of the scatterer. In chapter 3, the broadband focused reflection will be used as the first building block of matrix imaging for a local aberration correction. Related to this issue, a focusing criterion has been defined from the focused reflection matrix in order to quantify locally the impact of aberrations on each pixel of the ultrasound image. Compared to the coherence factor generally used in the literature [11, 145], our focusing parameter is shown to be more sensitive since it gathers the aberrations undergone by both the incident and reflected waves during their travel through the medium. The spatial resolution of its mapping is also better because of the confocal gain provided by the focused reflection matrix. This focusing parameter will be used in chapter 4 as a figure of merit for the estimation of the medium speed of sound.

Finally, in this section we analyzed the reflection matrix in a focal basis at the focal time, *i.e.* at the required time for an incident wave to travel from the probe to the virtual source and for a back-scattered wave generated at the virtual sensor to come back to the probe.

II.3 The time-focused reflection matrix

This content is confidential – please contact the author for more information.

Conclusion

This chapter is dedicated to a matrix analysis of the ultrasound reflection matrix that contains all the available information on the medium. This matrix corresponds to the inter-element impulse matrix of the entire system. It links any input signals *i.e.* insonifications to any output one *i.e.* measured signals. Based on the linearity and reciprocity of the wave propagation, this matrix approach uses matrix operation to extract information on the medium.

We first review some of the major milestones that have contributed to the success of this approach. We observed that the first techniques, *i.e.* time-reversal method and the DORT method, directly analyze the reflection matrix in the transducer basis $\mathbf{R}_{\mathrm{uu}}$. These techniques enable to learn how to focus inside a complex and sparse medium without any *a priori* information. Based on a speed of sound hypothesis and on the useful concept of virtual source, a more recent work produced by Robert and Fink [61] investigates the reflection matrix in a dual basis $\mathbf{R}_{\mathrm{ur}}$. This matrix contains the medium responses generated by virtual sources embedded within the medium and measured by the probe transducer. The author has demonstrated that the analysis of this matrix enables to measure and correct for receive aberrations. While this matrix is acquired from focused insonification, we extend this analysis in chapter 3.

We then illustrated how all the current insonification sequences *i.e.* plane waves, diverging waves and converging waves, can be described via a common matrix formalism as various input bases of the reflection matrix. In this case, the beamforming process constitutes a change of basis between a far-field basis and a focused basis made of vir-

tual transducers located within the medium. This analogy leads to the focused reflection matrix that contains the medium responses between arrays of virtual sources and sensors at the focusing time, meaning at the time where the incident wave is set to be located around its focal point. We first performed a frequency-dependent analysis of this matrix, which enables to quantify locally the frequency content of echoes generated by each multi-frequency resolution cell. In chapter 4 we build upon this analysis to point out promising perspectives for characterization of the scatterer and the estimation of the medium attenuation. We then turned our attention to the broadband focused reflection matrix $\overline{\mathbf{R}}_{\mathrm{rr}}$ and introduced the concept of common-mid-point frame. This configuration is used to provide a local measurement of the medium input-output resolution that is independent of the medium reflectivity. By comparing this local resolution with an ideal one, we built the focusing criterion that is able to probe the focusing quality of the ultrasound image. This new indicator will be used in chapter 3 to quantify the benefits of a new aberration correction technique and in chapter 4, as a figure of merit for the determination of the medium speed of sound.

Finally, we studied the time focused reflection matrix $\overline{\mathbf{R}}_{\mathrm{rr}}(\Delta\tau)$, which contains the temporal responses of the medium between arrays of virtual transducers. This matrix enables to study the reflection matrix outside the particular ballistic time (associated with the US image) and focusing time (associated with the broadband focused reflection matrix). In particular, we first studied this matrix in the virtual source frame, or virtual sensor frame and demonstrated experimentally that the ultrasound image results from a numerical time-reversal experiment. We then investigated the wave-front frame and the wave-front matrix $\mathbf{R}_{\mathrm{w}}$ that fully described the pressure field generated by a given virtual source and seen from the probe. $\mathbf{R}_{\mathrm{w}}$ will be extensively used in chapter 4 for the medium characterization. Finally, we pointed out that the time-focused reflection matrix is able to describe conventional beamforming technique through a matrix approach.

In this chapter we introduced the time focused reflection matrix that is able to describe all focusing imaging technique via a common matrix formalism. In the following chapter, we will use this matrix (or the focused reflection matrix) as a first building block for aberration correction (chapter 3) and multiple characterization technique (chapter 4).

Appendices

II.A Experimental acquisitions

Phantom experiment: The acquisitions were performed using a medical ultrafast ultrasound scanner (Aixplorer, Supersonic Imagine, Aix-en-Provence, France) driving a $4-15$ MHz array composed of 256 transducer elements with a pitch $p = 0.2$ (SL15-4, Supersonic Imagine). The ultrasound sequence consists in transmitting 41 steering angles spanning from -20^o to 20^o, according to a hypothesis on the tissue speed of sound $c_0 = 1540$ m/s [14]. The pulse repetition frequency is set at 1000 Hz. The emitted signal is a sinusoidal burst that lasts for three half periods of the central frequency $f_c = 7.5$ MHz. For each excitation, the back-scattered signal is recorded by the 192 transducers of the probe over a time length $\Delta\tau = 80$ μs at a sampling frequency $f_s = 30$ MHz.

Human calf experiment: The acquisition was performed using a medical ultrafast ultrasound scanner (Aixplorer Mach-30, Supersonic Imagine, Aix-en-Provence, France) driving a $5-18$ MHz array composed of 192 transducer elements with a pitch $p = 0.2$ (SL18-5, Supersonic Imagine). The ultrasound sequence consists in transmitting 101 steering angles spanning from -25^o to 25^o, according to a hypothesis on the tissue speed of sound $c_0 = 1580$ m/s [14]. The pulse repetition frequency is set at 1000 Hz. The emitted signal is a sinusoidal burst that lasts for three half periods of the central frequency $f_c = 7.5$ MHz. For each excitation, the back-scattered signal is recorded by the 192 transducers of the probe over a time length $\Delta\tau = 80$ μs at a sampling frequency $f_s = 40$ MHz.

II.B Truncated focused reflection matrix

This first appendix provides a theoretical explanation of the maximal lateral distance ΔX_{max} between the two virtual transducers. Performing a change of basis between the focused basis and the plane wave basis can be analyzed as a spatial Fourier transform. To avoid aliasing, a Shannon criterion should be respected. As stated in section II.2.1, the focused reflection matrix is the result of the convolution of the input and output focusing matrices with the medium reflectivity [Eq. II.18]. In absence of aberration, $\mathbf{H}_{\text{in}}$ can be written:

$$\mathbf{H}_{\text{in}} = \mathbf{P_0} \times \mathbf{P_0}^{\dagger}, \tag{II.46}$$

and in term of coefficients:

$$H(\mathbf{r}_{\text{in}}, \mathbf{r}, f) = \sum_{\theta} \exp\left[i \frac{2\pi}{\lambda} \, (x_{in} - x) \, \sin(\theta) \right]. \tag{II.47}$$

This equation is a spatial Fourier transform that requires the following condition:

$$\Delta x^{\max} = \frac{\lambda}{2\delta\theta_{in}}, \tag{II.48}$$

with $\Delta x^{\max}$ the maximal transverse distance between the two virtual transducers and $\delta\theta_{in}$ is the angle step fixed by the ultrasound sequence used to insonified the medium. A similar criterion also exists in receive for $\mathbf{H}_{\text{out}}$, however, the ultrasound probes are

generally designed with a pitch $p \propto \lambda$ or $p \propto \lambda/2$. The transmit condition is then generally the limiting one for plane wave imaging modes.

II.C Derivation of the incoherent input-output PSF in the broadband regime

This content is confidential – please contact the author for more information.

II.D Extraction of the coherent wave from multiple propagation movie in a speckle regime

This content is confidential – please contact the author for more information.

Chapter III

Matrix approach of aberration correction

Contents

In the previous chapters, we have seen that the image formation process requires an hypothesis on the medium speed of sound. A mismatch between this model and the medium speed of sound induces some errors on the estimation of the echoes round-trip time-of-flight, which degrades the focusing quality. In transmission, the incident waves are no longer confined within a diffraction limited focal spot, while in reception, the beamforming process selects echoes that arise from a larger areas. The transmitted and received PSFs are thus enlarged, which degrade the image quality.

Inspired by the pioneer work of Robert *et al.* [49], we develop in this chapter a new matrix approach of aberration correction based on the distortion matrix concept. Whereas the reflection matrix $\mathbf{R}$ holds the wave fronts that are reflected from the medium, the distortion matrix $\mathbf{D}$ contains the deviations from an ideal reflected wave front that would be obtained in the absence of inhomogeneities. This matrix is expressed within a *dual basis* that links any virtual transducer embedded within the medium, to the aberration that any incident or reflected wave undergo through its propagation within the medium. Despite the random reflectivity of the medium (in the speckle regime), this matrix exhibits long-range correlations. Such spatial correlations can be taken advantage of to decompose the field-of-view into a set of isoplanatic modes and their corresponding wavefront distortions in the far-field.

In this chapter, we develop the distortion matrix approach for acoustic imaging. In view of medical ultrasound applications, we show that this method could tackle the case of both specular and speckle regime. This new technique uses the broadband focused reflection matrix $\overline{\mathbf{R}}_{\mathrm{rr}}$ as a first building block. Two experiments are used to illustrate this chapter, (*i*) an *in-vitro* experiment where a tissue-mimicking phantom is imaged through a thick layer of plexiglass; and (*ii*) an *in-vivo* experiment on the calf of a healthy patient. This second experiment has already been studied in the previous chapter. We recall that an extensive review of the major techniques of aberration correction is provide in the first chapter [see Par. I.2].

This chapter is divided in four parts. We first demonstrate how projecting the reflection matrix into the far-field allows the suppression of specular reflections and multiple reverberations (clutter noise). By means of the plexiglas experiment, we then tackle the case of transverse aberration correction in the case of a single isoplanatic patch. The last two sections are dedicated to the more challenging configuration where the field of view is composed of multiple isoplanatic patches. Two strategies have been developed. The first method is inspired from the DORT method, that demonstrates that under certain conditions there is a one-to-one association between each eigenstate of the reflection matrix and each point-like target in the medium. Similarly, the analysis of the distortion

matrix reveals a one-to-one association between each isoplanatic patch p and each eigenstate of this matrix. Its effective rank $\mathcal{H}$ then constitutes an estimation on the number of isoplanatic patches in the field-of-view (FOV). The minimization of $\mathcal{H}$, enables a quantitative measurement of the local speed of sound of the medium in the FOV. The second approach consists in a local analysis of the distortion matrix. Even if some assumptions are required on the spatial extent of the medium isoplanatic patch, this method provides an estimation of the medium propagation matrices that link any focal point embedded within the medium to the transducer or plane wave basis.

In this chapter we restrain ourselves to the particular configuration were the two virtual transducers are located at the same depth. The following techniques use the broadband focused reflection matrix $\overline{\mathbf{R}}_{xx}(z)$ developed in chapter 2 as a first building block.

We first consider the *in-vitro* experiment were a 15 mm-thick layer of plexiglass is placed between the probe and a tissue-mimicking phantom [Fig. 1B]. This experiments mimics strong aberration induced by a thick layer located at shallow depth, such as a transcranial experiment. Figure 1B displays the associated plane wave US image $\mathcal{I}(\mathbf{r})$. We recall that this image contains all the confocal signals of the broadband focused reflection (FR) matrix, *i.e.* the diagonal signals of $\overline{\mathbf{R}}_{xx}(z)$ at each focal depth z [see Par. II.2.2]. These matrices are obtained by means of the propagation matrices $\mathbf{P}_0$ and $\mathbf{G}_0$ [Eqs. II.14a and II.14b], which are defined based on an assumption of a homogeneous medium, with a speed of sound of $c = 1540$ m/s. Unsurprisingly the US image in Fig. 1B is strongly degraded by the plexiglass layer for two reasons. First, the plexiglass speed of sound is around $c_{\text{plexi}} \sim 2750$ m/s [146]. The medium (composed of the plexiglas layer and phantom) is thus far from being homogeneous and a huge error is made on the hypothesis of speed of sound. It leads to a poor resolution of the image that is highlighted by the bright point like scatterers. Second, multiple reverberations between the plexiglass walls and the probe induce strong horizontal specular echoes. In the following, we show that a matrix approach to wave imaging is particularly appropriate to correct for these two issues.

III.1 Removing Multiple Reverberations with the Far-Field Reflection Matrix

Reverberation signals are a common problem in medical ultrasound imaging, often originating from multiple reflections at tissue interfaces or between bones in the human body. Here, we observe strong horizontal artifacts at shallow depths of the image (Fig. 1B), which are due to waves which have undergone multiple reflections – often called reverberations in the literature – between the parallel walls of the plexiglass layer. In the following, we show that these signals can be isolated and suppressed using the reflection matrix.

To project the reflection matrix into the far-field, we define a free-space transmission matrix, $\mathbf{T}_0$, which corresponds to the Fourier transform operator. Its elements link any transverse wave number k_x in the Fourier space to the transverse coordinate x of any point $\mathbf{r}$ in a supposed homogeneous medium:

$$T_0\left(k_x, x\right) = \exp - (ik_x x). \tag{III.1}$$

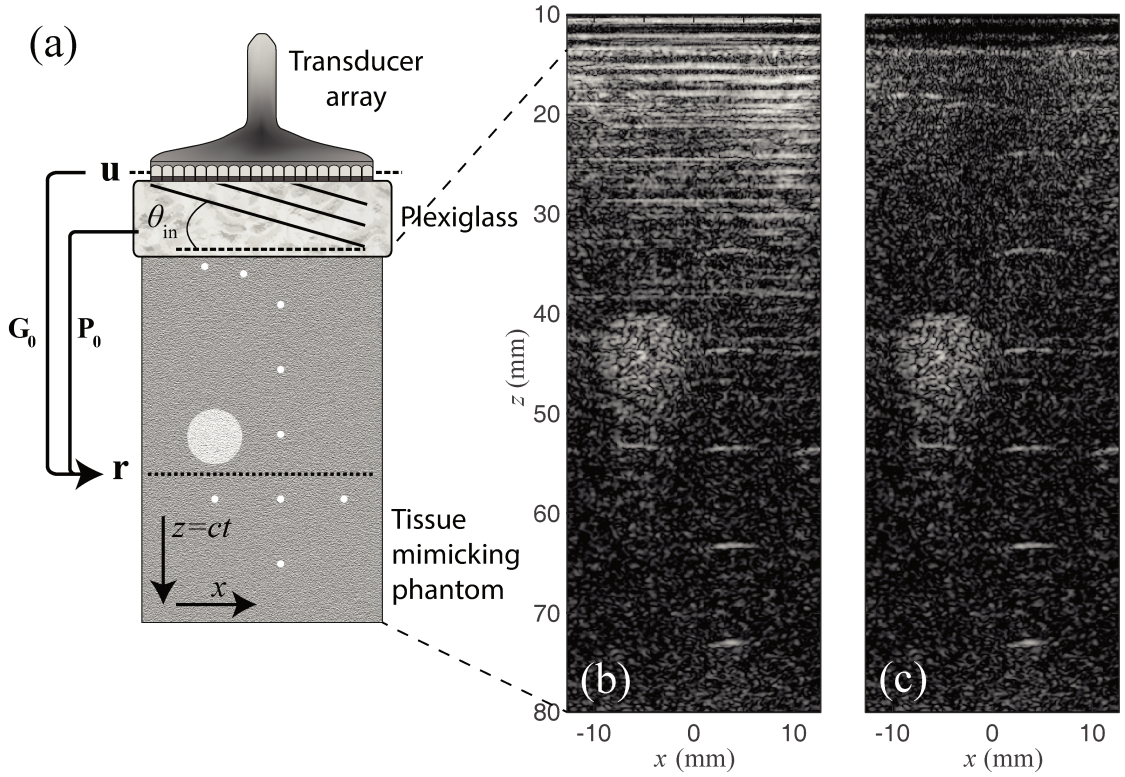

Fig. 1 *Matrix imaging. (A) Sketch of the in-vitro experimental acquisition. A plexiglass layer is placed between the phantom and the probe. (b) Conventional ultrasound image computed at $c_0 = 1540$ m/s (c) Ultrasound image after the removal of multiple reflections.*

Each matrix $\overline{\mathbf{R}}_{\mathrm{xx}}(z)$ can now be projected in the far field via the matrix product

$$\overline{\mathbf{R}}_{\mathrm{kk}}(z) = \mathbf{T}_0 \times \overline{\mathbf{R}}_{\mathrm{xx}}(z) \times \mathbf{T}_0^{\top}, \tag{III.2}$$

where the symbol $\top$ stands for matrix transpose. The resulting matrix $\overline{\mathbf{R}}_{\mathrm{kk}}(z) = [\overline{R}(k_{\mathrm{out}}, k_{\mathrm{in}}, z)]$ contains the reflection coefficients of the sample at depth z between input and output wave numbers k_{in} and k_{out}. Figure 2(c) displays the far-field reflection matrix $\overline{\mathbf{R}}_{\mathrm{kk}}(z)$ depth $z = 19$ mm. Surprisingly, this matrix is dominated by a strongly enhanced reflected energy along its main anti-diagonal ($k_{\mathrm{out}} + k_{\mathrm{in}} = 0$). To understand this phenomenon, the reflection matrix $\overline{\mathbf{R}}_{\mathrm{kk}}(z)$ can be expressed as follows:

$$\overline{\mathbf{R}}_{\mathrm{kk}}(z) = \mathbf{T}(z) \times \mathbf{\Gamma}(z) \times \mathbf{T}^{\top}(z), \tag{III.3}$$

where$\mathbf{\Gamma}(z) = [\Gamma(x, x', z)]$ describes the scattering processes inside the medium [See par.II.2.1]. In the single scattering regime, $\mathbf{\Gamma}(z)$ is diagonal and its elements correspond to the medium reflectivity $\gamma(x, z)$ at depth z. $\mathbf{T}(z)$ is the true transmission matrix between the Fourier basis and the focal plane at depth z. Each column of this matrix corresponds to the wavefront that would be recorded in the far-field due to emission from a point source located at $\mathbf{r} = (x, z)$ inside the sample.

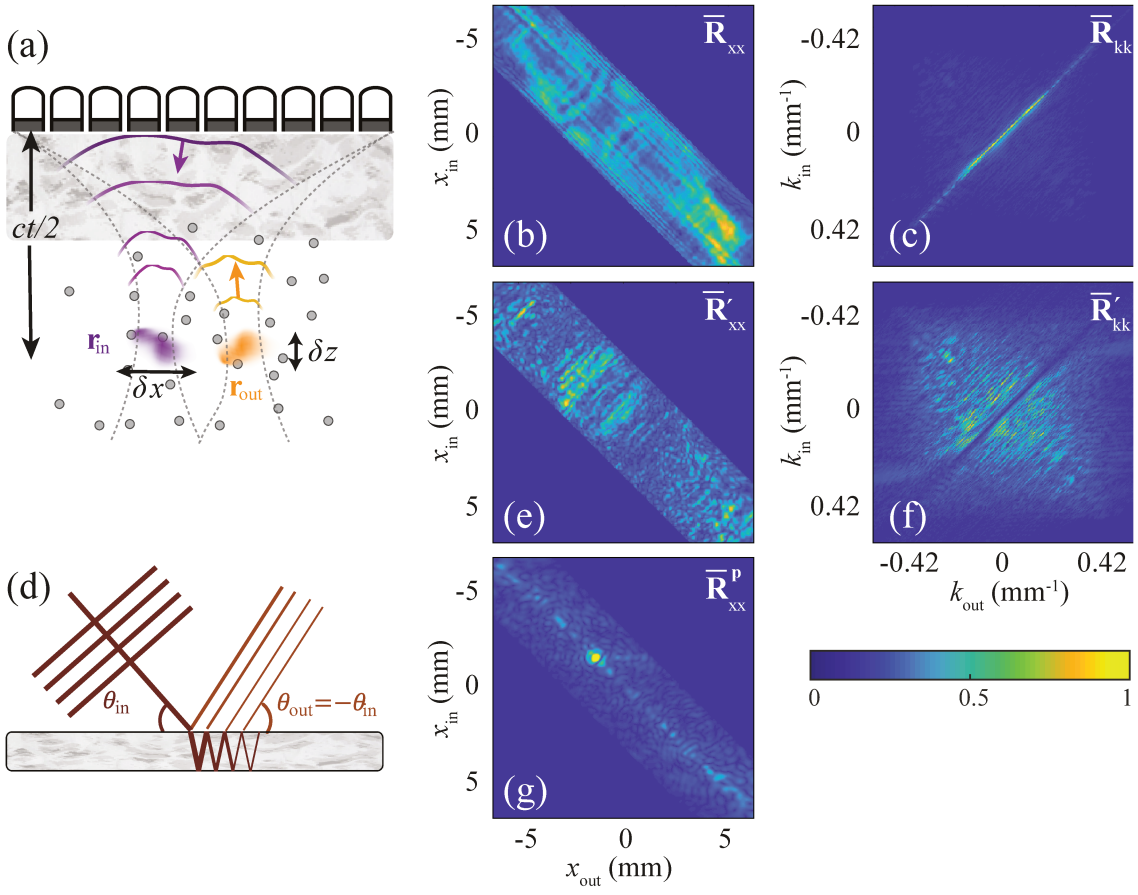

Fig. 2 *Removing multiple reflections with the matrix approach.(a) Focused beamforming applied to* $\mathbf{R}_{u\theta}(\omega)$ *[Eqs. II.15-II.34] yields the focused reflection matrix* $\mathbf{R}_{rr}$ *that contains the set of impulse responses between virtual transducers* $\mathbf{r}_{in}$ *and* $\mathbf{r}_{out}$ *at each depth* z*. (d) Sketch of multiple reflections between parallel surfaces. (b,e,g) Amplitude of the broadband focused reflection matrices* $\overline{\mathbf{R}}_{xx}(z)$*,* $\overline{\mathbf{R}}'_{xx}(z)$ *[Eq. III.2] and* $\overline{\mathbf{R}}^{1}_{xx}(z)$*, computed at* $z = 19$ *mm. These matrix are computed before any post-processing, after multiple scattering filtering [Eq. III.7] and after aberration correction [Eq. III.27], respectively. (c,f) Reflection matrix expressed in the far-field basis,* $\overline{\mathbf{R}}_{kk}$ *and* $\overline{\mathbf{R}}'_{kk}$ *computed before and after the cancellation of the main anti-diagonal* $(k_{in} + k_{out} = 0)$ *in* $\overline{\mathbf{R}}_{kk}$*.*

In appendix, III.A a theoretical expression of $\overline{\mathbf{R}}_{\mathrm{kk}}$ is derived in the single scattering regime under an isoplanatic hypothesis. Interestingly, the norm-square of its coefficients $R(k_{\mathrm{out}}, k_{\mathrm{in}}, z)$ is shown to be independent of aberrations. It directly yields the spatial frequency spectrum of the scattering medium at depth z:

$$\left|\overline{R}(k_{\mathrm{out}}, k_{\mathrm{in}}, z)\right|^2 = \left|\tilde{\gamma}(k_{\mathrm{out}} + k_{\mathrm{in}}, z)\right|^2, \tag{III.4}$$

where $\tilde{\gamma}(k_x, z) = \int dx \gamma(x, z) \exp(-ik_x x)$ is the 1D Fourier transform of the sample reflectivity $\gamma(x, z)$. In the single scattering regime, the matrix $\overline{\mathbf{R}}_{\mathrm{kk}}$ displays a deterministic coherence along its anti-diagonals [89, 147] that can be seen as a manifestation of the memory effect in reflection [148]. Each anti-diagonal ($k_{\mathrm{in}} + k_{\mathrm{out}} =$ constant) encodes one spatial frequency of the sample reflectivity. For the system under study here, reflections occurring between the parallel surfaces of the plexiglass obey $k_{\mathrm{in}} + k_{\mathrm{out}} = k_0 \sin\theta_0$, where $k_0 = \omega_0/c$ is the wave number at the central frequency and θ_0 is the angle between the top face of the plexiglass and the transducer array (Fig. 2(d). Hence, signatures of such reflections should arise along the main anti-diagonal ($k_{\mathrm{in}} + k_{\mathrm{out}} = 0$) of $\overline{\mathbf{R}}_{\mathrm{kk}}$. We can take advantage of this sparse feature in $\overline{\mathbf{R}}_{\mathrm{kk}}$ to filter out signals from reverberation, independently of aberrations induced by the plexiglass.

To this aim, we developed a multiple reflection filter that consists in applying an adaptive Gaussian filter to remove the specular contribution that lies along the main anti-diagonal of $\overline{\mathbf{R}}_{\mathrm{kk}}$, such that:

$$\overline{R}'(k_{\mathrm{out}}, k_{\mathrm{in}}) = \overline{R}(k_{\mathrm{out}}, k_{\mathrm{in}}) \left[1 - \alpha e^{-|k_{\mathrm{out}}+k_{\mathrm{in}}|^2/\delta k^2}\right]. \tag{III.5}$$

The width δk of the Gaussian filter scales as the inverse of the transverse dimension Δx of the field of view: $\delta k = \Delta x^{-1}$. The parameter α defines the strength of the filter:

$$\alpha_{\mathrm{kk}} = \frac{\langle|\overline{R}(k_{\mathrm{out}}, k_{\mathrm{in}})|\rangle_{\Delta k > \delta k}}{\langle|\overline{R}(k_{\mathrm{out}}, k_{\mathrm{in}})|\rangle_{\Delta k < \delta k}} - 1, \tag{III.6}$$

where the symbol $\langle \cdots \rangle$ denotes an average over the couples $(k_{\mathrm{out}}, k_{\mathrm{in}})$ separated by a distance $\Delta k = |k_{\mathrm{out}} + k_{\mathrm{in}}|$ smaller or larger than δk. When the specular component dominates, the parameter α_{kk} tends to 1 and the Gaussian filter is fully applied: The main anti-diagonal of $\overline{\mathbf{R}}_{\mathrm{kk}}$ is then set to zero [Fig.2(f)]. When there is no peculiar specular contribution, the parameter α_{kk} tends to 0 and the Gaussian filter is not applied: The main anti-diagonal of $\overline{\mathbf{R}}_{\mathrm{kk}}$ remains unchanged.

Then, the inverse operation of Eq. III.2 can be applied to the filtered matrix $\overline{\mathbf{R}}'_{\mathrm{kk}}$ to obtain a filtered focused reflection matrix:

$$\overline{\mathbf{R}}'_{\mathrm{xx}}(z) = \mathbf{T}^{\dagger}_{\mathbf{0}}(z) \times \overline{\mathbf{R}}'_{\mathrm{kk}}(z) \times \mathbf{T}^{*}_{\mathbf{0}}(z). \tag{III.7}$$

Fig. 2(e) shows an example of $\overline{\mathbf{R}}'_{\mathrm{xx}}(z)$. Comparison with the original matrix in Fig. 2(c) shows that the low spatial frequency components of the reflected wavefield have been removed from the diagonal of $\overline{\mathbf{R}}_{\mathrm{xx}}(z)$. The resulting $\overline{\mathbf{R}}'_{\mathrm{xx}}(z)$ now exhibits solely random coefficients – a characteristic of ultrasonic speckle. However the halo of single scattering is difficult to perceive due to the very poor transverse resolution.

Finally, figure 1(c) shows the filtered US image $\overline{\mathcal{I}}'\mathbf{r}$ calculated from $\mathbf{R}'_{xx}$ (Eq. II.16). The removal of multiple reflections has enabled the discovery of previously hidden bright

targets at shallow depths. However, as confirmed by the observation of the focused reflection matrix, the confocal image still suffers from severe aberrations.

This specular filter is adapted to this particular experiment. To generalize the following equation, no distinction will be done between $\overline{\mathbf{R}}'_{\mathrm{xx}}(z)$ and $\overline{\mathbf{R}}_{\mathrm{xx}}$.

III.2 The distortion matrix concept, fundamental bases

In the field of optic, Badon *et al.*[149] have introduced the distortion matrix concept for optical imaging of extended specular reflectors in a strong aberration regime. Here, we show how this approach can be extended to the speckle regime to correct for aberrations. Based on the plexiglas/phantom system, we first investigate the case of a single isoplanatic patch in the field of view. By changing the speed of sound hypothesis, we then move to a more complex situation where the field of view is decomposed into multiple isoplanatic patch. To help the reader, figure 3 displays a global flowchart of the aberration correction process that summarizes the key steps.

To begin, we first base our demonstration on the above mentioned experiment of the plexiglass/phantom system imaged at $c_0 = 1540$ m/s. The aberrating layer (plexiglas) is invariant by lateral translation. Consequently, a given plane wave of incident angle θ_{in} that travels through this layer is only delayed. As the hypothesis of speed of sound matches the one of the second medium, the wave suffers no further aberrations. Therefore all the focal points located within the phantom are impacted by the aberration resulting in a unique isoplanatic patch in the field of view. This experiment is thus ideal to validate the basis of our aberration correction.

Figure 2(e) shows the filtered broadband focused reflection matrix $\overline{\mathbf{R}}'_{\mathrm{xx}}$. In chapter 2 II.2.2 we showed that this matrix is characterized by a halo of high intensity located along the diagonal that comes from single scattering process. More precisely, it appears when the two virtual transducers are overlapping with each other. However, in figure 2(e), this halo nearly disappears due to the huge broadening of the broadband input and output PSFs, $\overline{\mathbf{H}}_{\mathrm{in}}$ and $\overline{\mathbf{H}}_{\mathrm{out}}$, induced by the aberrations. Mathematically, this phenomenon can be described by Eq. II.37. As we only investigate transverse aberration in this chapter, this equation is approached by the following one:

$$\overline{R}(x_{\mathrm{out}}, x_{\mathrm{in}}, z) = \int dx \overline{H}_{\mathrm{out}}(x, x_{\mathrm{out}}, z)\gamma(x, z)\overline{H}_{\mathrm{in}}(x, x_{\mathrm{in}}, z). \tag{III.8}$$

By means of a matrix formalism, this equation can be written as:

$$\overline{\mathbf{R}}_{\mathrm{xx}}(z) = \overline{\mathbf{H}}_{\mathrm{out}}(z) \times \mathbf{\Gamma}(z) \times \overline{\mathbf{H}}^{\top}_{\mathrm{in}}(z), \tag{III.9}$$

This approximation simply consists in assuming that the reflection matrix contains the medium temporal Dirac impulse responses. This approximation is similar to the one used in the annex **??**. In this case, the axial resolution is point-like, which drastically simplifies the following theoretical study.

To isolate and correct for these aberration effects, we will build upon the memory effect [See Par. I.2.1.2]. This phenomenon describes the fact all focal points that belong to the same isoplanatic patch are impacted by the same aberration. Thus, their input and output PSFs are spatially invariant. For aberration correction, our strategy is the

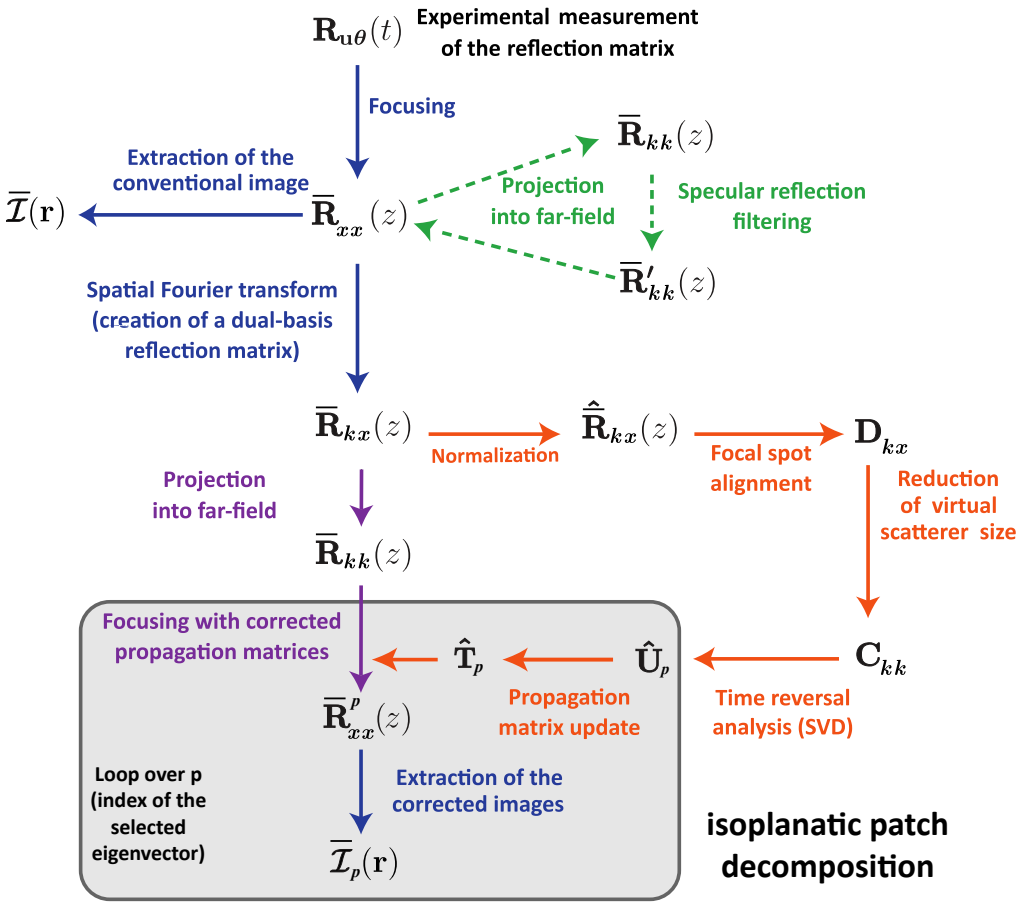

Fig. 3 *Schematic flowchart of the decomposition of the field-of-view into multiple isoplanatic patches along the green path (top dashed lines), reverberation suppression is performed. Along the orange path loops, the distortion matrix approach is applied to extract aberration laws, and to use them to update the estimation of the propagation matrix* $\hat{\mathbf{T}}_\mathbf{p}$.

following: (*i*) highlight these spatial correlations by building a dual-basis matrix (the distortion matrix) that connects any input focal point in the medium with the distortion exhibited by the corresponding reflected wavefront in a correcting plane, *e.g.* the far-field plane [149], and (*ii*) take advantage of these correlations to accurately estimate the aberration.

III.2.1 Projection in the far-field

In adaptive focusing, the aberrating layer is often modeled as a random phase screen. For an optimal correction, ultrasonic data should be back-propagated to the plane containing the aberrating layer. Indeed, from this plane, the aberration is spatially-invariant. By applying the phase conjugate of the aberration phase law, aberrations can be fully compensated at any point of the medium. However, in real life, speed-of-sound inhomo-

geneities are distributed over the whole medium and aberrations can take place everywhere. In that case, the strategy is to back-propagate ultrasound data in several planes from which the aberration phase law should be estimated and then compensated. The correction planes should be chosen according to the following criterion: Maximizing the size of isoplanatic patches. In the present case of a multi-layered media, a far-field plane is the most adequate since plane waves are the propagation invariants in this geometry. We will see in the calf experiment that the probe plane is a good choice for aberrations induced by the skin or fat layers.

To isolate the effects of aberration in the reflection matrix, $\overline{\mathbf{R}}'_{\mathrm{xx}}(z)$ is first projected into the Fourier basis in reception by using the free-space transmission matrix $\mathbf{T}_0$:

$$\overline{\mathbf{R}}_{\mathrm{kx}}(z) = \mathbf{T}_0 \times \overline{\mathbf{R}}'_{\mathrm{xx}}(z). \tag{III.10}$$

$\overline{\mathbf{R}}_{kx}(z)$ contains the set of far-field aberrated wave-fronts generated by each virtual source $\mathbf{r}_{\mathrm{in}}$. Figure 4(A) shows the phase of $\overline{\mathbf{R}}_{\mathrm{kx}}(z)$ obtained at $z = 30$ mm. We recall that by using the central frequency f_c as a reference frequency, the transverse wave number can be associated with a plane wave of angle $\dot{\theta}$, such that $k_x = k_c \sin(\dot{\theta})$, with $k_c = 2\pi f_c/c$ the wave number at the central frequency. Expressing the far-field projection as a plane wave decomposition is useful to define the boundaries of this basis. The maximum transverse wave number is indeed related to β the maximum angle of wave illumination (in transmit mode) or collection (in receive mode) by the array [white dashed lines on Figure 4(A)]. The matrix $\overline{\mathbf{R}}_{\mathrm{kx}}(z)$ will be used to tackle the aberrations in the receive plane-wave basis (*i.e.* received far-field basis).

We might expect to observe correlations between the columns of matrices $\overline{\mathbf{R}}_{\mathrm{kx}}(z)$ displayed in Figs. 4(a). Neighbor virtual sources $\mathbf{r}_{\mathrm{in}}$ belong *a priori* to the same isoplanatic patch. The associated wave-fronts in the transducer plane or in the far-field should thus be, in principle, strongly correlated since they travel through the same area of the aberrating layer. However, such correlations are not obvious by eye in Figs. 4(a). In the following, we show how to reveal those hidden correlations by introducing the distortion matrix.

III.2.2 The distortion matrix

To reveal the isoplanaticity of the reflected wave-field, each aberrated wave-front [Fig. 4(d)] contained in the reflection matrix $\overline{\mathbf{R}}_{\mathrm{kx}}(z)$ should be decomposed into two components: (*i*) a geometric component described by $\mathbf{T}_0(z)$ [Fig. 4(e)], which contains the ideal wave-front induced by the virtual source $\mathbf{r}_{\mathrm{in}}$ that would be obtained in the homogeneous medium used to model the wave propagation [Fig. 4(e)]; (*ii*) a distorted component due to the mismatch between the propagation model and reality [Fig. 4(f)]. A key idea is to isolate the latter contribution by subtracting, from the experimentally measured wave-front, its ideal counterpart. Mathematically, this operation can be done by means of an Hadamard product between $\overline{\mathbf{R}}_{\mathrm{kx}}(z)$ and $\mathbf{T}_0^*(z)$:

$$\mathbf{D}_{\mathrm{kx}}(z) = \overline{\mathbf{R}}_{\mathrm{kx}}(z) \circ \mathbf{T}_0^*(z). \tag{III.11}$$

$\mathbf{D}_{\mathrm{kr}} = \mathbf{D}_{\mathrm{kx}}(z) = [D(k_{\mathrm{out}}, \{x_{\mathrm{in}}, z\})]$ is called the distortion matrix. By injecting Eq. III.10 in Eq. III.11, the coefficient of the distortion matrix can be expressed as:

$$D(k_{\mathrm{out}}, r_{\mathrm{in}}) = \sum_{x_{\mathrm{out}}} \overline{R}(\Delta x_{\mathrm{out}}, x_{\mathrm{in}}, z) \ \exp\left[ik_{\mathrm{out}}\Delta x_{\mathrm{out}}\right]. \tag{III.12}$$

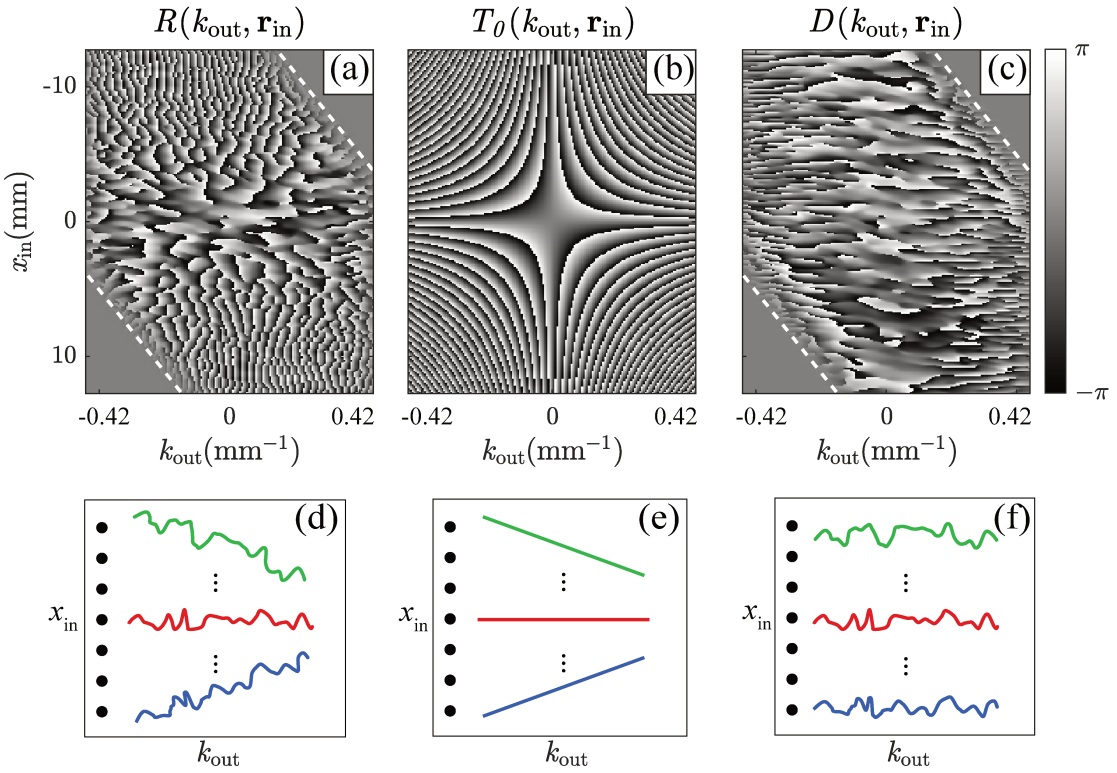

Fig. 4 *Revealing the correlations of the reflected wavefield. (A) Phase of the reflection matrix* $\overline{\mathbf{R}}_{kx}(z)$ *at depth* $z = 30$ *mm. (B) Phase of the free-space transmission matrix* $\mathbf{T}_0$ *at the same depth (*$c = 1540$ *m/s). (C) Phase of the distortion matrix* $\mathbf{D}_{kx}$ *deduced from* $\overline{\mathbf{R}}_{kx}(z)$ *and* $\mathbf{T}_0$*. (D,E,F) Sketches of the wave-fronts contained in the matrices displayed in (A,B,C)*

Where $\Delta x_{\text{out}} = x_{\text{out}} - x_{\text{in}}$. Mathematically, each row of $\mathbf{D}_{\text{kr}}$ is the Fourier transform of the focused wave-field re-centered around each focusing point $\mathbf{r}_{\text{in}}$. The distortion matrix $\mathbf{D}_{\text{kr}}$ can thus be seen as a reflection matrix for different realizations of virtual sources, all shifted at the origin of the focal plane.

Note that, the medium under investigation is composed of bright stars. However, such situation rarely happens in the case of *in-vivo* measurement. To ensure that the concept introduced in this section can be applied to the speckle regime, and thus that it works without any beacon, we normalized the reflection matrix:

$$\hat{\overline{\mathbf{R}}}_{\text{kx}}(z) = [R(k_{\text{out}}, x_{\text{in}}, z)/|R(k_{\text{out}}, x_{\text{in}}, z)|] \tag{III.13}$$

In that case, any focal point is associated to the same signal level, and only the phase of the reflection matrix will be used to correct for aberration. Note that this operation is not encouraged for aberration correction as it improve the noise level. In the following $\hat{\overline{\mathbf{R}}}_{\text{kx}}$ will be confused with $\overline{\mathbf{R}}_{\text{kx}}$ for sake of clarity.

$\mathbf{D}_{\text{kr}}$ connects any input focal point $\mathbf{r}_{\text{in}}$ to the distorted component of the reflected wavefield in the plane wave basis. Compared to $\overline{\mathbf{R}}_{\text{kx}}$ [Fig. 4(a)], $\mathbf{D}_{\text{kx}}$ exhibits long-range

correlations [Fig. 4(c)]. While the original reflected wavefronts display a different tilt for each focal point $\mathbf{r}_{\text{in}}$, their distorted component displays an almost invariant aberration phase law over all $\mathbf{r}_{\text{in}}$.

To support our identification of spatial correlations in $\mathbf{D}_{\text{kx}}$ with isoplanatic patches, $\mathbf{D}_{\text{kx}}$ is now expressed mathematically. We begin with the simplest case of an isoplanatic aberration which implies, by definition, a spatially-invariant input focal spot: $\overline{H}_{\text{in}}(x, x_{\text{in}}, z) = \overline{H}_{\text{in}}(x - x_{\text{in}})$. As stated above, the plexiglas/phantom experiment imaged at $c_0 = 1540$ m/s, corresponds exactly to this situation. Under this hypothesis, the injection of Eqs. III.9 and III.10 into Eq.III.11 gives the following expression for $\mathbf{D}_{\text{kx}}$ [see appendix III.C)]:

$$\mathbf{D}_{\text{kx}}(z) = \mathbf{T} \times \mathbf{S}(z), \tag{III.14}$$

where the matrix $\mathbf{S}$ is the set of incoherent virtual sources re-centered at the origin such that

$$S(x', x_{\text{in}}, z) = \gamma(x' + x_{\text{in}}, z)\overline{H}_{\text{in}}(x'). \tag{III.15}$$

$x' = x - x_{\text{in}}$ represents a new coordinate system centered around the input focusing point. These virtual sources are spatially incoherent due to the random reflectivity of the medium, and their size is governed by the spatial extension of the input focal spot. This random reflectivity leads to the short-scale phase-shifts that are observed between the lines of $\mathbf{D}_{\text{kr}}$ [Fig. 4]. The physical meaning of Eqs. III.14 and III.15 is the following: Removing the geometrical component of the reflected wavefield in the far-field as done in Eq.III.11 is equivalent to shifting each virtual source to the central point $x_{\text{in}} = 0$ of the imaging plane. $\mathbf{D}_{\text{kx}}$ is still a type of reflection matrix, but one which contains different realizations of virtual sources all located at the origin [Fig. 5(c,right)]. This superposition of the input focal spots will enable the unscrambling of the propagation and scattering components in the reflected wavefield.

Within a given isoplanatic patch, the spatial invariance of the PSFs, injecting Eq. III.8 into Eq. III.12

$$D(k_{\text{out}}, x_{\text{in}}, z) = \tilde{H}_{\text{out}}(k_{\text{out}}) \int dx \gamma(x + x_{\text{in}}, z) H_{\text{in}}(x) e^{ik_{\text{out}}x} \tag{III.16}$$

The physical meaning of this last equation is the following: the aberrations can be modelled by a transmittance $\tilde{H}_{\text{out}}(k_{\text{out}})$. This transmittance is directly the Fourier transform of the output PSF $H_{\text{out}}(x)$:

$$\tilde{H}_{\text{out}}(k_{\text{out}}) = \sum_x H_{\text{out}}(x) e^{-ik_{\text{out}}x} \tag{III.17}$$

The aberration matrix $\tilde{\mathbf{H}}_{\text{out}}$ directly provides the *true* transmission matrix $\mathbf{T}$ between the transducers and any point of the medium:

$$\mathbf{T} = \tilde{\mathbf{H}}_{\text{out}} \circ \mathbf{T}_0 \tag{III.18}$$

This transmission matrix $\mathbf{T}$ is the holy grail for ultrasound imaging since its phase conjugate directly provides the focusing laws that need to be applied in the received plane wave basis to optimally focus on each point of the medium.

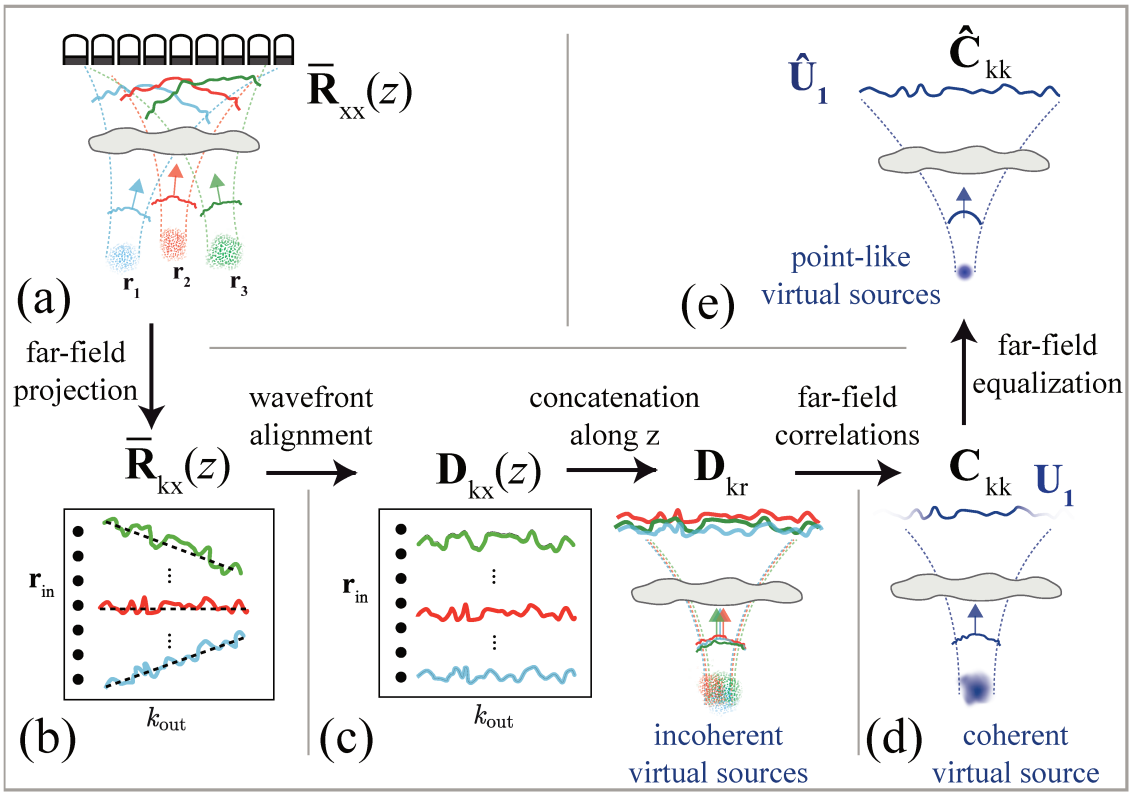

Fig. 5 *Time reversal analysis of the distortion matrix. (a) Each input focused illumination gives rise to a tilted reflected wavefront. (b) After far-field projection [Eq. III.10], each wavefield is stored along a line of* $\overline{\mathbf{R}}_{kx}(z)$. *(c) By removing the geometrical tilt (dashed black line in (c)) of each reflected wavefront [Eq. III.11], a set of distortion matrices* $\mathbf{D}_{kx}(z)$ *is obtained at each depth* z. *These matrices are concatenated to yield a full-field distortion matrix* $\mathbf{D}_{kx}$. $\mathbf{D}_{kx}$ *is equivalent to a reflection matrix but with input focal spots* $\overline{H}_{in}(x - x_{in})$ *virtually shifted at the same location [Eq. III.14]. (d) In the far-field, its correlation matrix* $\mathbf{C}_{kk}$ *mimics the time reversal operator associated with a virtual specular reflector whose scattering distribution* $|H_{in}(x)|^2$. *(e) The normalized correlation matrix* $\hat{\mathbf{C}}_{kk}$ *makes the virtual reflector point-like [see appendix III.D]. Its eigenvalue decomposition [Eq. III.25] then yields the transmission matrix over each isoplanatic patch contained in the FOI [Eq. III.26].*

III.2.3 Time reversal analysis of the distortion matrix

The next step is to extract and exploit the correlations of $\mathbf{D}_{\mathrm{kx}}$ for imaging. In the specular scattering regime, $\mathbf{D}_{\mathrm{kx}}$ is dominated by spatial correlations in the input focal plane [149]. This is due to the long-range coherence of the sample reflectivity for specular reflectors. Conversely, in the speckle scattering regime, the sample reflectivity $\gamma(\mathbf{r})$ is random: $\langle\gamma(\mathbf{r})\gamma^*(\mathbf{r}')\rangle = \langle|\gamma|^2\rangle\delta(\mathbf{r}-\mathbf{r}')$, where δ is the Dirac distribution and the symbol $\langle\cdots\rangle$ denotes an ensemble average. In this case, correlations in the Fourier plane dominate. To extract them, the correlation matrix $\mathbf{C}_{\mathrm{kk}} = N^{-1}\mathbf{D}_{\mathrm{kx}}\mathbf{D}_{\mathrm{kx}}^{\dagger}$ is an excellent tool. The coefficients of $\mathbf{C}_{\mathrm{kk}}$ are obtained by averaging the angular correlations of the distorted wave-field $D(k_{\mathrm{out}}, \mathbf{r}_{\mathrm{in}})$ over the N input focusing points $\mathbf{r}_{\mathrm{in}} = (x_{\mathrm{in}}, z)$:

$$C(k_x, k_x') = N^{-1}\sum_{\mathbf{r}_{\mathrm{in}}} D(k_x, \mathbf{r}_{\mathrm{in}})D^*(k_x', \mathbf{r}_{\mathrm{in}}). \tag{III.19}$$

$\mathbf{C}_{\mathrm{kk}}$ can be decomposed as the sum of a covariance matrix $\langle\mathbf{C}_{\mathrm{kk}}\rangle$ and a perturbation term $\delta\mathbf{C}_{\mathrm{kk}}$:

$$\mathbf{C}_{\mathrm{kk}} = \langle\mathbf{C}_{\mathrm{kk}}\rangle + \delta\mathbf{C}_{\mathrm{kk}}. \tag{III.20}$$

$\mathbf{C}_{\mathrm{kk}}$ will converge towards $\langle\mathbf{C}_{\mathrm{kk}}\rangle$ if the incoherent source term $\mathbf{S}$ of Eq. III.14 is averaged over enough independent realizations of disorder, i.e. if the perturbation term $\delta\mathbf{C}_{\mathrm{kk}}$ tends towards zero. In fact, the intensity of $\delta\mathbf{C}_{\mathrm{kk}}$ scales as the inverse number M of resolution cells in the FOV [150]. In the present case, $M = L_xL_z/(\delta x\delta z) \sim 10000$, where (L_x, L_z) is the spatial extent of the overall FOV and $(\delta x, \delta z)$ is the spatial extent of each resolution cell [Fig. 2(A)]. In the following, we will thus assume a convergence of $\mathbf{C}_{\mathrm{kk}}$ towards its covariance matrix $\langle\mathbf{C}_{\mathrm{kk}}\rangle$ due to disorder self-averaging.

Let us now express the covariance matrix $\langle\mathbf{C}_{\mathrm{kk}}\rangle$ theoretically. This allows $\langle\mathbf{C}_{\mathrm{kk}}\rangle$ to be written as [see appendix III.D]:

$$\langle\mathbf{C}_{\mathrm{kk}}\rangle = \mathbf{T}\times\mathbf{\Gamma}_H\times\mathbf{T}^{\dagger}, \tag{III.21}$$

where $\mathbf{\Gamma}_H$ is diagonal and its coefficients are directly proportional to $|H_{\mathrm{in}}(x)|^2$. $\mathbf{\Gamma_H}$ is equivalent to a scattering matrix associated with a virtual coherent reflector whose scattering distribution corresponds to the input focal spot intensity $|H_{\mathrm{in}}(x)|^2$ (Fig. 5(d)). Expressed in the form of Eq. III.21, $\langle\mathbf{C}_{\mathrm{kk}}\rangle$ is analogous to a reflection matrix associated with a single scatterer of reflectivity $|H_{\mathrm{in}}(x)|^2$.

For such an experimental configuration, it has been shown that an iterative time reversal process converges towards a wavefront that focuses perfectly through the heterogeneous medium onto this scatterer [105, 106]. Interestingly, this time-reversal invariant can also be deduced from the eigenvalue decomposition of the time-reversal operator $\mathbf{RR}^{\dagger}$ [105, 106, 113] [See paragraph II.1.1 on the time reversal and DORT methods]. The same decomposition could thus be applied to $\mathbf{C}_{\mathrm{kk}}$ in order to retrieve the wavefront that would perfectly compensate for aberrations and optimally focus on the virtual reflector. This effect is illustrated in Fig. 5(d). It is important to emphasize, however, that the induced focal spot is enlarged compared to the diffraction limit [114, 151]. For the goal of diffraction-limited imaging, the size of this focal spot should be reduced. In the following, we express this situation mathematically, and show how to resolve it.

Based on the Van Cittert-Zernike theorem [11], we show that the correlation coefficients $C(k'_x, k_x)$ can be expressed as:

$$C(k_{\text{out}}, k'_{\text{out}}) \propto \langle|\gamma|^2\rangle \tilde{H}_{\text{out}}(k_{\text{out}})\tilde{H}^*_{\text{out}}(k_{\text{out}}, \mathbf{r}_{\text{p}}) \left[\tilde{H}_{\text{in}} * \tilde{H}_{\text{in}}\right](k_{\text{out}} - k'_{\text{out}}). \tag{III.22}$$

These coefficients are directly proportional to the Fourier transform of the scattering distribution $|H_{\text{in}}(x)|^2$ [see appendix III.D]. To reduce the size of the virtual reflector, one can equalize the Fourier spectrum of its scattering distribution. Interestingly, this can be done by normalizing the correlation matrix coefficients as follows

$$\hat{C}(k'_x, k_x) = C(k'_x, k_x)/|C(k'_x, k_x)|. \tag{III.23}$$

This operation is illustrated by Fig. 5(e). The normalized correlation matrix $\hat{\mathbf{C}}_{\text{kk}} = \left[\hat{C}(k'_x, k_x)\right]$ can be expressed as:

$$\hat{\mathbf{C}}_{\text{kk}} = \mathbf{T} \times \mathbf{\Gamma}_\delta \times \mathbf{T}^\dagger. \tag{III.24}$$

In contrast to the operator $\mathbf{\Gamma}_H$ of Eq. III.21, $\mathbf{\Gamma}_\delta$ is a scattering matrix associated with a point-like (diffraction-limited) reflector at the origin [Fig 5(e)]. A reflection matrix associated with such a point-like reflector is of rank 1 [105, 106]; this property should also hold for the normalized correlation matrix $\hat{\mathbf{C}}_{\text{kk}}$ in the case of spatially-invariant aberrations. As we will see, the first eigenvector of $\hat{\mathbf{C}}_{\text{kk}}$ yields the distorted component of the wavefront, and its phase conjugation enables compensation for aberration, resulting in optimal focusing within the corresponding isoplanatic patch.

Although the operation of Equation III.23 tends to make the size of the focal spot point-like, it also increases the noise level. Indeed, correlation coefficients associated with large angle differences are more likely to be noisy. In $\mathbf{C}_{\text{kk}}$ these signals are initially characterized by a low intensity. The normalization process then enhances these signals. While, in the phantom experiment, the SNR is quite high, it is not necessary the case for the calf experiment. This aspect will be discused later.

Beyond the isoplanatic case, the eigenvalue decomposition of $\hat{\mathbf{C}}_{\text{kk}}$ can be written as follows:

$$\hat{\mathbf{C}}_{\text{kk}} = \mathbf{U}\mathbf{\Sigma}\mathbf{U}^\dagger. \tag{III.25}$$

$\mathbf{\Sigma}$ is a diagonal matrix containing the eigenvalues σ_i in descending order: $\sigma_1 > \sigma_2 > .. > \sigma_N$. $\mathbf{U}$ is a unitary matrix that contains the orthonormal set of eigenvectors $\mathbf{U}_i$. In a conventional iterative time reversal experiment [105, 105], there is a one-to-one association between each eigenstate of the reflection matrix and each point-like target in the medium. The corresponding eigenvalue σ_i is related to the scatterer reflectivity and the eigenvector $\mathbf{U}_i$ yields the transmitted wavefront that focuses on the corresponding reflector. In this work, iterative time reversal is applied to $\hat{\mathbf{C}}_{\text{kk}}$. Each isoplanatic patch in the FOI gives rise to a virtual reflector at the origin associated with a different aberration phase law. We thus expect a one-to-one association between each isoplanatic patch p and each eigenstate of $\hat{\mathbf{C}}_{\text{kk}}$: for each isoplanatic patch, the eigenvector $\mathbf{U}_{\text{p}} = [U_{\text{p}}(k_x)]$ should yield the corresponding distorted wavefront in Fourier space, and the eigenvalue σ_{p} should provide an indicator of the focusing quality in that patch.

Figure 6(D) displays the normalized eigenvalues $\hat{\sigma}_i = \sigma_i / \sum_{j=1}^{N} \sigma_j$ of the correlation matrix $\hat{\mathbf{C}}_{\text{kk}}$ associated with the plexiglas/phantom system imaged at $c_0 = 1540$ m/s. We

clearly observe the predominance of a single eigenvector, which confirms the hypothesis of a single isoplanatic patch. Figure 6(E) shows its phase expressed in the received plane wave basis and constitutes an estimation of the receive aberration $\tilde{H}_{\text{out}}(k_{\text{out}})$. It displays a concave shape that is characterized of a speed of sound mismatch. Indeed, in the case of a wrong speed of sound hypothesis, the time-of-flight and thus the error is minimal for the angle $\theta_{\text{out}} = 0$.

III.2.4 Aberration correction in a single isoplanatic patch

Now that the first eigenstate is known, an estimator $\hat{\mathbf{T}}_{\text{p}}$ of the transmission matrix can now be calculated by combining the free-space $\mathbf{T}_0$ matrix and the normalized eigenvector $\hat{\mathbf{U}}_{\text{p}} = [U_{\text{p}}(k_x)/|U_{\text{p}}(k_x)|]$:

$$\hat{\mathbf{T}}_{\text{p}} = \hat{\mathbf{U}}_{\text{p}} \circ \mathbf{T}_0. \tag{III.26}$$

In the present example, only the first singular vector is studied, thus $p = 1$. The normalization of $\mathbf{U_p}$ ensures an equal contribution of each spatial frequency in $\hat{\mathbf{T}}_{\text{p}}$. It is thus a phase aberration correction. This point will be discussed later. Then, the transmission matrices $\hat{\mathbf{T}}_{\text{p}}$ can be used to project the reflection matrix into the focused basis, *i.e.* in the basis where the aberration has been estimated:

$$\overline{\mathbf{R}}^{\text{p}}_{\text{xx}} = \hat{\mathbf{T}}^{\dagger}_{\text{p}} \times \overline{\mathbf{R}}_{\text{kk}} \times \hat{\mathbf{T}}^{*}_{\text{p}}. \tag{III.27}$$

(We recall that in the present experiment, we correct for the filtered reflection matrix $\overline{\mathbf{R}}'_{\text{kk}}$). Note that, $\hat{T}_{\text{p}}$ has been estimated via the analysis of the aberration in reception. Thanks to the reciprocity of the wave propagation, we use the same aberration correction in transmission. This aspect will be discussed later.

Figures 2(e) and (g) illustrate the benefit of our matrix approach at depth $z = 19$ mm. While the original matrix $\overline{\mathbf{R}}'_{\text{xx}}$ exhibits a significant spreading of the backscattered energy over its off-diagonal elements [Fig. 2(e)], the corrected reflection matrix $\overline{\mathbf{R}}^{1}_{\text{xx}}$ (Eq. III.27) is almost diagonal [Fig. 2(g)]. This feature demonstrates that the input and output focal spots are now close to be diffraction-limited and that aberrations have been almost fully corrected by the transmission matrix $\mathbf{T_1}$ at depth $z = 19$ mm.

The diagonal elements of this corrected reflection matrix $\overline{\mathbf{R}}^{1}_{\text{xx}}$ yield the confocal image $\mathcal{I}_1(\mathbf{r})$ displayed in Fig. 6F. We observe a well-resolved and contrasted image of the phantom, meaning that $\mathbf{T_1}$ perfectly corrects for aberration over the entire FOV.

The corresponding Strehl ratio map $\mathcal{S}_1$ is shown in Fig. 6G. The clarity of the ultrasound image compared to the initial (Fig. 6A) and intermediate (Fig. 6B) ones, and the marked improvement in $\mathcal{S}_1$ compared to that of Fig. 6C demonstrate the effectiveness of this transmission matrix approach. A satisfying Strehl ratio $\mathcal{S}_1 \sim 0.4$ is reached over the entire field of view, and a factor of five improvement is observed at shallow and large depths where the impact of the aberrating layer is the strongest. Such an improvement of the focusing quality is far from being negligible as it translates to a gain of 14 dB in image contrast.

While we developed the focusing criterion in chapter 2, we show here that the gain in image quality can directly be quantified from the distortion matrix via the Strehl ratio, $\mathcal{S}$ [152]. Initially introduced in the context of optics, $\mathcal{S}$ is defined as the ratio of the peak intensity of the imaging system point spread function with aberration to that without.

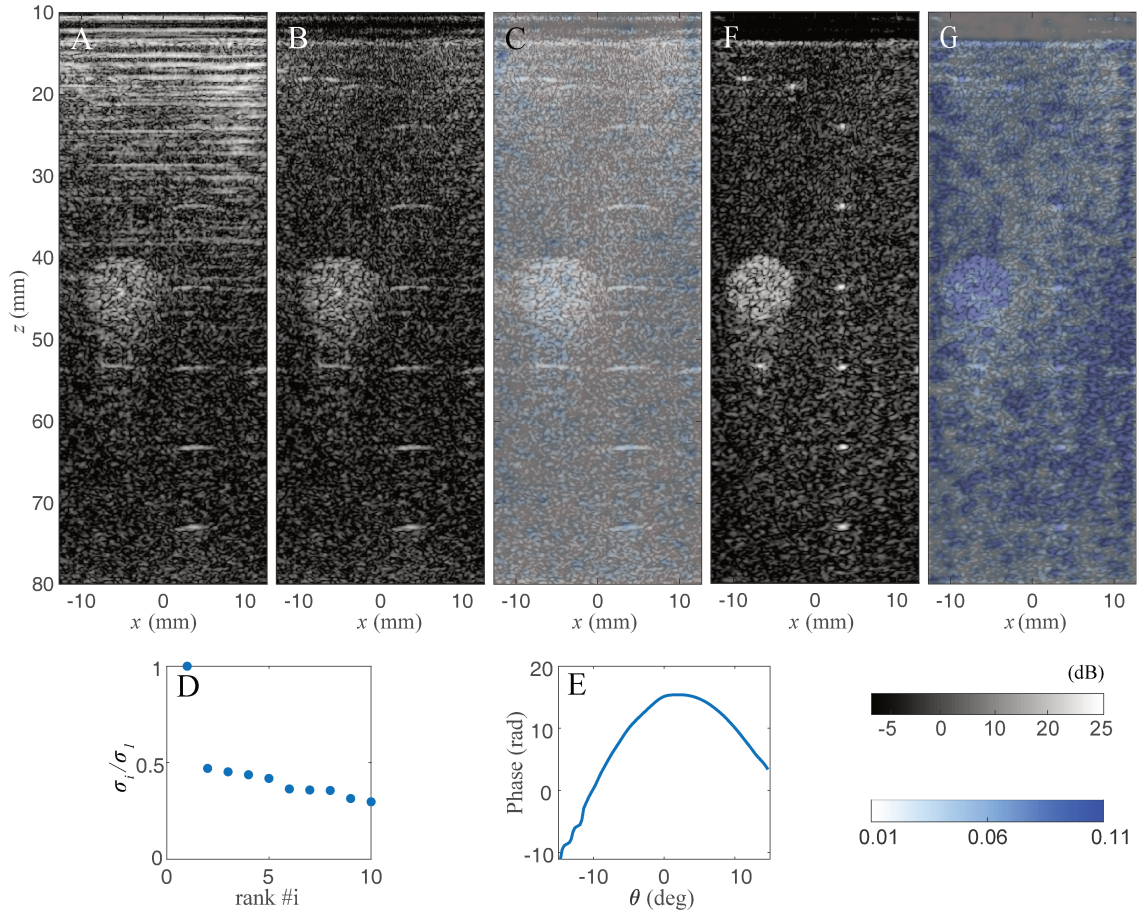

Fig. 6 *Matrix imaging based with a correct phantom wave velocity model. (A) Original ultrasound confocal image. (B) The ultrasound image after the removal of multiple reflections is shown, along with (C) the corresponding map of the Strehl ratio $\mathcal{S}$. (D) The normalized correlation matrix displays an eigenvalue spectrum dominated by one eigenstate. (E) The phase of the corresponding eigenvector is used to correct for aberrations both at input and output. (F) The ultrasound image after matrix aberration correction is shown, with (G) the corresponding map of the Strehl ratio $\mathcal{S}_{\mathcal{F}}$. The ultrasound images and Strehl ratio maps are displayed with the same dB- (B&W) and linear (color) scales, respectively.*

Equivalently, it can also be defined in the far-field as the squared magnitude of the mean aberration phase factor:

$$\mathcal{S}(\mathbf{r}_{\text{in}}) = \left| \langle D(k_{\text{out}}, \mathbf{r}_{\text{in}}) \rangle_{k_{\text{out}}} \right|^2, \tag{III.28}$$

where the symbol $\langle \cdots \rangle$ denotes an average over the variable in the subscript (which here is the output transverse wave number k_{out}). The Strehl ratio ranges from 0 for a completely degraded focal spot to 1 for a perfect focusing and enables an estimation of the focus quality at each point of the image. $\mathcal{S}$ is directly proportional to the focusing parameter introduced by Mallart and Fink in the context of ultrasound imaging [11]. As pointed out in paragraph, II.2.4.2 this criterion is more dependent on the medium reflectivity. To assess the focusing quality of the corrected image $\mathcal{S}^{\text{p}}$, we compute corrected distortion matrix associated with the corrected focused reflection matrix $\overline{\mathbf{R}}_{\text{rr}}^{\text{p}}$.

Compared to the initial value $\mathcal{S}$ displayed in Fig. 6(c), $\mathcal{S}^1$ show an improvement of the focusing quality by a factor five over the entire field of view [6(g)]. Such an improvement of the focusing quality is far from being negligible as it translates to a gain of 14 dB in image. contrast.

This proof of concept experiment opens a number of additional questions. First, despite our best efforts, the measured Strehl ratio SF does not approach the ideal value of one. Several reasons can account for this: 1) a part of the reflected wave field has been lost at shallow depth when specular reflections and clutter noise have been removed; 2) experimental noise and multiple scattering events taking place upstream of the focal plane could hamper our measure of the Strehl ratio, especially at large depths; and 3) the same correction applies to the whole frequency bandwidth, while the aberrations are likely to be dispersive (although for the phantom/plexiglass system considered here, dispersion should not be very strong). Second, this first experiment only involves a single isoplanatic patch over the entire field of view. Based on the same system but image with a different speed of sound hypothesis, we now show in the following paragraph that eigenvectors associated with a higher rank can be used to correct simultaneously for aberration laws associated to multiple isoplanatic patches.

III.3 Isoplanatic patch decomposition and Shannon Entropy.

In the previous study, we analyzed the plexiglas/phantom system at $c_0 = 1540$ m/s. We have shown that this particular speed of sound hypothesis is interesting, as it creates a single isoplanatic patch in the field of view. However, this speed of sound is not the one that minimizes the image aberration. Figure 8(a) shows the same system imaged at $c_0 = 1800$ m/s, *i.e.* at an intermediate speed of sound between the phantom and the plexiglas one. Compared to the first experiment image obtained at $c_0 = 1540$ m/s [Fig. 6A], this second experiment produces an ultrasound image that is characterized by a higher image quality. However, we show in this paragraph, that even if these aberrations are less intense, they induce multiple isoplanatic patch.

III.3.0.1 FOV decomposition into isoplanatic patches

The above described process is applied to this new experiment. By means of propagation matrices $\mathbf{P}_0$ and $\mathbf{G}_0$ defined at $c_0 = 1800$ m/s, a broadband focused reflection matrix

$\overline{\mathbf{R}}_{\mathrm{xx}}(z)$ is computed. By removing the multiple reverberations, we construct the filtered reflection matrix $\overline{\mathbf{R}}'_{\mathrm{xx}}(z)$ [Eq. III.7], whose diagonal signals contains the filtered US image $\overline{\mathcal{I}}'\mathbf{r}$ [Fig. 8(b)]. This matrix is then expressed in a dual basis to create $\overline{\mathbf{R}}_{\mathrm{kx}}(z)$ [Eq. III.10]. This matrix links the aberrated wave-front generated by each virtual source and measured in the output plane wave (or far-field) basis. By comparing with the ideal reflection matrix, we compute the distortion matrix $\mathbf{D}_{\mathrm{kr}}$ that contains the aberrated component of each aberrated wave-front [Eq. III.12]. Finally we perform a SVD of its normalized correlation matrix $\hat{\mathbf{C}}_{\mathrm{kk}}$ [Eq. III.25]. We recall that figure 3 displays a global flowchart of the aberration correction process.

Figure 7(a) displays the normalized eigenvalues $\hat{\sigma}_i = \sigma_i / \sum_{j=1}^{N} \sigma_j$ of the correlation matrix $\hat{\mathbf{C}}_{\mathrm{kk}}$. If the convergence towards the covariance matrix were complete, *i.e.* if the number of independent realization of aberrated component is large enough, the rank of $\hat{\mathbf{C}}_{\mathrm{kk}}$ should yield the number of isoplanatic patches in the ultrasound image. In Fig. 7(a), a few eigenvalues seem to dominate, but it is not clear how many are significantly above the noise background. To solve this problem, we consider the Shannon entropy $\mathcal{H}$ of the eigenvalues $\hat{\sigma}_i$ [153, 154]:

$$\mathcal{H}(\hat{\sigma}_i) = -\sum_{i=1}^{N} \hat{\sigma}_i \log_2(\hat{\sigma}_i)\,. \tag{III.29}$$

Shannon entropy yields the least biased estimate possible for the information available, *i.e.* the data set with the least artifact for a given signal-to-noise ratio. This number can be seen as an effective rank of the correlation matrix. It can thus be used as an indicator of how many eigenstates are required to create an adequate ultrasound image (without being affected by the perturbation term in Eq.III.20 [149]), *i.e.* how many isoplanatic patches in the field of view.

In this second experiment, the eigenvalues of Fig. 7(a) have an entropy of $\mathcal{H} \simeq 2.85$ [Fig. 7(c)]). Hence, only the three first eigenstates should be required to construct an unaberrated image of the medium. Figure 7B shows the phase of the three first eigenvectors $\mathbf{U}_{\mathrm{p}}$. $\mathbf{U}_1$ is almost flat and exhibits a phase standard deviation of 0.28 radians, indicating that no correction for aberration (or a very minimal one) is required for optimal focusing in the isoplanatic patch associated with that vector. $\mathbf{U}_2$ and $\mathbf{U}_3$ display a phase standard deviation of 1.36 and 1.62 radians, respectively.

Based on these three aberration law, we create three updated propagation matrices $\mathbf{T}_{\mathrm{p}}$. Each one of them provide a corrected reflection matrix $\overline{\mathbf{R}}^{\mathrm{p}}_{\mathrm{rr}}$ [Eq. III.27]. We finally extract three corrected US images $\mathcal{I}_{\mathrm{p}}(\mathbf{r})$ that are displayed on figures 7(d,f,h). We observe that each estimator $\hat{\mathbf{T}}_{\mathrm{p}}$ of the transmission matrix reveals a well-resolved and contrasted image of the phantom over distinct isoplanatic patches. $\mathbf{U_1}$ is associated with an isoplanatic patch at mid-depth ($z \simeq 45-55$ mm). As previously anticipated, correction by $\mathbf{U_1}$ leaves the image almost unchanged (compare Fig 8(a) to Fig 7(d)). This isoplanatic patch does not require aberration correction because the model wave velocity $c = 1800$ m/s is already close to the integrated speed of sound value at mid-depth. However, the phases of $\mathbf{U_2}$ and $\mathbf{U_3}$ exhibit curved shapes which indicate an incorrect model for the speed of sound c_0 (Fig 7B). While the convex shape of $\mathbf{U}_2$ suggests an underestimation of c_0, the concave shape of $\mathbf{U}_3$ indicates overestimation. Correction with the phase of each eigenvector compensates for the associated distortion effect: the confocal images show an optimized contrast and resolution at large depths ($z > 70$ mm) for $\hat{\mathbf{P}}_{\mathbf{2}}$ [Fig. 7(f)] and shallow depths

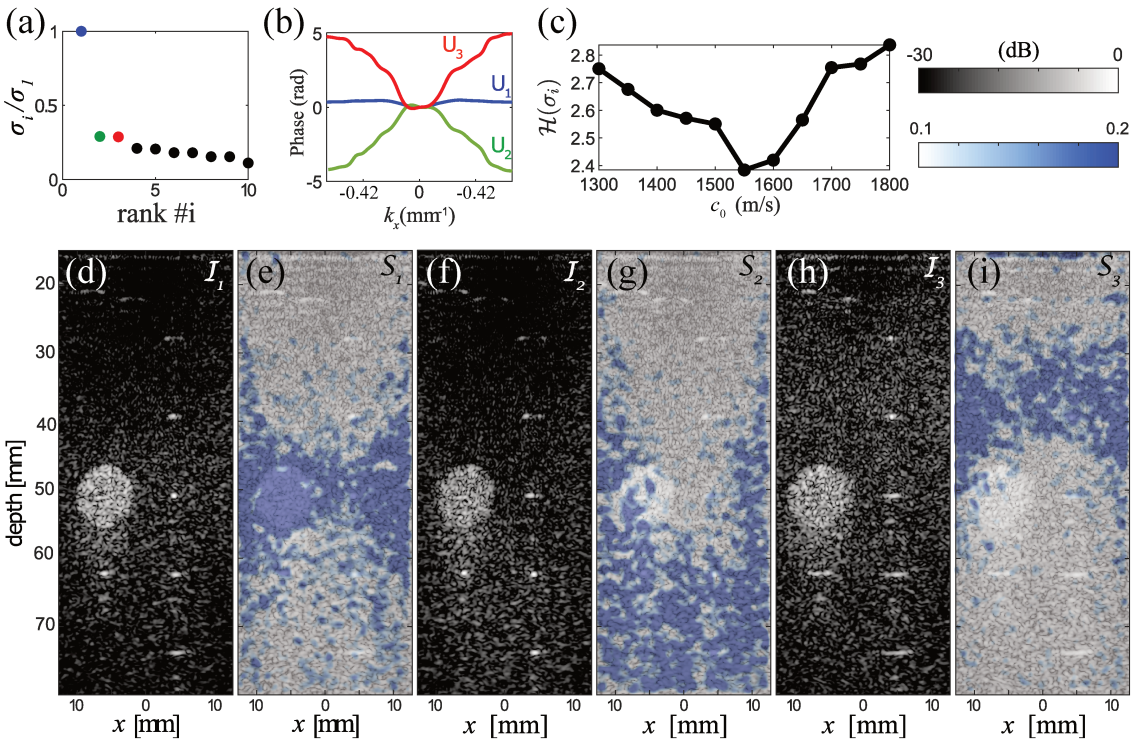

Fig. 7 *Retrieving the transmission matrix* $\mathbf{T}$ *from the correlation matrix* $\hat{\mathbf{C}}_{kk}$. *Results of the SVD of* $\hat{\mathbf{C}}_{kk}$ *are shown: (a) Normalized eigenvalues* $\tilde{\sigma}_p$, *and (b) the phase of the three first eigenvectors,* $\mathbf{U}_p$. *(c) Entropy* $\mathcal{H}$ *[Eq. III.29] of the eigenvalues* σ_i *is plotted versus the model speed of sound* c_0. *(d,F,H) corrected images* $\mathcal{I}_p(\mathbf{r})$ *are shown with (e,g,i) their corresponding Strehl ratio maps* $\mathcal{S}_p(\mathbf{r})$, *deduced from the three first transmission matrices* $\hat{\mathbf{P}}_p$ *[Eq. III.28]. The US images and Strehl ratio maps are displayed with the same dynamic, respectively.*

($25 < z < 40$ mm) for $\hat{\mathbf{P}}_\mathbf{3}$ [Fig. 7(h)].

Figures 7(e,g,i) show the three maps of Strehl ratio associated with the three corrected US images. These maps enable direct visualization of the isoplanatic area in which each different aberration correction is effective, allowing quantitative confirmation of our previous qualitative analysis of confocal images. Moreover, $\mathcal{S}_\mathrm{p}$ enables an estimation of the focus quality at each point of the image. Compared to the initial value $\mathcal{S}$ displayed in Fig. 8(c), $\mathcal{S}_2$ and $\mathcal{S}_3$ show an improvement of the focusing quality by a factor 3 at large and shallow depths, respectively [Figs. 7(g,h,i)]

The results displayed in Fig. 7 show that the decomposition of the imaging problem into isoplanatic patches, originally demonstrated with $\mathbf{D}_\mathrm{kx}$ for large specular reflectors in optics [149], also holds in a random speckle regime if we consider, this time, the normalized correlation matrix $\hat{\mathbf{C}}_\mathrm{kk}$. In fact, the process actually performs even better in speckle than for specular reflectors, since it is possible to discriminate between aberrations in input and output, and hence to correct for each independently. The drawback here lies in the fact that corrections over each isoplanatic patch are difficult to combine. To address this

issue, we will perform a local analysis of the distortion matrix.

III.3.0.2 Shannon entropy minimization, a local indicator of the medium speed of sound

The information held in the distortion matrix can be used very flexibly, enabling multiple routes towards aberration-free full-field imaging. Here, we propose a novel approach to measure locally the medium the speed of sound *via* a minimization of the Shannon entropy.

This technique is based on two observations. First, we demonstrated that in the previous paragraphs there is a direct relation between the Shannon entropy $\mathcal{H}(\sigma_i)$ of the normalized correlation matrix $\hat{\mathbf{C}}_{\mathrm{kk}}$ and the number N_p of isoplanatic patches contained in the region of interest. Second, we observe that if the assume speed of sound c_0 matches the local speed of sound of the medium in the region of interest (ROI) c; then, the aberrated wave-front generated by each virtual source of this ROI occur between the top of this ROI and the probe. In the case of a stratified medium and for this particular speed of sound, these aberrations then induce a single isoplanatic patch in the ROI that can be corrected only by the first singular vector.

Therefore, by correcting the ultrasound image by means of the first eigenvector $\mathbf{U_1}$, the Shannon entropy associated with a corrected distortion matrix probes the ability of $\mathbf{U_1}$ to correct for all the aberrations in the ROI. This corrected Shanon entropy is then minimal when the ROI is composed of a single isoplanatic patch, and thus when the assumed speed of sound matches the medium one.

Figure 7(c) provides a first proof-of-concept of this idea. It shows the entropy $\mathcal{H}(\sigma_i)$ as a function of the speed of sound c_0 used to model the propagation of ultrasonic waves in the FOI considered (here, the phantom down to $z = 80$ mm). $\mathcal{H}(\sigma_i)$ exhibits a minimum around $c = 1550$ m/s, which is close to the speed of sound c_p in the phantom.

Note that while the entropy $\mathcal{H}_1(\sigma_i)$ displays a minimum, it does not reach the ideal value of 1. A first reason for this is the perturbation term in Eq. III.20: experimental noise and an insufficient number of input focal points can hinder perfect smoothing of the fluctuations caused by the random sample reflectivity. Another potential reason is that imperfections in the probe or plexiglass layer could induce lateral variations of the aberrations upstream of the ROI.

III.3.1 Conclusion

The distortion matrix approach described in the previous two sections provides a powerful tool for imaging inside a heterogeneous medium with *a priori* unknown characteristics. Aberrations can be corrected without any guide stars or prior knowledge of the speed of sound distribution in the medium. While our method is inspired by previous works in ultrasound imaging [47, 11, 38, 61, 62], and is built on the recent introduction of the distortion matrix in optics [149], it features several distinct and important advances. The first is its primary building block: the broadband focused reflection matrix that precisely selects the echoes originating from a single scattering event at each depth. This operation is decisive in terms of signal-to-noise ratio since it drastically reduces the detrimental contribution of out-of-focus and multiply-scattered echoes. Equally importantly, this matrix captures all of the input-output spatial correlations of these singly-scattered echoes.

The approach presented here also introduces the projection of the reflection matrix in the far-field. This enables the elimination of artifacts from multiple reflections between parallel surfaces, revealing previously hidden parts of the image. Here, we have only examined reflections from surfaces which are parallel to the ultrasound array, which is more relevant for imaging layered materials than it is for imaging human tissue. While signatures of other flat surfaces should be identifiable as correlations in off-antidiagonal lines of $\overline{\mathbf{R}}_{\mathrm{kk}}$ or in other mathematical bases [155], reverberations from uneven or curved surfaces can not, at present, be addressed with this method.

For aberration correction, projection of the reflection matrix into a dual basis allows the isolation of the distorted component. Then, all of the input focal spots can be superimposed onto the same (virtual) location. The normalized correlation of these distorted wave-fields, and an average over disorder, then enables the synthesis of a virtual coherent reflector. Unlike related works in acoustics [38, 61, 62], this virtual scatterer is point-like, i.e. not limited by the size of the aberrated focal spot. Here, we demonstrate how the randomness of a scattering medium can be leveraged to identify multiple isoplanatic patches at the same time and correct for associated aberrations both input and output.

By means of a two layer medium, we have first tackled the case of a single isoplanatic patch in the field of view. The analysis of the distortion matrix enables to extract an aberration law that perfectly corrects for aberration over the entire region. By modifying the hypothesis of speed of sound, we have then turned our attention to a more complex configuration where the medium under investigation is composed of multiple isoplanatic patches. We demonstrate how the randomness of a scattering medium can be leveraged to identify multiple isoplanatic patches at the same time and correct for associated aberrations both input and output.

While this elegant approach does not requires any assumption on the number of isoplanatic patches, the drawback here lies in the fact that corrections over each isoplanatic patch are difficult to combine. To address this issue, we will perform a local analysis of the distortion matrix called matrix aberration correction. In addition, we only investigate aberrations in reception. To tackle the case of laterally varying aberrations, we will also study the aberrations in transmission.

Finally, figure 8(d) shows the results of this matrix aberration correction of aberration correction. We observe that this technique enables to produce an optimal ultrasound image despite of multiple isoplanatic patches.

III.4 Matrix imaging for local aberration correction

In the previous section, we introduced the concept of distortion matrix. Based on the plexiglas/phantom system, we show how to perform an isoplanatic patch decomposition that enables to (*i*) estimate the number of isoplanatic patches in the field of view, (*ii*) estimate simultaneously the aberration laws associated with each one of these patches (*iii*) perfectly and individually correct for aberration. To perform this analysis we used a simple stratified medium. In this case, we demonstrated that aberration are better corrected in the plane wave basis and the entire analysis was performed in the received plane wave basis. Transmitted aberration have been estimated based on the reciprocity of the wave propagation. This first route requires any assumption on the aberrations

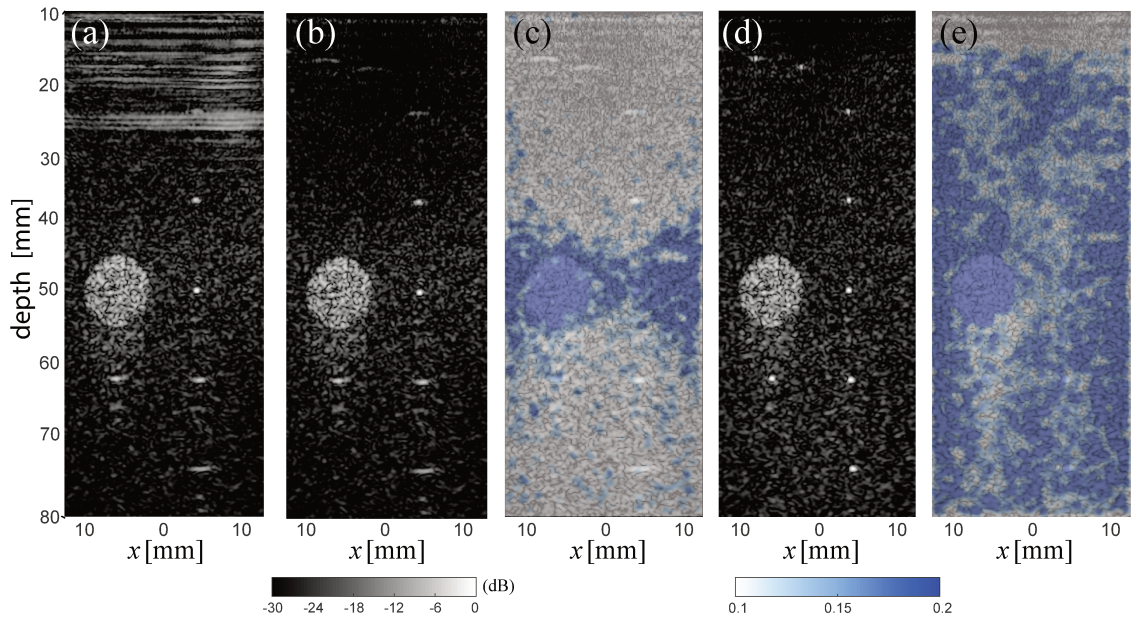

Fig. 8 *Matrix aberration correction. (a) Original ultrasound confocal image with $c = 1800$ m/s. (b) The ultrasound image after the removal of multiple reflections is shown, along with (c) the corresponding map of the Strehl ratio $\mathcal{S}$.(d) The ultrasound image after the matrix aberration correction is shown, with (e) the corresponding map of the Strehl ratio $\mathcal{S}_{\mathcal{F}}$. The ultrasound images and Strehl ratio maps are displayed with the same dB- (B&W) and linear (color) scales, respectively.*

to correct and on their associated isoplanatic patches. However, it suffers from a major drawback that lies in the fact that corrections over each isoplanatic patch are difficult to combine.

In this section, we propose an other routes for aberration via a local analysis of the distortion matrix. We base our analysis on the calf experiment and we assume that no *a priori* information on the medium is available. To tackle this issue, we investigate a four-iterative correction process in order to analyze aberration both at the input and output basis, and both in the plane wave and transducer basis. As the previous section described the rigorous mathematical foundations and basic experimental proof-of-concepts of matrix imaging, the current section provides a complementary description of the method, explaining each step in details. While these new insights are crucial for implementing matrix imaging, this section also provides additional information about the physical mechanism behind the aberration correction process. In the previous section, the aberration correction process was described in the far-field basis, we first describe each step of the aberration correction process in the transducer basis under the isoplanatic hypothesis. Then, we show how to go beyond this limit and retrieve a different focusing law for each pixel of the image. Finally, we propose an entire aberration correction strategy and discuss each step that provides a global understanding of all the capabilities of this elegant and flexible matrix imaging approach.

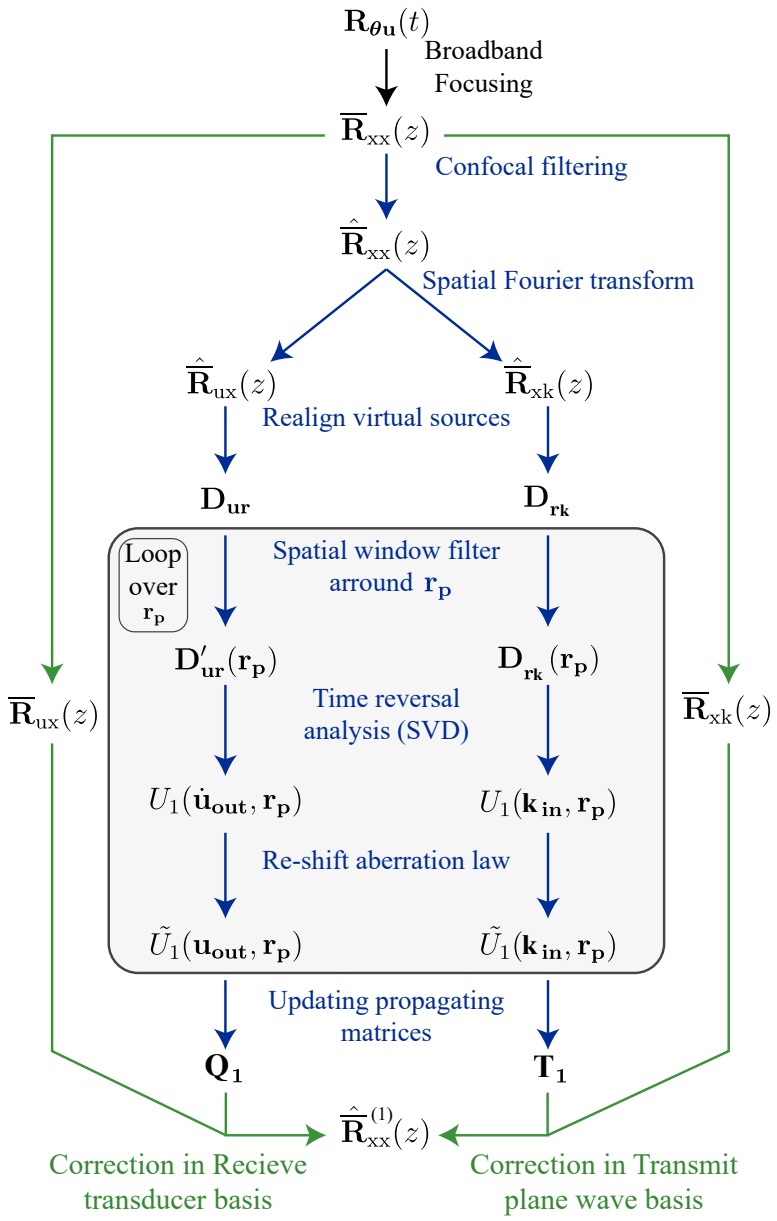

Fig. 9 *Workchart of the first iteration of the aberration correction process. The transmitted and received correcting basis are the plane wave and transducer basis, respectively. The blue steps of the process refer to the estimation of the aberration phase laws, while the green steps refer to the aberration correction. The gray rectangle symbolizes a loop over all the spatial window centered on* $\mathbf{r}_p$.

III.4.1 Filtering multiple scattering and noise

As stated above, the first step consists in computing the broadband focused reflection matrix $\overline{\mathbf{R}}_{xx}(z)$ [Eq. II.34] by means of $\mathbf{P}_0$ and $\mathbf{G}_0$ [Eqs. II.14a and II.14b]. In the matrix $\overline{\mathbf{R}}_{xx}$, we recall that the singly-scattered echoes are concentrated along the diagonal of the matrix, while multiply-scattered echoes spread over all the coefficients of the reflection matrix [69]. The spatial extension of this halo along the anti-diagonals of this matrix highlights the input-output PSF II.2.4.

For US imaging, only the singly-scattered echoes are of interest. The multiply-scattered echoes can be partly removed by means of an adaptive confocal filter [156, 139]. It consists in weighting the coefficients $\overline{R}(x_{\text{in}}, x_{\text{out}}, z)$ of the focused reflection matrix as a function of the distance $|x_{\text{out}} - x_{\text{in}}|$ between the virtual transducers, such that:

$$\hat{\overline{R}}(x_{\text{out}}, x_{\text{in}}) = \overline{R}(x_{\text{out}}, x_{\text{in}}) \exp\left[-\frac{|\, x_{\text{out}} - x_{\text{in}}\,|^2}{2l_c(\mathbf{r})^2}\right]. \tag{III.30}$$

The chosen filter has a Gaussian-shaped with a characteristic size $l_c(\mathbf{r})$ that matches the input-output resolution $\overline{w}(\mathbf{r})$. For areas where the estimation of $\overline{w}(\mathbf{r})$ fails, l_c is arbitrarily set to $5\overline{\delta x}_0$.

Figures 10(b,c) show the original broadband focused reflection matrix $\overline{\mathbf{R}}_{xx}$ and the filtered one $\hat{\overline{\mathbf{R}}}_{xx}$ respectively, computed at $z = 28$ mm [white continuous line on figure 12(d)]. By applying this confocal filter, a part of the multiple scattering contribution found in $\overline{\mathbf{R}}_{xx}$ is removed. However, $\hat{\overline{\mathbf{R}}}_{xx}$ still contains a residual multiple scattering component since the latter one also occurs along close diagonal coefficients. Note that this filter has no impact on the raw ultrasound image since the confocal signals are unaffected. However, it constitutes a necessary step for the determination of the aberration law as it greatly improves the SNR.

III.4.2 Projection of the reflection matrix in the correction basis

In adaptive focusing, the aberrating layer is often modeled as a random phase screen. For an optimal correction, ultrasonic data should be back-propagated to the plane containing the aberrating layer. Indeed, from this plane, the aberration is spatially-invariant. By applying the phase conjugate of the aberration phase law, aberrations can be fully compensated at any point of the medium. However, in real life, speed-of-sound inhomogeneities are distributed over the whole medium and aberrations can take place everywhere. In that case, the strategy is to back-propagate ultrasound data in several planes from which the aberration phase law should be estimated and then compensated. The correction planes should be chosen according to the following criterion: Maximizing the size of isoplanatic patches. For multi-layered media, a far-field plane is the most adequate since plane waves are the propagation invariants in this geometry. For aberrations induced by the skin or fat layers, the probe plane is a good choice. In this section, the aberration correction will be performed in these two planes as they coincide also to the emission and reception bases used to record the reflection matrix. However, note that, in practice, other correction planes can be chosen according to the imaging problem.

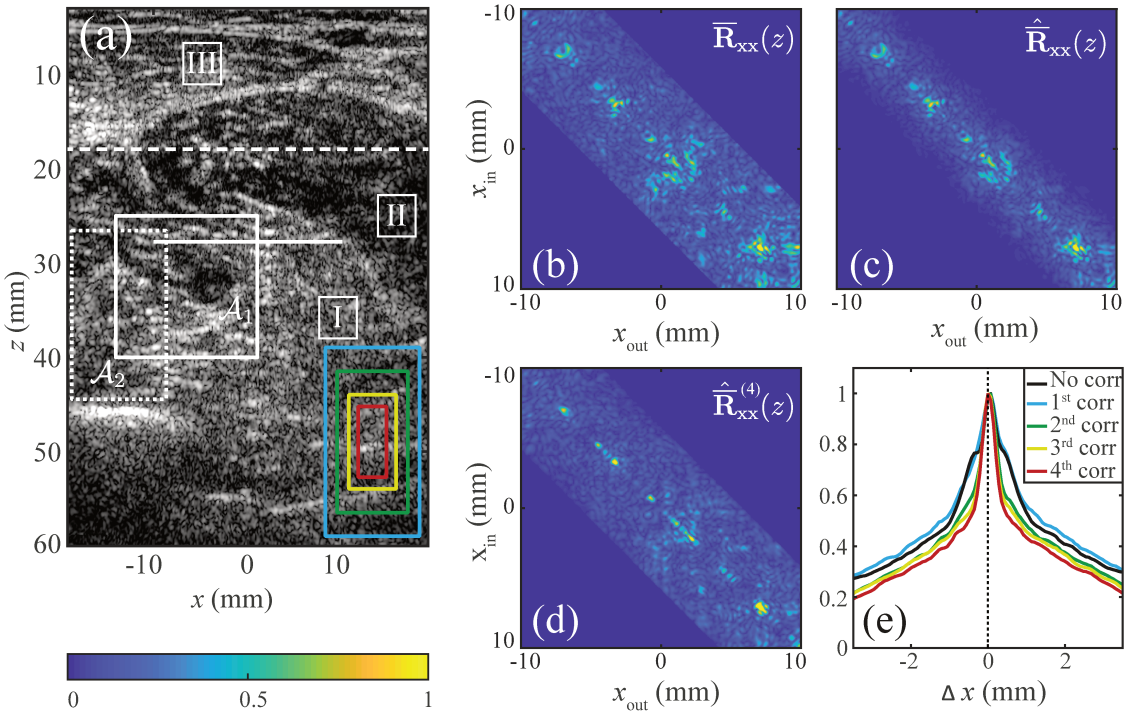

Fig. 10 *(a) US image. The continuous white line highlights the location of the FR matrixs displayed in Figs. 10(a-c). The continuous white square $\mathcal{A}_1$ defines the area used for estimating the average CMP intensity profiles displayed in Fig. 10(d). The dotted white square $\mathcal{A}_2$ highlights the spatial window used for computing the correlation matrix displayed on Fig. 13. The four colored straight rectangles correspond to the spatial windows W_L used for the four iterative corrections (from the largest to the smallest).*
Evolution of the broadbandfocused reflection matrix $\overline{\mathbf{R}}_{xx}(z)$ during the aberration correction process at depth $z = 28$ mm [white continuous line in (a)]. (b) Original focused reflection matrix $\overline{\mathbf{R}}_{xx}(z)$. (c) To estimate the aberration phase laws, a confocal filter is first applied to $\hat{\overline{\mathbf{R}}}_{xx}(z)$ to reject a large part of the electronic noise and multiple scattering background, thereby improving the SNR [Eq. III.30]. (d) Corrected FR matrix $\overline{\mathbf{R}}^{(4)}_{rr}$ obtained after the fourth iteration of the correction process. The single scattering contribution that initially spreads over off-diagonal coefficients is now concentrated along the diagonal of $\overline{\mathbf{R}}^{(4)}_{xx}(z)$, meaning that the resolution has been drastically improved. (d) Evolution of the CMP intensity profiles $\overline{I}^{(i)}_{av}(\mathbf{r}, \Delta x)$ spatially averaged over the area $\mathcal{A}_1$ [Fig. (d)] at each iteration i of the aberration correction process.

III.4.2.1 Projection in the far-field

As described in paragraph III.2.1, to project the reflected wave-field in the far-field, a spatial Fourier transform should be applied to the outpout of $\hat{\overline{\mathbf{R}}}_{\mathrm{xx}}(z)$:

$$\hat{\overline{\mathbf{R}}}_{\mathrm{kx}}(z) = \mathbf{T_0} \times \hat{\overline{\mathbf{R}}}_{\mathrm{xx}}(z). \tag{III.31}$$

where $\mathbf{T_0}$ is the Fourier transform operator,

$$T_0(k_x, x) = \exp\left(ik_x x\right), \tag{III.32}$$

and k_x the transverse wave number. $\hat{\overline{\mathbf{R}}}_{\mathrm{kx}}(z)$ contains the set of far-field aberrated wavefronts generated by each virtual source $\mathbf{r}_{\mathrm{in}}$. Figure 11(a) shows the phase of $\hat{\overline{\mathbf{R}}}_{\mathrm{kx}}(z)$ obtained at $z = 18$ mm [dashed white line on figure 12(a)]. Using the central frequency f_c as a reference frequency, the transverse wave number can be associated with a plane wave of angle $\dot{\theta}$, such that $k_x = k_c \sin(\dot{\theta})$, with $k_c = 2\pi f_c/c$ the wave number at the central frequency. Expressing the far-field projection as a plane wave decomposition is useful to define the boundaries of this basis. The maximum transverse wave number is indeed related to β the maximum angle of wave illumination (in transmit mode) or collection (in receive mode) by the array [white dashed lines on Figure 11(a)]. The matrix $\hat{\overline{\mathbf{R}}}_{\mathrm{kx}}(z)$ will be used to tackle the aberrations in the receive plane wave basis.

A reciprocal projection can also be performed at the input of $\overline{\mathbf{R}}_{\mathrm{xx}}(z)$:

$$\hat{\overline{\mathbf{R}}}_{\mathrm{xk}}(z) = \hat{\overline{\mathbf{R}}}_{\mathrm{xx}}(z) \times \mathbf{T_0}^{\top}. \tag{III.33}$$

The coefficients $\hat{\overline{R}}(x_{\mathrm{out}}, k_{\mathrm{in}}, z)$ correspond to the wave-field probed by the virtual transducer at $\mathbf{r}_{\mathrm{out}}$ if a plane wave of transverse wave number k_{in} illuminated the medium. Figure 11(d) shows the phase of $\hat{\overline{\mathbf{R}}}_{\mathrm{kx}}(z)$ obtained at $z = 18$ mm. This matrix will be used to investigate the aberrations in the transmit plane wave basis.

III.4.2.2 Projection in the transducer basis

Similarly, to analyze aberrations in the transducer plane, we consider the free-space transmission matrix $\mathbf{Q}_0$ defined between the focused and the transducer bases at the central frequency f_c:

$$\mathbf{Q}_0 = \mathbf{T}_0^{-1} \times \left(\mathbf{P}_z \circ \mathbf{T}_0\right), \tag{III.34}$$

where the symbol $\circ$ stands for the Hadamard product and $\mathbf{P}_z = [P_z(k_x, z)]$ is the plane wave propagator at the central frequency:

$$P_z(k_x, z) = e^{i\sqrt{k_c^2 - k_x^2}z}. \tag{III.35}$$

The elements of $\mathbf{Q}_0$ link any point $\mathbf{r}$ in the focal plane to any transducer u:

$$Q_0(x, z, u) = \sum_{k_x} e^{i(k_x(x-u) + \sqrt{k_c^2 - k_x^2}z)}. \tag{III.36}$$

The operator $\mathbf{Q}_0$ can be given a physical interpretation by reading the terms of Eq. III.34 from right to left: (i) a spatial Fourier transform using the operator $\mathbf{T}_0$ to project the

wave-field in the plane wave basis; (ii) the plane wave propagation modeled by the propagator $\mathbf{P}_z$ between the focal and transducers' planes over a distance z; (iii) an inverse Fourier transformation $\mathbf{T}_0^{-1}$ that finally projects the wave-field in the transducer basis. To enlighten the physical meaning of this operator, its coefficients can be expressed under the Fresnel approximation as follows:

$$Q_0(\mathbf{r},u) \approx e^{ik_c z} e^{ik_c x^2/(2z)} e^{ik_u(u-x)}, \tag{III.37}$$

where $k_u = k_c u/z$ can be seen as a transverse wave number. Using this operator $\mathbf{Q}_0$, the matrix $\hat{\overline{\mathbf{R}}}_{\mathrm{xx}}$ can be projected in the transducer basis either at input,

$$\hat{\overline{\mathbf{R}}}_{\mathrm{xu}}(z) = \hat{\overline{\mathbf{R}}}_{\mathrm{xx}}(z) \times \mathbf{Q_0}^{\top} \tag{III.38}$$

or output,

$$\hat{\overline{\mathbf{R}}}_{\mathrm{ux}}(z) = \mathbf{Q_0} \times \hat{\overline{\mathbf{R}}}_{\mathrm{xx}}(z), \tag{III.39}$$

Each column of $\hat{\overline{\mathbf{R}}}_{\mathrm{xu}}(z)$= $[\hat{\overline{R}}(x_{\mathrm{out}},u_{\mathrm{in}},z)]$ is the wave-field received by the virtual transducer at $\mathbf{r}_{\mathrm{out}}$ for an incident wave-field emitted from a transducer at u_{in}. Reciprocally, each row of $\hat{\overline{\mathbf{R}}}_{\mathrm{ux}}(z) = [R(u_{\mathrm{out}},x_{\mathrm{in}},z)]$ contains the wave-front recorded by the transducers for a virtual source in the focal plane at $\mathbf{r}_{\mathrm{in}}$. Figure 11(d) shows the phase of $\hat{\overline{\mathbf{R}}}_{\mathrm{ux}}(z)$ obtained at $z = 18$ mm [dashed white line on Fig. 12(d)]. Similarly to the plane wave basis, the spatial extension of the reflected wave-field in the transducer basis coincides with the physical aperture of the array used to collect the echoes coming from a depth z [white dashed lines on Figure 11(d)].

III.4.2.3 Discussion

We might expect to observe correlations between the columns of matrices $\hat{\overline{\mathbf{R}}}_{\mathrm{kx}}(z)$ and $\hat{\overline{\mathbf{R}}}_{\mathrm{ux}}(z)$ displayed in Figs. 11(a) and (d). Neighbor virtual sources $\mathbf{r}_{\mathrm{in}}$ belong *a priori* to the same isoplanatic patch. The associated wave-fronts in the transducer plane or in the far-field should thus be, in principle, strongly correlated since they travel through the same area of the aberrating layer. However, such correlations are not obvious by eye in Figs. 11(a) and (d). This phenomenon is caused by the random reflectivity of the medium. Similarly to the previous section, we show how the distortion matrix is able to reveal those hidden correlations. Here, we will mostly consider the transducer basis as the far-field case has already been tackled in in paragraph III.2.2

III.4.3 The distortion matrix

To reveal the isoplanaticity of the reflected wave-field, each aberrated wave-front [Fig. 11(g)] contained in the reflection matrix $\hat{\overline{\mathbf{R}}}_{\mathrm{ux}}(z)$ should be decomposed into two components: (*i*) a geometric component described by $\mathbf{Q}_0(z)$ [Fig. 11(e)], which contains the ideal wave-front induced by the virtual source $\mathbf{r}_{\mathrm{in}}$ that would be obtained in the homogeneous medium used to model the wave propagation [Fig. 11(h)]; (*ii*) a distorted component due to the mismatch between the propagation model and reality [Fig. 11(i)]. A key idea is to isolate the latter contribution by subtracting, from the experimentally measured

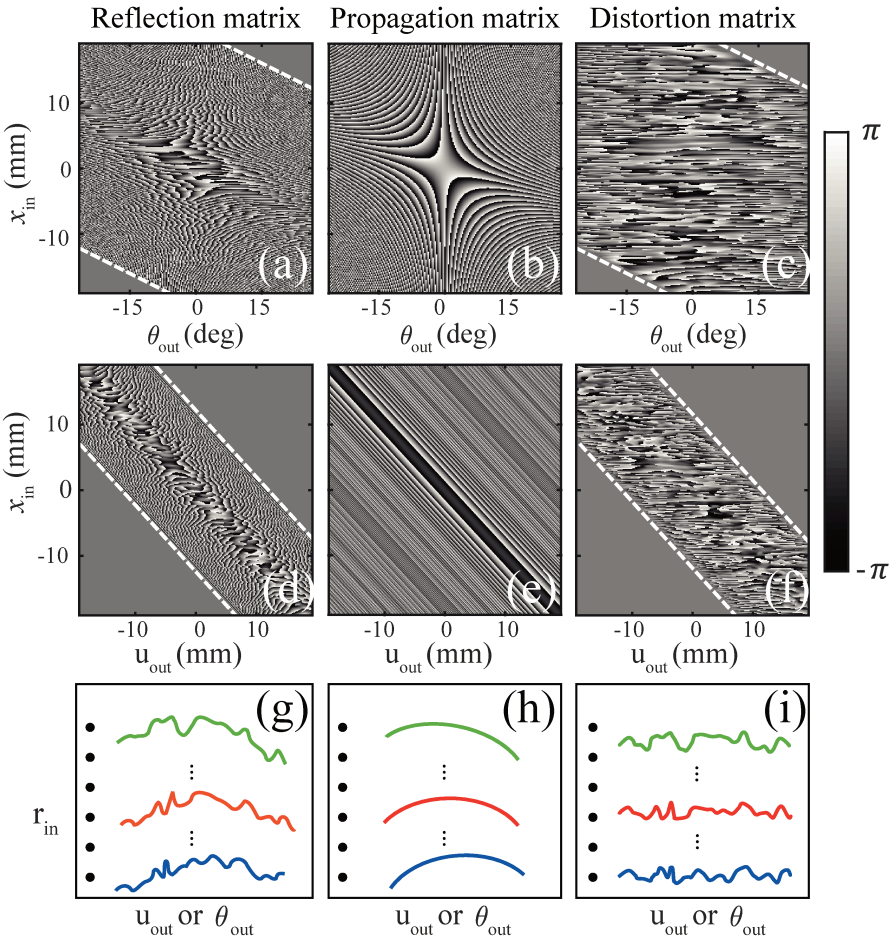

Fig. 11 *Revealing the correlations of the reflected wavefield. By comparing the reflection matrices (a,d,g), to their corresponding transmission matrices (b,e,h), the distortion matrices (c,f,i) extract long range correlation that can be visualized between their lines. However, those correlations are somehow hidden by the random reflectivity of the medium imposed by the speckle regime. These matrices are expressed in a dual basis that link the focused basis in transmit* $\mathbf{r}_{in}$ *to a correcting basis in receive, which can be either the spatial Fourier basis (plane waves basis)* θ_{out} *(a,b,c) or the transducer basis* u *(d,e,f). For both cases, the edge of the reflection and distortion matrices are removed according to* $\beta(\mathbf{r})$*, the maximum angles of wave illumination or collection by the array for each virtual source located at* $\mathbf{r}_{in}$ *(white dashed lines). (g,h,i) Sketches of the wave-fronts contained in the matrices displayed above.*

wavefront, its ideal counterpart. Mathematically, this operation can be done by means of an Hadamard product between $\hat{\overline{\mathbf{R}}}_{\mathrm{ux}}(z)$ and $\mathbf{Q}_0^*(z)$:

$$\mathbf{D}_{\mathrm{ux}}(z) = \hat{\overline{\mathbf{R}}}_{\mathrm{ux}}(z) \circ \mathbf{Q}_0^*(z). \tag{III.40}$$

$\mathbf{D}_{\mathrm{ur}} = \mathbf{D}_{\mathrm{ux}}(z) = [D(u_{\mathrm{out}}, \{x_{\mathrm{in}}, z\})]$ is called the distortion matrix. It connects any input focal point $\mathbf{r}_{\mathrm{in}}$ to the distorted component of the reflected wavefield in the transducer basis. Using Eq. III.37, the coefficients of the distortion matrix can be written as follows under the Fresnel approximation:

$$D(u_{\mathrm{out}}, \{x_{\mathrm{in}}, z\}) = \sum_{x_{\mathrm{out}}} \hat{\overline{R}}(x_{\mathrm{out}}, x_{\mathrm{in}}, z) \exp\left[i\frac{k_c}{2z}(x_{\mathrm{out}}^2 - x_{\mathrm{in}}^2)\right] \exp\left[i\frac{k_c}{z}u_{\mathrm{out}}(x_{\mathrm{out}} - x_{\mathrm{in}})\right], \tag{III.41}$$

For $(x_{\mathrm{in}} + x_{\mathrm{out}}) << \lambda_c z/\delta x$, the parabolic phase term can be neglected. In that case, Eq. III.41 becomes:

$$D(u_{\mathrm{out}}, \{x_{\mathrm{in}}, z\}) = \sum_{\delta x} \hat{\overline{R}}(x_{\mathrm{in}} + \delta x, x_{\mathrm{in}}, z) \exp\left[i\frac{k_c}{z}u_{\mathrm{out}}\ \delta x\right], \tag{III.42}$$

with $\delta x = x_{\mathrm{out}} - x_{\mathrm{in}}$. Mathematically, each row of $\mathbf{D}$ is the Fourier transform of the focused wave-field re-centered around each focusing point $\mathbf{r}_{\mathrm{in}}$. Again, the distortion matrix $\mathbf{D}$ can thus be seen as a reflection matrix for different realizations of virtual sources, all shifted at the origin of the focal plane ($x_{in} = 0$) [Figs. 14(a,b)]. The co-location of the virtual sources at the same point accounts for the much larger correlation degree between the columns of $\mathbf{D}_{\mathrm{ux}}$ [Fig. 11(f)] than for the reflection matrix $\hat{\overline{\mathbf{R}}}_{\mathrm{ux}}$ [Fig. 11(d)].

Note that equivalent distortion matrices, $\mathbf{D}_{\mathrm{xu}}$, $\mathbf{D}_{\mathrm{kx}}$ and $\mathbf{D}_{\mathrm{xk}}$ can be built from the other reflection matrices previously defined, $\hat{\overline{\mathbf{R}}}_{\mathrm{xu}}$, $\hat{\overline{\mathbf{R}}}_{\mathrm{kx}}$ and $\hat{\overline{\mathbf{R}}}_{\mathrm{xk}}$. For $\mathbf{D}_{\mathrm{xu}}$, the same reasoning as above can be used by exchanging input and output. For the far-field distortion matrices, $\mathbf{D}_{\mathrm{kx}}$ and $\mathbf{D}_{\mathrm{xk}}$, the demonstration has already been done in a previous work [40]. The comparison between the phase of $\hat{\overline{\mathbf{R}}}_{\mathrm{kx}}$ [Fig. 11(a)] and $\mathbf{D}_{\mathrm{kx}}$ [Fig. 11(c)] highlights the high correlation degree of the distorted wave-fields in the far-field thanks to the virtual shift of all the input focal spots at the origin.

III.4.3.1 Local distortion matrices

Virtual sources, that belong to the same isoplanatic patch, should give rise to strongly correlated distorted wave-fronts despite the random reflectivity of the medium [Fig. 11(c,f)]. To correct for multiple isoplanatic patches in the field-of-view, we first show in the previous section III.2 [40, 149] that the distortion matrix can be analyzed over the whole field-of-view. Its effective rank is then equal to the number of isoplanatic patches contained in this field-of-view, while its singular vectors yield the corresponding aberration phase laws. The proof-of-concept of this fundamental result has first been demonstrated in optics for specular reflectors [149], then in ultrasound speckle for multi-layered media [40].

For ultrasound *in-vivo* imaging, the fluctuations of the speed-of-sound occur both in the lateral and axial directions. For instance, the strong fluctuations of the F-map displayed in Fig. 12(a) illustrate the complexity of the speed-of-sound distribution in the

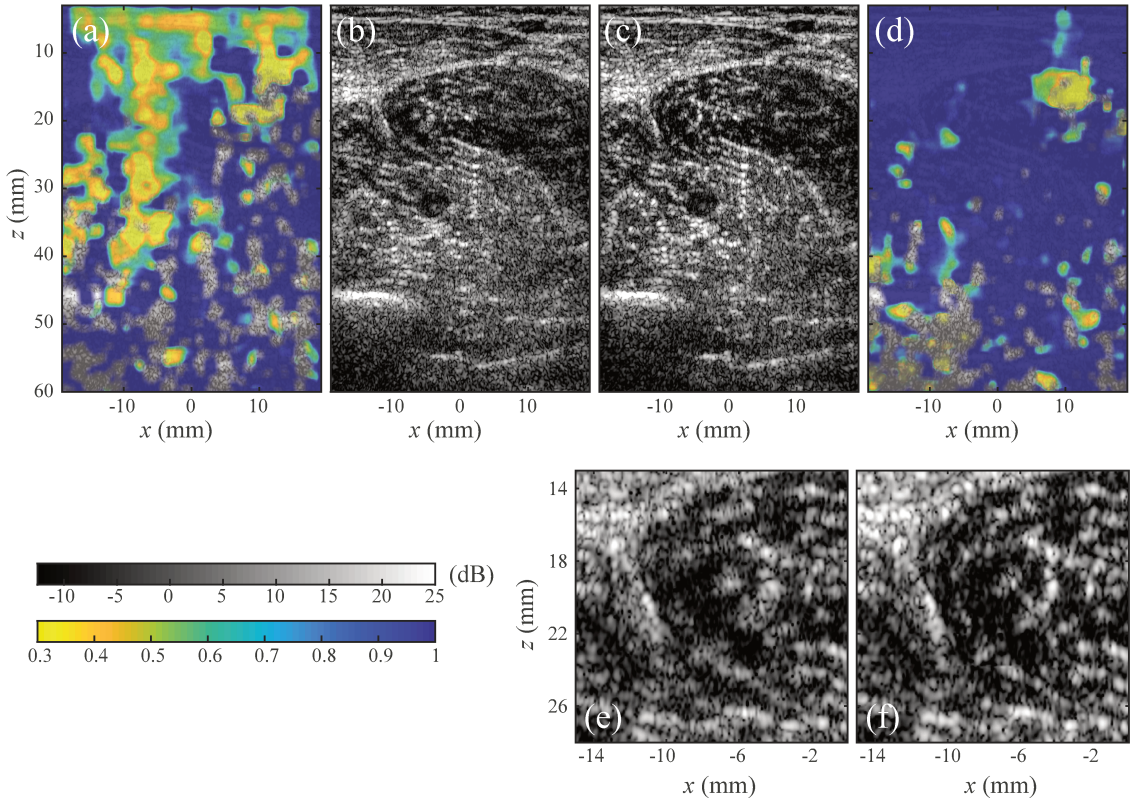

Fig. 12 *Results of the aberration correction process applied to the in-vivo case of the human calf. (a) Focusing criterion superimposed to the corresponding conventional ultrasound image. (b) Conventional multi-focus image. (c) Corrected multi-focus image after the matrix imaging process. (d) Focusing criterion superimposed to the corrected image. (e,f) Zoom on the initial and corrected images, respectively. The ultrasound images have been normalised by their mean intensity.*

human calf. In this case, any point in the medium is associated with a distinct aberration phase law. A transmission matrix that connects the correction basis and the focused basis should thus be found. A local strategy should thus be employed for the distortion matrix. The idea is to take advantage of the finite coherence area of the aberration phase law around each focusing point.

The field-of-illumination (FOI), which gathers all the location of the virtual source is thus divided into overlapping regions that are defined by their central midpoint $\mathbf{r}_\mathrm{p}$ and spatial extension $\Delta\mathbf{r} = \{\Delta x, \Delta z\}$. All the distorted components associated with focusing points $\mathbf{r}_\mathrm{in}$ located within each region are extracted and stored in a local distortion matrix $\mathbf{D}'_\mathrm{ur}(\mathbf{r}_\mathrm{p})$:

$$D'(u_\mathrm{out}, \mathbf{r}_\mathrm{in}, \mathbf{r}_\mathrm{p}) = D(u_\mathrm{out}, \mathbf{r}_\mathrm{in})\ W_{\Delta\mathbf{r}}(\mathbf{r}_\mathrm{in} - \mathbf{r}_\mathrm{p}), \tag{III.43}$$

with $W_{\Delta\mathbf{r}}$ a spatial window function:

$$W_{\Delta\mathbf{r}}(\mathbf{r}) = W_{\Delta x,\Delta z}(\mathbf{r}) = \begin{cases} 1 & \text{for } |x| < \Delta x \\ & \quad \text{and } |z| < \Delta z \\ 0 & \text{otherwise} \end{cases}$$

Ideally, each sub-distortion matrix should gather a set of focusing points $\mathbf{r}_{\text{in}}$ belonging to the same isoplanatic patch. In reality, the isoplanicity condition is never completely fulfilled. A delicate compromise has thus to be made on the size $\Delta\mathbf{r}$ of the window function: sufficiently small to approach the isoplanatic condition, sufficiently large to have access to enough independent realizations of disorder [see appendix III.E]. This last point will be discussed at the end of paragraph. III.4.4 and the strategy developed for the choice of $\Delta\mathbf{r}$ will be tackled in paragraph III.4.8.

III.4.3.2 Isoplanicity

For sake of analytical tractability, the isoplanatic condition is assumed to be fulfilled over each region of size $\Delta\mathbf{r}$. This hypothesis implies that the broadband PSFs $\overline{H}_{\text{in}}$ and $\overline{H}_{\text{out}}$ are invariant by translation in each region: $\overline{H}_{\text{in/out}}(x', x, z) = \overline{H}_{in/out}(x' - x, z, \mathbf{r}_{\text{p}})$. Injecting Eq. III.8 into Eq. III.42 leads to the following expression for the $\mathbf{D}$-matrix coefficients:

$$D(u_{\text{out}}, \mathbf{r}_{\text{in}}, \mathbf{r}_{\text{p}}) = \tilde{H}_{\text{out}}(u_{\text{out}}, \mathbf{r}_{\text{p}}) \int dx \gamma(x + x_{\text{in}}, z) \overline{H}_{\text{in}}(x, \mathbf{r}_{\text{p}}) e^{i\frac{k_c}{2z}u_{\text{out}}x} \tag{III.44}$$

The physical meaning of this last equation is the following: Around each point $\mathbf{r}_{\text{p}}$, the aberrations can be modelled by a transmittance $\tilde{H}_{\text{out}}(u_{\text{out}}, \mathbf{r}_{\text{p}})$. This transmittance is directly the Fourier transform of the output PSF $\overline{H}_{\text{out}}(x, \mathbf{r}_{\text{p}})$:

$$\tilde{H}_{\text{out}}(u_{\text{out}}, \mathbf{r}_{\text{p}}) = \sum_x \overline{H}_{\text{out}}(x, \mathbf{r}_{\text{p}}) e^{-i\frac{k_c}{2z}u_{\text{out}}x} \tag{III.45}$$

The aberration matrix $\tilde{\mathbf{H}}_{\text{out}}$ directly provides the *true* transmission matrix $\mathbf{Q}$ between the transducers and any point $\mathbf{r}_{\text{p}}$ of the medium:

$$\mathbf{Q} = \tilde{\mathbf{H}}_{\text{out}} \circ \mathbf{Q}_0 \tag{III.46}$$

This transmission matrix $\mathbf{Q}$ is the holy grail for ultrasound imaging since its phase conjugate directly provides the focusing laws that need to be applied on each transducer to optimally focus on each point $\mathbf{r}_{\text{p}}$ of the medium.

III.4.3.3 Singular value decomposition

To extract the aberration phase law $\tilde{H}_{\text{out}}(u_{\text{out}}, \mathbf{r}_{\text{p}})$ from each local distortion matrix, we can notice from Eq. III.44 that each line of $\mathbf{D}_{\text{ur}}(\mathbf{r}_{\text{p}})$ is the product between $\tilde{H}_{\text{out}}(u_{\text{out}}, \mathbf{r}_{\text{p}})$ and a random term associated with each virtual source. This explains the strong correlations exhibited by $\mathbf{D}_{\text{ur}}(\mathbf{r}_{\text{p}})$ in Fig. 11(f). To unscramble the deterministic term $\tilde{H}_{\text{out}}(u_{\text{out}}, \mathbf{r}_{\text{p}})$ from the random virtual source term in Eq. III.44, the singular value decomposition (SVD) of $\mathbf{D}(\mathbf{r}_{\text{p}})$ is an adequate tool. It writes as follows

$$\mathbf{D}_{\text{ur}}(\mathbf{r}_{\text{p}}) = \mathbf{U}(\mathbf{r}_{\text{p}}) \times \mathbf{\Sigma}(\mathbf{r}_{\text{p}}) \times \mathbf{V}^{\dagger}(\mathbf{r}_{\text{p}}), \tag{III.47}$$

or, in terms of matrix coefficients,

$$D(u_{\rm out},\mathbf{r}_{\rm in},\mathbf{r}_{\rm p}) = \sum_i U_i(u_{\rm out},\mathbf{r}_{\rm p})\mathbf{\Sigma}(\mathbf{r}_{\rm p})V_i^*(\mathbf{r}_{\rm in},\mathbf{r}_{\rm p}).$$

$\mathbf{\Sigma}$ is a diagonal matrix containing the singular value $\sigma_i(\mathbf{r}_{\rm p})$ in descending order: $\sigma_1 > \sigma_2 > .. > \sigma_N$. $\mathbf{U}(\mathbf{r}_{\rm p})$ and $\mathbf{V}(\mathbf{r}_{\rm p})$ are unitary matrices that contain the orthonormal set of output and input eigenvectors, $\mathbf{U}_i(\mathbf{r}_{\rm p}) = [U_i(u_{\rm out},\mathbf{r}_{\rm p})]$ and $\mathbf{V}_i(\mathbf{r}_{\rm p}) = [V_i(\mathbf{r}_{\rm in},\mathbf{r}_{\rm p})]$. To intuit the result of this SVD, one can consider the asymptotic case of a point-like input focusing beam $[H_{\rm in}(x) = \delta(x)]$. In this ideal case, Eq. III.44 becomes $D(u_{\rm out},\mathbf{r}_{\rm in},\mathbf{r}_{\rm p}) = \tilde{H}_{\rm out}(u_{\rm out},\mathbf{r}_{\rm p})\gamma(\mathbf{r}_{\rm in})$. The comparison with Eq. III.47, shows that the matrix $\mathbf{D}_{\rm ur}(\mathbf{r}_{\rm p})$ is then of rank 1. The first output singular vector $\mathbf{U}_1(\mathbf{r}_{\rm p})$ yields the aberration transmittance $\tilde{\mathbf{H}}_{\rm out}(\mathbf{r}_{\rm p})$ while the first input eigenvector $\mathbf{V}_1(\mathbf{r}_{\rm p})$ directly provides the medium reflectivity. In reality, the input PSF $H_{\rm in}$ is of course far from being point-like but one can expect that the first output singular vector will still constitute a reliable estimator of $\tilde{\mathbf{H}}_{\rm out}(\mathbf{r}_{\rm p})$. To check this intuition, the SVD of $\mathbf{D}_{\rm ur}(\mathbf{r}_{\rm p})$ should be predicted theoretically.

III.4.4 Correlation matrix

To do so, a study of the correlation matrix $\mathbf{C}_{\rm uu}(\mathbf{r}_{\rm p})$ in the transducer basis is needed:

$$\mathbf{C}_{\rm uu}(\mathbf{r}_{\rm p}) = \frac{1}{N_{\rm in}}\mathbf{D}'_{u\mathbf{r}}(\mathbf{r}_{\rm p}) \times \mathbf{D}'^{\dagger}_{u\mathbf{r}}(\mathbf{r}_{\rm p}), \tag{III.48}$$

with $N_{\rm in}$ the number of virtual sources contained in each spatial window $W_{\Delta\mathbf{r}}$. The SVD of $\mathbf{D}(\mathbf{r}_{\rm p})$ is indeed equivalent to the eigenvalue decomposition of $\mathbf{C}_{\rm uu}(\mathbf{r}_{\rm p})$:

$$\mathbf{C}_{\rm uu}(\mathbf{r}_{\rm p}) = \mathbf{U}(\mathbf{r}_{\rm p}) \times \mathbf{\Sigma}^2(\mathbf{r}_{\rm p}) \times \mathbf{U}^{\dagger}(\mathbf{r}_{\rm p}). \tag{III.49}$$

or, in terms of matrix coefficients,

$$\mathbf{C}_{\rm uu}(\mathbf{r}_{\rm p}) = \sum_i \sigma_i^2(\mathbf{r}_{\rm p})U_i(u_{\rm out},\mathbf{r}_{\rm p})U_i^*(u_{\rm out},\mathbf{r}_{\rm p}). \tag{III.50}$$

The eigenvalues σ_i^2 of $\mathbf{C}_{\rm uu}(\mathbf{r}_{\rm p})$ are the square of the singular values of $\mathbf{D}_{\rm ur}(\mathbf{r}_{\rm p})$. The eigenvectors $\mathbf{U}_i(\mathbf{r}_{\rm p})$ of $\mathbf{C}_{\rm uu}(\mathbf{r}_{\rm p})$ are the output singular vectors of $\mathbf{D}_{\rm ur}(\mathbf{r}_{\rm p})$. The study of $\mathbf{C}_{\rm uu}(\mathbf{r}_{\rm p})$ should thus lead to the prediction of the singular vectors $\mathbf{U}_i(\mathbf{r}_{\rm p})$. The coefficients of $\mathbf{C}_{\rm uu}$ can be seen as an average over $\mathbf{r}_{\rm in}$ of the spatial correlation of each distorted wave-field:

$$C(u,u',\mathbf{r}_{\rm p}) = \frac{1}{N_{\rm in}}\sum_{\mathbf{r}_{\rm in}} D(u,\mathbf{r}_{\rm in},\mathbf{r}_{\rm p})\ D^*(u',\mathbf{r}_{\rm in},\mathbf{r}_{\rm p}). \tag{III.51}$$

To be efficient, the average requires a large enough number of independent focal spot. Mathematically, it means that the correlation matrix $\mathbf{C}_{\rm uu}$ converges towards its covariance matrix $\langle\mathbf{C}_{\rm uu}\rangle$. It allows to approach the random reflectivity by its average $\langle\gamma(\mathbf{r})\gamma^*(\mathbf{r}')\rangle = \langle|\gamma|^2\rangle\delta(\mathbf{r}-\mathbf{r}')$. In the following, we will thus assume that this convergence condition is fulfilled. Under this assumption, injecting Eq. III.44 into Eq. III.51 leads to:

$$C(u_{\rm out},u'_{\rm out},\mathbf{r}_{\rm p}) \propto \langle|\gamma|^2\rangle\tilde{H}_{\rm out}(u_{\rm out},\mathbf{r}_{\rm p})\tilde{H}^*_{\rm out}(u'_{\rm out},\mathbf{r}_{\rm p}) \left[\tilde{H}_{\rm in} * \tilde{H}_{\rm in}\right](u_{\rm out}-u'_{\rm out},\mathbf{r}_{\rm p}), \tag{III.52}$$

where the symbol $*$ stands for a correlation product. This equation is the equivalent in the transducer basis of the one presented in the previous section [Eq. III.22] for the plane wave basis. A more rigourous description is provided in paragraphIII.2.3 and appendix III.D for the case of plane wave basis.

The correlation term, $\tilde{H}_{\text{in}} \circledast \tilde{H}_{\text{in}}$, results from the Fourier transform of the input PSF intensity $|H_{\text{in}}|^2$. Equation III.52 is reminiscent of the Van Cittert-Zernike theorem for an aberrating layer [11, 49]. This theorem states that the spatial correlation of a random wavefield generated by an incoherent source is equal to the Fourier transform of the intensity distribution of this source (here the input aberrated focal spots).

By confronting Eq. III.52 with Eq. III.50, one can show that the eigenvectors $\mathbf{U}_p$ of the correlation matrix $\mathbf{C}_{\text{uu}}$ will be proportional to the aberration transmittance $\tilde{H}_{\text{out}}(u_{\text{out}}, \mathbf{r}_{\text{p}})$. However, their amplitude is also modulated by the eigenvectors $\mathbf{W}_i$ of the correlation matrix $\tilde{\mathbf{H}}_{\text{in}} \circledast \tilde{\mathbf{H}}_{\text{in}}$, such that

$$\mathbf{U}_i(\mathbf{r}_{\text{p}}) \propto \tilde{\mathbf{H}}_{\text{out}}(\mathbf{r}_{\text{p}}) \circ \mathbf{W}_i(\mathbf{r}_{\text{p}}). \tag{III.53}$$

The eigenvectors $\mathbf{W}_i$ can be derived by solving a second order Fredholm equation with Hermitian kernel [151, 157]. An analytical solution can be found for certain analytical form of the correlation function $\tilde{H}_{\text{in}} \circledast \tilde{H}_{\text{in}}$. In absence of aberration [$\tilde{H}_{\text{in}}(u_{\text{in}}) = 1$], the correlation function $\tilde{H}_{\text{in}} \circledast \tilde{H}_{\text{in}}$ should be equal to a triangle function that spreads over the whole correlation matrix [49]. In presence of aberrations, a significant drop of δu_{in}, the spatial correlation length of $\tilde{H}_{\text{in}} \circledast \tilde{H}_{\text{in}}$ measured in the transducer basis is expected. δu_{in} is actually inversely proportional to the spatial extent δx_{in} of the input PSF $\overline{H}_{\text{in}}$: $\delta u_{in} \sim \lambda z/\delta x_{\text{in}}$ [11]. Figure 13 (a) illustrates that fact by showing the modulus of the correlation matrix $\mathbf{C}_{\text{uu}}(\mathbf{r}_{\text{p}})$ computed over the area $\mathcal{A}_2$ in Fig. 12(d). If we assume that the aberrations only induce phase shift (corresponding to a temporal delay) ($|\tilde{H}_{\text{out}}(u_{\text{out}}, \mathbf{r}_{\text{p}})| = 1$), the modulus of $\mathbf{C}_{\text{uu}}$ is actually a direct estimator of $\tilde{\mathbf{H}}_{\text{in}} \circledast \tilde{\mathbf{H}}_{\text{in}}$. As shown by Fig. 13 (a), the correlation function $\tilde{H}_{\text{in}} \circledast \tilde{H}_{\text{in}}$ is far from having a triangular shape and it decreases rapidly with the distance $|u_{\text{out}} - u'_{\text{out}}|$.

The shape of the corresponding eigenvectors $\mathbf{W}_i(\mathbf{r}_{\text{p}})$ depends on the exact form of the correlation function. For instance, a sinc correlation function implies 3D prolate spheroidal eigenfunctions[151]; a Gaussian covariance function leads to Hermite-Gaussian eigenmodes[114]. As the correlation function $\tilde{H}_{\text{in}} \circledast \tilde{H}_{\text{in}}$ is, in first approximation, real and positive, a general trend is that the first eigenvector $\mathbf{W}_1(\mathbf{r}_{\text{p}})$ shows a nearly constant phase. This is a very important property since it means that the phase of the first eigenvector $\mathbf{U}_1(\mathbf{r}_{\text{p}})$ is a direct estimator of $\tilde{\mathbf{H}}_{\text{out}}(\mathbf{r}_{\text{p}})$ [blue dashed line in Fig. 13(c)]. The modulus of $\mathbf{U}_1(\mathbf{r}_{\text{p}})$, *i.e* $\mathbf{W}_1(\mathbf{r}_{\text{p}})$, generally exhibits a single lobe around $u_{\text{out}} = 0$. Its typical width is the correlation length δu_{in}. The higher rank eigenvectors $\mathbf{W}_i(\mathbf{r}_{\text{p}})$ are more complex and exhibit a number of lobes that scales with their rank i. The blue and black lines in Figure 13(d) show the modulus of the first two eigenvectors of the matrix $\mathbf{C}_{\text{uu}}$ displayed in Fig. 13(a). We recognize the typical signature of the two first eigenmodes with one and two lobes respectively.

Note that to insure the validity of the theoretical prediction of Eq. III.53, we show in appendix III.E that The number N_{in} of independent input focusing points in each region should be at least four times larger than the number $M_\delta = \delta x/\delta x_0$ of transverse resolution cells δx mapping the aberrated focal spot δx_0.

$$N_{\text{in}} > 4M_\delta. \tag{III.54}$$

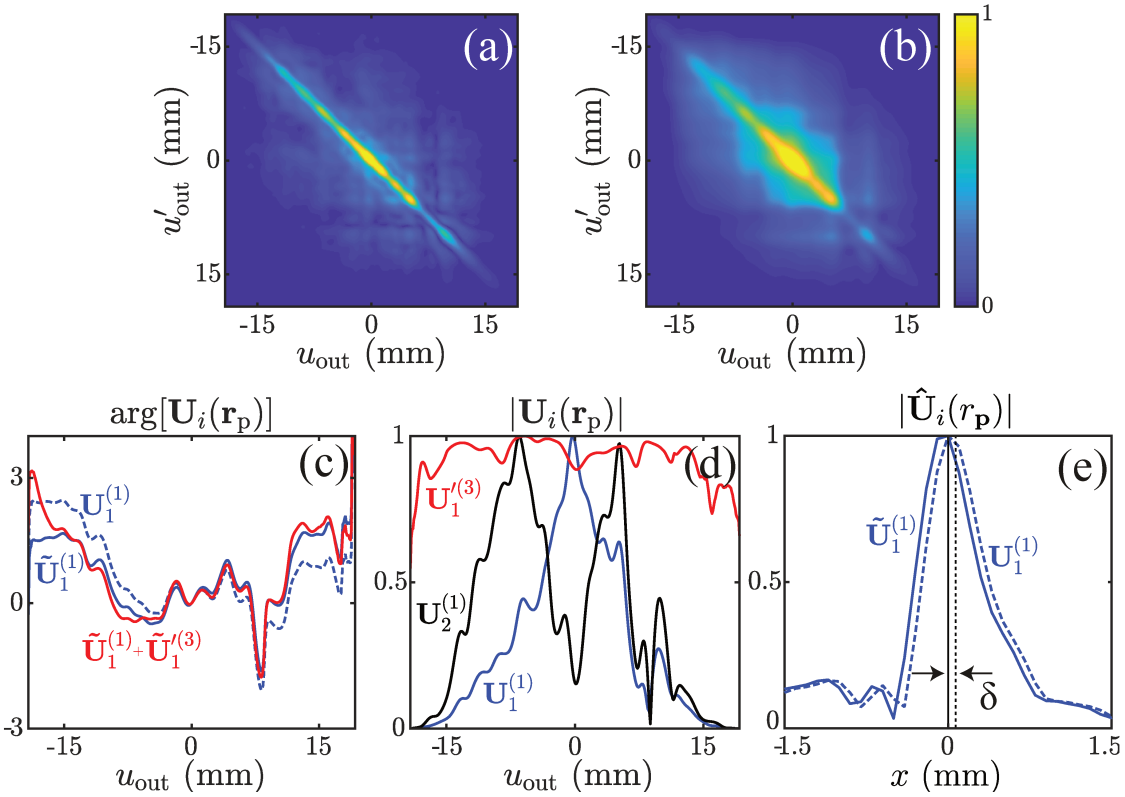

Fig. 13 *Extraction of the aberration law from the correlation matrix in the output transducer basis. (a,b) Amplitude of* $\mathbf{C}_{uu}$ *and* $\mathbf{C}_{uu}^{(3)}$ *corresponding to area* $\mathcal{A}_2$ *[Fig. 12(d)]. Due to the transmit aberrations, the phase of* $\mathbf{U}_1^{(1)}$ *contains a tilted output aberration law. This linear component is removed by projecting,* $\mathbf{U}_1^{(1)}$ *towards the focal basis to measure the offset* δ *of corresponding focal spot. The aberration law* $\tilde{\mathbf{U}}_1^{(1)}$ *is obtained based by removing this tilt. (d) The amplitude of its eigenvectors are ruled by hermito-Gaussian mode that prevent from extracting any useful information for the aberration correction process. To improve the correction the normalized correlation matrix is investigated during the third iteration* $\hat{\mathbf{C}}_{uu}$ *(red curve). By iterating the aberration correction process, the size of coherent virtual source is reduced, which enlarges the correlation length of the aberration law, which is visible along the anti-diagonal of the correlation matrix (a-b) and improves the estimation of the aberration law at large angle.*

This condition is decisive for the choice of the area $\Delta\mathbf{r}$ over which each local distortion matrix can be investigated. Because M_δ decreases after each iteration of the aberration correction process, the spatial window can be reduced accordingly, allowing an access with a better spatial resolution to the aberration matrix $\tilde{\mathbf{H}}_{\text{out}}$.

To sum up this paragraph, we have shown that the phase of the first singular vector $\mathbf{U}_1$ of the output distortion matrix $\mathbf{D}_{\text{ur}}(\mathbf{r}_\text{p})$ is an estimation of the output aberration phase law. However, this estimation is degraded by the aberrations in transmit. The support of $\mathbf{U}_1$ actually scales as the correlation width δu_{in} of aberrations in the transducer basis. For aberration correction, it is thus important to consider the normalized vector $\hat{\mathbf{U}}_1 = [U_1(u_{\text{out}})/|U_1(u_{\text{out}})|]$ that only implies a phase shift and not the full amplitude of $\mathbf{U}_1$ as it is however done in Ref. [66]. In the latter case, the bounded support of $\mathbf{U}_1$ would limit the probe aperture to the correlation width δu_{in}. For a strong level of aberrations, it can deeply degrade the resolution of the corrected image.

In the next paragraph, a time reversal picture of the correlation matrix is given to interpret physically the different theoretical results: (*i*) Give a physical interpretation of the SVD process; (*ii*) Explain and solve a potential artifact that consists in a lateral shift of the corrected PSF.

III.4.5 Time reversal picture

The previous paragraph has shown that the aberration phase law can be extracted from the SVD of the distortion matrix $\mathbf{D}_{\text{ur}}(\mathbf{r}_\text{p})$. This operation can be actually seen as a fictive time reversal experiment. Expressed in the form of Eq. III.52, $\mathbf{C}_{\text{uu}}$ is analogous to a reflection matrix $\mathbf{R}$ associated with a single scatterer of reflectivity $|H_{\text{in}}(x)|^2$ [Fig. 14c].

For such an experimental configuration, it has been shown that an iterative time reversal process converges towards a wavefront that focuses perfectly through the heterogeneous medium onto this scatterer [105, 106]. Interestingly, this time-reversal invariant can also be deduced from the eigenvalue decomposition of the time-reversal operator $\mathbf{R}\mathbf{R}^\dagger$ [105, 106, 113]. The same decomposition could thus be applied to $\mathbf{C}$ in order to retrieve the wavefront that would perfectly compensate for aberrations and optimally focus on the virtual reflector. This effect is illustrated in Fig. 14c. It is important to emphasize, however, that the coherent reflector is enlarged compared to the diffraction limit. As seen before (Eq. III.53), a set of eigenmodes $\mathbf{U}_i$ are thus obtained and focus on different parts of the virtual reflector [114][151]. Generally, the first eigenvector $\mathbf{U}_1$ focuses on the center of the virtual reflector since it maximizes the back-scattered energy. Its phase thus directly maps onto the aberration transmittance. However, it might not be the case if the scattering distribution $|\overline{H}_{\text{in}}(x)|^2$ is too complex. $\mathbf{U}_1$ then focuses on the brightest spot of the input PSF $|\overline{H}_{\text{in}}(x)|^2$. The phase of $\mathbf{U}_1$ may display a linear phase ramp compared to the aberration phase law (Fig. 13c). It results in a lateral shift of the imaging PSF (Fig. 13e) that can generate artifacts on the final corrected image [38]. In Appendix III.F, we show how to compensate this linear phase ramp, resulting in a better estimation of the aberration law $\hat{\mathbf{U}}_1$.

III.4.6 Transmission matrix imaging

Now that an estimator $\hat{\mathbf{U}}_1$ of the aberration phase law $\tilde{\mathbf{H}}_{\text{out}}$ has been established, its phase conjugate can be used as a focusing law to compensate for aberrations. To do so, the first step consists in back-propagating the broadband focused reflection matrix $\overline{\mathbf{R}}_{\text{xx}}(z)$ [Eq. II.34] towards the correction basis (here the output transducer plane):

$$\overline{\mathbf{R}}_{\text{ux}}(z) = \mathbf{Q_0} \times \overline{\mathbf{R}}_{\text{xx}}(z). \tag{III.55}$$

Note that this equation is similar to Eq. III.38, except that the filtered focused reflection matrix $\hat{\overline{\mathbf{R}}}_{\text{xx}}(z)$ is here replaced by the raw focused reflection matrix $\overline{\mathbf{R}}_{\text{xx}}(z)$. In that way, we make sure that no single-scattered echo is removed during the aberration correction process.

An estimator of the transmission matrix $\mathbf{Q_1}$ at point $\mathbf{r}_{\text{p}}$ is then deduced from the free space transmission matrix $\mathbf{Q_0}$ and the phase conjugate of the aberration phase law estimator $\hat{U}_1'(u, \mathbf{r}_{\text{p}})$:

$$Q_1(u, \mathbf{r}_{\text{p}}) = Q_1(u, \mathbf{r}_{\text{p}}) \hat{U}_1'^{*}(u, \mathbf{r}_{\text{p}}). \tag{III.56}$$

The correction at reception is then performed by re-focusing the reflection matrix at output by means of the estimator $\mathbf{Q}_1$ of the transmission matrix:

$$\overline{\mathbf{R}}_{\text{xx}}^{(1,out)}(z) = \mathbf{Q}_1^{\dagger} \times \hat{\overline{\mathbf{R}}}_{\text{ux}}(z). \tag{III.57}$$

where the index 1 in upper script stands for the first iteration of the aberration correction process and the symbol 'out' stands for an aberration correction only performed at output.

Figure 9 sums up all the key steps of the aberration correction process. The aberration correction in the receive mode corresponds to the left wing of this scheme. To complete this aberration correction process, the aberrations should now be corrected in the transmit mode (right wing of the scheme). Thanks to the spatial reciprocity of wave propagation, similar operations can be performed in the transmit mode by exchanging virtual sources and sensors. Note also that the correction basis can differ at input and output. At emission, the focused reflection matrix $\overline{\mathbf{R}}_{\text{xx}}^{(1,out)}(z)$ can, for instance, be projected in the plane wave basis [40] instead of the transducer basis.

The result of this first iteration of the aberration correction process is a new focused reflection matrix $\overline{\mathbf{R}}_{\text{xx}}^{(1)}(z)$ that has been corrected both at emission and reception. This process can then be iterated. We will refer to the focused reflection matrix obtained after the n^{th} iteration step as $\overline{\mathbf{R}}_{\text{xx}}^{(n)}(z)$. The iteration of the aberration process is useful since the quality of focus is improved at each step. It results in better resolved virtual transducers that, in return, provides a better estimation of the aberration phase law (in particular at large angles in the plane wave basis or on the edge of the array in the transducer basis). This virtuous cercle is reinforced by an estimation to the transmission matrix that can be performed at a higher resolution. Indeed, as the size of the virtual transducers decreases, the number of resolution cells contained in each focal spot, $M_{\delta}^{(n)} = \delta x^{(n)}/\delta x_0$, decreases as well. The extension $\Delta\mathbf{r}$ of the spatial window function $W_{\Delta\mathbf{r}}$ can thus be reduced while still ensuring a satisfying estimation of the aberration phase law (Eq. III.54). A gradual reduction of the spatial window $\Delta\mathbf{r}$ leads to an estimation of the transmission matrix $\mathbf{Q}$ at a higher resolution.

Finally, we describe in the following paragraph how to accelerate this convergence process by making the virtual reflector artificially point-like.

III.4.7 Normalized correlation matrix

At the n^{th} iteration of the process, the correlation matrix $\mathbf{C}_{uu}^{(n)}$ can be written as follows (Eq. III.52),

$$C^{(n)}(u_{\text{out}}, u'_{\text{out}}, \mathbf{r}_{\text{p}}) \propto \langle|\gamma|^2\rangle \tilde{H}_{\text{out}}^{(n)}(u_{\text{out}}, \mathbf{r}_{\text{p}}) \tilde{H}_{\text{out}}^{(n)*}(u'_{\text{out}}, \mathbf{r}_{\text{p}}) \left[\tilde{H}_{\text{in}}^{(n)} \circledast \tilde{H}_{\text{in}}^{(n)}\right](u_{\text{out}} - u'_{\text{out}}, \mathbf{r}_{\text{p}}), \quad \text{(III.58)}$$

where $\tilde{H}_{\text{out}}^{(n)}$ and $\tilde{H}_{\text{in}}^{(n)}$ accounts for the residual aberration transmittance at output and input, respectively, at the beginning of the n^{th} iteration.

In this section we have shown that the first singular vector of $\mathbf{C}_{\text{uu}}$ can be used to estimate the aberration law in reception. However, this estimation is damaged by the correlation term $\left[\tilde{H}_{\text{in}}^{(n)} \circledast \tilde{H}_{\text{in}}^{(n)}\right]$, which modulates the singular vector $\mathbf{U}_i$ by an envelop function $\mathbf{W_i}$.

As said before, the correlation function $\left[\tilde{H}_{\text{in}}^{(n)} \circledast \tilde{H}_{\text{in}}^{(n)}\right]$ accounts for the finite size of the virtual reflector in Eq. III.58 [Fig. 14D]. To make this virtual reflector point-like, we propose in the previous section [see III.2.3] to consider the normalized correlation matrix $\hat{\mathbf{C}}_{uu}^{(n)}(\mathbf{r}_{\text{p}})$:

$$\hat{C}^{(n)}(u_{\text{out}}, u'_{\text{out}}, \mathbf{r}_{\text{p}}) = C^{(n)}(u_{\text{out}}, u'_{\text{out}}, \mathbf{r}_{\text{p}}) / |C^{(n)}(u_{\text{out}}, u'_{\text{out}}, \mathbf{r}_{\text{p}})|. \quad \text{(III.59)}$$

This normalization process equalizes the Fourier spectrum of the virtual reflector. Indeed, if the aberrating structures in the medium are only inducing phase distortions $[|\tilde{H}^{(n)}(u_{\text{out}})| = 1]$, injecting Eq. III.52 into Eq. III.59 the normalized correlation matrix coefficients $\hat{C}^{(n)}(u_{\text{out}}, u'_{\text{out}}, \mathbf{r}_{\text{p}})$ can actually be expressed as follows:

$$\hat{C}^{(n)}(u_{\text{out}}, u'_{\text{out}}, \mathbf{r}_{\text{p}}) = \tilde{H}_{\text{out}}(u_{\text{out}}, \mathbf{r}_{\text{p}}) \tilde{H}_{\text{out}}^{*}(u'_{\text{out}}, \mathbf{r}_{\text{p}}) \quad \text{(III.60)}$$

where $\tilde{H}_{\text{out}}(u_{\text{out}}, \mathbf{r}_{\text{p}})$ is expressed in this form, the normalized correlation matrix $\hat{\mathbf{C}}_{uu}^{(n)}$ is analogous to a reflection matrix $\mathbf{R}$ associated with a single point-like scatterer [Fig. 14d]. As in an iterative time-reversal experiment with a point-like target[105], $\hat{\mathbf{C}}_{uu}$ is of rank one and its eigenvector $\mathbf{U}_1'^{(n)}(\mathbf{r}_{\text{p}})$ directly provides the residual aberration phase law:

$$\mathbf{U}'^{(n)}_1(\mathbf{r}_{\text{p}}) = \tilde{H}_{\text{out}}^{(n)}(u_{\text{out}}, \mathbf{r}_{\text{p}}) \quad \text{(III.61)}$$

Figure 13 illustrates the benefit of the normalization of $\mathbf{C}_{uu}^{(n)}$ by considering the example of the region $\mathcal{A}_2$ in Fig. 10(a). Figure 13(b) shows the modulus correlation matrix $\mathbf{C}_{uu}^{(2)}$ at the beginning of the 2^{nd} step. The comparison with its initial value [Fig. 13(a)] already shows the drastic flattening of the correlation function $\left[\tilde{H}_{\text{in}}^{(n)} \circledast \tilde{H}_{\text{in}}^{(n)}\right]$ after the first iteration of the aberration correction process. This flattening is a direct indicator of the gain in focusing quality at input. It also makes possible the normalization of $\mathbf{C}_{uu}^{(2)}$ as the SNR is drastically improved over the off-diagonal elements of $\mathbf{C}_{\text{uu}}$. Figure 13(d) shows the modulus of $\mathbf{U}_1'^{(3)}(\mathbf{r}_{\text{p}})$ (red curve). Compared to the modulus of $\mathbf{U}_1^{(1)}(\mathbf{r}_{\text{p}})$ (blue line), we observe that the signature of the first Hermito-Gaussian mode $\mathbf{W}_1$ has been suppressed. The red curve in 13(c) displays the accumulated phase of the aberration

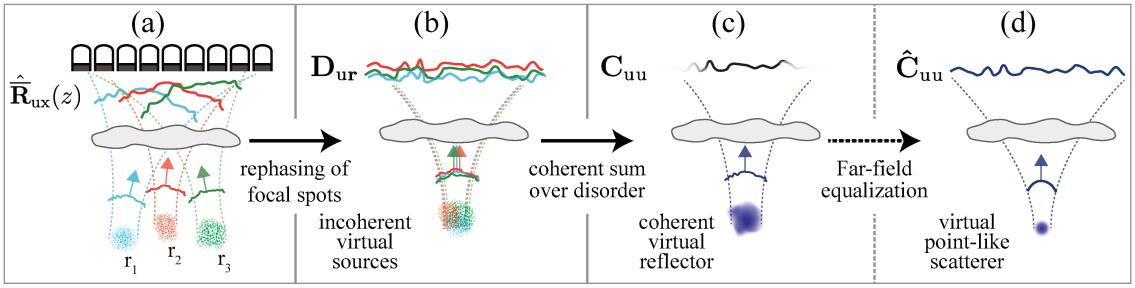

Fig. 14 *Sketch of the time reversal analysis of the distortion matrix [69]. (A) Each row of the reflection matrix* $\mathbf{R}_{\grave{u}\mathbf{r}}$ *corresponds to the reflected wavefield induced by the associated virtual source* $\mathbf{r_{in}}$*. (B) By removing the geometrical curvature of each reflected wavefront [eq. III.11], the resulting distortion matrix extracts the aberrated component of those wavefront. From an other point of view, all the wavefront are realigned as if they were generated by input focal spots that are virtually shifted at the origin (Eq. III.11). (C) The correlation matrix* $\mathbf{C}$ *of the distortion matrix* $\mathbf{D}$ *mimics the time reversal operator applied to a virtual specular reflector that results from the average of all the shifted input focal spot. Its first eigenvector* $V_1(k)$ *then yields the mean aberrated component to focus on this specular reflector. (d) The normalized correlation matrix* $\hat{\mathbf{C}}$ *makes the virtual reflector point-like. Its singular value decomposition can then provide a higher accuracy for large spatial frequencies* $\mathbf{k}$ *of the estimated aberration law at the price of increasing noise.*

transmittance estimator, $\hat{\mathbf{U}}'^{(2)}_1 \circ \hat{\mathbf{U}}^{(i)}_1$. Here $n = 2$ and we observe that the third correction introduces a significant modification of the aberration phase law on the edge of the ultrasound probe, around $u_{\text{out}} = -17$ mm. A better estimation of the aberration phase law has been provided on the edges of the transducer array thanks to the normalization of the correlation matrix.

Although the normalization operation in Eq. III.59 tends to make the virtual scatterer point-like, it also increases the noise level. Indeed, correlation coefficients associated with transducers far from each other are more likely to be noisy [Fig. 13(a)]. This alternative time reversal process should thus be applied at the end of an iterative aberration correction process. The convergence of the correlation matrix towards its covariance matrix is nearly achieved and the first iteration correction step improves the signal to noise ratio [Fig. 13(b)].

III.4.8 Results

We apply our matrix approach of aberration correction to the ultrasound image of the human calf [Fig. 12(b,c)]. We first discuss the choice of parameters and the strategy to correct for an entire image before interpreting the results. All the parameters used for the entire correction process are gathered in Table 1.

While we describe a correction in the plane wave basis in the previous section [40], the present one shows how this procedure can be adjusted for the transducer basis. The

choice of the correcting basis does not modify the wavefront distortions. However, the spatial extension of the associated isoplanatic patches is deeply affected by this choice, impacting the results of the aberration correction process. Depending on the location of the aberrator and/or its spatial dimension, one basis is more suitable than the other to extract the aberration law. For instance, a local perturbation of the medium speed of sound located at shallow depth, will deeply impact the transducers that are directly located above. Capturing this fluctuation in the plane wave basis is much more difficult as it results in slight modifications of each plane wave, which may just emerge from the noise. On the contrary, let's consider a stratified medium that is invariant by lateral translation. A plane wave that propagates through such medium is only tilted without additional distortion. The distortion then only depends on the angle of the plane wave and not on the location of the virtual transducer, resulting in a single isoplanatic patch for each stratification. For *in-vivo* application, both kind of heterogeneities appear. The organs under study are generally separated from the probe by multiple layers of skin, adipose and/or muscle tissues. This kind of heterogeneities are thus better corrected in the plane wave basis. In addition, the waves may travel through local heterogeneities such as superficial veins that are better captured in the transducer basis. In the present case, no information on the shape of the aberrator is available *a priori*. We thus propose to correct successively in the transducer basis and in the plane wave basis, both in transmit and in receive. We arbitrarily choose to begin the correction process by the correcting bases that match the ones used for the acquisition: plane wave basis in transmit, transducer basis in receive. We start by correcting the transmit aberrations as this process may also correct for unwanted movement of the medium that occurred during the acquisition.

To provide an aberration correction for the entire image in the complex situation where multiple isoplanatic patches are contained in the field of view, an effective strategy consists in using a moving spatial window $W_{\Delta\mathbf{r}}$ [section III.4.4] and to compute an aberration law for each image sector [40, 66, 65]. The dimension of the spatial window is a key parameter as it impacts the accuracy and the spatial resolution of the aberration law estimation. On the one hand, if the spatial window is larger than the isoplanatic patch, the hypothesis of partially-invariant aberrations is not valid and the region of interest contains more than one isoplanatic patch. The correction process will then provide an average aberration that may not perfectly focus on any patch. On the other hand, if the window function is too small, the hypothesis of invariant aberration in the field-of-illumination is maintained, but the number of independent virtual transducers is too small, preventing the correlation matrix to converge toward the covariance matrix, which degrades the resulting aberration law [40]. To bypass this issue, we propose to perform a four-iterative correction for which $W_{\Delta\mathbf{r}}$ is reduced at each iteration. After each iteration, the previous correction improves the quality of focus and thus reduces the size of the virtual sources. It enhances the SNR and decreases the number of resolution cells within the aberrated focal spot. It thus reduces the minimal size of the field-of-illumination, allowing to correct for smaller isoplanatic patches. The four colored straight rectangles of figure 10(a) reflect the size of the spatial window used to correct the image. The dimensions of the spatial window $[dx, dz]$ are given in table 1. To avoid edge effects, a 75% overlapping is applied to correct for each field-of-illumination.

The confocal filter [Par. III.4.1] also needs to be carefully set. To be efficient, the characteristic size of the confocal filter $l_c(\mathbf{r})$ should match the input-output resolution

Table 1 – Parameters used for the entire aberration correction process. For each iteration, a confocal filter of maximum caracteristic length $Nw_0(\mathbf{r})$ is first applied to $\mathbf{R}_{\mathrm{rr}}$. Then a moving windows of size $[dx, dz]$ select a field of illumination. The correction is applied in transmit and in receive, either in the transducer basis $\dot{\mathbf{u}}$ or in the spatial Fourier basis $\dot{\theta}$

Correction iteration	1	2	3	4
N	10	10	8	6
dx (mm)	10	7.5	5	3
dz (mm)	20	15	10	7.5
Transmit basis	$\dot{\theta}_{\mathrm{in}}$	$\dot{\mathbf{u}}_{\mathrm{in}}$	$\dot{\theta}_{\mathrm{in}}$	$\dot{\mathbf{u}}_{\mathrm{in}}$
Receive basis	$\dot{\mathbf{u}}_{\mathrm{out}}$	$\dot{\theta}_{\mathrm{out}}$	$\dot{\mathbf{u}}_{\mathrm{out}}$	$\dot{\theta}_{\mathrm{out}}$
First Side	in	out	in	out
SVD type	$\mathbf{C}$	$\mathbf{C}$	$\hat{\mathbf{C}}$	$\hat{\mathbf{C}}$

$w(\mathbf{r})$ in order to select all the singly-scattered echoes and to remove the maximum of multiple-scattered echoes. If $l_c(\mathbf{r})$ is too large or if no filter is applied, the multiple-scattered echoes increases the noise level associated with incoherent signal. In Equation III.20, this level is characterized by $\delta\mathbf{C}$. The convergence of the correlation matrix towards its covariance matrix is thus more difficult and requires more realizations of independent aberrated components. If $l_c(\mathbf{r})$ is too small, some singly-scattered echoes are removed. This filter then acts as a Hanning window that smooths out the resulting aberration phase law. $l_c(\mathbf{r})$ is then defined by the measurement of $w(r)$. For areas where this estimation has failed [gray area on Fig. 12(d)], $l_c(\mathbf{r})$ is set to $Nw_0(\mathbf{r})$ with N an integer. As the local resolution of the image improves with the successive iteration, the confocal filter is thus more and more selective, which improved its efficiency to remove multiple-scattered echoes and electronic noise.

Finally, we introduced two types of time reversal analysis based on the SVD of $\mathbf{C}$ or $\hat{\mathbf{C}}$. The first one is more robust and less sensitive to the noise level, but also less accurate at large angles of illumination or collection. It is then used for the first two iterative corrections while the last two corrections are based on $\hat{\mathbf{C}}$.

Figures 10 (b,d) display the original and corrected focused reflection matrices, computed at depth $z = 18$ mm [straight white line on Fig. 10(d)]. The single scattered signals that are initially spread around the diagonal are now re-centered on a thinner diagonal, meaning that the local input-output resolution has improved. Figure 10(e) shows the common-midpoint intensity profiles averaged over the area $\mathcal{A}_1$ for each iteration. The average input-output resolutions computed at -3 dB are displayed in table 2. After the fourth correction, this average resolution is equal to $\langle w^{(4)} \rangle = 0.21$ mm. Compared to the average theoretical resolution, which is equal to $w_0 = 0.19$ mm, the fourth correction nearly reaches the optimal resolution defined by the diffraction limit. By comparing the initial input-output resolution w with the corrected one w_4, we define an improving factor

Table 2 – -3 db input-output resolution averaged over the area $\mathcal{A}_2$ [Fig. 12(d)]. Theoretical resolution $w_0 = 0.19$ mm

Correction iteration	0	1	2	3	4
$\langle w \rangle_{\text{-3 dB}}$ (mm)	0.57	0.57	0.28	0.24	0.21

of the input-output resolution:

$$\epsilon = \left\langle \frac{|w_4(\mathbf{r}) - w(\mathbf{r})|}{w(\mathbf{r})} \right\rangle_{\hat{\mathbf{r}}}, \tag{III.62}$$

where $\langle ... \rangle_{\hat{\mathbf{r}}}$ denotes a spatial average over focusing points. For the area $\mathcal{A}_1$, this factor is equal to $\epsilon = 40$ %.

Figures 12(b,c) display the original ultrasound image of the human calf with the corrected one. The two images are normalized by their mean intensity and are displayed using the same dynamic. We see a significant improvement of the image quality. The probe is set perpendicular to the muscle fibers. Therefore, those fibers appear as strong point-like scatterers in the ultrasound image. The aberration correction reveals some of those fibers and the ones that are already visible on the original image appear more brighter (left part of the image, around the vein located at $[x, z] = [-3, 32]$ mm), which testified about the improvement of the image resolution. The boundaries between each type of soft tissue are better defined and display a better continuity. Figures 12(e,f) are a zoom of the ultrasound images. The aberration correction reveals some structures that are completely blurred on the original image. To validate those qualitative observations, the focusing criterion associated with the original $F(\mathbf{r})$ and corrected one $F^{(4)}(\mathbf{r})$ are displayed on figures 12(a,d). Most of the aberrations have been corrected and the focusing criterion is now close to 1 for a large part of the image, meaning that the focusing quality is optimal. However, according this criterion, the aberration correction process fails for two areas (gray areas on the image). The first one is located at the bottom left part of the image and corresponds to the fibula (bone). Echoes associated with this area mainly come from multiple scattered paths, an effect that we do not attempt to treat in this article. On the top right part of the image, the focusing criterion reveals a circular area that is not well reconstructed. Two reasons could explain this result. First, plane wave imaging supposes that the medium is not moving during the entire acquisition process. Here, the ultrasound sequence is quite long (101 firings at 1000 Hz) and the existence of a vein at shallow depth could disrupt this hypothesis. Secondly, the signal to noise ratio associated with this area is quite low, the estimation of the aberration law is thus more difficult. Note that at least, the focusing criterion can now be better estimated which means that some aberrations have been corrected. The entire image shows an average improvement factor of the resolution $\epsilon = 36\%$. Note that this factor underestimates the improvement of the image resolution as only focal points for which the estimation of F and $F^{(4)}$ have succeed. It means that areas that are initially too degraded due to aberrations and that are well reconstructed after the aberration correction process are not taken into account. To quantify the contrast enhancement induced by the aberration correction process, the average signal level within the vein (located at $[x, z] = [-3, 32]$ mm) is compared to the one measured on the bright area located just below the vein. Compared to the original image, the corrected image shows a contrast improvement of 2.0 dB

III.4.9 Discussion

The results presented above validate the matrix approach of aberration correction for *in-vivo* measurement in the complex case of human calf imaging. This medium is representative of *in-vivo* ultrasound imaging where the medium under investigation is heterogeneous and composed of different kind of tissues. It includes both highly and weakly scattering areas, which can be tricky for aberration correction techniques. The back-scattered signals are generated either by unresolved scatterers (speckle regime), bright point-like scatterers (muscle fibers) and specular objects that are bigger than the image resolution (for example, skin tissue at shallow depth around $z = 5$ mm). Previous works have shown that the concept of the distortion matrix can be applied both to the specular regime [149] and to the speckle regime [40, 158]. The present article provides additional insights in the aberration correction that are essential for applying this technique to *in-vivo* case where both regimes are found. For each kind of reflector, the image resolution is improved.

To be efficient, the aberration correction process requires that the focused reflection matrix fully describes the aberrated focal spot. In other word, the maximal distance Δx between the input and output focal spot needs to be larger than the input-output resolutions w. It means that the number of degrees of freedom available to control the wavefront needs to be higher than the number of resolution cells within the aberrated focal spot. Therefore, there is a link between the aberration complexity and the number of required excitations to perfectly correct for aberrations. Consequently, as long as the aberrated focal spots are smaller than the maximal distance Δx, the matrix approach of aberration correction can be applied to data sets that contain fewer transmit excitations such as the one used for ultrafast imaging modes.

Figure 15 shows the spatial distribution of aberration laws accumulated over the four iterations and computed in the plane wave and transducer bases, both at the input and output. Aberrations are shown to be strongly position-dependent and to display short-scale fluctuations. Some aberration laws corresponding to adjacent areas [Fig. 15 B, D, C] are highly correlated, both in the plane wave or transducer bases, meaning that their associated rectangle areas belong to the same isoplanatic patch. Figures (A1, B1, C1, D1) display a concave curvature shape in the plane wave basis, meaning that the assumed speed-of-sound used to beamform the image is under-estimated [40]. In most cases, the estimated aberrations laws in transmit are highly correlated to the receive ones, both in transmit and in receive. This behavior stems from the reciprocity of the wave propagation. In other words, the transmit and back-scattered waves travel through the same heterogeneities, resulting in the nearly same aberrations. Some adaptive techniques [61, 65, 66] use this phenomenon to correct both at the emission and reception by the same aberration law estimated either in transmit or in receive. However, for some areas, the transmit and receive aberration laws are definitely not identical [Fig. B1, C1, E1, F2,...]. This non-reciprocity of the aberration laws stems from the differences between the transmit basis, *e.g.* the plane wave basis, and the receive one *e.g.* the transducer basis. Therefore, for acquisitions that do not use the same transmit and receive basis, correcting for aberration with the same phase law both in transmit and receive does not provide an optimal focusing quality [61, 66]. The truncated aspect of some of the aberration laws (e.g. Figs. A2 and D2) results from the maximal angles of illumination

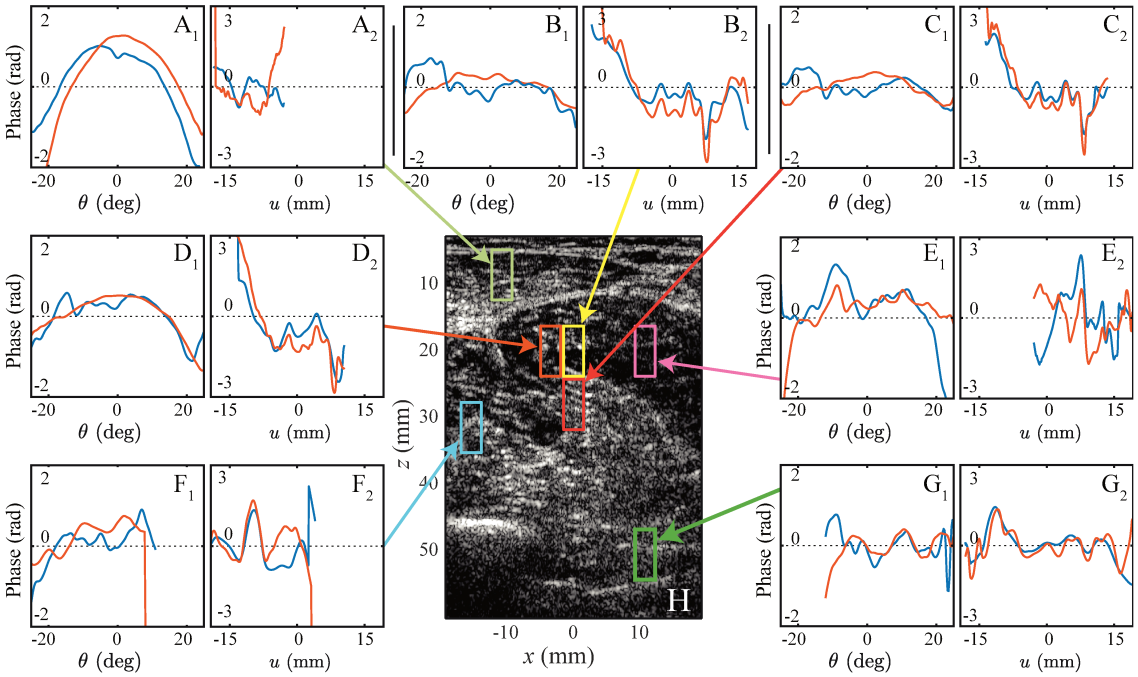

Fig. 15 *Examples of cumulative aberration laws resulting from the entire aberration correction process, computed in transmit (blue curves) and in receive (red curves) and expressed in the plane wave basis $\dot{\theta}$ (1) or in the transducer basis $\dot{\mathbf{u}}$ (2). The dimension of the selected areas is defined by the size of the spatial window used for the fourth correction.*

or collection imposed by the finite size of the ultrasonic array. Interestingly, a comparison of, for example, Figs. 15A and 15G, highlights the fact that while the plane wave basis is perfectly suited to shallow depth imaging, its interest is reduced at large depth since only a few angles reaches the focal point. The transducer basis displays an inverse behavior, for focusing point located at shallow depth, only few transducers are used to correct for aberrations, whereas the entire basis is used for large focal depth.

While our method is inspired by previous works in ultrasound imaging [47, 11, 38, 49, 62, 65, 66], it features several distinct and important differences. The first one is its primary building block: the broadband focused reflection matrix that precisely selects all the single-scattered echoes originating from each focal point. It is a decisive step since it drastically reduces the detrimental contribution of out-of-focus and multiply-scattered echoes. The more recent techniques select those echoes either by applying a fix time gating around the initial time-delay used to focus inside the medium [49, 62, 65], or by investigating the signal coherence only along the time delay law [66]. Secondly, the matrix approach provides a generalization of the virtual transducer interpretation [49]. By decoupling the location of the input and output focal spot, this approach becomes flexible enough to identify and correct for aberrations at both input and output. In addition, the aberrations can be estimated in any correcting bases. This technique can thus easily be applied to focused excitations, diverging waves, or to other geometries like curved probes

or phase arrays, without increasing the complexity.

III.5 Conclusion and perspectives

In summary, we successfully applied the concept of matrix approach of aberration correction ([40]) to the complex case of *in-vivo* human calf imaging. In this chapter, we provide a mathematical and physical description of the aberration correction mechanism. It provides a new point of view on the challenging topic of adaptive imaging.

By focusing at distinct points in emission and reception, one can build a focused reflection matrix that contains the impulse responses between a set of virtual transducers mapping the entire medium. By projecting the reflection matrix toward a dual basis, we extract a new distortion matrix that essentially connects any focal point inside the medium with the distortion that a wavefront, emitted or recorded from that point, experiences due to heterogeneities. A time-reversal analysis of the distortion matrix enables the estimation of the transmission matrix that links each sensor and image voxel. The distortion matrix provides a powerful tool for imaging inside a heterogeneous medium with *a priori* unknown characteristics. Aberrations can be corrected without any guide stars or exact knowledge of the speed of sound distribution in the medium. By using the high flexibility of the matrix approach, aberrations are successively corrected in transmit and in receive with separate aberration phase laws that are expressed both in the plane wave and transducer basis. This aberration correction process provides an optimal focusing quality.

Unexplored but promising perspectives for this work include the analyze of frequency-dependent aberrations to extend the distortion matrix to the case of dispersive heterogeneous media. Aberration correction would then consist in a time reversal of the aberrated wavefront rather than the simple phase conjugation presented in this paper [62].

Appendices

III.A Reflection matrix in the far-field basis

As stated in the accompanying paper (Eq. 6), the far-field reflection matrix $\overline{\mathbf{R}}_{\mathrm{kk}}$ can be expressed as follows:

$$\overline{\mathbf{R}}_{\mathrm{kk}}(z) = \mathbf{T}(z) \times \mathbf{\Gamma}(z) \times \mathbf{T}^{\top}(z). \tag{III.63}$$

where $\mathbf{\Gamma}(z) = [\Gamma(x, x', z)]$ describes the scattering processes inside the medium. In the isoplanatic limit, the aberrations can be modeled by a far-field phase screen of transmittance $\tilde{\mathbf{H}} = [\tilde{H}(k_x)]$, where $\tilde{H}(k_x) = \int dx\ \overline{H}(x)\ \exp(-ik_x x)$ is the 1D Fourier transform of the input or output point spread function, $\overline{H}(x)$, which is defined in Eq. 9 of the accompanying paper. The transmission matrix $\mathbf{T}$ can then be expressed as an Hadamard product between $\tilde{\mathbf{H}}$ and $\mathbf{T_0}$, the free-space transmission matrix,

$$\mathbf{T} = \tilde{\mathbf{H}} \circ \mathbf{T_0}. \tag{III.64}$$

The injection of this last equation into Eq. III.3 yields the following expression for the far-field reflection matrix coefficients

$$R(k_{\mathrm{out}}, k_{\mathrm{in}}, z) = \tilde{H}(k_{\mathrm{in}})\tilde{\gamma}(k_{\mathrm{in}} + k_{\mathrm{out}}, z)\tilde{H}(k_{\mathrm{out}}), \tag{III.65}$$

where $\tilde{\gamma}(k_x, z) = \int dx\, \gamma(x, z) \exp(-ik_x x)$ is the 1D Fourier transform of the sample reflectivity $\gamma(x, z)$. Assuming the aberration as a phase screen ($|\tilde{H}(k_x)| = 1$), the norm-square of the coefficients of $\overline{\mathbf{R}}_{\mathrm{kk}}(z)$ (Eq. III.65) are given by

$$|R(k_{\mathrm{out}}, k_{\mathrm{in}}, z)|^2 = |\tilde{\gamma}(k_{\mathrm{out}} + k_{\mathrm{in}}, z)|^2 . \tag{III.66}$$

Each antidiagonal of $\overline{\mathbf{R}}_{\mathrm{kk}}$ (where $k_{\mathrm{in}} + k_{\mathrm{out}} = \text{constant}$) encodes one spatial frequency of the sample reflectivity.

III.B Reflection matrix in the dual basis

The dual reflection matrix $\overline{\mathbf{R}}_{\mathrm{kr}} = \overline{\mathbf{R}}_{\mathrm{kx}}(z)$ is obtained by projecting $\overline{\mathbf{R}}_{\mathrm{kk}}$ into the focused basis in emission:

$$\overline{\mathbf{R}}_{\mathrm{kx}}(z) = \overline{\mathbf{R}}_{\mathrm{kk}}(z) \times \mathbf{T}_0^{*}. \tag{III.67}$$

Injecting Eq. III.3 into this last equation leads to the following expression for $\overline{\mathbf{R}}_{\mathrm{kx}}(z)$:

$$\overline{\mathbf{R}}_{\mathrm{kx}}(z) = \mathbf{T} \times \mathbf{\Gamma}(z) \times \overline{\mathbf{H}}_{\mathrm{in}}^{\top}, \tag{III.68}$$

where $\overline{\mathbf{H}} = \mathbf{T}_0^{\dagger}\mathbf{T}$ is the focusing matrix whose columns corresponds to the input focal spots $\overline{H}(x, x_{\mathrm{in}})$. In the isoplanatic limit, $\overline{H}_{\mathrm{in}}(x, x_{\mathrm{in}}) = \overline{H}_{\mathrm{in}}(x - x_{\mathrm{in}})$. The elements of $\overline{\mathbf{R}}_{\mathrm{kr}}$ can then be expressed as

$$R(k_{\mathrm{out}}, \mathbf{r}_{\mathrm{in}}) = \int dx\, T(k_{\mathrm{out}}, x)\gamma(x, z)\overline{H}_{\mathrm{in}}(x - x_{\mathrm{in}}). \tag{III.69}$$

To investigate the far-field correlations of the reflected wavefield, the spatial correlation matrix $\mathbf{B}_{\mathrm{kk}} = \overline{\mathbf{R}}_{\mathrm{kr}}\overline{\mathbf{R}}_{\mathrm{kr}}^{\dagger}$ should be considered. $\mathbf{B}_{\mathrm{kk}}$ can be decomposed as the sum of a covariance matrix $\langle \mathbf{B}_{\mathrm{kk}} \rangle$ and a perturbation term $\delta\mathbf{B}_{\mathrm{kk}}$:

$$\mathbf{B}_{\mathrm{kk}} = \langle \mathbf{B}_{\mathrm{kk}} \rangle + \delta\mathbf{B}_{\mathrm{kk}}, \tag{III.70}$$

where the symbol $\langle \cdots \rangle$ denotes an ensemble average.

In the speckle regime, the random nature of the sample reflectivity $\gamma(\mathbf{r})$ means that $\langle \gamma(\mathbf{r})\gamma^{*}(\mathbf{r}') \rangle = \langle |\gamma|^2 \rangle \delta(\mathbf{r} - \mathbf{r}')$, where δ is the Dirac distribution. The correlation matrix should converge towards the covariance matrix $\langle \mathbf{B}_{\mathrm{kk}} \rangle$ for a large number of independent realizations. More precisely, the intensity of the perturbation term in Eq.III.70, $|\delta B(k, k')|$, should scale as the inverse of M, the number of independent resolution cells contained in the field of view [150, 159, 160].

Assuming the convergence of $\mathbf{B}_{\mathrm{kk}}$ towards $\langle \mathbf{B}_{\mathrm{kk}} \rangle$ in the speckle regime, the correlation coefficients $B(k_{\mathrm{out}}, k'_{\mathrm{out}})$ can be expressed as follows

$$B(k_{\mathrm{out}}, k'_{\mathrm{out}}) = \langle |\gamma|^2 \rangle \int x\, T(k_{\mathrm{out}}, x)\gamma_R(x)T^{*}(k'_{\mathrm{out}}, x) \tag{III.71}$$

where

$$\gamma_R(x) = \int d\mathbf{r}_{\mathrm{in}}\, \Omega(x_{\mathrm{in}}, z) \left| \overline{H}_{\mathrm{in}}(x - x_{\mathrm{in}}) \right|^2. \tag{III.72}$$

The function $\Omega(\mathbf{r})$ denotes the spatial domain occupied by the field of view:

$$\Omega(\mathbf{r}) = \begin{cases} 1 & \text{for } \mathbf{r} \text{ inside the field of view} \\ 0 & \text{otherwise.} \end{cases}$$

Equation III.71 can be rewritten as the following matrix product

$$\mathbf{B}_{\mathrm{kk}} \propto \mathbf{T} \times \mathbf{\Gamma}_{\mathbf{R}} \times \mathbf{T}^{\dagger}, \tag{III.73}$$

where $\mathbf{\Gamma}_{\mathbf{R}}$ is a diagonal scattering matrix associated with a virtual object. Its coefficients $\gamma_R(x)$ correspond to the convolution of the input focal spot intensity $|\overline{H}_{\mathrm{in}}(x)|^2$ with the whole field of view $\Omega(x)$. Its spatial extent thus spans the entire field of view (Fig. III.B.1).

Expressed in the form of Eq. III.73, $\mathbf{B}_{\mathrm{kk}}$ is analogous to the time-reversal operator obtained for a single scatterer of reflectivity $\gamma_R(x)$ [38, 61]. If this virtual scatterer were point-like, $\mathbf{B}_{\mathrm{kk}}$ would be of rank 1 and its eigenvector would correspond to the wavefront that focuses perfectly through the heterogeneous medium onto the virtual scatterer, even in presence of strong aberrations [105, 106]. Here, however, this is far from being the case. The eigenvalue decomposition of $\mathbf{B}_{\mathrm{kk}}$ yields a set of eigenmodes which focus on different parts of the same virtual scatterer over restricted angular domains [114, 151]. One solution to this degeneracy is to limit the field of view in order to reduce the size of the virtual reflector and increase the angular aperture of the eigenwavefronts. However, a restricted field of view means a lack of averaging over disorder. The perturbation term in Eq. III.70 would no longer be negligible and iterative time reversal would not converge towards the optimal aberration phase law. As we will see in the next section, the distortion matrix concept avoids this impossible compromise.

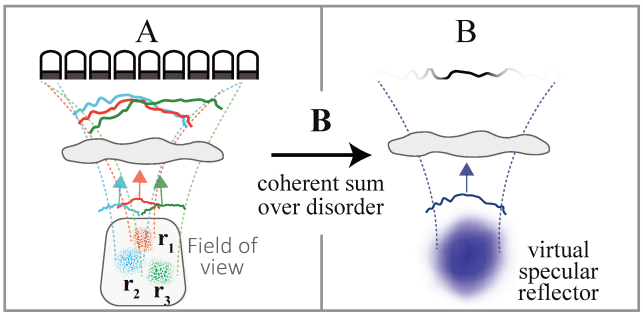

Fig. III.B.1 *Time reversal analysis of the reflection matrix. (A) Each row of* $\overline{\mathbf{R}}_{kx}(z)$ *corresponds to the reflected wavefield induced by each input focal point* $\mathbf{r}_{in}$*. (B) When* $\mathbf{B}_{kk}$ *(the correlation matrix of* $\overline{\mathbf{R}}_{kx}(z)$*) is calculated, the sample reflectivity is smoothed out (spatially averaged).* $\mathbf{B}_{kk}$ *thus mimics the time reversal operator associated with a virtual specular reflector of scattering distribution* $\gamma_R(x)$ *that scales as the field of view* $\Omega(x)$ *(Eq. III.72).*

III.C Distortion matrix in the dual basis

The distortion matrix $\mathbf{D}(z)$ is defined as the Hadamard product between the reflection matrix $\overline{\mathbf{R}}_{\mathrm{kx}}(z)$ and the reference transmission matrix $\mathbf{T}_0^*$. In terms of matrix coefficients, this can be written

$$D(k_{\mathrm{out}}, \mathbf{r}_{\mathrm{in}}) = R(k_{\mathrm{out}}, \mathbf{r}_{\mathrm{in}}) T_0^*(k_{\mathrm{out}}, \mathbf{r}_{\mathrm{in}}). \tag{III.74}$$

Injecting Eqs. III.64 and III.69 into the last equation yields the following expression for $D(k_{\mathrm{out}}, \mathbf{r}_{\mathrm{in}})$:

$$D(k_{\mathrm{out}}, \mathbf{r}_{\mathrm{in}}) = \hat{H}(k_{\mathrm{out}}) \int dx\, T_0(k_{\mathrm{out}}, x - x_{\mathrm{in}}) \gamma(x, z) \overline{H}_{\mathrm{in}}(x - x_{\mathrm{in}}). \tag{III.75}$$

To investigate the far-field correlations of the distorted wavefield, the spatial correlation matrix $\mathbf{C}_{\mathrm{kk}} = \mathbf{D}_{\mathrm{kx}} \mathbf{D}_{\mathrm{kx}}^{\dagger}$ is investigated. As previously observed with $\mathbf{B}_{\mathrm{kk}}$, $\mathbf{C}_{\mathrm{kk}}$ should converge towards the covariance matrix $\langle \mathbf{C}_{\mathrm{kk}} \rangle$ for a large number of independent realizations, i.e. a large number N of input focusing points. Assuming this condition is fulfilled in the speckle regime, the correlation coefficients $C(k_{\mathrm{out}}, k'_{\mathrm{out}})$ can be expressed as follows

$$C(k_{\mathrm{out}}, k'_{\mathrm{out}}) = \langle |\gamma|^2 \rangle \int dx' T(k_{\mathrm{out}}, x') \gamma_D(x') T^*(k'_{\mathrm{out}}, x'), \tag{III.76}$$

where

$$\gamma_D(x') = \left| \overline{H}_{\mathrm{in}}(x') \right|^2. \tag{III.77}$$

Equation III.76 can be rewritten as the following matrix product

$$\mathbf{C}_{\mathrm{kk}} \propto \mathbf{T} \times \mathbf{\Gamma}_{\mathbf{D}} \times \mathbf{T}^{\dagger}, \tag{III.78}$$

where $\mathbf{\Gamma}_{\mathbf{D}}$ is a diagonal scattering matrix associated with a virtual object centered at the origin. Its coefficients $\gamma_D(x)$ correspond to the input focal spot intensity $|H_{\mathrm{in}}(x)|^2$. Expressed in the form of Eq. III.78, $\mathbf{C}_{\mathrm{kk}}$ is analogous to the time-reversal operator obtained

for a single scatterer of reflectivity $\gamma_D(x)$ [38, 61]. The unscrambling of input focal spots which is made possible by $\mathbf{D}_{\mathrm{kx}}$ allows the size of the virtual reflector to be reduced to δx, the dimension of the aberrated focal spot (see Fig. 4D of the accompanying paper). This is an important improvement over what is offered by $\mathbf{B}_{\mathrm{kk}}$, the correlation matrix constructed from reflection matrix $\mathbf{R}$.

III.D Normalized correlation matrix

As we will see now, this virtual reflector can even be made point-like by considering a normalized correlation matrix (Eq. 18 of the accompanying paper). To demonstrate this assertion, Eq.III.78 is rewritten with the help of Eq. III.64:

$$C(k_{\mathrm{out}},k'_{\mathrm{out}}) \propto \langle|\gamma|^2\rangle \tilde{H}_{\mathrm{out}}(k_{\mathrm{out}})\tilde{H}^*_{\mathrm{out}}(k'_{\mathrm{out}}) \left[\tilde{H}_{\mathrm{in}} \circledast \tilde{H}_{\mathrm{in}}\right](k_{\mathrm{out}}-k'_{\mathrm{out}}), \tag{III.79}$$

where the symbol $\circledast$ stands for a correlation product. This correlation term in Eq. III.79 results from the Fourier transform of the input focal spot $|\overline{H}_{\mathrm{in}}(x)|^2$ in Eq.III.78. This formulation is reminiscent of the Van Cittert Zernicke theorem for an aberrating layer, which links the spatial correlation of a wavefield to the Fourier transform of the intensity distribution from an incoherent source (here the input focal spots) [11]. In other words, the support of the coherence function $\left[\tilde{H}_{\mathrm{in}}\circledast\tilde{H}_{\mathrm{in}}\right](k_{\mathrm{out}}-k'_{\mathrm{out}})$ scales as the inverse of the input focal spot size δx.

The approach for reducing the size of this virtual scatterer is to render the autocorrelation term flat. Since $|\overline{H}_{\mathrm{in}}(k_x)| = 1$, this can be done by considering the normalized correlation matrix $\hat{\mathbf{C}}_{\mathrm{kk}}$ (Eq. 17) whose coefficients are given by

$$\hat{C}(k_{\mathrm{out}},k'_{\mathrm{out}}) \propto \langle|\gamma|^2\rangle \hat{H}_{\mathrm{out}}(k_{\mathrm{out}})\hat{H}^*_{\mathrm{out}}(k'_{\mathrm{out}}). \tag{III.80}$$

This last equation is valid if the convergence of $\mathbf{C}_{\mathrm{kk}}$ towards the covariance matrix $\langle\mathbf{C}_{\mathrm{kk}}\rangle$ is achieved, i.e. if a large enough number N of input focusing points is considered. Equation III.80 can be rewritten as the following matrix product

$$\mathbf{C}_{\mathrm{kk}} \propto \mathbf{T}\times\mathbf{\Gamma}_\delta\times\mathbf{T}^\dagger, \tag{III.81}$$

where $\mathbf{\Gamma}_\delta$ is a diagonal scattering matrix associated with a point-like scatterer centered at the origin, such that $\gamma_\delta(x)=\delta(x)$ (see Fig. 4E of the accompanying paper).

Expressed in the form of Eq. III.81, $\hat{\mathbf{C}}_{\mathrm{kk}}$ is analogous to the time-reversal operator obtained for a point-like scatterer. Equation III.80 confirms that $\hat{\mathbf{C}}_{\mathrm{kk}}$ is of rank 1 and the corresponding eigenvector $\mathbf{U_1}$ directly provides the aberration phase law:

$$\mathbf{U_1} \equiv [\tilde{H}_{\mathrm{out}}(k_{\mathrm{out}})]. \tag{III.82}$$

An estimator $\bar{\mathbf{T}}$ of the transmission matrix can then be deduced (Eq.22 of the accompanying paper).

III.E Convergence of the matrix approach

Until now, for sake of simplicity, we have assumed that $\hat{\mathbf{C}}_{\mathrm{kk}}$ converges towards the covariance matrix $\langle\hat{\mathbf{C}}_{\mathrm{kk}}\rangle$. However, this is not always the case for restricted fields-of-illumination. Even if this convergence is not achieved, the covariance matrix $\langle\hat{\mathbf{C}}_{\mathrm{kk}}\rangle$ can

still be retrieved by means of the eigenvalue decomposition of $\hat{\mathbf{C}}_{\mathrm{kk}}$. In the isoplanatic limit, the covariance matrix $\langle\hat{\mathbf{C}}_{\mathrm{kk}}\rangle$ is indeed of rank 1 (Eq. III.80). We expect the aberration transmittance $\hat{H}(k_{\mathrm{out}})$ to be contained in first eigenvector $\hat{\mathbf{U}}_{\mathbf{1}}$ of $\hat{\mathbf{C}}_{\mathrm{kk}}$. To derive a necessary condition for this, the matrix $\hat{\mathbf{C}}_{\mathrm{kk}}$ should be written as a sum of the covariance matrix $\left\langle\hat{\mathbf{C}}_{\mathrm{kk}}\right\rangle$ and a perturbation term $\delta\hat{\mathbf{C}}_{\mathrm{kk}}$:

$$\hat{\mathbf{C}}_{\mathrm{kk}} = \left\langle\hat{\mathbf{C}}_{\mathrm{kk}}\right\rangle + \delta\hat{\mathbf{C}}_{\mathrm{kk}}. \tag{III.83}$$

The matrix $\langle\hat{\mathbf{C}}_{\mathrm{kk}}\rangle$ is of rank 1 and associated with a single eigenvalue $\hat{\sigma}_1$. The matrix $\delta\hat{\mathbf{C}}_{\mathrm{kk}}$ can be considered as a correlated random matrix. Its rank is equal to the number M_δ of independent speckle grains in the far-field. In first approximation, the eigenvalues of $\delta\hat{\mathbf{C}}_{\mathrm{kk}}$ can be assumed to follow the eigenvalue distribution of a Hermitian random matrix of size M_δ. $\langle\hat{\mathbf{C}}_{\mathrm{kk}}\rangle$ will emerge along the first eigenstate of $\hat{\mathbf{C}}_{\mathrm{kk}}$ if [96]

$$\frac{\hat{\sigma}_1^2}{\left\langle\sum_{i=1}^{M_\delta}\sigma_i^2\right\rangle} > \frac{4}{M_\delta}. \tag{III.84}$$

The factor 4 comes from the superior bound of the Marcenko-Pastur law [161]– the distribution that the normalized squared eigenvalues of $\delta\hat{\mathbf{C}}_{\mathrm{kk}}$ are supposed to follow. To make this last inequality more explicit, we express the first eigenvalue $\hat{\sigma}_1$ of the covariance matrix and the mean sum of the squared eigenvalues of $\mathbf{C}_{\mathrm{kk}}$, $\left\langle\sum_{i=1}^{M_\delta}\sigma_i^2\right\rangle$. On one hand, because $\langle\hat{\mathbf{C}}_{\mathrm{kk}}\rangle$ is of rank 1, the square of its eigenvalue $\hat{\sigma}_1^2$ is equal to the trace of $\langle\hat{\mathbf{C}}_{\mathrm{kk}}\rangle\langle\hat{\mathbf{C}}_{\mathrm{kk}}\rangle^\dagger$:

$$\hat{\sigma}_1^2 = \sum_{k_{\mathrm{out}}}\sum_{k'_{\mathrm{out}}} |\langle\hat{C}\rangle(k_{\mathrm{out}}, k'_{\mathrm{out}})|^2 = N_k^2, \tag{III.85}$$

where N_k is the dimension of the matrix $\mathbf{C}_{\mathrm{kk}}$. On the other hand, the mean sum of the squared eigenvalues σ_i^2 is equal to the trace of $\mathbf{C}_{\mathrm{kk}}\mathbf{C}_{\mathrm{kk}}^\dagger$:

$$\left\langle\sum_{i=1}^{M_\delta}\sigma_i^2\right\rangle = \left\langle\sum_{k_{\mathrm{out}}}\sum_{k'_{\mathrm{out}}}|\hat{C}(k_{\mathrm{out}}, k'_{\mathrm{out}})|^2\right\rangle. \tag{III.86}$$

Injecting Eq. III.83 into the last equation yields

$$\begin{aligned}\left\langle\sum_{i=1}^{M_\delta}\sigma_i^2\right\rangle &= \sum_{k_{\mathrm{out}}}\sum_{k'_{\mathrm{out}}}|\langle\hat{C}\rangle(k_{\mathrm{out}}, k'_{\mathrm{out}})|^2 + \sum_{k_{\mathrm{out}}}\sum_{k'_{\mathrm{out}}}\langle|\delta\hat{C}(k_{\mathrm{out}}, k'_{\mathrm{out}})|^2\rangle \\ &= N_k^2 + \sum_{k_{\mathrm{out}}}\sum_{k'_{\mathrm{out}}}\langle|\delta\hat{C}(k_{\mathrm{out}}, k'_{\mathrm{out}})|^2\rangle.\end{aligned} \tag{III.87}$$

Since the coefficients $\hat{C}(k_{\mathrm{out}}, k'_{\mathrm{out}})$ are of modulus 1, their variance is directly given by their phase fluctuations:

$$\left\langle\left|\delta\hat{C}(k_{\mathrm{out}}, k'_{\mathrm{out}})\right|^2\right\rangle = \left\langle\left|\arg\left\{\hat{C}(k_{\mathrm{out}}, k'_{\mathrm{out}})\right\}\right|^2.\right\rangle \tag{III.88}$$

For a large number N of input focusing points, the variance $\left\langle \left| \delta\hat{C}(k_{\text{out}}, k'_{\text{out}}) \right|^2 \right\rangle$ of the normalized correlation matrix coefficients can be expressed as follows [159, 150]

$$\left\langle \left| \arg\left\{ \hat{C}(k_{\text{out}}, k'_{\text{out}}) \right\} \right|^2 \right\rangle \simeq N^{-1} \left(|C(k_{\text{out}}, k'_{\text{out}})|^{-2} - 1 \right). \tag{III.89}$$

Injecting Eqs. III.88 and III.89 into Eq. III.87 leads to

$$\left\langle \sum_{i=1}^{M_\delta} \sigma_i^2 \right\rangle \simeq N^{-1} \sum_{k_{\text{out}}} \sum_{k'_{\text{out}}} |C(k_{\text{out}}, k'_{\text{out}})|^{-2}. \tag{III.90}$$

For analytical tractability, we will replace $|C(k_{\text{out}}, k'_{\text{out}})|$ by its average over all pairs $(k_{\text{out}}, k'_{\text{out}})$. Interestingly, this mean correlation value scales directly as the inverse of M_δ, where M_δ is the number of independent speckle grains in the far-field [149]. The previous equation can then be simplified as follows:

$$\left\langle \sum_{i=1}^{M_\delta} \sigma_i^2 \right\rangle \sim N_k^2 M_\delta^2 / N. \tag{III.91}$$

Injecting Eqs. III.85 and III.91 into Eq. III.84 yields our final expression of the success condition:

$$N > 4M_\delta. \tag{III.92}$$

The number N of input focusing points in the field-of-illumination should be large compared to the number M_δ of independent speckle grains in the far-field. The latter quantity is equal to the ratio between the support Δk of the distorted wavefield in the spatial frequency domain, and its correlation width δk:

$$M_\delta = \Delta k / \delta k. \tag{III.93}$$

Each distorted wavefield is produced by a virtual incoherent source in the focal plane whose size is given by the extension δx of the input focal spot. By the van Cittert Zernike theorem, the correlation width δk scales as the inverse of δx. Reciprocally, the spatial frequency support Δk scales as the inverse of the coherence length of the wavefield in the focal plane, i.e the resolution cell δx_0. M_δ is thus equal to the number of resolution cells δx_0 mapping the aberrated focal spot:

$$M_\delta = \delta x / \delta x_0. \tag{III.94}$$

The condition of Eq. III.92 can thus be translated as follows: the number N of input focusing points forming the field-of-illumination should be one order of magnitude larger than the number of resolution cells mapping the aberrated focal spot. This result is fundamental since it governs our strategy for full-field imaging. An iterative procedure is employed and consists in progressively correcting aberrations over smaller and smaller fields-of-illumination.

III.F Linear phase ramp artifact

Generally, the first eigenvector $\mathbf{U}_1$ focuses on the center of the virtual reflector since it maximizes the back-scattered energy. However, it might not be the case if the scattering distribution $|H_{\text{in}}|^2$ is too complex. In that case, the phase of $\mathbf{U}_1$ can display a linear phase ramp that results in a lateral shift of the imaging PSF. If no effort is made to remove this shift, each selected area defined by the spatial window function (Eq. III.43) could suffer from arbitrary lateral shifts compared to the original image. This artifact can be suppressed by removing the linear component of the phase of $\mathbf{U}_1$ [60]. One way to do it consists in reversing Eq. III.45 to estimate the lateral extension of the PSF H_1 associated with the estimated aberration phase law $\hat{\mathbf{U}}_1$:

$$H_1(x, \mathbf{r}_{\text{p}}) = \sum_{u_{\text{out}}} \hat{U}_1(u_{\text{out}}) e^{i \frac{k_c}{2z} u_{\text{out}} x} \tag{III.95}$$

If this PSF $H_1(x)$ is not centered on the origin ($x = 0$), the offset δ is computed by measuring the auto-convolution function $[|H_1| \circledast |H_1|]$. The maximum of this function actually indicates the barycenter of the PSF energy [Fig. 13e]. The auto-convolution peak is obtained for $x = 2\delta$. A corrected aberration phase law $\hat{U}_1'(u_{\text{out}}, \mathbf{r}_{\text{p}})$ is finally computed by translating the PSF $H_1(x)$ of a distance $-\delta$ and by back-propagating the shifted PSF towards to the transducer basis:

$$\hat{U}_1'(u_{\text{out}}, \mathbf{r}_{\text{p}}) = \sum_{x} H_1(x - \delta, \mathbf{r}_{\text{p}}) e^{-i \frac{k_c}{2z} u_{\text{out}} x} \tag{III.96}$$

By combining Eqs. III.95 and III.96, the articfact correction can be seen as a compensation of a linear phase ramp in $\overline{\mathbf{U}}_1(\mathbf{r}_{\text{p}})$:

$$\hat{U}_1'(u_{\text{out}}, \mathbf{r}_{\text{p}}) = \hat{U}_1(u_{\text{out}}, \mathbf{r}_{\text{p}}) e^{-i \frac{k_c}{2z} \delta (u_{\text{out}} - x)/z} \tag{III.97}$$

Fig. 13(c) illustrates this linear ramp compensation by comparing the phases of $\hat{\mathbf{U}}_1$ and $\hat{\mathbf{U}}_1'$ computed for the area $\mathcal{A}_2$ in Fig. 12(a). The vector $\hat{\mathbf{U}}_1'$ is the final estimator of the aberration phase transmittance $\tilde{\mathbf{H}}_{\text{out}}$. It is also important to note that an aberrating layer with a particular shape such as wedges will introduce a linear phase ramp in their associated aberration phase law. For such a particular case, there is an uncertainty on the origin of the offset. The removal of a linear phase ramp should thus be used with caution as it could cancel the benefits of the aberration correction process.

Chapter IV

Matrix approach of quantitative ultrasound imaging

Contents

A disease generally modifies some of the mechanical properties of the medium. Any indirect indicator that is based on such properties then becomes a relevant bio-indicator for assessing, monitoring and detecting the stage of this disease. For instance, transient elastography [26] is one of the most accurate non-invasive bio-marker for the diagnostic of

malignant tumors. More precisely, this technique enables the distinction between benign or malignant breast tumors. It is based on the estimation of the tissues' Young modulus that is assumed to be directly linked to the shear wave velocity.

In this chapter we build upon the focused reflection matrix and the time-focused reflection matrix to provide new techniques to (*i*) estimate the medium speed of sound, (*ii*) quantify the multiple-scattering-rate in the back-scattered echoes, and (*iii*) characterize locally the nature and anisotropy of the scatterers via their radiation pattern and frequency response. Note that the last section of chapter 1 provides a non-exhaustive review of the major state-of-the-art techniques associated with each topic [Par. I.3]. These techniques fall into the concept of matrix imaging and constitutes only examples of the wide range of applications that can be tackled by this elegant matrix formalism.

IV.1 Speed of sound measurement

As stated in paragraph I.3.1, speed of sound measurement techniques mainly fall in two categories. The first kind probes the medium integrated speed of sound, which corresponds to an average estimation of the medium speed of sound (SoS) over the round-trip paths, *i.e.* the average speed of sound between the probe and the point under investigation. These techniques provide an accurate measurement of the medium speed of sound in the case of homogeneous tissues. Their bias is generally less than 1% (corresponding to less than 10 m/s). However, by construction, they are not suitable to *in-vivo* ultrasound imaging where the medium is generally heterogeneous. For instance, in the case of liver imaging, the probe is placed between the patient ribs and the waves travel through multiple layers of skin, fat, and muscle tissues before reaching the organ to study. The second type of techniques provides a local measurement of the medium speed of sound. This information is generally extracted from an analysis of the realigned signals. Indeed, this matrix contains information on the errors of time-of-flight induced by an incorrect SoS model, for specific transmitted and received path. The local SoS measurement then results from the resolution of an inverse problem that links the local slowness of the medium (inverse speed of sound) to the cumulative error along each path.

In this section we first show how the focusing criterion can be used as a robust figure of merit of an iterative process that converges towards the best speed of sound model. Both homogeneous and stratified SoS model are investigated to work towards a local measurement of the medium speed of sound. A second promising technique is then developed based on the analysis of the time-focused reflection matrix and wave-front frame. It achieves to combine a high spatial resolution of 2D integrated SoS maps with a low computational burden. It then constitutes a promising technique for 2D SoS maps at quasi real-time.

IV.1.1 Analysis of the focusing criterion, a robust figure of merit for optimal focusing

IV.1.1.1 Calibration experiment, analysis of a homogeneous medium

The focusing criterion quantifies locally the quality of focus. As stated in paragraph II.2.4, it is built upon the measurement of the lateral input-output resolution. We recall

that this resolution is measured by means of the focused reflection matrix expressed in the common-mid-point frame, at the focusing time ($\Delta\tau = 0$). Here we only study the lateral extension of the broadband input-output PSF. It thus corresponds to the configuration where the two virtual transducers are located at the same depth. We recall that the broadband focused reflection matrix is then noted $\overline{\mathbf{r}}_{\mathrm{xx}}(z)$ [Par. II.2.2].

This lateral resolution is sensitive to the cumulative impact of transmitted and received aberrations, which stem from an incorrect SoS model. The quality of focus and thus the focusing criterion is then optimal when the speed of sound model $c_0(\mathbf{r})$ matches the speed of sound of the medium $c_{\mathrm{t}}(\mathbf{r})$. This focusing criterion can thus be used as a figure of merit of an iterative process in order to converge towards the best SoS model. To this end, synthetic beamforming techniques based on unfocused illumination, *e.g.* plane waves or diverging waves, are particularly well suited. No assumption on the medium speed of sound is required for these insonifications and the beamforming process is performed numerically. Therefore, only a single insonification sequence is required to build focused reflection matrices according to various speed of sound models.

In the following, we study the case of a plane plane wave illumination sequence. We remind the fact that each plane wave can be analyzed as a lateral spatial frequency that is linked to the incident angle via the relation $k_{\mathrm{in}}^{\mathrm{x}} = 2\pi f/c_{\mathrm{t}} \sin(\theta_{\mathrm{in}})$. While this spatial frequency is independent of the speed of sound model, it is not the case of the incident angle. This phenomenon requires to be compensated in the iterative process based on the Snell-Descartes laws:

$$\frac{\sin\theta_c}{c} = \text{constant}. \tag{IV.1}$$

Across the iterative process, various assumptions on the medium SoS are performed. A special attention must be paid on the fact that the axial component of the ultrasound image is actually a time axis. It is translated into a spatial axis thanks to the SoS model. Therefore, a change of the SoS model, implies an axial translation of the resulting image. To be efficient, the iterative algorithm should compare the focusing quality of echoes associated with the exact same region, which will be imaged based on various SoS model $c(\mathbf{r})$. This phenomenon is overcome by working at a constant time-of-flight, meaning that the scatterers are designated based on their focused time τ. As it is more practical to consider the axial axis as a spatial axis, this method is equivalent to study the reflection matrix by means of a homogeneous speed of sound of reference c_0. Therefore, a scatterer located at z_0 in the SoS model of reference, will be find at depth z in a stratified medium $c(z)$, such as:

$$\tau = \frac{z_0}{c_0} = \int_0^z \frac{dz}{c(z)}. \tag{IV.2}$$

This speed of sound is arbitrary chosen as $c_0 = 1540$ m/s. Note that in the following, we only investigate stratified medium. In the case of a 2D SoS model, a lateral compensation should also be performed.

To begin, we study the case of a homogeneous medium with an unknown speed of sound c_t, *e.g.* a conventional phantom experiment [Fig. 1(a)]. In this case, we assess the focusing quality at location $\mathbf{r}_0 = \{x, z_0\}$, (defined at c_0) for various speed of sound

hypotheses c, by means of the following propagation matrices:

$$P_1\left(\mathbf{r}_0, k^{\mathrm{x}}, c, f\right) = \exp\left[i2\pi f\left(\frac{\sin\theta_0}{c_0}x + \frac{z_0}{c_0}\cos\theta_c\right)\right], \tag{IV.3a}$$

$$G_1\left(\mathbf{r}_0, u, c, f\right) = \sum_{k^{\mathrm{x}}} P_1\left(\mathbf{r}_0, k^{\mathrm{x}}, c, f\right)\ \exp\left[-ik^{\mathrm{x}}\ u\right], \tag{IV.3b}$$

where

$$\theta_c = \mathrm{asin}\left(\frac{c}{c_0}\sin\theta_0\right). \tag{IV.4}$$

We observe that $P_1\left(\mathbf{r}_0, k^{\mathrm{x}}, c, f\right) = P_0\left(\mathbf{r}, k^{\mathrm{x}}, c, f\right)$ therefore, this propagation matrix simply performs an additional axial shift to find the exact same echoes at a given depth independently of the SoS hypothesis. Note that to maintain the diffraction phenomenon identical from one speed of sound model to the other, we derived the propagation matrix $\mathbf{G}_1(c, f)$ from $\mathbf{P_1}(c, f)$. Consequently, to focus inside the medium, the transducer basis $\mathbf{u}$ is first converted into a plane wave basis $\mathbf{k}^{\mathrm{x}}$ by means of the spatial Fourier operator $\mathbf{T}$. In a matrix formalism, equation IV.3 can be written as:

$$\mathbf{G}_1(c, f) = \mathbf{P}_1(c, f) \times \mathbf{T}^*(f). \tag{IV.5}$$

This operation allows to use the exact same lateral wave number in reception. In addition, this operation will be quite useful to tackle the case of stratified SoS models.

To sum up, the focusing criterion $F(\mathbf{r}_0, c)$ is computed for all focal spots $\mathbf{r}$ and an ensemble of speed of sound hypotheses c. Due to the speckle regime, a spatial averaging is required to smooth out the medium reflectivity. Mathematically, this spatial average consists in using a spatial moving window $W_{l_x,l_z}(\mathbf{r}_0, c)$. The speed of sound $\hat{c}_1(\mathbf{r}_\mathrm{p})$ finally corresponds to the speed of sound model that maximizes the average focusing criterion associated with the spatial window centered on $\mathbf{r}_\mathrm{p}$:

$$\hat{c}_1(\mathbf{r}_\mathrm{p}) = \max_c\left[\left\langle F(\mathbf{r}, c)\ W_{l_x,l_z}(\mathbf{r}_0 - \mathbf{r}_\mathrm{p}, c)\right\rangle_{\mathbf{r}_0}\right], \tag{IV.6}$$

with

$$W_{l_x,l_z}(\mathbf{r}) = \begin{cases} 1 & \text{, for } |x| < l_x\frac{c}{c_0} \text{ and } |z| < l_z, \\ 0 & \text{, otherwise.} \end{cases} \tag{IV.7}$$

$\{l_x, l_z\}$ are the spatial dimensions of the spatial window set at c_0. Note that, to maintain constant the number of lateral resolution cells within the selected area, the lateral dimension of the spatial window depends on the hypothesis of speed of sound c. This correction is not necessary for l_z as the axial shift is already compensated. In the following experiments, the spatial window has been arbitrarily defined as $\{l_x, l_z\} = \{24, 2\}$ mm [white rectangle on Fig. 1]. As a result, only an axial profile $\hat{c}_1(z)$ is estimated. As we only assumed homogeneous SoS model, $\hat{c}_1$ estimates the medium speed of sound averaged over the entire crossed section. It is thus an integrated speed of sound measurement:

$$\frac{1}{\hat{c}_1(z_\mathrm{p})} = \int_0^{z_p} dz\ \frac{1}{c_{\mathrm{t}(z)}}. \tag{IV.8}$$

Note that figure [Fig. 2(e)] shows an example of the maximization process used to estimate the medium's integrated speed of sound [Eq. IV.6]. More details are provided later.

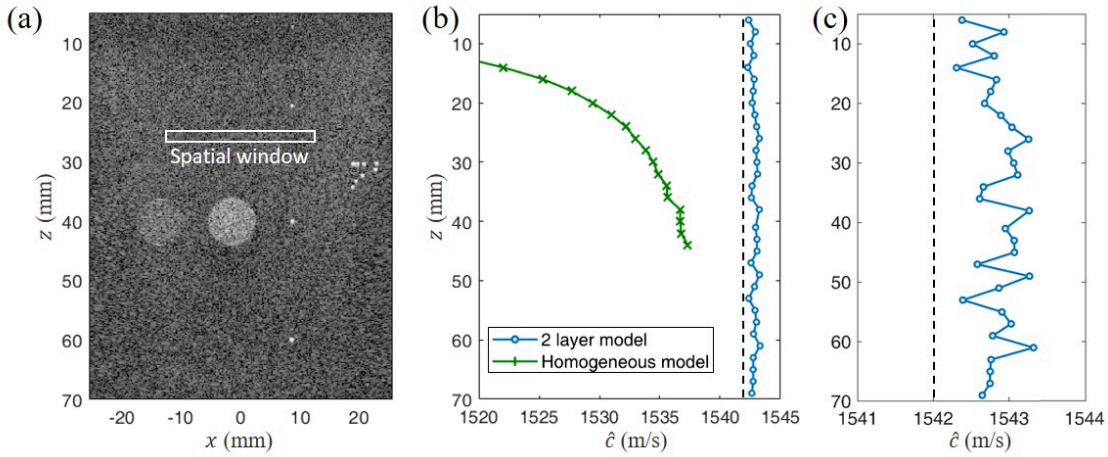

Fig. 1 *Calibration experiment based on homogeneous phantom. (a) Ultrasound image. The white rectangle corresponds to the spatial window used to measure the integrated SoS. (b) Integrated SoS profiles $\hat{c}_1(z)$ and $\hat{c}_2(z)$, obtained from the optimization of homogeneous speed of sound models (green curve) and two-layer models (blue curve), respectively. The first layer of the two-layers model corresponds to the probe lens. Its properties are determined via an optimization process, whose figure of merit is the global curvature of $\hat{c}_2(z)$. Reference phantom speed of sound $c_{phantom} = 1542 \pm 10$ m/s (dark dotted curve). (c) lateral zoom of figure b*

The green curve of figure [Fig. 1] shows the resulting profile $\hat{c}_1(z_p)$ in a homogeneous phantom. The manufacturer's specification is $c_{\text{phantom}} = 1542 \pm 10$ m/s. Unfortunately, a huge bias is observed especially at shallow depth ($\Delta_c \sim 20$ m/s at $z = 15$ mm). Furthermore, to the contrary of the expected result, $\hat{c}_1(z_p)$ is not a constant function and increases with depth. It seems to converge toward the phantom speed of sound. This bias is likely due to the aberrations induced by both the probe lens and matching layers. Indeed, this structure is characterized by an average speed of sound and thickness around $c_1 \sim 1000$ m/s and $h_1 \sim 1$ mm, respectively. (The exact manufacturer's values are classified information). As a result, the medium under investigation is a two-layer medium composed of the probe lens and the phantom. In this case, $\hat{c}_1$ measures the average speed of sound of these two layers. Note that the relative error on the time-of-flight induced by the probe lens compared to the total time of flight decreases with the focal plane. At large depth, the medium can then be seen as quasi-homogeneous, thus the convergence of c_l towards c_{phantom}. For imaging purposes, the aberrations induced by the probe lens are weak and mainly concern shallow depths. Usually these areas do not constitute a region of interest. Therefore, the interest of correcting for these aberrations is quite low for US imaging. However, in the case of speed of sound measurement, the impact of the probe lens is huge and needs to be corrected. To this end we modify the propagation matrix to

consider a two-layer SoS model

$$P_2\left(\mathbf{r}_0, k^{\mathrm{x}}, c_0, f\right) = \exp\left[i2\pi f \left(\frac{\sin\theta_0}{c_0} x \; + \; \underbrace{\frac{h_1}{c_1}\cos\theta_1}_{1^{\mathrm{st}}\text{ layer at } c_1} \; + \; \underbrace{\left(\frac{z_0}{c_0} - \frac{h_1}{c_1}\right)\cos\theta_c}_{2^{\mathrm{nd}}\text{ layer at } c} \right) \right]. \quad \text{(IV.9)}$$

For a given lens thickness h_1 and speed of sound c_1, the focusing criterion is computed as a function of the second medium speed of sound c. In this case, the optimal focusing criterion enables to estimate the integrated speed of sound in the second layer:

$$\frac{1}{\hat{c}_2(z_p)} = \int_h^{z_p} dz \; \frac{1}{c_{\mathrm{t}(z)}}. \quad \text{(IV.10)}$$

The analysis of $\hat{c}_2(z_p)$ is used to calibrate the lens feature. Indeed, equation IV.10 is unbiased, *i.e.* $\hat{c}_2(z_p) \sim c_{\mathrm{phantom}}$, only if the lens parameters are accurate. We then perform an iterative process in order to find these parameters that maximizes this figure of merit. However, the manufacturer's specification of the phantom SoS is not accurate enough to be used as an efficient figure of merit (± 10 m/s). To overcome this issue, we search for the lens parameters that produce a constant integrated speed of sound profile $\hat{c}_2(z_p)$. Mathematically, we minimize the standard deviation of $\hat{c}_2(z_p)$. Note that as the speed of sound measurement is mainly based on the estimation of the optimal times-of-flight, only the ratio h_1/c_1 can be determined. Experimentally, we arbitrarily choose to fix c_1 according to the manufacturer's specification and to optimize the lens thickness h_1. Blue curves of figures 1(b,c) show the integrated SoS profile $\hat{c}_2(z_p)$ that results from the optimization process. The average and standard deviation of the integrated speed of sound profile is $\langle \hat{c}(z_{\mathrm{p}}) \rangle_{z_{\mathrm{p}}} = 1542.8 \; \pm \; 0.5$ m/s, which is in excellent agreement with the manufacturer's specification.

IV.1.1.2 Towards a local speed of sound profile, the case of stratified medium

Based on this calibration, we study a more complicated configuration where the medium is assumed as stratified. The idea simply consists in estimating the integrated speed of sound at shallow depth and take advantage of this measurement to update the stratified propagation matrices to probe the medium SoS at larger depth. The proposed algorithm can be seen as an iterative process, whose each step is used to characterize a precise layer i. As the first layer of the medium corresponds to the probe lens, the initialization of this process has already been described and the speed of sound in the second layer can be measured based on $\hat{c}_2$. We denote $z_0^{(i)}$ the depth of the interface (defined at the reference speed of sound c_0) between the i^{th}-layer and the $(i+1)^{\mathrm{th}}$-layer. Ingeniously, these layers are defined so that they match the apparent structure of the medium that are observed by means of an US image computed at c_0. We denote c_i and h_i the speed of sound and thickness of the i^{th}-layer.

We then describe the i^{th}-step that consists in estimating the thickness and speed of sound of the i^{th}-layer based on the results of the $(i-1)$-first steps. In order to create the focused reflection matrix at the focal plane z_0, such as $z_0^{(i-1)} < z_0 < z_0^{(i)}$ we defined the

propagation matrices ($\mathbf{G}_i$ and $\mathbf{P}_i$) associated with a i-SoS layer model:

$$P_i\left(\mathbf{r}_0, k^{\mathrm{x}}, c, f\right) = \exp\left[i2\pi f \left(\frac{\sin\theta_0}{c_0} x \; + \; \underbrace{\left(\frac{z_0}{c_0} - \sum_{n=1}^{i-1} \frac{h_n}{c_n} \right) \cos\theta_c}_{i^{\text{th}} \text{ layer at c}} \; + \; \underbrace{\sum_{n=1}^{n=i-1} \frac{h_n}{c_n} \cos\theta_n}_{(i-1) \text{ first layers}} \right) \right], \quad \text{(IV.11)}$$

The optimization process of the focusing criterion enables to measure $\hat{c}_i$ the integrated speed of sound in the i^{th}-layer. We observe that only the speed of sound in the i^{th}-layer is optimized. By assuming that the previous steps accurately characterize the $(i-1)$ first layers, $\hat{c}_i(z_{\mathrm{p}})$ becomes a local estimation of the medium speed of sound and can be expressed as:

$$\frac{1}{\hat{c}_i(z_{\mathrm{p}})} = \int_{z_0^{i-1}}^{z_p} dz_0 \; \frac{1}{c_{\mathrm{t}(z_0)}} \quad \text{(IV.12)}$$

The estimation of $\hat{c}_i(z_0^{(i)})$ at depth $z_0^{(i)}$, which corresponds to the interface between the layer i and $(i+1)$, gives access to the average speed of sound c_i in i^{th}-layer,

$$c_i = \hat{c}_i(z_0^{(i)}). \quad \text{(IV.13)}$$

Finally, this speed of sound is used to measure the thickness h_i of the i^{th}-layer. Indeed, the round-trip time of flight of the echoes is the same for the homogeneous model defined at c_0 or for the stratified model. h_i can then be expressed as:

$$h_i = c_i \left[\frac{z_0^{(i)}}{c_0} - \sum_{n=1}^{n=i-1} \frac{h_n}{c_n} \right]. \quad \text{(IV.14)}$$

This process is then iterated to characterized the $(i+1)^{\text{th}}$-layer. Finally, an entire profile of wave velocity throughout the medium is constructed by combining the integrated speed of sound profiles associated with each layer:

$$\hat{c}(z_{\mathrm{p}}) = \hat{c}_i(z_{\mathrm{p}}), \text{ for } z_0^{(i-1)} < z_0 < z_0^{(i)}. \quad \text{(IV.15)}$$

Last but not least, note that the integrated speed of sound profile maximizes the image quality. Therefore, it is possible to construct an optimal ultrasound image by selecting the diagonal of the focused reflection matrices computed at each depth with the optimized speed of sound model. This technique enables to correct only for the lateral aberration. In addition, a first order axial aberration correction can finally be performed. As stated in paragraph I.1.5 this correction simply consists in modifying the axial axis of the ultrasound image to take into account the optimized stratified model. Similarly to equation IV.14 the scatterer located within the i^{th}-layer at depth z_0 in the homogeneous model should appear at depth $\hat{z}$ defined by:

$$\hat{z} = c_i \left[\frac{z_0}{c_0} - \sum_{n=1}^{n=i-1} \frac{h_n}{c_n}. \right]. \quad \text{(IV.16)}$$

Based on this equation, the axial correction can be performed by means of an interpolation technique from the laterally corrected image. Unfortunately, this correction as not been performed in the following example.

IV.1.1.3 Experimental measurement of a quasi-local speed of sound profile

We apply this algorithm on two configurations: (*i*) an *in-vitro* experiment where the medium under investigation is composed of a 18.4-mm thick layer of bovine tissue placed on top of the previously studied phantom [Fig. 2]; and (*ii*) an *in-vivo* experiment that probes the liver of a healthy volunteer [Fig. 4](a). The first experiment mimics the case of liver imaging. Indeed, in such *in-vivo* experiment, the liver is separated from the probe by multiple layers of skin, fat and muscle tissues. We first rely on the *in-vitro* experiment to assess the accuracy of our approach as no reference speed of sound values are available for the analysis of the *in-vivo* experiment.

1st experiment, the bovine tissue/phantom system Figure 2 shows the results of the *in-vitro* experiment. Figure (d) displays the ultrasound image computed in the homogeneous model (at c_0). The interface $z_0^{(2)}$ between the bovine tissue and the phantom is easily identifiable. For $z_0 < z^{(2)}$, the integrated speed of sound $\hat{c}_2$ is determined in the bovine tissue based on the two-layer model described in the calibration [blue curve on Fig. 2(f)]. This sub-SoS profile is quite constant $c_{\text{steak}} = 1570$ m/s and agrees well with the commonly cited value of $c_{\text{muscle}} = 1576 \pm 1.1$ m/s [162]. Figure (b) Shows the focused reflection matrix at the interface. As stated in paragraph II.2.4, to accurately model the input-output resolution, the nature of the scatterer should be determined. The interface is definitely a specular scatterer as at least one of its dimensions is higher than the wavelength. This characteristic is visible on figure (b). Indeed, the correlation length of confocal signals (diagonal signals) is clearly higher than the resolution cell. Based on this assumption, the focusing criterion is computed for various hypothesis of speed of sound c associated with the second layer (bovine tissue) [blue curve of Fig. 2(e)]. The optimal focusing criterion is close to one, meaning that a quasi-perfect focusing quality is reached. This maximum is obtained for $c_2 \approx$ 1573 m/s. This value will now be used in order to focus inside the phantom via a three-layer model. The red curve of figure (e) shows the optimization process at $z_0 = [29 : 31]$ mm. In this case, the speckle assumption is used for the focusing criterion. The optimal configuration is reached for $\hat{c}_3(z_0) = 1544$ m/s, which is close to the estimated speed of sound that results from the calibration step. The red curve of figure (f) shows the sub-SoS profile obtained in the phantom layer $\hat{c}_3$ with an average value of $\langle c_p \rangle = 1547$ m/s ($z > 30$ mm). Compared to the calibration experiment, we observe a bias of 4 m/s. As stated in the first chapter [Par. I.3.1], this accuracy is quite reasonable for clinical applications. Note that, at depths just below the interface between the bovine tissue and phantom layer, a bias is observed. This effect can be explained by the fact that the measurement error $\Delta c_p/c_p$ on the wave velocity scales as the inverse of z_p, the depth of the focal plane from the phantom surface [see Appendix IV.A, Eq. IV.43]:

$$\left(\frac{\Delta c_p}{c_p}\right)^2 \sim \frac{1}{(k_p z_p)^2} \frac{\sin\beta}{\operatorname{arctanh}(\sin\beta) - \beta^2/\sin\beta} \frac{\Delta F}{F}, \tag{IV.17}$$

with $k_p = 2\pi f_c/c_p$. As the precision with which the focusing criterion F can be measured is $\Delta F/F \sim 5 \times 10^{-4}$ [see Fig. 2(e)], a precision of $\Delta c_p \sim 5$ m/s for the wave velocity in the second layer (the phantom) will only be reached for $z_p >\sim 10$ mm. This value is in qualitative agreement with the axial resolution of the wave velocity profile displayed in

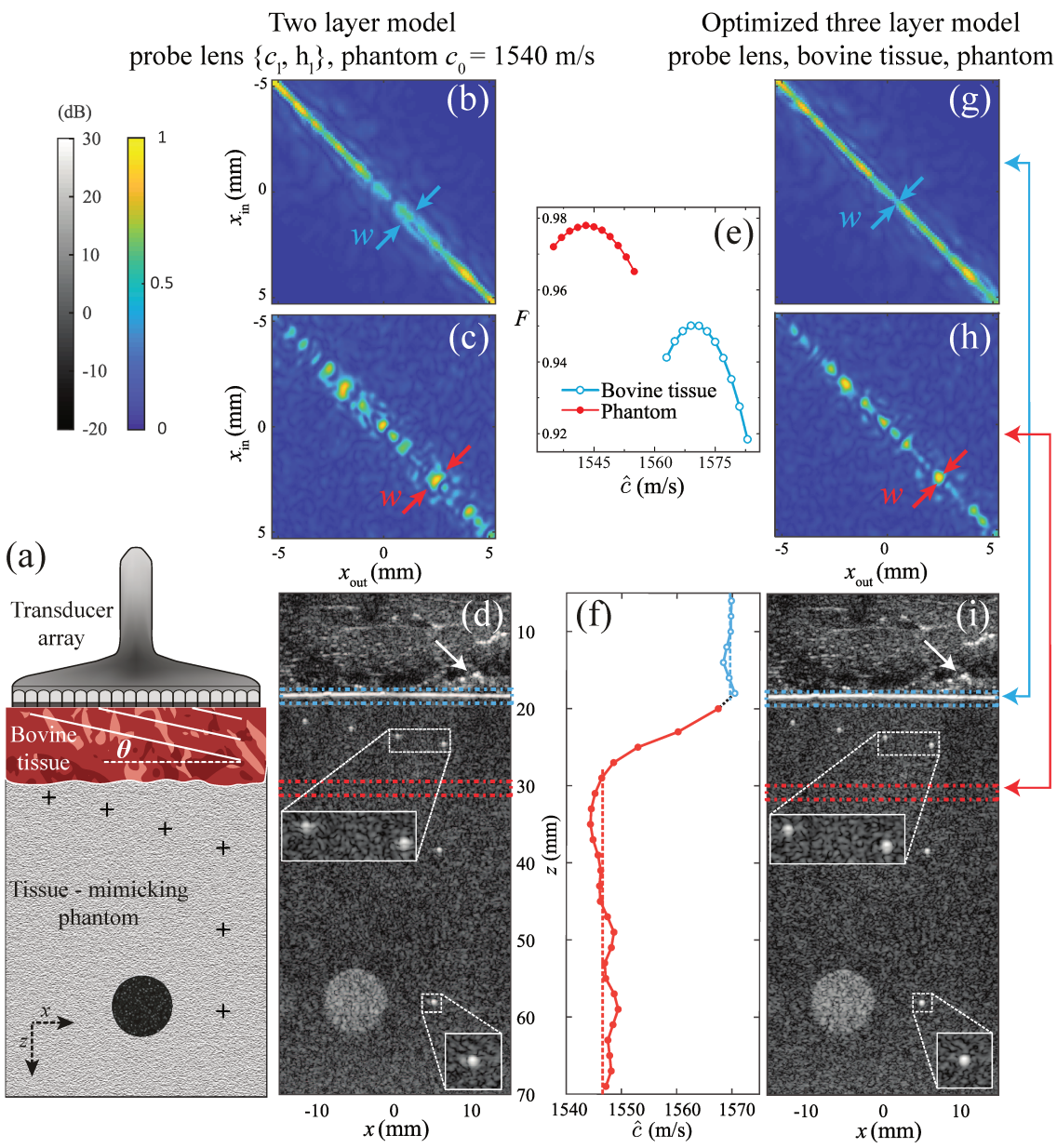

Fig. 2 *Speed of sound measurement of an in-vitro stratified bovine tissue/phantom experiment (a). (b,c) Matrix* $\overline{\mathbf{r}}_{xx}(z)$ *is displayed at depth* $z = 18.4$ *mm and 30 mm, respectively, assuming a two-layer model SoS model* ($c_1 = c_l$ *and* $c_2 = c_0 = 1540$ *m/s). The local image resolution* w *is extracted from each anti-diagonal of* $\overline{\mathbf{r}}_{xx}(z)$ *to measure the focusing criterion. (d) Corresponding ultrasound image. (e) Optimization of the focusing criterion. Measurement of* $\hat{c}_2(z_p = 18.4$ *mm) (blue curve) and* $\hat{c}_3(z_p = 30$ *mm) (red curve). (f) Speed of sound profile* $\hat{c}$ *composed of the two sub-SoS profiles* $\hat{c}_2$ *(blue curve) and* $\hat{c}_3$ *(blue curve) associated with the bovine tissue and phantom, respectively. (g,h,f) Focused reflection matrices* $\overline{\mathbf{r}}_{xx}(z)$ *and ultrasound image, respectively, obtained after the optimization process.*

Fig. 2(d). In addition, as in any inverse problem, a small error on the SoS of the first layer impacts the determination of the speed of sound in the second medium just below the interface.

Figure2(d,i) display the ultrasound images computed with the initial two-layer model (probe lens + medium, $c_0 = 1540$ m/s) and with the optimized three-layer model, respectively. It can be seen by eye that the optimized model slightly improves the imaging of bright targets, but that there is no clear difference in areas of speckle. Figure(b,g) show their respective focused reflection matrices $\bar{\mathbf{r}}_{\mathrm{xx}}(z)$ computed at the specular interface bovine tissue/phantom $z_0 = 18.4$ mm and (c,h) inside a speckle region of the phantom at $z_0 = 30$ mm. A striking improvement of the input-output resolution $w(\mathbf{r})$ (measured along the anti-diagonal of $\bar{\mathbf{r}}_{\mathrm{xx}}(z)$) is observed at both depths. This observation is confirmed by their respective map of focusing criterion in figure 3. The initial two-layer model induces a poor quality of focus over a large part of the image. It can be attributed to the fact that the presence of the bovine tissue layer was not taken into account in the initial two-layer model. The optimized three-layer is finally able to correct for these aberrations. However, as the chosen spatial window is quite large to efficiently smooth out the fluctuations of the speckle reflectivity, some local aberrations can still be visible at $\{x, z\} = \{10, 25\}$ mm. These aberrations may be induced by the bubbles located within the bovine tissue (that has not been degassed) [white arrows on Fig. 2(d,i)]. Note that the second algorithm that measures the integrated SoS overcomes this limitation as its required spatial average is deeply reduced [Par. IV.1.2]. The significance of this result is that, in regions of speckle, $F(\mathbf{r})$ is far more sensitive than image brightness to the quality of focus and speed of sound. As many integrated speed of sound measurements are based on image brightness [163, 164, 165], $F(\mathbf{r})$ thus constitutes an important new metric for speed of sound measurement in heterogeneous media.

2nd experiment, the *in-vivo* liver experiment The results of the *in-vivo* liver imaging of the healthy volunteer are shown on Figure 4. On the ultrasound image (a), four distinct tissue layers can be identified: skin, fat, muscle, and liver tissue. In this case, the medium under investigation is decomposed in five layers (the four above mentioned and the probe lens). Figure 4(b) shows the estimated speed of sound profile $\hat{c}(z_{\mathrm{p}})$ plotted as a function of depth and constructed based on the combination of each sub-profile $\hat{c}_i(z_{\mathrm{p}})$. We are thus able to estimate the speed of sound for each tissue layer. In the skin, previous authors have reported speed of sound values in the range of $c_{\mathrm{skin}} \approx 1500 - 1750$ m/s, with an average value of $c_{\mathrm{skin}} \sim 1625$ [166]. The wide range of values for c_{skin} is most likely due to the significant sensitivity of this parameter on skin hydration, as well as variations in temperature, age of the cadaver skin examined, and region of the body from which the skin was extracted. Thus, more accurate approaches for this measurement would be valuable. Our method gives an estimate of $c_{\mathrm{skin}} \approx 1651$ m/s, which to our knowledge constitutes the first in vivo measurement of c_{skin} in this frequency range. Indeed, as the skin is located at shallow depth, higher frequencies are generally used to benefit from a higher resolution without SNR issue due to attenuation. In the fat layer, we find an average value of $c_{\mathrm{fat}} = 1413 \pm 6$ m/s. (The standard deviation of the values in this layer is used as an estimate of the experimental uncertainty.) Our result agrees with previously reported results of $c_{\mathrm{fat}} = 1427 \pm 12.7$ m/s [167]. In the muscle layer, our measured average value of $c_{\mathrm{muscle}} = 1582 \pm 9$ m/s agrees with the commonly cited

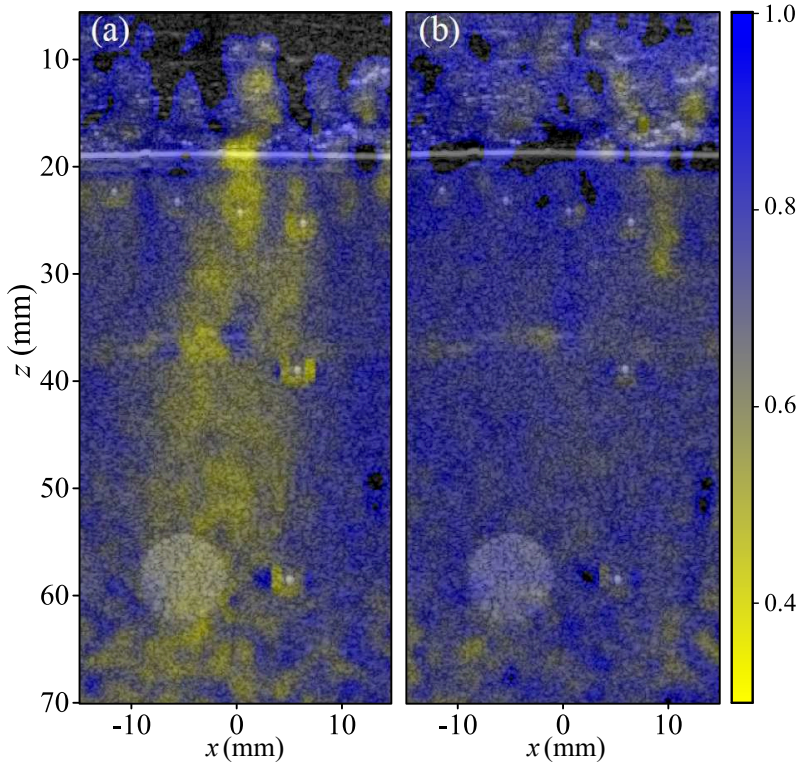

Fig. 3 *Maps of local focusing parameter $F(\mathbf{r})$ for the bovine tissue/phantom experiment, superimposed over the US image of Fig. 2(c). (a) The homogeneous model with a two-layer model ($c_1 = c_l$ and $c_2 = c_0 = 1540$ m/s) results in a poor quality of focus in some areas. (b) The optimized three-layer model used to construct $\overline{\mathbf{R}}_{xx}(z)$ results in close to ideal focus quality throughout the image.*

value of $c_{\text{muscle}} = 1576 \pm 1.1$ m/s [162]. Finally, we find an average speed of sound in the liver of $c_{\text{liver}} = 1559 \pm 8$ m/s, consistent with previous measurements in healthy human liver [168, 169, 64, 76]. Overall, this approach enables the simultaneous measurement of c in four human tissue layers using one experimental data set, with no dependence on the initial guess for c_0. It thus constitutes a significant advance over state of the art methods for speed of sound measurement in human tissue (c.f. Refs [64, 72, 76]).

Finally, we emphasize that we have concentrated here only on the relationship between virtual transducers located in the same focal planes at the ballistic time. Moreover, this approach has been applied to a medium which can be modeled by a stack of various horizontal layers. However, it is equally possible to consider responses between, for example, angled or curved focal planes, which could simplify similar quantitative imaging in organs such as the brain.

IV.1.2 A more local integrated speed of sound measurement

This content is confidential – please contact the author for more information.

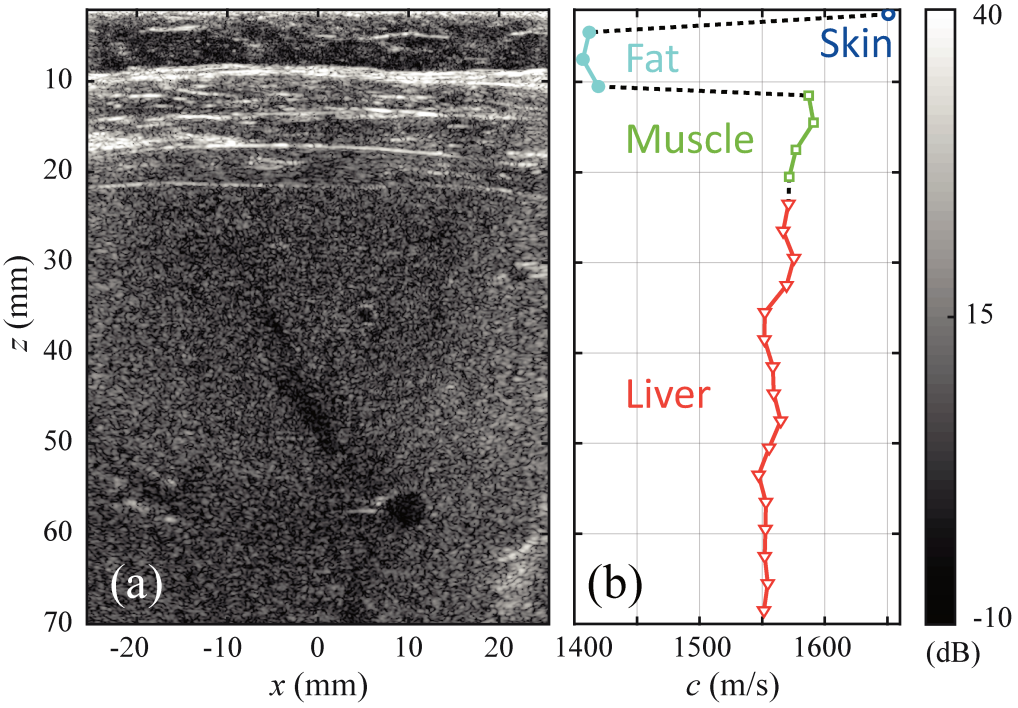

Fig. 4 *In-vivo imaging of a human liver. (a) Ultrasound image. Four layers can be identified as skin, fat, muscle, and liver tissues. (b) Complete speed of sound profile $\hat{c}(z_p)$ that results from the sub-SoS profiles $\hat{c}_i(z_p)$ associated with each layer.*

IV.1.3 Conclusion

Based on the matrix formalism, we introduced two new techniques to probe the medium integrated speed of sound. To a certain extent, both of these iterative processes rely on the quantification of the focusing quality either in the common-mid-point frame via the focusing criterion or in the wave-front frame via the wave-front matrix. We observe that the focusing criterion probes the cumulative impact of the transmitted and received aberrations on the lateral resolution of the ultrasound image. The wave-front matrix enables to measure the axial offset induced by either the transmitted or received aberrations. We observe that both techniques don't take advantage of the exact same information. It thus may be interesting to combine these two approaches to improve the spatial resolution and accuracy of the integrated speed of sound map.

Thanks to their high spatial resolution and high accuracy, these new algorithms show great promises for the determination of the local speed of sound map, which remains the ultimate goal of any speed of sound measurement technique. Two approaches can be followed to invert this ill-posed problem. On the one hand, it can be done physically by finding the best heterogeneous propagation matrices that optimizes the focusing quality. The use of stratified propagation matrices is in line with this objective. Note that it can also be applied to the second algorithm. On the other hand, a more numerical approach has been proposed by the team of M. Jaeger in the CUTE method [75, 76]. Instead

of finding the best propagation matrices that minimizes the aberrations, this second approach consists in finding the best local speed of sound distribution that matches some indicators, *e.g.* common-mid-angle realigned signals in the case of the CUTE method, or the integrated speed of sound map in our case.

We recall that the CUTE method investigates the correlation of the realigned signals to compute an estimation of the medium local speed of sound via an inversion of the problem. Beside this delicate inversion which is not done here, there is a great difference between the CUTE method and the above described algorithm. Indeed, to our understanding, the new CUTE method correlates realigned signals associated with the same common-mid-angles. This technique investigates the memory effect to produce time-of-flight error maps that are associated with each common-mid angle. This approach enables to keep an information on the wave traveled path. Our approach uses all the transmitted and received angles for beamforming process. Nonetheless, we induce some flexibility by splitting the location of the transmitted and received focal spot. The resulting integrated speed of sound map may be more accurate than the time-of-flight error maps. However, it does not contains any information on the traveled path that could be used to invert the problem. An in-between technique could be to compute for each associated virtual transducer, multiple wave-front images based on transmitted or received sub-aperture aperture. In this case, the impact of reduced aperture should be carefully studied.

Finally, all this study was performed by means of broadband signals. However, this work can be extended to the analysis of frequency dependent 2D-common-mid-point matrices and 2D-wave-front matrices. This additional information may be relevant either to enhance the measurement of the integrated speed of sound, or to tackle the case of dispersive media (varying speed of sound with frequency). As always, as it implies as lower frequency bandwidth, a trade off must be found between additional information, spatial resolution and accuracy.

IV.2 Multiple scattering quantification

So far, we have used the matrix formalism to analyze the impacts of the speed of sound hypothesis on the image formation process. We proposed new techniques to either improve this assumption or correct for aberrations. However, these techniques only investigate the single scattered echoes. Therefore, even is the SoS hypothesis is not valid, the time-of-flight of these echoes are still assumed to be linked to the location of the scatterer. In this section, we go beyond the limited case of single scattered echoes and turn our attention towards multiple scattered one. These signals have traditionally been seen as a nightmare for classical wave imaging, as it presents as an incoherent background which can greatly degrade image contrast. Because they are extremely sensitive to the micro-architecture of the medium, multiply scattered waves can be a valuable tool for the characterization of scattering media. Note that a brief review of the multiple scattering process is provided in the first chapter [Par. I.3.2]. We notably describe some of the major studies that characterize this phenomenon both in a transmission or in a reception configuration, for strongly or weakly scattering media. For medical ultrasound image, the soft tissues are usually weakly scattering media that are imaged in a reflection configuration. In this case, most of the state-of-the-art technique that investigate the multiple scattering process has

been developed by A. Aubry during his PhD at Institut Langevin [90].

In this section, we analyze the focused reflection matrix at the focal time. We limit ourselves to the configuration where $z_{\text{in}} = z_{\text{out}} = z$. The focused reflection matrix is then denoted $\bar{\mathbf{r}}_{\text{xx}}(z)$. To study the multiple scattering process, we turn our attention to points that are associated with a low single scattering contribution. In this focused reflection matrix $\bar{\mathbf{r}}_{\text{xx}}(z)$, these signals correspond to off-diagonal signals such as $x_{\text{out}} - x_{\text{in}} > w(\mathbf{r})$. Figure 5 (b) shows $\bar{\mathbf{r}}_{\text{xx}}(z)$ at $z = 45$ mm in a phantom experiment [white line on figure 6(a)]. At points far from the diagonal, signal can still be observed and show long-scale fluctuation of their intensity. Because each matrix $\bar{\mathbf{r}}_{\text{xx}}(z)$ is investigated at the ballistic time ($t = 2z/c$), the only possible physical origin of echoes between distant virtual transducers is the existence of multiple scattering paths occurring at depths shallower than the focal depth, as sketched in figure 5(a).

In this section, we propose two methods to measure the ratio of multiple scattered intensity in the ultrasound image. The first technique analyzes the spatial reciprocity of this matrix in the common-mid-point frame, while the second investigates the enhancement factor of the coherent back-scattering pick in the plane wave basis. We illustrate our arguments with the homogeneous phantom experiment and the bovine/phantom one. We finally applied our technique to the liver *in-vivo* experiment of a healthy volunteer. We will see that a significant amount of multiple scattering takes place in the three investigated ultrasound experiments.

IV.2.1 Multiple scattering in the focused basis

As stated in paragraph I.3, the reflection matrix is composed of three contributions: (*i*) the single scattering component, (*ii*) the multiple-scattering component, (*iii*) the electronic noise. In the first chapter we describe these components in the transducer basis, *i.e.* in the matrix $\mathbf{R}_{\text{uu}}$. In order to provide a more local analysis, we study the intensity of each contribution in the focused basis, and more precisely in the common-mid-point frame. We recall that $I(\mathbf{r}, \Delta x)$ denotes the intensity profile associated with the common-mid-point $\mathbf{r}$ [Eq. II.23]:

$$I(\mathbf{r}, \Delta x) = \left| R(x + \Delta x/2, x - \Delta x/2, z) \right|^2 , \tag{IV.18}$$

As previously observed, to study the multiple scattering process, an ensemble average is required, which is replaced by a spatial average. Once again, we rely on a moving spatial window to mathematically describe this spatial average [Eq. IV.7]:

$$I_{\text{av}}(\mathbf{r}_{\text{p}}, \Delta x) = \left\langle I(\mathbf{r}, \Delta x)\ W_{l_x, l_z}(\mathbf{r} - \mathbf{r}_{\text{p}}) \right\rangle_{\mathbf{r}} . \tag{IV.19}$$

We then investigate the three component intensities in an average common-mid-point intensity profile:

1. The single scattering component, $I_S(\mathbf{r})$. Signals from single scattering mainly lie along the near-confocal elements of $\bar{\mathbf{r}}_{\text{xx}}(z)$ [$\Delta r < w(\mathbf{r})$]. This contribution is used to quantify and correct for aberrations and to measure the medium speed of sound.

2. The multiple scattering component, $I_M(\mathbf{r})$. This contribution can be split into two terms: An *incoherent* part which corresponds to interferences between waves taking different paths through the medium, and a *coherent* part which corresponds to

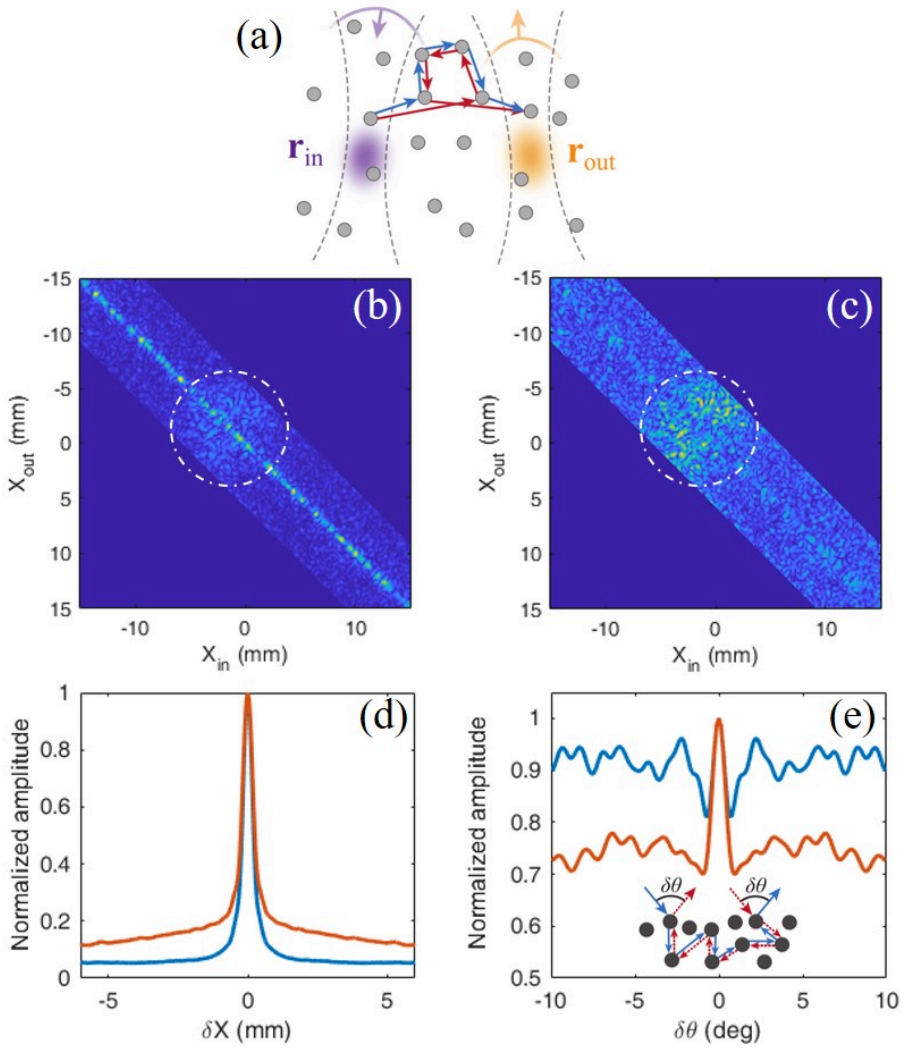

Fig. 5 *Observation of multiple scattered signals in a phantom experiment. (a) Sketch of multiple scattering paths (red or blue path) involved in the matrix* $\bar{\mathbf{r}}_{xx}(z)$*. The constructive interference between reciprocal paths occurs only when* $|rout - rin| < \delta x$ *(CBS). (b,c) Amplitude of* $\bar{\mathbf{r}}_{xx}(z)$ *and* $\bar{\mathbf{R}}_{xx}(z)$ *computed at* $z = 45$ *mm [6(a)]. They are analyzed to measure the multiple scattering rates in the focal or plane wave bases, respectively. The white dotted circle highlights multiple scattered echoes. (d,e) Normalized mean intensity profiles measured in the focused basis* $I_{av}(\mathbf{r}, \Delta x)$ *and (b) the far-field* $I_{av}(\mathbf{r}, \Delta\theta)$*. They are associated with areas of same color on Fig. 6.*

the interference of waves with their reciprocal counterparts [see the blue and red paths in figure 5(a). Referred to as coherent backscattering (CBS), this interference phenomenon results in an enhancement (of around two) in intensity at exact backscattering, *i.e.* at $\Delta r = 0$ [Par. I.3].

3. Electronic noise, I_N. This contribution can decrease the contrast of an ultrasound image in the same way as $I_M(\mathbf{r})$. Noise contributes to a roughly constant background level to the backscattered intensity profiles $I_{\text{av}}(\mathbf{r}, \Delta x)$.

To estimate the level of each contribution, the relevant indicators are the mean confocal intensity $I_{\text{on}}(\mathbf{r})$ and off-diagonal intensity $I_{\text{off}}(\mathbf{r})$ of $\bar{\mathbf{r}}_{\text{xx}}(z)$. The confocal intensity $I_{\text{on}}(\mathbf{r})$ is given by

$$I_{\text{on}}(\mathbf{r}) = I_{\text{av}}(\mathbf{r}, \Delta x = 0) = I_S(\mathbf{r}) + 2I_M(\mathbf{r}) + I_N, \tag{IV.20}$$

where the factor of 2 accounts for the CBS enhancement of the multiple scattering intensity at the source location. $I_{\text{off}}(\mathbf{r})$ is the sum of the multiple scattering incoherent background and of the additive noise component:

$$I_{\text{off}}(\mathbf{r}) = \langle I_{\text{av}}(\mathbf{r}, \Delta x)\rangle_{\Delta x > w(\mathbf{r})} = I_M(\mathbf{r}) + I_N, \tag{IV.21}$$

where $\langle \cdots \rangle_{\Delta x > w(\mathbf{r})}$ indicates an average over off-diagonal elements of $\bar{\mathbf{r}}_{\text{xx}}(z)$, which obey $\Delta x > w(\mathbf{r})$. This average constitutes an average over several realizations of disorder, which is necessary to suppress the fluctuations from constructive and destructive interference between the various possible multiple scattering paths through the sample.

Figure 5(d) shows two examples of normalized intensity profiles obtained in the homogeneous phantom experiment $I_{\text{av}}(\mathbf{r}, \Delta x)/I_{\text{av}}(\mathbf{r}, \Delta x = 0)$. Each profile has been averaged over a different zone of the ultrasound image [Fig. 6(a)]. Blue and red curves (solid and dotted rectangles) correspond to zones located respectively above and below the bright speckle disk. It is clear that the incoherent background I_{off} is higher in the deeper (red) zone, suggesting that either the multiple scattering component or the noise is greatly enhanced behind the reflective object. The focused reflection matrix $\bar{\mathbf{r}}_{\text{xx}}(z)$ displayed on figure 5(b) is computed for signals located just below the bright disk. We observe an intensity enhancement of off-diagonal signals that are associated with virtual transducers, whose lateral location matches the one of the bright disk. As the noise level is approximately constant, this intensity enhancement is then induced by multiple scattered echoes.

Figure 7(a) shows the average common-mid-point intensity profile associated with three regions of the medium [Fig. 7(c)], in the bovine tissue/phantom experiment. The same observation can be made for the two areas located above (blue curves) and below (red curves) the bright disk. Nonetheless, the contrast of incoherent background between these two areas is weaker than in the homogeneous phantom experiment. This phenomenon is probably caused by the lower SNR in this second experiment. Indeed, these regions are located at larger depth compared to the first experiment, and the attenuation phenomenon in the bovine tissue is probably more intense. Surprisingly, the incoherent background I_{off} is far from being negligible in the red zone at shallower depths (dashed line rectangle).

To investigate these phenomena further, we define two new indicators: (1) the multiple-to-single scattering ratio:

$$\rho(\mathbf{r}) \equiv \frac{I_M}{I_S}, \tag{IV.22}$$

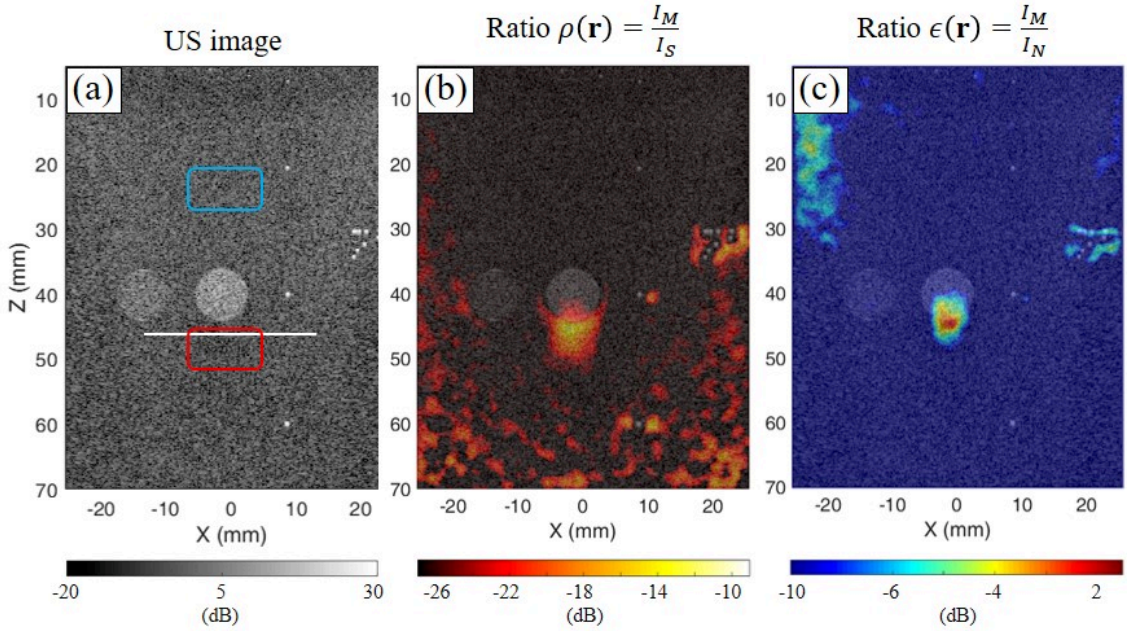

Fig. 6 *(a) US image of the homogeneous phantom experiment. (b, c) Maps of multiple scattering rates superimposed over the ultrasound image, $\rho(\mathbf{r})$ [Eq. IV.26] and (c) $\epsilon(\mathbf{r})$ [Eq. IV.27], respectively.*

and (2) the multiple scattering-to-noise ratio,

$$\epsilon(\mathbf{r}) \equiv \frac{I_M}{I_N}. \tag{IV.23}$$

To calculate these quantities, it is necessary to be able to distinguish between I_M, I_N, and I_S. However, only two indicators have been studied so far I_{on} and I_{off}. A third property is thus required for the differentiation. Experimentally, the noise level can be estimated by means of a dedicated acquisition. It simply consists in recording signals without any excitation. By applying the exact same post-processing,*e.g.* synthetic beamforming, the electronic noise level is measured in each point of the US image. Here, we propose to investigate the spatial reciprocity of the wave propagation. Indeed, while the single and multiple scattering components of reciprocal signals are identical, the noise component is incoherent from one signal to the other. More precisely, two signals are reciprocal if the location of their virtual source and sensor are exactly exchange *i.e.* $R(\mathbf{r}_{\text{in}}, \mathbf{r}_{\text{out}})$ and $R(\mathbf{r}_{\text{out}}, \mathbf{r}_{\text{in}})$. In the common-mid-frame this configuration corresponds to $R(\text{r}, \Delta x/2)$ and $R(\text{r}, -\Delta x/2)$. As a result, this observation enables to separate the multiple scattering contribution from the noise level by the analysis of off-axis signals. Note that, to be valid, this assumption requires that the entire process is reciprocal, meaning that the transmitted and received beamforming parameters are identical, as well as the transmitted and received basis. If this condition is not fulfilled, it leads to an underestimation of the multiple scattering component as some multiple scattered echoes will be considered as noise.

To this end, we defined the coefficient of symmetry α, which probes the average correlation between each couple of reciprocal point of the focused reflection matrix in the common-mid-point frame:

$$\alpha(\mathbf{r}_\mathrm{p}) = \left\langle \left\langle \frac{\mathrm{Re}\left[R(\mathbf{r},\Delta x)\ R^*(\mathbf{r},-\Delta x)\right]}{|R(\mathbf{r},\Delta x)|\ |R(\mathbf{r},-\Delta x)|} \right\rangle_{\Delta x > w(\mathbf{r})} W_{l_x,l_z}(\mathbf{r}-\mathbf{r}_\mathrm{p}) \right\rangle_{\mathbf{r}} \tag{IV.24}$$

Note that to discriminate I_M from I_N, only the signals outside the single scattered halo are considered. Again, a spatial average is required to smooth out the fluctuation of the pressure field. I_off can then be decomposed as a symmetrical contribution *i.e.* I_M and an anti-symmetrical one I_N [Eq. IV.21], such as:

$$I_M(\mathbf{r}) = \alpha(\mathbf{r})\ I_\mathrm{off}(\mathbf{r}) \quad \text{and} \quad I_N(\mathbf{r}) = (1-\alpha(\mathbf{r}))\ I_\mathrm{off}(\mathbf{r}) \tag{IV.25}$$

By combining equation IV.25 and IV.20 the contribution on single scattering can be determined. Finally, Maps of multiple scattering rates can be expressed as:

$$\rho(\mathbf{r}) = \frac{\alpha(\mathbf{r})\ I_\mathrm{off}(\mathbf{r})}{I_\mathrm{on}(\mathbf{r}) - (\alpha(\mathbf{r})+1)\, I_\mathrm{off}(\mathbf{r})}, \tag{IV.26}$$

and

$$\epsilon(\mathbf{r}) = \frac{\alpha(\mathbf{r})}{1-\alpha(\mathbf{r})}. \tag{IV.27}$$

Before analyzing the results of these multiple scattering ratio, we show that these two ratios can also be estimated in the plane wave basis.

IV.2.2 Coherent back-scattering as a direct probe of spatial reciprocity

An elegant approach to probe spatial reciprocity is the measurement of the CBS effect in the plane-wave basis (the far-field). The CBS effect can be observed by measuring the average backscattered intensity as a function of the angle $\Delta\theta \equiv \theta_\mathrm{in} - \theta_\mathrm{out}$ between the incident and reflected waves. In the presence of multiple scattering, this profile displays a flat plateau (the incoherent background), on top of which sits a CBS cone centered around the exact back-scattering angle $\Delta\theta = 0$. The cone is solely due to constructive interference from waves following reciprocal paths inside the sample [Fig. 7(b)]. Thus, CBS in the far-field is a direct probe of spatial reciprocity in the focused basis [86, 87].

To quantify the CBS effect we first need to eliminate contributions from single scattering. To this end, the reflection matrices $\bar{\mathbf{r}}_\mathrm{xx}(z)$ are first normalized such that their diagonal at each depth exhibits a constant mean intensity:

$$\dot{R}(\mathbf{r},\Delta x) = \frac{R(\mathbf{r},\Delta x)}{\sqrt{I_\mathrm{av}(\mathbf{r},\Delta x)}}. \tag{IV.28}$$

Each common-mid-point pressure field is normalized by the common-mid-point intensity profile measured in a surrounding region by means of the spatial window. This operation eliminates the dominant contribution to intensity from diagonal elements in $\bar{\mathbf{r}}_\mathrm{xx}(z)$, which is equivalent to drastically reduce the single scattering component. Figures 5(b,c) compare the focused reflection matrix before $\bar{\mathbf{r}}_\mathrm{xx}(z)$ and after the normalization $\dot{\mathbf{R}}_\mathbf{xx}(z)$ at

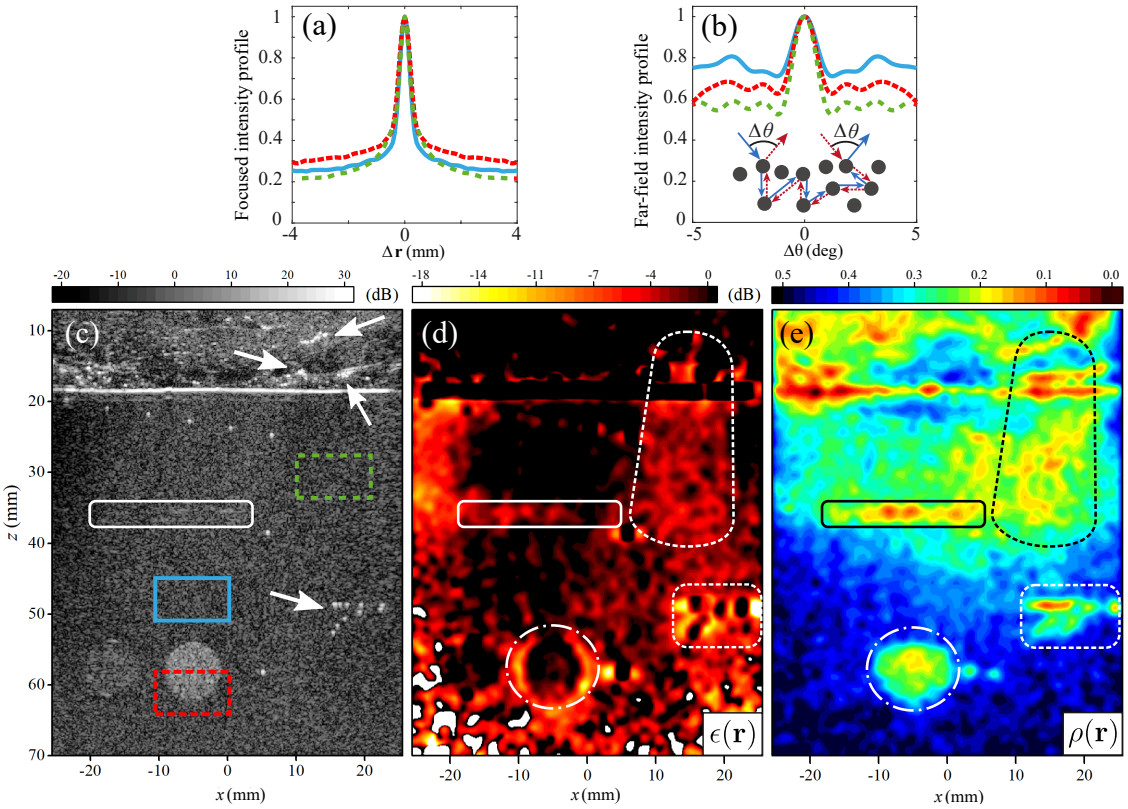

Fig. 7 *Normalized mean intensity profiles are displayed for (a) the focused basis* $I_{av}(\mathbf{r}, \Delta x)$ *and (b) the far-field* $I_{av}(\mathbf{r}, \Delta\theta)$*, are displayed for the different areas highlighted in (c) the corresponding ultrasound image based on an optimized speed of sound model [Par. IV.1] . Maps of multiple scattering rates (d)* $\rho(\mathbf{r})$ *[Eq. IV.26] and (e)* $\epsilon(\mathbf{r})$ *[Eq. IV.27] are shown, superimposed on the ultrasound image.*

depth $z = 45$ mm in the phantom experiment. As the intensity halo of single scattering induced by the beamforming process disappears, we better observe the enhancement of the multiple scattered intensity induced by the bright disk, located above the focal plane under study in the phantom experiment.

To perform a local analysis of the normalized focused reflection matrix, we select only a subspace of $\dot{\mathbf{R}}_{\mathbf{xx}}(z)$ by means of a spatial window matrix, whose non-zero coefficients are associated with common-mid-points signals $\mathbf{r}' = (\mathbf{r}_{\text{in}} + \mathbf{r}_{\text{out}})/2$ belonging to the area $\mathcal{A}$ surrounding $\mathbf{r}$:

$$M(x_{\text{out}}, x_{\text{in}}, z, \mathbf{r}) = \begin{cases} \dot{R}(x_{\text{out}}, x_{\text{in}}, z) & \text{for } (\mathbf{r}' - \mathbf{r}) \text{in} \mathcal{A} \\ 0 & \text{elsewhere.} \end{cases}$$

We then analyze this set of sub-matrices $\mathbf{M}_{xx}(z, \mathbf{r})$ in the far-field to probe the far-field CBS. Similarly to the work done in chapter 3 for aberration correction, the matrix

formalism makes it easy to project $\mathbf{M}_{xx}(z,\mathbf{r})$ into the plane-wave basis. More precisely, we use the free-space transmission matrix, $\mathbf{P}_0$ [Eq. II.14a]. It enables to project the focused reflection matrix into the far-field basis that contains the spatial frequencies k_{in} and k_{out}. At the central frequency and for a given speed of sound, this basis can be seen as a plane wave basis:

$$\mathbf{M}_{\theta\theta}(z,\mathbf{r}) = \mathbf{T_0}^{\top}(z,f_c) \times \mathbf{M}_{xx}(z,\mathbf{r}) \times \mathbf{T_0}(z,f_c)\,.$$

$\mathbf{M}_{\theta\theta}(z,\mathbf{r})$ contains the normalized reflection coefficients in the θ_{out} direction for an angle of incidence θ_{in} induced by scatterers contained in the area $\mathcal{A}$ centered around $\mathbf{r}$. An average far-field mean intensity can now be calculated as a function of the reflection angle $\Delta\theta$:

$$I_{\text{av}}(\mathbf{r},\Delta\theta) = \left\langle |M(\theta+\Delta\theta/2,\theta-\Delta\theta/2,z,\mathbf{r})|^2 \right\rangle_{\theta,z},$$

where the symbol $\langle..\rangle$ denotes an average over the variables in the subscript, i.e. all angles which obey $\theta = (\theta_{\text{in}}+\theta_{\text{out}})/2$ and the thickness z of the area $\mathcal{A}$.

The normalized intensity profiles $I_{\text{av}}(\mathbf{r},\Delta\theta)/I_{\text{av}}(\mathbf{r},\Delta\theta=0)$ that correspond to the selected areas in the homogeneous phantom experiment and in the bovine tissue/phantom one, are shown in figures 6(e) and 7(b), respectively. For each area, a CBS cone is clearly visible, showing that the experimental data do contain contributions from multiple scattering. Just as with the CBS peak in the focused basis, the area located below the bright disk (red curves) is characterized by a higher amount of multiple scattering than the one located above this structure (blue curves).

To estimate the relative weight of the noise and multiple scattering contributions, we examine the mean intensity for two cases: (1) at exact back-scattering:

$$I_{\text{av}}(\mathbf{r},\Delta\theta=0) = 2I_M(\mathbf{r}) + I_N(\mathbf{r}), \tag{IV.29}$$

and (2) at angles away from the CBS peak:

$$\langle I_{\text{av}}(\mathbf{r},\Delta\theta)\rangle_{\Delta\theta>\theta_c} = I_M(\mathbf{r}) + I_N(\mathbf{r}), \tag{IV.30}$$

where θ_c is the width of the CBS peak and $\langle\cdots\rangle_{\Delta\theta>\theta_c}$ indicates an average over all angles $\Delta\theta$ which obey $\Delta\theta>\theta_c$.

Note that in the plane wave basis, $\langle I_{\text{av}}(\mathbf{r},\Delta\theta)\rangle_{\Delta\theta>\theta_c}$ and $I_{\text{av}}(\mathbf{r},\Delta\theta=0)$ are the two indirect indicators used to extract the multiple scattering contribution from the noise. As the single scattering component has been suppressed in this approach, only two indicators are required.

We finally defined the enhancement factor of the CBS peak by:

$$\chi(\mathbf{r}) = \frac{I_{\text{av}}(\mathbf{r},\Delta\theta=0)}{\langle I_{\text{av}}(\mathbf{r},\Delta\theta)\rangle_{\Delta\theta>\theta_c}}. \tag{IV.31}$$

$\chi(\mathbf{r}')$ can have values ranging from 1 to 2; it is at a minimum when $I_M=0$ and at a maximum when all backscattered echoes originate from multiple scattering.

The multiple scattering-to-noise ratio $\epsilon(\mathbf{r})$ [Eq. IV.27] can be expressed as a function of the enhancement factor $\chi(\mathbf{r})$ by injecting Eqs. IV.29 and IV.30 into Eq. IV.31:

$$\epsilon(\mathbf{r}) = \frac{\chi(\mathbf{r})-1}{2-\chi(\mathbf{r})}. \tag{IV.32}$$

The multiple-to-single scattering ratio $\rho(\mathbf{r})$ [Eq. IV.22] can be derived by injecting the last equation into Eqs. IV.20 and IV.21:

$$\rho(\mathbf{r}) = \frac{[\chi(\mathbf{r}) - 1] \cdot I_{\text{off}}(\mathbf{r})}{I_{\text{on}}(\mathbf{r}) - \chi(\mathbf{r}) \cdot I_{\text{off}}(\mathbf{r})}. \tag{IV.33}$$

The comparison between the multiple scattering rates obtained either in the plane wave basis [Eq. IV.33 and IV.32] or in the focused basis [Eq. IV.27 and IV.26] confirms the link between the enhancement factor of the CBS and the reciprocity of the wave propagation, *i.e.* the symmetry of the focused matrix:

$$\alpha(\mathbf{r}) = \chi(\mathbf{r}) - 1. \tag{IV.34}$$

IV.2.3 Maps of multiple scattering rates

Figures 6(b,c), 7(d,e) and 8 (b,c) show the maps of $\rho(\mathbf{r})$ and $\epsilon(\mathbf{r})$ for the three experiments. These maps have been computed in the focused basis. We will observe that they help to provide an overall assessment of the factors impacting image quality.

We first analyze the homogeneous phantom experiment [Fig. 6]. We observe that the two MS rates $\rho(\mathbf{r})$ and $\epsilon(\mathbf{r})$ are characterized by high values just below the bright disk around $z = 45$ mm. These halos of high amplitude are the signature of multiple scattered echoes that has been generated by the above structure. Indeed, this structure is a cylinder made of a higher density of unresolved scatterer, which reduces the mean free-path. As stated at the beginning of this part, these MS echoes appear below the location where they have been generated. This phenomenon is inherent to the construction of the focused reflection matrix, which selects echoes at the ballistic time.

Figure 7 shows maps of MS rates associated with the in-vivo liver experiment. Note that they are computed based on the optimized two-layer model developed for SoS measurement [Par. IV.1]. We observed that compared to the homogeneous case, the presence of the bovine tissue drastically modifies the two maps of MS rates. High values within and below the bovine tissue suggests that multiple scattering process does occur inside the first layer. In particular, the top right area highlighted by the dashed line seems to be impacted by a significant amount of multiple scattering that may arise from the bright scatterers located within the bovine tissue (white arrows). These scatterers are likely resonating bubbles, which creates the observed "tail" of multiple scattering at larger depths. Interestingly, the focusing criterion associated with this image reveals an apparent poor focusing quality [3(b)], even with the optimized speed of sound model. The compensation for an incorrect hypothesis for c does not compensate for the effect of multiple scattering or reflections. The solid lines outline the image area that suffers from artifacts due to the double reflection event between the probe and the bovine tissue-phantom interface. Interestingly we observe just below the bovine tissue on the left part of the maps, around $\{x, z\} = \{-25, 25\}$ mm that the two rates show a different behavior. A significant enhancement of $\rho(\mathbf{r})$ is observed that is not visible on the map of $\epsilon(\mathbf{r})$. To analyze this phenomenon, we observe that the ultrasound image shows a relatively low brightness. It then means that this area is characterized by a low single scattered intensity while the multiple scattered one may not present any significant enhancement. In addition, discrete areas in which $\epsilon(\mathbf{r})$ is very high (> 0 dB) are indicative of artifacts caused by

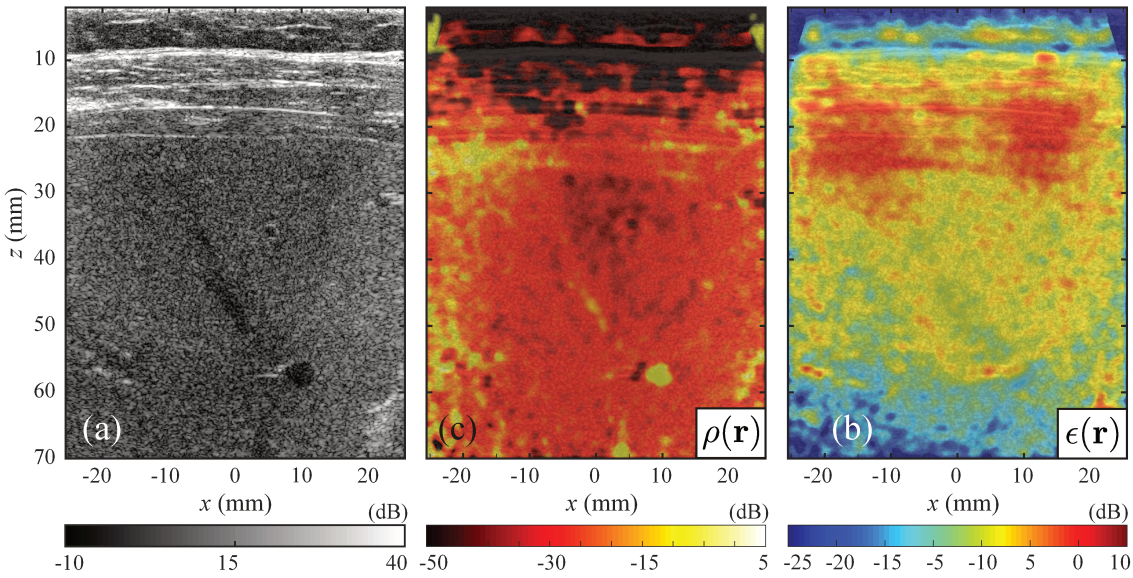

Fig. 8 *(a) US image of the in-vivo liver of a healthy volunteer. (b, c) Maps of multiple scattering rates superimposed over the ultrasound image, $\rho(\mathbf{r})$ [Eq. IV.26] and (c) $\epsilon(\mathbf{r})$ [Eq. IV.27], respectively.*

multiple reverberations from the tissue layers ($z = 10 - 30$ mm) or in structures such as veins, for instance at $(z, x) \approx (56, 5)$ mm. Strikingly, we also find a significant amount of multiple scattering relatively evenly distributed across areas of speckle (compared to the bovine tissue/phantom experiment [Fig. 7]). This observation is confirmed by the map $\rho(\mathbf{r})$ [Fig. 8(b)]. The analysis of these two indicators show that even if some multiple scattering contribution can be significantly detected, its intensity level is quite low in this experiment compared to the single scattered intensity.

These examples show that the multiple scattering rates combined with the measurement of $F(\mathbf{r})$ and the analysis of the ultrasound image provide a sensitive local mapping of the heterogeneities in the medium which includes both small- and large-scale variations of the refractive index. In this context, we would like to mention the recent work of Velichko [170], which measures a quantity similar to $\rho(\mathbf{r})$ as a function of depth and frequency. While noise is not treated separately from multiple scattering, their results emphasize the clear relation between local measurements of multiple scattering and the reliability of ultrasound images. Integration of our focused reflection matrix approach could improve their axial resolution, and help extend their analysis to 2D spatial mapping.

Beyond image reliability, the maps of multiple scattering rates provide a great deal of quantitative information about the system under investigation. Because $\epsilon(\mathbf{r})$ is calculated from the off-diagonal elements of $\overline{\mathbf{r}}_{\mathrm{xx}}(z)$, it contains only negligible contributions from single scattering, and thus constitutes an interesting new contrast for imaging which is much more sensitive to the micro-structure of the medium than it is to its reflectivity. Conversely, because $\rho(\mathbf{r})$ is independent of noise, it can constitute a useful bio-marker for medical imaging deep inside tissue, and a potentially valuable tool for future research seeking to characterize multiple scattering media, even at large depths where I_N becomes

important.

IV.2.4 Conclusion

In this section we have shown that the focused reflection matrix measured in the focal plane enables a local examination of multiple-scattering processes deep inside weakly scattered media in a reflection configuration. We have demonstrated the effectiveness of using fundamental interference phenomena such as coherent back-scattering, a hallmark of multiple scattering processes, to discriminate between multiple scattering and measurement noise. Based on this initial result, additional matrix operation of the focused reflection matrix finally quantifies the contribution of singly scattered echoes in the ultrasound image. A novel imaging method is proposed based on the multiple-scattering contrast. In this early work we have analyzed two multiple scattering rates $\rho(\mathbf{r}) = I_M(\mathbf{r})/I_S(\mathbf{r})$ and $\epsilon(\mathbf{r}) = I_M(\mathbf{r})/I_N(\mathbf{r})$. To our knowledge, such 2D maps have never before been demonstrated, and current state-of-the-art methods cannot produce such well-resolved local information about acoustic multiple scattering. Unexplored but promising perspective of this work will be to extract from $\rho(\mathbf{r})$ quantitative maps of scattering parameters such as the elastic mean free path or the absorption length [148, 35], and transport parameters such as the transport mean free path [83, 171, 172] or the diffusion coefficient [83, 84, 173]. While diffuse tomography in transmission only provides a macroscopic measurement of such parameters, preliminary studies have demonstrated how a reflection matrix recorded at the surface can provide transverse measurements of transport parameters [86, 87, 139, 97].

On the other hand, it will be interesting (and is immediately possible) to create maps of $\rho(\mathbf{r})$ and $\epsilon(\mathbf{r})$ in scattering media such as breast, lung and bone. Recent work such as that by Mohanty *et al.* [174] suggests that such maps may be better at imaging heterogeneous scattering media than conventional ultrasound ultrasound. However, for bone and flat layers of tissue such as muscle, a current limitation is the coexistence of multiple scattering and artifacts from reverberant echoes or reflections caused by interfaces between tissues with different acoustic impedances. The separation of these effects will be the subject of future work.

Finally, this analysis can be drastically enhanced by investigating the time focused reflection matrix. For instance, in the case of weakly scattering medium, the multiple scattering contribution essentially results from a double scattering process. By probing all the potential configurations at the exact time of double scattering, the time-focused reflection matrix can be used to highlight this contribution. However, one of the major challenges will lie in the separation of the double scattering contribution and the single one. This drawback can be avoided by studying echoes outside the single scattering cone. Note that this is the approach used in this section where off diagonal signals are investigated.

IV.3 Anisotropy of scatterer

This content is confidential – please contact the author for more information.

IV.4 Temporal and spectral responses of virtual transducers

This content is confidential – please contact the author for more information.

IV.5 Conclusion

In this chapter we have shown that the focused matrix and time-focused matrix can be used to characterize various properties of the propagation medium. Compared to state-of-the art techniques, these methods analyze propagation phenomena in the focal basis and not in a far-field basis (transducer or plane wave basis). This main feature results in a more local information on the medium to study.

We first accurately measure the medium integrated speed of sound via either the maximization of the focusing criterion or the determination of the focal spot location in the wave-front matrices. We have also demonstrated that a more local speed of sound can be measured by considering stratified speed of sound models that are built from shallow depth to deep depth. We have then shown that the focused reflection matrix enables a local examination of the multiple-scattering process deep inside the medium. Based on the reciprocity of the wave propagation, this phenomenon can be directly probed in the focal basis by measuring the symmetry of the focused reflection matrix or in the plane wave basis via the analysis of the coherent back-scattering process. This study led to the construction of new maps that quantify the level of the multiple scattered intensity compared to the single scattered intensity and noise level. We have then turned our attention to the characterization of the local anisotropy of scatterer in fibrous media. The fiber orientation is measured based on the determination of a main direction of back-scattered intensity by means of the coherent wave-front matrices. Finally, we have shown that the confocal matrix probes locally the frequency spectrum of echoes generated by each resolution cell. It can thus be used as a first building block for (*i*) the determination of frequency dependent parameters that govern the wave propagation, *e.g.* the attenuation length and (*ii*) the local characterization of the nature of scatterers. It can notably be applied to the particular case of resonant structures.

While all these techniques are not at the same stage of maturity, they all rely on a matrix formalism of the wave propagation. They illustrate the wide range of techniques that fall under the concept of matrix imaging.

Appendices

IV.A Measurement errors on the focusing criterion and the speed of sound

In this work, we have defined the focusing parameter F as the ratio between the width w_0 of the ideal diffraction-limited PSF and the width w of the experimentally measured PSF. In optics, the Strehl S ratio is generally used to quantify aberration [152]. It is defined as the ratio between the maximum of the PSF intensity, I, and that in the ideal diffraction-limited case, I_0. Due to energy conservation, we have $I_0 \times w_0 = I \times w$. The focusing criterion and Strehl ratio, as well as their relative measurement errors, are thus equivalent:

$$F \equiv S \tag{IV.35}$$

and

$$\frac{\Delta F}{F} \equiv \frac{\Delta S}{S}. \tag{IV.36}$$

S can also be expressed as the square magnitude of the averaged aberration transmittance $e^{i\phi(\sin\theta)}$ [152]:

$$S = \left| \left\langle e^{i\phi(\sin\theta)} \right\rangle_{\sin\theta} \right|^2, \tag{IV.37}$$

where $\phi(\sin\theta)$ is the far-field phase delay induced by the mismatch between the propagation model and the real medium in direction θ.

In Fig. 2, a two-layer medium is used to model the bovine tissue/phantom system. Assuming that the wave velocity c_t is properly estimated in the first layer (bovine tissue), the phase $\phi(\sin\theta)$ accumulated in the phantom is given by

$$\phi(\sin\theta) = k_p z_p \cos(\theta_p), \tag{IV.38}$$

where $k_p = \omega/c_p$ is the wavenumber in the phantom and θ_p is the refraction angle in the phantom, obeying $\sin\theta_p/c_p = \sin\theta/c_t$. If a wrong value of c_p is used to model sound propagation in the phantom, the resulting phase distortion is given by

$$\Delta\phi(\sin\theta) = -\frac{k_p z_p}{\cos\theta_p}\eta, \tag{IV.39}$$

where $\eta = \Delta c_p/c_p$ is the relative error of the speed of sound hypothesis in the phantom. For the sake of simplicity, we will assume in the following that $\cos\theta \sim \cos\theta_p$. This approximation is justified by the small relative difference between c_p and c_t. Assuming relatively weak aberrations ($\Delta\phi(\sin\theta) << \pi$), the transmittance aberration function $e^{i\Delta\phi(\sin\theta)}$ can be expanded as

$$e^{i\Delta\phi(\sin\theta)} \sim 1 - i\frac{k_p z_p}{\cos\theta}\eta \quad - \quad \frac{1}{2}\left(\frac{k_p z_p}{\cos\theta}\right)^2 \eta^2 + \mathcal{O}\left(\eta^3\right). \tag{IV.40}$$

The angular average of $e^{i\phi(\sin\theta)}$ is then deduced

$$\begin{aligned}\left\langle e^{i\Delta\phi(\sin\theta)}\right\rangle_{\sin\theta} &= \frac{1}{\sin\beta}\int_0^{\sin\beta} e^{i\Delta\phi(\sin\theta)}d(\sin\theta)\\ &\sim 1 - ik_p z_p\eta\frac{\beta}{\sin\beta}\\ &\quad -\frac{1}{2}\left(k_p z_p\eta\right)^2\frac{\operatorname{arctanh}(\sin\beta)}{\sin\beta}\\ &\quad +\mathcal{O}\left(\eta^3\right).\end{aligned} \tag{IV.41}$$

Injecting the last expression into Eq. IV.37 leads to the following expression of the Strehl ratio :

$$\begin{aligned}S\sim 1 &- \frac{(k_p z_p\eta)^2}{\sin\beta}\left[\operatorname{arctanh}(\sin\beta) - \frac{\beta^2}{\sin\beta}\right]\\ &+ \mathcal{O}\left(\eta^3\right).\end{aligned} \tag{IV.42}$$

For weak aberrations ($F, S \sim 1$), the relative error $\Delta F/F$ [Eq. IV.36] of the focusing criterion can then be directly deduced from the previous expansion of the Strehl ratio:

$$\frac{\Delta F}{F} = \frac{(k_p z_p\eta)^2}{\sin\beta}\left[\operatorname{arctanh}(\sin\beta) - \frac{\beta^2}{\sin\beta}\right]. \tag{IV.43}$$

IV.B Determination of the medium speed of sound in the wave-front frame

This content is confidential – please contact the author for more information.

General conclusion and outlook

Throughout this thesis we developed a new matrix formalism for ultrasound imaging. While this method could describe all the current state-of-the-art imaging techniques, it is able to extract new information on the medium under investigation. This capacity is based on three major assets. First, the separation of the transmitted and received focal spots enables to measure the impulse responses between virtual transducers located within the medium at each pixel location. Second, a time-frequency analysis of these responses provides unprecedented characterizations of the medium reflectivity and wave propagation. Third, the flexibility of the matrix formalism allows the analysis of the reflection matrix from various configurations. It enables to take full advantage of the reciprocity of the wave propagation, and then to selectively extract relevant information on the medium for a given problem. To sum up, we review the major results of this thesis for each configuration.

We first studied the reflection matrix in the **focused basis**, *i.e.* between arrays of virtual transducers located within the medium. In front of the wealth of information provided by this matrix, we analyzed multiple subsets that allowed us to extract local information on the medium. The first studied configuration is the *confocal frame* that corresponds to the particular case where two virtual transducers are located at the exact same location. We review that the confocal ultrasound image exactly corresponds to this configuration at the focusing time, *i.e.* at the time where the incident wave has reached the focusing point. A temporal or frequency analysis of the reflection matrix in this frame enables the measurement of temporal and frequency response of scatterers embedded within each resolution cell [chap. 2]. This study shows promising routes for a local characterization of scatterers and for the quantification of the medium attenuation [chap.4].

We then considered *the common-mid-point frame* at the focusing time, which selects responses between virtual transducers that share the same common-mid-point. In this frame, we first proposed a new method to probe locally the transverse resolution of the ultrasound image, and thus to assess the quality of focus. It has been shown that the resulting focusing criterion is quasi-independent of the medium reflectivity and provides a better spatial resolution than state-of-the-art techniques [chap. 2]. This focusing criterion has then been used as a figure of merit to provide a robust and highly-resolved mapping of the medium speed of sound [chap. 4]. Independently, we proposed a novel imaging method based on the multiple-scattering contrast in the ultrasound image (chap.4). This technique is based on the reciprocity of the wave propagation. To our knowledge, such 2D maps have never before been demonstrated, and current state-of-the-art methods cannot produce such well-resolved local information about acoustic multiple scattering.

The *virtual transducer frame* (source or sensor) selects responses associated with a given virtual source or virtual sensor. Via a temporal analysis of the reflection matrix in this particular frame, we demonstrated experimentally that the ultrasound image results from a numerical time-reversal experiment. Each pixel of the ultrasound image corresponds to selected back-scattered echoes that are time-reversed and back-propagated toward their origin [chap. 2]. By following the back-scattered time-reversed wave within the medium, we introduced the *wave-front frame* associated with each virtual transducer. In this spatio-temporal frame, we were able to probe locally the pressure field generated (or collected) by each virtual transducer [chap. 2]. This unprecedented result provides relevant and local information on the wave propagation and on the nature of the associated scatterers. Based on this outcome, we proposed a second method to quantify the medium speed of sound and a new characterization of the anisotropy of scatterers with an improved spatial resolution [chap. 4].

The focused reflection matrix also allowed us to locally select echoes that have been generated by a given area. The analysis of these echoes in the **far-field basis** highlights particular correlations induced by two physical phenomena. First, we demonstrated that, based on the memory effect, specular reflections arise along echoes that share the same common-mid-angles. We took advantages of this effect to filter multiple reverberation artifacts caused by a plexiglass layer in an *in-vitro* experiment [chap. 3]. Second, we benefited from fundamental interference phenomena via the coherent back-scattering, a hallmark of multiple scattering processes, to discriminate between multiple scattering and measurement noise [chap. 4].

Last but not least, we successfully developed and applied the concept of matrix approach for aberration correction to *in-vivo* experiments [chap. 3]. To this aim we studied the reflection matrix in a **dual basis**. It contains the medium responses between two different planes. We introduce a novel operator, the so-called distortion matrix, a new distortion matrix that essentially connects any focal point inside the medium with the distortion that a wavefront, emitted or recorded from that point, experiences due to heterogeneities. A time-reversal analysis of the distortion matrix enables the estimation of the transmission matrix that links each sensor and image voxel. It leads to an optimal focusing quality for all pixels of the image.

All these above-mentioned techniques open new routes for ultrasound imaging and quantification. Promising perspectives associated with each technique have been pointed out throughout the thesis. It implies the characterization of propagation parameters such as the diffusion constant D, the absorption length and the mean free path l_e. It also concerns the medium scattering properties via a measurement of an effective density of scatterers or the detection and characterization of resonant scatterers such as bubbles.

While, we analyzed each of the above-mention phenomena independently, the efficiency of these techniques could be improved by combining these methods. Indeed, the medium characterization benefits from any improvement of the focusing quality, which provides more accurate information on the medium, which in turn could be taken into account to adapt the focusing process. While we have only investigated easy-to-image configurations, such process may be required to tackle the case of more difficult-to-image experiments such as transcranial or cardiac imaging.

More generally, we observe that all these results are based on a single plane wave insonification sequence. It could thus be interesting to apply the matrix formalism to an

ensemble of insonifications to extract new information on the medium temporal fluctuations by means of other matrix operators such as the Wigner smith operator.

Last but not least, the ability of these new methods to be used in real-time for clinical exam should now be assessed. It is an entirely different challenge from the work I have done in this thesis. I will actively take part in this second phase of development as I will continue to work for Supersonic Imagine after my thesis.

Scientific output

Publication in peer-reviewed journal

- W. Lambert, L. A. Cobus, T. Frappart, M. Fink and A. Aubry; "Distortion matrix approach for ultrasound imaging of random scattering media *Proceedings of the National Academy of Sciences* 117 (26) 14645-14656 (2020)

- W. Lambert, L. A. Cobus, M. Couade, M. Fink and A. Aubry; "Reflection matrix approach for quantitative imaging of scattering media"; *Physical Review X* 10, 021048 (2020)

Submitted manuscript in peer-reviewed journal

- W. Lambert, L. A. Cobus, M. Fink and A. Aubry; "Ultrasound Matrix Imaging. I. The focused reflection marix and the F-factor, arXiv:2103.02029 [physics.app-ph] (submittted in *IEEE Transactions on Medical Imaging*)

- W. Lambert, L. A. Cobus, M. Fink and A. Aubry; "Ultrasound Matrix Imaging. II. The distortion matrix for a local correction of aberration, arXiv:2103.02036[eess.IV] (submittted in *IEEE Transactions on Medical Imaging*)

Patents

- 28620/002FR1; A. Aubry, A. Badon, V. Victor, C. Boccara, L. Cobus, M. Fink. and W. Lambert; "PROCÉDÉS ET SYSTÈMES DE CARACTÉRISATION ULTRASONORE NON INVASIVE D'UN MILIEU HÉTÉROGÈNE"; 2018 – Distortion Matrix in ultrasound

- 28620/034FR1; A. Aubry, A. Badon, V. Victor, C. Boccara, L. Cobus, M. Fink and W. Lambert; "PROCÉDÉS ET SYSTÈMES DE CARACTÉRISATION OPTIQUE NON INVASIVE D'UN MILIEU HÉTÉROGÈNE"; 2018 – Distortion Matrix in optique

- FR1908904; W. Lambert, A. Aubry, L. Cobus and M. Fink; "PROCÉDÉ ET SYSTÈME DE CARACTÉRISATION ULTRASONORE NON INVASIVE D'UN MILIEU HÉTÉROGÈNE"; 2019 – Common-mid-point frame. Focusing criterion, speed of sound measurement and multiple scattering quantification.

- FR2009311; W. Lambert, A. Aubry, L. Cobus, T. Frappart and M. Fink; "PROCÉDÉ ET SYSTÈME DE CARACTÉRISATION ULTRASONORE D'UN MILIEU"; 2020 – Time focused reflection matrix.

- FR2009312; W. Lambert, A. Aubry, L. Cobus, T. Frappart and M. Fink; "PROCÉDÉ ET SYSTÈME DE CARACTÉRISATION ULTRASONORE D'UN MILIEU"; 2020 – Wave front frame, speed of sound measurement.

- FR2009313; W. Lambert, A. Aubry, L. Cobus, T. Frappart and M. Fink; "PROCÉDÉ ET SYSTÈME DE CARACTÉRISATION ULTRASONORE D'UN MILIEU"; 2020 – Wave front frame, axial aberration correction.

- FR2009314; W. Lambert, A. Aubry, L. Cobus, T. Frappart and M. Fink; "PROCÉDÉ ET SYSTÈME DE CARACTÉRISATION ULTRASONORE D'UN MILIEU"; 2020 – Wave front frame, quantification of the scatterer anisotropy

- FR2009315; W. Lambert, A. Aubry, L. Cobus, T. Frappart and M. Fink; "PROCÉDÉ ET SYSTÈME DE CARACTÉRISATION ULTRASONORE D'UN MILIEU"; 2020 – Confocal frame, local spectrum quantification.

Peer-reviewed abstract for oral presentation

- W. Lambert, L. Cobus, M. Fink and A. Aubry; "Approche matricielle de la propagation des ondes en milieux complexes - Imagerie et quantification ultrasonores " Congrès Français d'Acoustique; Le Havre (France), 2018.

- W. Lambert, L. Cobus, M. Fink and A. Aubry; "Reflection matrix approach for ultrasound imaging and quantification"; IEEE International Ultrasonics Symposium; Kobe (Japan) 2018

- W. Lambert, L. Cobus, M. Fink and A. Aubry; "Matrix Approach of aberration correction in ultrasound imaging"; International Congress on Ultrasonics; Bruges (Belgium) 2019

- W. Lambert, L. Cobus, M. Fink and A. Aubry; "Reflection matrix approach for ultrasound tomography of speed-of-sound and multiple scattering"; International Congress on Ultrasonics; Bruges (Belgium) 2019

- W. Lambert, L. Cobus, M. Fink and A. Aubry; "Reflection matrix approach for ultrasound tomography of speed-of-sound and multiple scattering"; IEEE International Ultrasonics Symposium; Glasgow (Scotland) 2019

- W. Lambert, L. Cobus, M. Fink and A. Aubry; "Matrix Approach of aberration correction in ultrasound imaging"; IEEE International Ultrasonics Symposium; Glasgow (Scotland) 2019

- W. Lambert, L. Cobus, M. Fink and A. Aubry; "Matrix approach of aberration correction in ultrasound imaging: an in-vivo proof-of-concept"; Online 2020.

Bibliography

[1] T. L. Szabo; *Diagnostic ultrasound imaging: inside out* (Academic Press) (2004). 3, 4, 62

[2] "Verasonic probes"; https://verasonics.com/verasonics-transducers/; accessed: 2020-08-04. 5

[3] J. W. Goodman; *Introduction to Fourier Optics* (McGraw-Hill, Inc.) (1996). 5, 19, 34

[4] J. Provost, C. Papadacci, J. E. Arango, M. Imbault, M. Fink, J.-L. Gennisson, M. Tanter & M. Pernot; "3D ultrafast ultrasound imaging in vivo"; Physics in Medicine & Biology **59**, p. L1 (2014). 6

[5] F. A. Duck; *Physical properties of tissues: a comprehensive reference book* (Academic press) (2013). 8

[6] G. S. Kino; *Acoustic waves: devices, imaging and analog signal processing*; 43 KIN (Prentice Hall) (1987). 8

[7] L. M. Hinkelman, T. L. Szabo & R. C. Waag; "Measurements of ultrasonic pulse distortion produced by human chest wall"; J. Acoust. Soc. Am. **101**, pp. 2365–2373 (1997). 9, 29

[8] M. Born & E. Wolf; *Principles of optics (Seventh edition)* (Cambridge University Press, Cambridge) (2003). 11, 12, 79

[9] K. Watanabe; *Integral transform techniques for Green's functions* (Springer, Cham, Switzerland) (2014). 15, 75

[10] D. H. Chambers & A. Gautesen; "Time reversal for a single spherical scatterer"; The Journal of the Acoustical Society of America **109**, pp. 2616–2624 (2001). 17

[11] R. Mallart & M. Fink; "Adaptive focusing in scattering media through sound-speed inhomogeneities: The van Cittert Zernike approach and focusing criterion"; The Journal of the Acoustical Society of America **96**, pp. 3721–3732 (1994). 18, 19, 36, 39, 40, 54, 91, 93, 110, 113, 116, 129, 139, 144

[12] F. Zernike; "The concept of degree of coherence and its application to optical problems"; Physica **5**, pp. 785–795 (1938). 19

[13] A. Tourin, A. Derode, A. Peyre & M. Fink; "Transport parameters for an ultrasonic pulsed wave propagating in a multiple scattering medium"; The Journal of the Acoustical Society of America **108**, pp. 503–512 (2000). 20, 47, 51

[14] F. A. Duck; "Acoustic properties of tissue at ultrasonic frequencies"; Physical properties of tissue: A comprehensive reference book pp. 73–124 (1990). 21, 29, 85, 95

[15] R. Kuc & M. Schwartz; "Estimating the acoustic attenuation coefficient slope for liver from reflected ultrasound signals"; IEEE Transactions on Sonics and Ultrasonics **26**, pp. 353–361 (1979). 21

[16] Y. Labyed & T. A. Bigelow; "A theoretical comparison of attenuation measurement techniques from backscattered ultrasound echoes"; The Journal of the Acoustical Society of America **129**, pp. 2316–2324 (2011). 21

[17] S. W. Flax, N. J. Pelc, G. H. Glover, F. D. Gutmann & M. McLachlan; "Spectral characterization and attenuation measurements in ultrasound"; Ultrasonic Imaging **5**, pp. 95–116 (1983). 21

[18] K. J. Parker & R. C. Waag; "Measurement of ultrasonic attenuation within regions selected from B-scan images"; IEEE transactions on biomedical engineering pp. 431–437 (1983). 21

[19] T. A. Bigelow & W. D. O'Brien Jr; "Impact of local attenuation approximations when estimating correlation length from backscattered ultrasound echoes"; The Journal of the Acoustical Society of America **120**, pp. 546–553 (2006). 21

[20] K. J. Parker, R. M. Lerner & R. C. Waag; "Comparison of techniques for in vivo attenuation measurements"; IEEE Transactions on Biomedical engineering **35**, pp. 1064–1068 (1988). 21

[21] L. X. Yao, J. A. Zagzebski & E. L. Madsen; "Backscatter coefficient measurements using a reference phantom to extract depth-dependent instrumentation factors"; Ultrasonic imaging **12**, pp. 58–70 (1990). 21

[22] H. Kim & T. Varghese; "Hybrid spectral domain method for attenuation slope estimation"; Ultrasound in medicine & biology **34**, pp. 1808–1819 (2008). 21

[23] C. Burckhardt, P.-A. Grandchamp & H. Hoffmann; "An experimental 2 MHz synthetic aperture sonar system intended for medical use"; IEEE Transactions on Sonics and Ultrasonics **21**, pp. 1–6 (1974). 22, 70

[24] M. Karaman, P.-C. Li & M. O'Donnell; "Synthetic aperture imaging for small scale systems"; IEEE transactions on ultrasonics, ferroelectrics, and frequency control **42**, pp. 429–442 (1995). 22, 70

[25] G. Matrone, A. Ramalli, A. S. Savoia, P. Tortoli & G. Magenes; "High frame-rate, high resolution ultrasound imaging with multi-line transmission and filtered-delay multiply and sum beamforming"; IEEE transactions on medical imaging **36**, pp. 478–486 (2016). 23

[26] G. Montaldo, M. Tanter, J. Bercoff, N. Benech & M. Fink; "Coherent Plane Wave Compounding for Very High Frame Rate Ultrasonography and Transient Elastography I . Introduction"; IEEE Trans. Ultrason., Ferroelectr., Freq. Control **56**, pp. 489–506 (2009). 23, 26, 28, 75, 149

[27] L. Sandrin, S. Catheline, M. Tanter, X. Hennequin & M. Fink; "Time-resolved pulsed elastography with ultrafast ultrasonic imaging"; Ultrasonic imaging **21**, pp. 259–272 (1999). 23

[28] J. Bercoff, S. Chaffai, M. Tanter, L. Sandrin, S. Catheline, M. Fink, J. Gennisson & M. Meunier; "In vivo breast tumor detection using transient elastography"; Ultrasound in medicine & biology **29**, pp. 1387–1396 (2003). 23

[29] M. Berson, A. Roncin & L. Pourcelot; "Compound scanning with an electrically steered beam"; Ultrasonic imaging **3**, pp. 303–308 (1981). 23

[30] T. K. Song & J. H. Chang; "Synthetic aperture focusing method for ultrasound imaging based on planar waves"; (2004); uS Patent 6,736,780. 23

[31] J. Cheng & J.-y. Lu; "Extended high-frame rate imaging method with limited-diffraction beams"; IEEE transactions on ultrasonics, ferroelectrics, and frequency control **53**, pp. 880–899 (2006). 23

[32] J. Kortbek, J. A. Jensen & K. L. Gammelmark; "Synthetic aperture sequential beamforming"; in "2008 IEEE Ultrasonics Symposium," pp. 966–969 (IEEE) (2008). 28, 29, 72

[33] O. M. H. Rindal, A. Rodriguez-Molares & A. Austeng; "A simple, artifact-free, virtual source model"; in "2018 IEEE International Ultrasonics Symposium (IUS)," pp. 1–4 (IEEE) (2018). 29

[34] K. H. Nicolaides; "Nuchal translucency and other first-trimester sonographic markers of chromosomal abnormalities"; American journal of obstetrics and gynecology **191**, pp. 45–67 (2004). 30, 31

[35] A. Aubry & A. Derode; "Multiple scattering of ultrasound in weakly inhomogeneous media: Application to human soft tissues"; The Journal of the Acoustical Society of America **129**, pp. 225–233 (2011). 30, 32, 47, 48, 171

[36] F. Roddier; *Adaptive optics in astronomy* (Cambridge University Press, Cambridge) (1999). 33, 34, 35

[37] B. A. Angelsen; *Ultrasound imaging: waves, signals, and signal processing. 2. Propagation and scattering in heterogeneous, nonlinear tissue with contrast agent imaging and Doppler measurements* (Emantec) (2000). 33

[38] T. Varslot, H. Krogstad, E. Mo & B. A. Angelsen; "Eigenfunction analysis of stochastic backscatter for characterization of acoustic aberration in medical ultrasound imaging"; The Journal of the Acoustical Society of America **115**, pp. 3068–3076 (2004). 34, 36, 39, 116, 117, 131, 139, 142, 144

[39] M. Fink; "Time reversal of ultrasonic fields. I. Basic principles"; IEEE transactions on ultrasonics, ferroelectrics, and frequency control **39**, pp. 555–566 (1992). 34, 62, 63, 64

[40] W. Lambert, L. A. Cobus, T. Frappart, M. Fink & A. Aubry; "Distortion matrix approach for ultrasound imaging of random scattering media"; Proceedings of the National Academy of Sciences (2020). 35, 41, 82, 125, 132, 134, 135, 138, 140

[41] I. Freund, M. Rosenbluh & S. Feng; "Memory Effects in Propagation of Optical Waves through Disordered Media"; Phys. Rev. Lett. **61**, pp. 2328–2331 (1988). 35, 36

[42] S. Feng, C. Kane, P. A. Lee & A. D. Stone; "Correlations and Fluctuations of Coherent Wave Transmission through Disordered Media"; Phys. Rev. Lett. **61**, pp. 834–837 (1988). 35, 36

[43] G. Osnabrugge, R. Horstmeyer, I. N. Papadopoulos, B. Judkewitz & I. M. Vellekoop; "Generalized optical memory effect"; Optica **4**, pp. 886–892 (2017). 35

[44] J. Mertz, H. Paudel & T. G. Bifano; "Field of view advantage of conjugate adaptive optics in microscopy applications"; Applied optics **54**, pp. 3498–3506 (2015). 35, 36

[45] O. Katz, P. Heidmann, M. Fink & S. Gigan; "going through scattering layers and around corners via speckle correlations"; Nat. Photonics **8**, p. 784 (2014). 36

[46] S. Shahjahan, A. Aubry, F. Rupin, B. Chassignole & A. Derode; "A random matrix approach to detect defects in a strongly scattering polycrystal: How the memory effect can help overcome multiple scattering"; Applied Physics Letters **104**, p. 234105 (2014). 36

[47] M. O'Donnell & S. Flax; "Phase-aberration correction using signals from point reflectors and diffuse scatterers: measurements"; IEEE Trans. Ultrason., Ferroelectr., Freq. Control **35**, pp. 768–774 (1988). 36, 39, 116, 139

[48] W. F. Walker & G. E. Trahey; "Speckle coherence and implications for adaptive imaging"; J. Acoust. Soc. Am. **101**, p. 1847 (1997). 36

[49] J.-L. Robert & M. Fink; "Green's function estimation in speckle using the decomposition of the time reversal operator: Application to aberration correction in medical imaging"; J. Acoust. Soc. Am. **123**, p. 866 (2008). 36, 40, 72, 98, 129, 139

[50] G. C.-H. Ng; *The application of translating transmit apertures in adaptive ultrasonic imaging*; Ph.D. thesis; Duke University (1997). 36

[51] D.-L. Liu & R. C. Waag; "Estimation and correction of ultrasonic wavefront distortion using pulse-echo data received in a two-dimensional aperture"; IEEE transactions on ultrasonics, ferroelectrics, and frequency control **45**, pp. 473–490 (1998). 36

[52] M. Tanter, J.-L. Thomas & M. Fink; "Focusing and steering through absorbing and aberrating layers: Application to ultrasonic propagation through the skull"; The Journal of the Acoustical Society of America **103**, pp. 2403–2410 (1998). 37, 66

[53] J. J. Dahl, M. S. Soo & G. E. Trahey; "Spatial and temporal aberrator stability for real-time adaptive imaging"; IEEE transactions on ultrasonics, ferroelectrics, and frequency control **52**, pp. 1504–1517 (2005). 37

[54] L. Nock, G. E. Trahey & S. W. Smith; "Phase aberration correction in medical ultrasound using speckle brightness as a quality factor"; The Journal of the Acoustical Society of America **85**, pp. 1819–1833 (1989). 37

[55] R. Ali & J. J. Dahl; "Distributed phase aberration correction techniques based on local sound speed estimates"; in "2018 IEEE International Ultrasonics Symposium (IUS)," pp. 1–4 (IEEE) (2018). 38

[56] G. Maimbourg, A. Houdouin, T. Deffieux, M. Tanter & J.-F. Aubry; "3D-printed adaptive acoustic lens as a disruptive technology for transcranial ultrasound therapy using single-element transducers"; Physics in Medicine & Biology **63**, p. 025026 (2018). 38

[57] F. B. Jensen, W. A. Kuperman, M. B. Porter & H. Schmidt; *Computational ocean acoustics* (Springer Science & Business Media) (2011). 38

[58] J. A. Sethian & A. M. Popovici; "3-D traveltime computation using the fast marching method"; Geophysics **64**, pp. 516–523 (1999). 39

[59] S. D. Silverstein & D. P. Ceperley; "Autofocusing in medical ultrasound: the scaled covariance matrix algorithm"; IEEE transactions on ultrasonics, ferroelectrics, and frequency control **50**, pp. 795–804 (2003). 39

[60] S.-E. Måsøy, T. Varslot & B. Angelsen; "Iteration of transmit-beam aberration correction in medical ultrasound imaging"; The Journal of the Acoustical Society of America **117**, pp. 450–461 (2005). 39, 147

[61] J.-L. Robert & M. Fink; "The time-reversal operator with virtual transducers: Application to far-field aberration correction"; The Journal of the Acoustical Society of America **124**, pp. 3659–3668 (2008). 40, 72, 73, 93, 116, 117, 138, 142, 144

[62] G. Montaldo, M. Tanter & M. Fink; "Time reversal of speckle noise"; Physical review letters **106**, p. 054301 (2011). 41, 91, 116, 117, 139, 140

[63] B.-F. Osmanski, G. Montaldo, M. Tanter & M. Fink; "Aberration correction by time reversal of moving speckle noise"; IEEE transactions on ultrasonics, ferroelectrics, and frequency control **59**, pp. 1575–1583 (2012). 41

[64] M. Imbault, A. Faccinetto, B.-F. Osmanski, A. Tissier, T. Deffieux, J.-L. Gennisson, V. Vilgrain & M. Tanter; "Robust sound speed estimation for ultrasound-based hepatic steatosis assessment"; Physics in Medicine & Biology **62**, p. 3582 (2017). 42, 44, 159

[65] G. Chau, M. Jakovljevic, R. Lavarello & J. Dahl; "A locally adaptive phase aberration correction (LAPAC) method for synthetic aperture sequences"; Ultrasonic imaging **41**, pp. 3–16 (2019). 41, 135, 138, 139

[66] H. Bendjador, T. Deffieux & M. Tanter; "The SVD Beamformer: Physical Principles and Application to Ultrafast Adaptive Ultrasound"; IEEE Transactions on Medical Imaging pp. 1–1 (2020). 41, 45, 131, 135, 138, 139

[67] C. Yoon, Y. Lee, J. H. Chang, T.-k. Song & Y. Yoo; "In vitro estimation of mean sound speed based on minimum average phase variance in medical ultrasound imaging"; Ultrasonics **51**, pp. 795–802 (2011). 43

[68] A. Benjamin, R. E. Zubajlo, M. Dhyani, A. E. Samir, K. E. Thomenius, J. R. Grajo & B. W. Anthony; "A novel approach to the quantification of the longitudinal speed of sound and its potential for tissue characterization (Part-I)"; Ultrasound in medicine & biology **44**, pp. 2739–2748 (2018). 43

[69] W. Lambert, L. A. Cobus, M. Couade, M. Fink & A. Aubry; "Reflection matrix approach for quantitative imaging of scattering media"; Physical Review X **10**, p. 021048 (2020). 43, 44, 50, 62, 75, 79, 82, 120, 134

[70] M. A. Fink & J.-F. Cardoso; "Diffraction effects in pulse-echo measurement"; IEEE transactions on sonics and ultrasonics **31**, pp. 313–329 (1984). 43

[71] M. E. Anderson & G. E. Trahey; "The direct estimation of sound speed using pulse–echo ultrasound"; The Journal of the Acoustical Society of America **104**, pp. 3099–3106 (1998). 44

[72] M. Jakovljevic, S. Hsieh, R. Ali, G. Chau Loo Kung, D. Hyun & J. J. Dahl; "Local speed of sound estimation in tissue using pulse-echo ultrasound: Model-based approach"; The Journal of the Acoustical Society of America **144**, pp. 254–266 (2018). 44, 159

[73] B. C. Byram, G. E. Trahey & J. A. Jensen; "A method for direct localized sound speed estimates using registered virtual detectors"; Ultrasonic imaging **34**, pp. 159–180 (2012). 44, 45

[74] M. Kondo, K. Takamizawa, M. Hirama, K. Okazaki, K. Iinuma & Y. Takehara; "An evaluation of an in vivo local sound speed estimation technique by the crossed beam method"; Ultrasound in medicine & biology **16**, pp. 65–72 (1990). 44

[75] M. Jaeger, G. Held, S. Peeters, S. Preisser, M. Grünig & M. Frenz; "Computed ultrasound tomography in echo mode for imaging speed of sound using pulse-echo sonography: proof of principle"; Ultrasound in medicine & biology **41**, pp. 235–250 (2015). 44, 46, 160

[76] P. Stähli, M. Kuriakose, M. Frenz & M. Jaeger; "Improved forward model for quantitative pulse-echo speed-of-sound imaging"; Ultrasonics p. 106168 (2020). 45, 46, 56, 159, 160

[77] M. v. van Rossum & T. M. Nieuwenhuizen; "Multiple scattering of classical waves: microscopy, mesoscopy, and diffusion"; Reviews of Modern Physics **71**, p. 313 (1999). 46

[78] J. Page, H. Schriemer, A. Bailey & D. Weitz; "Experimental test of the diffusion approximation for multiply scattered sound"; Physical Review E **52**, p. 3106 (1995). 47

[79] J. H. Page, P. Sheng, H. P. Schriemer, I. Jones, X. Jing & D. A. Weitz; "Group velocity in strongly scattering media"; Science **271**, pp. 634–637 (1996). 47

[80] J. H. Page, H. P. Schriemer, I. Jones, P. Sheng & D. A. Weitz; "Classical wave propagation in strongly scattering media"; Physica A: Statistical Mechanics and its Applications **241**, pp. 64–71 (1997). 47

[81] M. L. Cowan, K. Beaty, J. H. Page, Z. Liu & P. Sheng; "Group velocity of acoustic waves in strongly scattering media: Dependence on the volume fraction of scatterers"; Physical Review E **58**, p. 6626 (1998). 47

[82] Z. Zhang, I. Jones, H. P. Schriemer, J. H. Page, D. A. Weitz & P. Sheng; "Wave transport in random media: The ballistic to diffusive transition"; Physical Review E **60**, p. 4843 (1999). 47

[83] G. Bayer & T. Niederdränk; "Weak localization of acoustic waves in strongly scattering media"; Physical review letters **70**, p. 3884 (1993). 47, 50, 171

[84] A. Tourin, A. Derode, P. Roux, B. A. Van Tiggelen & M. Fink; "Time-dependent coherent backscattering of acoustic waves"; Physical review letters **79**, p. 3637 (1997). 47, 50, 51, 171

[85] A. Tourin, M. Fink & A. Derode; "Multiple scattering of sound"; Waves in random media **10**, pp. R31–R60 (2000). 47

[86] A. Aubry & A. Derode; "Ultrasonic imaging of highly scattering media from local measurements of the diffusion constant: Separation of coherent and incoherent intensities"; Physical Review E **75**, p. 026602 (2007). 47, 50, 52, 53, 74, 166, 171

[87] A. Aubry, A. Derode & F. Padilla; "Local measurements of the diffusion constant in multiple scattering media: Application to human trabecular bone imaging"; Applied Physics Letters **92**, p. 124101 (2008). 47, 50, 52, 166, 171

[88] A. Aubry & A. Derode; "Random matrix theory applied to acoustic backscattering and imaging in complex media"; Physical review letters **102**, p. 084301 (2009). 47

[89] A. Aubry & A. Derode; "Detection and imaging in a random medium: A matrix method to overcome multiple scattering and aberration"; Journal of Applied Physics **106**, p. 044903 (2009). 47, 48, 102

[90] A. Aubry; *Approche matricielle de l'opérateur de propagation des ondes ultrasonores en milieu diffusant aléatoire*; Theses; Université Pierre et Marie Curie - Paris VI (2008). 49, 50, 162

[91] Y. Kuga & A. Ishimaru; "Retroreflectance from a dense distribution of spherical particles"; JOSA A **1**, pp. 831–835 (1984). 50

[92] M. P. Van Albada & A. Lagendijk; "Observation of weak localization of light in a random medium"; Physical review letters **55**, p. 2692 (1985). 50

[93] P.-E. Wolf & G. Maret; "Weak localization and coherent backscattering of photons in disordered media"; Physical review letters **55**, p. 2696 (1985). 50

[94] E. Akkermans, P. Wolf, R. Maynard & G. Maret; "Theoretical study of the coherent backscattering of light by disordered media"; Journal de Physique **49**, pp. 77–98 (1988). 50

[95] E. Larose, L. Margerin, B. Van Tiggelen & M. Campillo; "Weak localization of seismic waves"; Physical review letters **93**, p. 048501 (2004). 50

[96] A. Aubry & A. Derode; "Singular value distribution of the propagation matrix in random scattering media"; Wave Random Complex **20** (2010). 51, 145

[97] K. Mohanty, J. Blackwell, T. Egan & M. Muller; "Characterization of the lung parenchyma using ultrasound multiple scattering"; Ultrasound in medicine & biology **43**, pp. 993–1003 (2017). 52, 171

[98] E. S. C. Koh & E. G. McNally; "Ultrasound of skeletal muscle injury"; in "Seminars in musculoskeletal radiology," , volume 11pp. 162–173 (© Thieme Medical Publishers) (2007). 54, 57

[99] T. S. Wu, P. J. Roque, J. Green, D. Drachman, K.-N. Khor, M. Rosenberg & C. Simpson; "Bedside ultrasound evaluation of tendon injuries"; The American journal of emergency medicine **30**, pp. 1617–1621 (2012). 54, 57

[100] A. Derode & M. Fink; "Spatial coherence of ultrasonic speckle in composites"; IEEE Transactions on ultrasonics, ferroelectrics, and frequency control **40**, pp. 666–675 (1993). 54, 58

[101] C. Papadacci, M. Tanter, M. Pernot & M. Fink; "Ultrasound backscatter tensor imaging (BTI): analysis of the spatial coherence of ultrasonic speckle in anisotropic soft tissues"; IEEE transactions on ultrasonics, ferroelectrics, and frequency control **61**, pp. 986–996 (2014). 55

[102] C. Papadacci, V. Finel, J. Provost, O. Villemain, P. Bruneval, J.-L. Gennisson, M. Tanter, M. Fink & M. Pernot; "Imaging the dynamics of cardiac fiber orientation in vivo using 3D Ultrasound Backscatter Tensor Imaging"; Scientific reports **7**, pp. 1–9 (2017). 55, 58

[103] M. Fink; "Time-reversal waves and super resolution"; Journal of Physics: Conference Series **124**, p. 012004 (2008). 62

[104] C. Prada, F. Wu & M. Fink; "The iterative time reversal mirror: A solution to self-focusing in the pulse echo mode"; The Journal of the Acoustical Society of America **90**, pp. 1119–1129 (1991). 62

[105] C. Prada & M. Fink; "Eigenmodes of the time reversal operator: A solution to selective focusing in multiple-target media"; Wave motion **20**, pp. 151–163 (1994). 62, 65, 109, 110, 131, 133, 142

[106] C. Prada, S. Manneville, D. Spoliansky & M. Fink; "Decomposition of the time reversal operator: Detection and selective focusing on two scatterers"; The Journal of the Acoustical Society of America **99**, pp. 2067–2076 (1996). 62, 65, 109, 110, 131, 142

[107] S. Popoff, G. Lerosey, R. Carminati, M. Fink, A. Boccara & S. Gigan; "Measuring the transmission matrix in optics: an approach to the study and control of light propagation in disordered media"; Physical review letters **104**, p. 100601 (2010). 62, 65, 69

[108] S. M. Popoff, A. Aubry, G. Lerosey, M. Fink, A.-C. Boccara & S. Gigan; "Exploiting the time-reversal operator for adaptive optics, selective focusing, and scattering pattern analysis"; Physical review letters **107**, p. 263901 (2011). 62, 65, 69

[109] A. Derode, A. Tourin, J. de Rosny, M. Tanter, S. Yon & M. Fink; "Taking advantage of multiple scattering to communicate with time-reversal antennas"; Physical Review Letters **90**, p. 014301 (2003). 62, 68

[110] S. Popoff, A. Goetschy, S. Liew, A. D. Stone & H. Cao; "Coherent control of total transmission of light through disordered media"; Physical review letters **112**, p. 133903 (2014). 62, 65, 69

[111] N. Bottenus; "Recovery of the complete data set from focused transmit beams"; IEEE transactions on ultrasonics, ferroelectrics, and frequency control **65**, pp. 30–38 (2017). 62

[112] A. A. Badon; *Approche matricielle de l'imagerie optique des milieux diffusants*; Ph.D. thesis; Sorbonne Paris Cité (2016). 62, 74

[113] C. Prada & J.-L. Thomas; "Experimental subwavelength localization of scatterers by decomposition of the time reversal operator interpreted as a covariance matrix"; The Journal of the Acoustical Society of America **114**, pp. 235–243 (2003). 65, 109, 131

[114] A. Aubry, J. de Rosny, J.-G. Minonzio, C. Prada & M. Fink; "Gaussian beams and Legendre polynomials as invariants of the time reversal operator for a large rigid cylinder"; The Journal of the Acoustical Society of America **120**, pp. 2746–2754 (2006). 65, 74, 109, 129, 131, 142

[115] J.-G. Minonzio, F. D. Philippe, C. Prada & M. Fink; "Characterization of an elastic cylinder and an elastic sphere with the time-reversal operator: application to the sub-resolution limit"; Inverse Problems **24**, p. 025014 (2008). 65

[116] M. Tanter, J.-L. Thomas & M. Fink; "Time reversal and the inverse filter"; The Journal of the Acoustical Society of America **108**, pp. 223–234 (2000). 65, 68

[117] J.-F. Aubry, M. Tanter, J. Gerber, J.-L. Thomas & M. Fink; "Optimal focusing by spatio-temporal inverse filter. II. Experiments. Application to focusing through absorbing and reverberating media"; The Journal of the Acoustical Society of America **110**, pp. 48–58 (2001). 65, 68

[118] M. Tanter, J.-F. Aubry, J. Gerber, J.-L. Thomas & M. Fink; "Optimal focusing by spatio-temporal inverse filter. I. Basic principles"; The Journal of the Acoustical Society of America **110**, pp. 37–47 (2001). 65, 68

[119] C. Prada, M. Tanter & M. Fink; "Flaw detection in solid with the DORT method"; in "1997 IEEE Ultrasonics Symposium Proceedings. An International Symposium (Cat. No. 97CH36118)," , volume 1pp. 679–683 (IEE E) (1997). 65

[120] G. Lerosey, J. De Rosny, A. Tourin & M. Fink; "Focusing beyond the diffraction limit with far-field time reversal"; Science **315**, pp. 1120–1122 (2007). 65, 68

[121] N. Mordant, C. Prada & M. Fink; "Highly resolved detection and selective focusing in a waveguide using the DORT method"; The Journal of the Acoustical Society of America **105**, pp. 2634–2642 (1999). 66

[122] A. Derode, A. Tourin & M. Fink; "Random multiple scattering of ultrasound. II. Is time reversal a self-averaging process?" Physical Review E **64**, p. 036606 (2001). 67, 68

[123] P. Roux, B. Roman & M. Fink; "Time-reversal in an ultrasonic waveguide"; Applied Physics Letters **70**, pp. 1811–1813 (1997). 67

[124] I. M. Vellekoop & A. Mosk; "Focusing coherent light through opaque strongly scattering media"; Optics letters **32**, pp. 2309–2311 (2007). 69

[125] S. Popoff, G. Lerosey, M. Fink, A. C. Boccara & S. Gigan; "Image transmission through an opaque material"; Nature communications **1**, pp. 1–5 (2010). 69

[126] A. Liutkus, D. Martina, S. Popoff, G. Chardon, O. Katz, G. Lerosey, S. Gigan, L. Daudet & I. Carron; "Imaging with nature: Compressive imaging using a multiply scattering medium"; Scientific reports **4**, p. 5552 (2014). 69

[127] P. del Hougne, M. Fink & G. Lerosey; "Optimally diverse communication channels in disordered environments with tuned randomness"; Nature Electronics **2**, pp. 36–41 (2019). 69

[128] B. Gérardin, J. Laurent, A. Derode, C. Prada & A. Aubry; "Full transmission and reflection of waves propagating through a maze of disorder"; Physical review letters **113**, p. 173901 (2014). 69

[129] O. Dorokhov; "Transmission coefficient and the localization length of an electron in N bound disordered chains"; JETP Lett **36**, pp. 318–321 (1982). 69

[130] S. Rotter, P. Ambichl & F. Libisch; "Generating particlelike scattering states in wave transport"; Physical review letters **106**, p. 120602 (2011). 69

[131] B. Gérardin, J. Laurent, P. Ambichl, C. Prada, S. Rotter & A. Aubry; "Particlelike wave packets in complex scattering systems"; Physical Review B **94**, p. 014209 (2016). 69

[132] P. Ambichl, A. Brandstötter, J. Böhm, M. Kühmayer, U. Kuhl & S. Rotter; "Focusing inside disordered media with the generalized Wigner-Smith operator"; Physical Review Letters **119**, p. 033903 (2017). 69

[133] S. Rotter & S. Gigan; "Light fields in complex media: Mesoscopic scattering meets wave control"; Reviews of Modern Physics **89**, p. 015005 (2017). 69

[134] K. L. Gammelmark & J. A. Jensen; "Multielement synthetic transmit aperture imaging using temporal encoding"; IEEE transactions on medical imaging **22**, pp. 552–563 (2003). 70

[135] J. A. Jensen, S. I. Nikolov, K. L. Gammelmark & M. H. Pedersen; "Synthetic aperture ultrasound imaging"; Ultrasonics **44**, pp. e5–e15 (2006). 72

[136] R. Zemp & M. F. Insana; "Imaging with unfocused regions of focused ultrasound beams"; The Journal of the Acoustical Society of America **121**, pp. 1491–1498 (2007). 72

[137] C. Passmann & H. Ermert; "A 100-MHz ultrasound imaging system for dermatologic and ophthalmologic diagnostics"; IEEE transactions on ultrasonics, ferroelectrics, and frequency control **43**, pp. 545–552 (1996). 72

[138] A. Aubry; *Approche matricielle de l'opérateur de propagation des ondes ultrasonores en milieu diffusant aléatoire*; Theses; Université Pierre et Marie Curie - Paris VI (2008). https://tel.archives-ouvertes.fr/tel-00811618. 74

[139] A. Badon, D. Li, G. Lerosey, A. C. Boccara, M. Fink & A. Aubry; "Smart optical coherence tomography for ultra-deep imaging through highly scattering media"; Sci. Adv. **2**, p. e1600370 (2016). 74, 120, 171

[140] C. Trottier; *Détection de défauts en milieu fortement diffusant par utilisation de capteurs multiéléments et filtrage de la diffusion multiple*; Ph.D. thesis; Sorbonne Paris Cité (2016). 74

[141] V. Barolle; *Approche matricielle de la tomographie à cohérence optique*; Ph.D. thesis; PSL Research University (2019). 74

[142] T. Blondel, J. Chaput, A. Derode, M. Campillo & A. Aubry; "Matrix Approach of Seismic Imaging: Application to the Erebus Volcano, Antarctica"; Journal of Geophysical Research : Solid Earth **123**, pp. 10,936–10,950 (2018). 74

[143] M. A. Lediju, G. E. Trahey, B. C. Byram & J. J. Dahl; "Short-lag spatial coherence of backscattered echoes: Imaging characteristics"; IEEE Trans. Ultrason. Ferroelectr. Freq. Control **58**, pp. 1377–1388 (2011). 91

[144] J. J. Dahl, D. Hyun, Y. Li, M. Jakovljevic, M. A. Bell, W. J. Long, N. Bottenus, V. Kakkad & G. E. Trahey; "Coherence beamforming and its applications to the difficult-to-image patient"; in "2017 IEEE International Ultrasonics Symposium (IUS)," pp. 1–10 (IEEE) (2017). 91

[145] K. Hollman, K. Rigby & M. O'Donnell; "Coherence factor of speckle from a multi-row probe"; in "1999 IEEE Ultrasonics Symposium. Proceedings. International Symposium (Cat. No.99CH37027)," (IEEE). 91, 93

[146] J. E. Carlson, J. van Deventer, A. Scolan & C. Carlander; "Frequency and temperature dependence of acoustic properties of polymers used in pulse-echo systems"; in "IEEE Symposium on Ultrasonics, 2003," , volume 1pp. 885–888 (2003). 99

[147] S. Kang, S. Jeong, H. Choi, W. Ko, T. D. Yang, J. H. Joo, J.-S. Lee, Y.-S. Lim, Q.-H. Park & W. Choi; "Imaging deep within a scattering medium using collective accumulation of single-scattered waves"; Nat. Photonics **9**, pp. 1–18 (2015). 102

[148] S. Shajahan, A. Aubry, F. Rupin, B. Chassignole & A. Derode; "A random matrix approach to detect defects in a strongly scattering polycrystal : how the memory effect can help overcome multiple scattering"; Appl. Phys. Lett. **104**, p. 234105 (2014). 102, 171

[149] A. Badon, V. Barolle, K. Irsch, A. C. Boccara, M. Fink & A. Aubry; "Distortion matrix concept for deep optical imaging in scattering media"; Science advances **6**, p. eaay7170 (2020). 103, 104, 109, 114, 115, 116, 125, 138, 146

[150] J.-L. Robert; *Evaluation of Green's functions in complex media by decomposition of the Time Reversal Operator: Application to Medical Imaging and aberration correction*; Ph.D. thesis; Universite Paris 7 - Denis Diderot (2007). 109, 142, 146

[151] J.-L. Robert & M. Fink; "The prolate spheroidal wave functions as invariants of the time reversal operator for an extended scatterer in the Fraunhofer approximation"; The Journal of the Acoustical Society of America **125**, pp. 218–226 (2009). 109, 129, 131, 142

[152] V. N. Mahajan; "Strehl ratio for primary aberrations: some analytical results for circular and annular pupils"; J. Opt. Soc. Am. **72**, pp. 1258–1266 (1982). 111, 173

[153] L. L. Campbell; "Minimum coefficient rate for stationary random processes"; Inf. Control **3**, pp. 360–371 (1960). 114

[154] S. J. Roberts, W. Penny & L. Rezek; "Temporal and spatial complexity measures for electroencephalogram based brain-computer interfacing"; Med. Biol. Eng. Comput. **37**, pp. 93–98 (1999). 114

[155] A. Rodriguez-Molares, A. Fatemi, L. Løvstakken & H. Torp; "Specular beamforming"; IEEE Transactions on Ultrasonics, Ferroelectrics, and Frequency Control **64**, pp. 1285–1297 (2017). 117

[156] T. Blondel, J. Chaput, A. Derode, M. Campillo & A. Aubry; "Matrix approach of seismic imaging: ApplicatihDon to the Erebus Volcano, Antarctica"; J. Geophys. Res.: Solid Earth **123**, pp. 10936–10950 (2018). 120

[157] R. G. Ghanem & P. D. Spanos; *Stochastic finite elements: a spectral approach* (Courier Corporation) (2003). 129

[158] T. Blondel; *Matrix Approach of Seismic Imaging*; Ph.D. thesis; PSL University (2019). 138

[159] M. Priestley; *Spectral analysis and time series* (Academic Press, London) (1988). 142, 146

[160] J. W. Goodman; *Statistical Optics* (Wiley, New York) (2000). 142

[161] M. Marčenko & L. Pastur; "Distributions of eigenvalues for some sets of random matrices"; Math. USSR-Sbornik **1**, pp. 457–483 (1967). 145

[162] B. Rajagopalan, J. F. Greenleaf, P. J. Thomas, S. A. Johnson & R. C. Bahn; *Variation of acoustic speed with temperature in various exised human tissues studied by ultrasound computerized tomography* (U.S. Department of Commerce) (1979). 156, 159

[163] S. R. Mehta, E. L. Thomas, J. D. BEll, D. G. Johnston & S. D. Taylor-Robinson; "Non-invasive means of measuring hepatic fat content"; World J Gastroenterol **14**, pp. 3476 – 3483 (2008). 158

[164] S. Dasarathy, J. Dasarathy, A. Khiyami, R. Joseph, R. Lopez & A. J. McCullough; "Validity of real time ultrasound in the diagnosis of hepatic steatosis: A prospective study"; Hepatology **51**, pp. 1061 – 1067 (2009). 158

[165] R. E. Zubajlo, A. Benjamin, J. R. Grajo, K. Kaliannan, J. X. Kang, A. K. Bhan, K. E. Thomenius, B. W. Anthony, M. Dhyani & A. E. Samir; "Experimental Validation of Longitudinal Speed of Sound Estimates in the Diagnosis of Hepatic Steatosis (Part II)"; Ultrasound Med Biol **44**, pp. 2749 – 2758 (2018). 158

[166] C. M. Moran, N. L. Bush & J. C. Bamber; "Ultrasonic propagation properties of excised human skin"; Ultrasound Med. Biol. **71**, pp. 1177–1190 (1995). 158

[167] R. L. Errabolu, C. M. Sehgala, R. C. Bahn & J. F. Greenleaf; "Measurement of ultrasonic nonlinear parameter in excised fat tissues"; Ultrasound Med. Biol. **14**, pp. 137 – 146 (1988). 158

[168] T. Lin, J. Ophir & G. Potter; "Correlations of sound speed with tissue constituents in normal and diffuse liver disease"; Ultrason. Imaging **9**, pp. 29 – 40 (1987). 159

[169] B. Boozari, A. Botthoff, I. Mederacke, A. Hahn, A. Reising, K. Rifai, H. Wedemeyer, M. Bahr, s. Kubicka, M. Manns & M. Gebel; "Evaluation of sound speed for detection of liver fibrosis: prospective comparison with transient dynamic elastography and histology"; J. Ultrasound Med. **29**, pp. 1581 – 8 (2010). 159

[170] A. Velichko; "Quantification of the effect of multiple scattering on array imaging performance"; IEEE Trans. Ultrason. Ferroelectr. Freq. Control. **67**, pp. 1–15 (2019). 170

[171] T. Jonckheere, C. A. Müller, R. Kaiser, C. Miniatura & D. Delande; "Multiple scattering of light by atoms in the weak localization regime"; Phys. Rev. Lett. **85**, pp. 4269–72 (2000)ISSN 1079-7114. 171

[172] P. E. Wolf, G. Maret, E. Akkermans & R. Maynard; "Optical coherent backscattering by random media: an experimental study"; J. Phys. France **49**, pp. 63–75 (1988). 171

[173] L. A. Cobus, B. A. van Tiggelen, A. Derode & J. H. Page; "Dynamic coherent backscattering of ultrasound in three-dimensional strongly-scattering media"; Eur. Phys. J. ST **226**, pp. 1549–1561 (2017). 171

[174] K. Mohanty, J. Blackwell, S. B. Masuodi, M. H. Ali, T. Egan & M. Muller; "1-Dimensional quantitative micro-architecture mapping of multiple scattering media using backscattering of ultrasound in the near-field: Application to nodule imaging in the lungs"; Appl. Phys. Lett **113** (2018). 171

RÉSUMÉ

L'échographie est basée sur deux hypothèses fondamentales. D'une part, la vitesse du son est considérée comme constante dans le milieu de propagation. D'autre part, les échos rétrodiffusés par les diffuseurs du milieu sont issus de phénomènes de diffusion simple. En réalité, ces hypothèses ne sont pas toujours vérifiées : des variations de vitesse du son entre les différents tissus sondés peuvent induire de fortes distorsions du front d'onde (aberrations) et des évènements de diffusion multiple peuvent survenir entre les réflecteurs du milieu. Ces deux phénomènes indésirables conduisent à une perte de résolution et de contraste de l'image échographique.
En échographie conventionnelle, les ondes ultrasonores sont générées et mesurées depuis un réseau de transducteurs piézo-électriques dont on peut contrôler de manière indépendante chacun des éléments. L'image échographique résulte d'une double focalisation simultanée, en entrée et sortie, des ondes ultrasonores en chaque point du milieu à imager. L'échographie matricielle, mise au point au cours de cette thèse, consiste au contraire à séparer les points de focalisation à l'émission et à la réception et ainsi mesurer les réponses du milieu entre ces transducteurs virtuels dont la position correspond à chaque pixel de l'image. L'ensemble de ces réponses forment une matrice de réflexion focalisée. A partir de cette matrice, une nouvelle approche de l'imagerie ultrasonore a été développée afin de tirer profit de toute l'information disponible sur le milieu étudié. En plus de pouvoir décrire sous un formalisme matriciel l'ensemble des techniques d'imagerie ultrasonore actuelles, l'imagerie matricielle a été développée en poursuivant plusieurs objectifs : (i) Améliorer et quantifier la qualité des images échographiques en corrigeant de manière locale les aberrations ; (ii) Caractériser localement le milieu de propagation en dressant une cartographie de sa vitesse du son et du taux de diffusion multiple ; (iii) Caractériser localement la nature et l'anisotropie des diffuseurs en étudiant leur réponse spectrale et leur diagramme de rayonnement.

Ce travail s'inscrit dans un cadre plus large dont l'objectif est de développer une approche matricielle de l'imagerie commune à tous les domaines de la physique des ondes pour lesquels un ensemble de capteurs peuvent être utilisés pour sonder le milieu à imager. Ce manuscrit décrit le développement de cette imagerie matricielle dans le contexte ultrasonore avec l'élaboration de nouveaux contrastes permettant une imagerie quantitative des tissus sondés en échographie.

MOTS CLÉS

Echographie, Imagerie, Aberrations, Diffusion multiple, Approche matricielle, Vitesse du son

ABSTRACT

Ultrasound imaging relies on two major assumptions. First, the medium is considered as homogeneous with a constant speed of sound. Second, the back-scattered wave-field only contains singly-scattered echoes. Nonetheless, the speed of sound varies greatly in different tissues. These fluctuations give rise to a distortion of the incident and back-scattered wave-fronts. Moreover, multiple scattering events can also occur between the scatterers of the medium. This multiple scattering contribution manifests itself as an incoherent background noise in the RF signal. Those two undesirable effects, namely aberrations and multiple scattering, thus lead to a loss of resolution and contrast in the ultrasound image.
Conventional ultrasound imaging techniques rely on arrays of transducers that can be individually controlled to emit or receive ultrasonic waves. State-of-the-art ultrasound images are based on a confocal method that consists in a double focusing, both in transmit and in receive, on each point of the medium corresponding to one pixel of the image. In this thesis, we propose a matrix approach of ultrasound imaging that basically consists in splitting the locations of the transmit and receive focal spots. This process gives access to the impulse responses between virtual transducers located within the medium at each pixel location. This set of responses form a so-called focused reflection matrix that contains all the available information on the medium under investigation. Besides describing all the current ultrasound imaging methods under a common matrix formalism, matrix imaging is able to take up several challenges: (i) quantify and enhance the ultrasound image quality via a local focusing criterion and a matrix aberration correction; (ii) develop novel quantitative imaging modes by building maps of the speed-of-sound and of a multiple-scattering-rate that may constitute relevant biomarkers for ultrasound diagnosis; (iii) characterize locally the nature and anisotropy of the scatterers via their frequency response and radiation pattern.

More generally, this work falls into a larger framework, which aims to develop a universal matrix approach that can be applied to any type of waves where multiple sensors can be used to shape incident wave-fronts and analyze reflected ones. This thesis describes this matrix approach in the ultrasound imaging context and paves the way towards a quantitative ultrasound imaging of soft tissues.

KEYWORDS

ULtrasound, Imaging, Aberration, Multiple scattering, Matrix approach, Speed of sound